Hisham Abu Samra

Novel Multi-Component Thin Films Prepared by Microwave Plasma Enhanced Chemical Vapour Deposition

Novel Multi-Component Thin Films Prepared by Microwave Plasma Enhanced Chemical Vapour Deposition

DISSERTATION

zur Erlangung des akademischen Grades eines
Doktors der Ingenieurwissenschaften

(DOKTOR-INGENIEUR)

vorgelegt von
M.Sc. Hisham Abu Samra
aus Jordanien

eingereicht bei der Naturwissenschaftlich-Technischen Fakultät
der Universität Siegen

Referent: Prof. Dr. rer. nat. habil. Xin Jiang

Korreferent:Prof. Dr. rer. nat. habil. Hans-Jörg Deiseroth

Ort und Tag der mündlichen Prüfung: Siegen, den 28. Oktober 2013

Zusammenfassung

In der vorliegenden Arbeit wurden verschiedene Hartstoffschichten hergestellt, sowie deren chemischen, mikrostrukturellen, mechanischen und tribologischen Eigenschaften charakterisiert um neue Möglichkeiten bei der Synthese solcher Beschichtungen aufzudecken und deren vielseitige Eigenschaften aufzuklären. Ziel dieser Untersuchungen ist es, neue und potentiell hochleistungsfähige Beschichtungen zu entwickeln, die die Leistungsfähigkeit und Lebensdauer von Werkzeugen und anderen Bauteilen erhöhen. Folgende, neuartige Multikomponenten-Schichten wurden entwickelt und werden hier diskutiert: (a) Nanokomposite basierend auf dem System Mo-B-N, und (b) verschiedene Dünnschichten, basierend auf dem leicht-Elemente System Si-B-C-N-O.

Um die erfolgreiche Synthese solcher Materialien zu ermöglichen, kommt die Elektronenzyklotronresonanz Mikrowellenplasma-unterstützten chemischen Gasphasenabscheidung (ECR-MWCVD, engl. Electron cyclotron resonance microwave plasma assisted chemical vapour deposition) zum Einsatz. Im Falle des ternären Mo-B-N Systems wurde eine Hybridtechnik aus ECR-MWCVD und ionenstrahlgestütztem Beschichtungsverfahren verwendet. Hierbei kam ein Gasgemisch aus BF_3-Ar-H_2-N_2 in He-Plasma zum Einsatz zusammen mit DC-gespannte Gitter-system aus Molybdän, um eine möglichst hohe Konzentration ionisierten Molybdäns in der Gasphase zu erreichen. Weiterhin wurde ein $Si(CH_3)_4$, CH_4, BF_3-Ar, N_2 und He Gasgemisch in H_2-reichem Plasma verwendet um verschiedene keramische Schichten im Si-B-C-N-O System abzuscheiden. Eine Anpassung der Stöchiometrie aller hergestellten Komponenten, deren Phasenzusammensetzung sowie der Struktur der Nanokomposite, verlangt eine genaue Kontrolle der Zusammensetzung der Gasphase und der Partikelenergie. Um ein tieferes, fundamentales Verständnis der Zusammenhänge zwischen Abscheidungsprozess, Struktur und Eigenschaften zu entwickeln, wurde eine Fülle analytischer Verfahren zur Aufklärung der chemischen, mikrostrukturellen, mechanischen und tribologischen Eigenschaften verwendet.

Die Ergebnisse der Experimente im Mo-B-N System zeigen, dass sowohl die Mikrostruktur als auch die Phasenzusammensetzung der Schichten kontrolliert werden können, indem die Zusammensetzung der Precursorgase entsprechend eingestellt werden. Um die oberflächennahen Reaktionen der Elemente Mo und B zu unlöslichen Nitriden mit komplexer Bindungsstruktur zu ermöglichen, ist die Beimischung von H_2 und BF_3 notwendig. Beobachtungen weisen darauf hin, dass Bornitrid bei den eingestellten Wachstumsparametern vollkommen amorph bleibt, während

die konkurrierenden Wachstumsprozesse des kristallinen Molybdännitrids zu einer Kornfeinung dieser Phase führen. Die Auswirkungen auf die Mikrostruktur, wie Morphologie, mikro- und makroskopische Spannungen, sowie Kristallitgrößen und -Verteilungen der Nanokomposite wurden im Hinblick auf die Schicht Zusammensetzung untersucht. Weiterhin besitzen die Schichten nanomechanische und tribologische Eigenschaften, die direkt mit deren Mikrostruktur und chemischer Zusammensetzung in Verbindung gebracht werden können. Wenn auch alle abgeschiedenen Schichten eine hohe Härte besitzen, fällt diese ab wenn der Anteil der weicheren BN Phase ansteigt. Nanokomposite mit einer bestimmten Zusammensetzung und Mikrostruktur zeigen eine verbesserte Elastizität und Widerstandsfähigkeit bei Untersuchungen mit dem Nanoindenter. Darüber hinaus zeigen Nanokratztests niedrige Reibkoeffizienten speziell bei solchen Nanokompositen, die die höchsten Elastizitäten aufweisen.

Multikomponenten-Hartstoffschichten basierend auf dem System Si-B-C-N-O zeigen eine Reihe attraktiver mechanischer und tribologischer Eigenschaften in Verbindung mit hoher thermischer Stabilität und Oxidationsbeständigkeit. Die Zuführung von Silizium ins Bindungsnetzwerk hat einen positiven und wesentlichen Einfluss auf die Minderung der Spannungen, die während des Beschichtungsprozesses entstehen. Wird bei geringen Substrat-Bias Spannungen und moderaten Substrattemperaturen abgeschieden, entstehen vollkommen amorphe, sehr glatte und hoch adhäsive Schichten bis zu hohen Dicken und auf einer breiten Palette von Substraten. Durch das Anpassen der Gas Zusammensetzung kann nicht nur die Schicht Zusammensetzung, sondern auch deren mechanische und tribologische Eigenschaften eingestellt und entsprechend modifiziert werden. Untersuchungen decken die Komplexität der chemischen Bindungen der Schichten auf. SiCNO Schichten bestehen zum größten Teil aus SiN_x und SiC_x Struktureinheiten, während bei SiBCNO Schichten Bor fast ausschließlich mit Stickstoff Bindungen eingeht. Schichten mit höherem Bor Gehalt zeigen einen erhöhten Anteil an B-C Bindungen. Das Bindungsnetzwerk besteht hier aus SiC_x und SiN_x zusammen mit $(BN)_x$ und $(BCN)_y$ Grundeinheiten. Durch diese Reihe an möglichen Zusammensetzungen ist es möglich die mechanischen Eigenschaften zu verändern bei gleichzeitigem Erhalt der Mikrostruktur. Unter einer bestimmten Zusammensetzung, zeigten die eine maximale Schichthärte von 24 GPa zusammen mit sehr höhe Elastizität von mehr als 90% und eine erhöhte Härte-zu-reduzierte Elastizitätsmodul verhältnis (H^3/E_r^2) von 0,5 GPa. Darüber hinaus wurde das tribologische Verhalten von SiCNO und SiBCNO Schichten, unter verschiedenen Lasten, Oberflächenbeschaffenheiten und Temperaturen untersucht. Bei der Untersuchung unter Umgebungsbedingungen bei Raumtemperatur zeigt sich ein extrem geringes Reibungsverhalten zwischen SiCNO bzw. SiBCNO und Diamant unter sehr kleinen Lasten. Das Hinzufügen von Bor verringert die Reibung, reduziert aber nicht wesentlich die Härte. Dagegen steigen die

Reibungskoeffizienten, wenn nach der Beschichtung eine Temperung bei 100– 400°C durchgeführt wird. Außerdem zeigen *in-situ* Tests bei Temperaturen bis 400°C gegen Aluminiumoxid ein verbessertes Reibverhalten der Schichten. Im Vergleich zu SiCNO, zeigen SiCBN Schichten eine geringere Reibung im Temperaturbereich zwischen 100 – 300°C.

Genaue thermische und spektrometrische Untersuchungen an Si-B-C-N-O Schichtsystemen zeigen eine hohe thermische Stabilität und Oxidationsbeständigkeit sowohl in inerter-, als auch in Umgebungsatmosphäre bei Temperaturen bis 1350°C. Die hohe thermische Stabilität der Schichten rührt von dem erweiterten Netzwerk starker chemischer Bindungen her, wohingegen die hohe Oxidationsresistenz durch Bildung einer passivierenden Oxidschicht auf der keramischen Schicht herrührt. Dieser entstandene Oxid-Panzer wurde hinsichtlich seiner Mikrostruktur und oberflächennahen Zusammensetzung durch spektroskopische und spektrometrische Untersuchungen aufgeklärt.

Weiterhin wurden Zusammenhänge zwischen tribologischem Verhalten, mechanischen Eigenschaften sowie oberflächennaher Zusammensetzung hergestellt um daraus die verschiedenen resultierenden Schichteigenschaften zu Erklären. Bei ultra-kleinen Lasten zeigte sich, dass die Reibungskoeffizienten bei steigendem, reduziertem Elastizitätsmodul steigen und beinahe exponentiell mit steigendem H/E_r Verhältnis abfallen. Es zeigt sich, dass der Reibungskoeffizient eng mit Änderungen der chemischen Zusammensetzung und der Terminierung der Oberfläche verknüpft ist. Ergänzende spektrometrische Untersuchungen zeigen, dass frisch abgeschiedene SiCNO und SiBCNO Schichten den höchsten Wert rückständigem Wasserstoff besitzen, der durch den im Beschichtungsprozess reichlich vorhanden Wasserstoff zurückbleibt. Dies führt zu sehr kleinen Reibkoeffizienten wenn mit einem Diamant-Gegenkörper geprüft wird. Wird nun bei 100-400°C getempert, bilden sich Hydroxyl-Gruppen an der Oberfläche. Bei Verwendung des Diamant-Gegenkörpert führt dies zu einer Erhöhung der Reibwerte. Diese Erhöhung war vor allem bei Temperaturen zwischen 100 und 200 °C zu messen, wobei SiCNO und SiBCNO beinahe das gleiche Verhalten zeigen. Führt man den tribologischen Test, nun aber mit einem Aluminiumoxid-Gegenkörper durch, wirkt die Hydrohyl-terminierte Oberfläche als Selbstschmierstoff und führt somit zu verminderter Reibung und vermindertem Verschließ. Die dargestellten Ergebnisse zeigen, dass bei genauer Kontrolle der Zusammensetzung und Struktur, die mechanischen Eigenschaften und das tribologische Verhalten der Schichten eingestellt werden können. Schichten mit verbesserter Elastizität und verminderter Reibung können ebenfalls in Systemen mit weniger Kohlenstoff und einer kleinen Beigabe Bor erreicht werden.

Abstract

In this work, the synthesis as well as chemical, microstructural, mechanical and tribological characterisation of several hard thin film systems were carried out to seek new synthetic routes for such surface coatings and to elucidate their range of properties. This was done to unveil novel and potentially high performance surface coatings which can be engineered to improve the performance and life expectancy of tools and diverse mechanical parts. The thesis will discuss the development of several novel mutli-component thin film systems, namely: (a) nanocomposites based on the Mo-B-N system, and (b) thin films based on the light elements Si-B-C-N-O system.

To enable the successful synthesis of such materials, magneto-active electron cyclotron resonance microwave plasma was used to assist in their chemical vapour deposition. In the case of thin films belonging to the Mo-B-N system, a hybrid ECR-MWCVD and ion-beam assisted deposition was implemented with a gas mixture consisting of BF_3-Ar-H_2-N_2 in He-plasma in order to ensure the *in-situ* generation of highly ionised molybdenum in the vapour phase. Furthermore, the deposition of thin films in the Si-B-C-N-O system was carried out by using a gas mixture of $Si(CH_3)_4$, CH_4, BF_3-Ar, N_2 and He in H_2-rich plasma. The stoichiometry of all the deposited compounds and the phase composition and structure of the nanocomposites which ensued were varied by adjusting gas phase composition and particle energy during deposition. A host of analytical methods were used to detail and elucidate the films' chemical, compositional, microstructural, mechanical and tribological characterisation properties in a bid to gain a deeper and fundamental understanding of their deposition process-structure-property relationships which impact their growth.

Experimental results indicated that both the microstructure and phase composition of the thin films in the Mo-B-N system can be modified by controlling the ratios of the precursor gases. Surface reactions leading to the simultaneous formation of two insoluble nitrides of the elements Mo and B with a complex chemical bonding nature were only possible by the addition of H_2 and BF_3. Analysis indicated that while boron nitride remained totally amorphous in the nanocomposite at the implemented growth conditions, the competitive growth process resulted in grain size refinement of the crystalline molybdenum nitride phase. The effects on the nanocomposite microstructure including morphology, micro- and macroscopic strain as well as domain sizes and distribution were all investigated and correlated with film composition. In addition, the thin films possessed nano-mechanical and tribological properties that were a direct consequence of their microstructure and chemical composition. Although all deposited films were hard, their hardness dropped as a result of increasing the proportion of the softer BN

phase. Nanocomposite films which were synthesised with a particular composition and microstructure exhibited enhanced elasticity and resilience as determined by Nanoindentation. Moreover, nanoscratch testing of the nanocomposites by Nanoindentation revealed low friction coefficients particularly with those of highest elasticity.

Multi-component hard films in the Si-B-C-N-O system demonstrated a range of attractive mechanical, tribological properties coupled with a high thermal stability and oxidation resistance. The introduction of silicon to the bonding network had the beneficial and significant effect of relaxing the film's growth stresses. When grown at low substrate biases and moderate substrate temperatures, totally amorphous, very smooth and strongly adhesive films were deposited to large thicknesses on a wide range of substrates. Not only could film composition be varied by adjusting the gas composition, their mechanical and tribological properties could be controlled and modified. Analysis revealed a complex nature of the films' chemical bonding. SiCNO films consisted mainly of SiN_x and SiC_x structural units, whereas in SiBCNO films, boron bonded almost exclusively with nitrogen. Films with a higher boron content featured increasing proportions of B-C bonds and the bonding network consisted of SiC_x and SiN_x together with $(BN)_x$ and $(BCN)_y$ structural units. As a consequence of these varied possibilities of compositions, the films' mechanical properties could be modified while keeping their microstructure unchanged. Film hardness reached a maximum of 24 GPa while having a hardness-to-reduced modulus ratio (H^3/E_r^2) ratio in the order of 0.5 GPa and maintaining high elastic recovery of more than 90%. The addition of small amounts of boron led to a slight increase in hardness and resilience. Moreover, the tribological behaviour of SiCNO and SiBCNO films was investigated in various loading regimes, surface conditions and test temperatures. When investigated at room temperature and ambient conditions, both SiCNO and SiBCNO exhibited superior low friction coefficient against diamond at ultra-low loads. The small additions of boron, while it did not significantly decrease hardness, results in reduced friction. However, friction coefficients increased after post-deposition annealing in the temperature range 100- 400°C. Moreover, reciprocating sliding at *in-situ* elevated temperatures up to 400°C and ambient conditions against alumina generally revealed an improved film performance. SiBCNO films had lower friction in the temperature range 100- 300°C when compared to SiCNO.

In addition, detailed thermal and spectrometric analysis of the Si-B-C-N-O films system revealed a high thermal stability and oxidation resistance up to 1350°C in both inert and ambient atmospheres. The films' high thermal stability was a result of the extended network of strong chemical bonds while the high oxidation resistance was attributed to the formation of passivating

oxide layers which formed on the ceramic film. Spectroscopic and spectrometric analyses were used to detail the microstructure and surface composition of the formed oxide scale.

In addition, correlations between the films' tribological behaviour, mechanical properties as well as surface composition were established and used to explain the variations in film behaviour. At ultra-low loads, the friction coefficients were found to increase with increasing the films' reduced elastic moduli and decreased almost exponentially with increasing the H/E_r ratio. The friction coefficient was found to be closely linked to changes in chemical composition and surface termination. Complementary spectrometric analysis revealed that as-deposited SiCNO and SiBCNO had the highest amount of residual hydrogen as a result of ubiquitous remains from the deposition process. This led to very low friction coefficients when tested against a diamond indenter. When annealed between 100- 400°C, the surfaces became populated with hydroxyl-groups causing the increased friction coefficient against diamond. This increase was most prominent for surfaces annealed between 100- 200°C and both SiCNO and SiBCNO films showed a somewhat similar behaviour. On the other hand, when tested against an alumina indenter, the hydroxyl-terminated surfaces provided a low shear layer which acted as a self-lubricator and contributed to a decrease in friction and wear. The obtained results demonstrate that it is possible to control the film's mechanical properties and tribological behaviour by adjusting film composition and structure. Films with improved elasticity and reduced friction could also be obtained in compositions with less carbon and slight addition of boron.

Acknowledgment

Firstly, I would to like to express my never ending gratitude to God Almighty for the countless blessings which He has bestowed upon me and for giving me the strength to conduct this work. May God accept this humble work as a contribution to the existing body of knowledge which serves to advance mankind.

Secondly, I would like to express my gratitude to my supervisor Professor Dr. Xin Jiang, for inspiring me to delve into the remarkable realm of thin films technology, for giving me the opportunity to carry out this research in his laboratories and for allowing me to conduct it with a high degree of autonomy while continuously giving his invaluable support and advice. I would also like to acknowledge the financial funding provided by the German Research Foundation (DFG JI 22/10-1).

Throughout this journey, I was fortunate to be surrounded by a collaborative group of friends and colleagues at the Chair of Surface and Materials Technology and to embark on an exciting and mutual learning process in the quest for new materials. Special thanks go to the following individuals: Thorsten Staedler for carrying out the Nanoindentations and for the countless stimulating discussions we had throughout this work. Thomas Degen whose technical assistance was central to the success of the deposition experiments and whose unique sense of humour was a welcome relief when things did not go right. Michael Vogel for numerous fruitful discussions pertaining to reactor design concepts and in assisting in the preparation of technical drawings as well as in editing the German abstract. Carsten Muders who was there ready to help and listen. Petra auf dem Brinke who introduced me to microscopy and assisted in metallographic sample preparation and imaging. Junhai Xia for assistance in taking high resolution transmission electron micrographs and acquiring electron diffraction data. Aditya Kumar for conducting Nanoscratch testing. Igor Aronov for carrying out tof-sims measurements. Roberto Verucchi from the Institute of Materials for Magnetism and Electronics in Trento for carrying out selected X-ray photoelectron spectroscopy measurements. Torsten Kowald for carrying out selected X-ray diffraction measurements on the Philips X'Pert diffractometer. Christian Pritzel for carrying out Thermogravimetric measurements. Wolfgang Kramer for giving me access to the X-ray diffractometer at LMW.

Last but not least, I would like to express my gratitude to my patient and supportive wife who never ceased to see the light at the end of the tunnel, who was a true companion through all the ups and downs that accompanied my research journey, and without whose believe in me I would not have gotten to this stage. And to my darling daughter whose arrival was a great highlight and coincided with the conclusion of this work.

Table of Contents

List of Symbols and Abbreviations

Symbols

%	percentage
&	and
(hkl)	crystallographic plane with the Miller indices (hkl)
[hkl]	crystallographic direction
~	ca.
<	less than
$<D_S>$	area-weighted grain size
$<D_V>$	Volume-weighted grain size
$<\varepsilon>^{1/2}$	root-mean-square strain
>	greater than
±	uncertainty
≤	less than and equal to
°	degree
°C	degrees Celsius
μ	Coefficient of Friction
a	lattice parameter
A	contact area
Å	Angstrom
$A_D(L)$	disorder (strain) coefficient
amu	atomic mass unit
$A_S(L)$	size coefficient
at.	atomic
A_x	integral area of the core level spectrum of element x
c	lattice parameter
C_x	atomic concentration of element x
D	Diffractometre's axis
D	Diameter
d	Grain diameter
$d_{0,hkl}$	Lattice spacing of the stress-free plane (hkl)
d_{hkl}	interplanar spacing of the crystallographic plane (hkl)
$d_{\psi,hkl}$	Lattice spacing of the plane (hkl) at a tilt angle of andψ
E	Elastic modulus (Young's Modulus)
e^-	electron
E	a residuals matrix
E_r	Reduced Elastic Modulus
eV	electron volt
eV	electron volt
F	flow rate
F	Friction
F_L	lateral (tangential) force
F_N	normal force

Γ_C	integral breadth of the Cauchy (Lorentz) function
Γ_{CD}	integral breadth of the Cauchy (Lorentz) function corresponding to strain broadening
Γ_{CS}	integral breadth of the Cauchy (Lorentz) function corresponding to size broadening
Γ_G	integral breadth of the Gauss function
Γ_{GD}	integral breadth of the Gauss function corresponding to strain broadening
Γ_{GS}	integral breadth of the Gauss function corresponding to size broadening
GHz	Gigahertz
GPa	10^9 Pascal
H	Hardness
h	hour
h_L	lateral displacement
h_N	normal displacement
i	matrix rows
I	Intensity
i	Indenter
φ	rotation angle about D_3
j	matrix columns
k	wear coefficient
k	kilo
K	Kelvin
K_α	K alpha X-ray emission line
$L = n\lvert a_3 \rvert$	column length of cells along the a_3 direction
L·λ	TEM camera constant
LO	longitudinal optical phonon
m	milli
m	mass
min.	minute
MPa	10^6 Pascal
n	nano
ν	Poisson's constant
p	pressure
π	pi
P	Probability
Pa	Pascal
PE	Pass Energy
ppm	parts per million
P^T	a transposed matrix which contains the loadings
θ	Bragg diffraction angle
r	radius
R	Residual Sum of Squares
rms	root-mean-square

R_{rms}	root-mean-square Roughness
s	second
$\boldsymbol{s}$	scattering vector
$\boldsymbol{\sigma}$	shape parameter
sub	Substrate
S/N	Signal-to-noise ratio
$\sigma_{Lattice}$	Lattice friction stress
σ_{macro}	macroscopic stress
σ_{micro}	microscopic stress
σ_{th}	thermal stress
σ_{yield}	Yield stress
T	temperature
T	Tesla
τ	shear strength
$\boldsymbol{T}$	a matrix which contains the scores
TE	Transverse Electric
TM	Transverse Magnetic
TO	transverse optical phonon
υ	wavenumber
V, v	volt
W	watt
W_{el}	Elastic recovery
$\boldsymbol{X}$	matrix
X	Specimen axis
ψ	tilt angle about D_1
z	elementary charge
α	grazing-incidence angle
Γ	Full-width at half maximum
Δ	difference
ε	emissivity factor
$\varepsilon_{\varphi\psi}$	Lattice strain at a rotation and tilt angles of φ and ψ, respectively.
λ	wavelength
μ	micro
ω	rotation angle about D_2
z	elementary charge of +1

Abbreviations

a-	Amorphous
a-C:H	Hydrogen containing amorphous carbon
AES	Auger electron spectroscopy
AFM	Atomic force microscopy

AS	Anti-symmetric or asymmetric
BE	Binding Energy
CDD	Coherently diffracting domains
COF	Coefficient of friction
CTE	Coefficient of thermal expansion
CVD	Chemical vapour deposition
DC	Direct current
DLC	Diamond-like carbon
ECR-MWCVD	Electron cyclotron resonance microwave plasma-enhanced chemical vapour deposition
EDS	Energy dispersive X-ray spectroscopy
EsB	Backscattered Electrons
fcc	face-centred cubic
FESEM	Field-emission scanning electron microscopy
FTIR	Fourier-transform infrared
FWHM	Full width at half maximum
GI-XRD	Grazing incidence X-ray diffraction
HAC	Hierarchal Agglomerate Clustering
HRTEM	High resolution transmission electron microscopy
ICSD	Inorganic Crystal Structure Database
IR	Infrared
JCPDS	Joint Committee for Powder Diffraction Service
LO	Longitudinal Optical
MFC	Mass Flow Controller
MVA	Multivariate Analysis
nc-	Nanocrystalline
PC	Principal Component
PCA	Principal Components Analysis
PDF	Powder Diffraction Data
PECVD	Plasma enhanced chemical vapour deposition
PVD	Physical vapour deposition
RF	Radio frequency
RH	Relative humidity
RT	Room temperature
SAED	Selected area electron diffraction
sccm	Standard cubic centimetre per second
SE	Secondary Electrons
SEM	Scanning electron microscopy
TEM	Transmission electron microscopy
TO	Transverse Optical
ToF-SIMS	Time-of-flight secondary ion mass spectrometry
XPS	X-ray photoelectron spectroscopy
XRD	X-ray diffraction
XSF	X-ray photoelectron sensitivity factor

1   Theoretical Background and General Aspects

Engineering a surface by coating it with a thin film is a concept that has long been pursued in order to give the coated surface a whole range of advantageous and beneficial properties which will aid specific applications. Both the thin film, which forms a surface coating, and the underlying substrate form a composite whose resultant traits emerge from a combination of characteristics which both parts provide. The notion behind surface engineering is that these new surface characteristics supersede those of uncoated or monolithic materials. Thus, the central aim of surface engineering is to modify the properties of bulk materials through the use of surface coating-substrate composites to aid specific applications. Engineering surfaces of technically important tools entails tailoring their chemical and physical properties to meet specific functions for an improved performance. As far as tribological applications are concerned, these new qualities enable the material to be compatible for use in hostile and aggressive environments and to have an improved resistance to corrosion, a heightened tribological performance with reduced wear and friction as well as to have the right balance between rigidity and compliance. For such applications, properties such as: adhesion, cohesion, friction, wear; hardness and elasticity as well as oxidation resistance, all have a direct influence on the performance and life time of the coated parts.

In this context, various thin film materials, design concepts as well as architectures have emerged and been implemented to overcome classical problems and limitations of bulk monolithic materials and improve tool performance under severe conditions. Strategies including the design of multi-functional nanocomposite coatings have proved successful and demonstrated improved performance.

1.1   A General Background

1.1.1   The Quest for Novel Hard Thin Films

In the area of hard thin films, considerable efforts have been made to synthesise hard materials due to their superior abrasion resistance. Classically, hard materials such as diamond, cubic boron nitride, and silicon carbide were successfully fabricated and applied to technical tools. While the fabrication of some of these materials have been mastered, considerable efforts are still being made to improve their deposition process. The enormous challenge associated with other materials may be attributed to finding ways of fabricating stable and adhesive surface coatings. Despite these challenges, such materials continue to arouse a lot of interest due to their hardness. Hardness is a complex property which is a measure of the ability of a material to resist plastic

deformation and is associated with a number of factors that are related to the nature of the material's chemical bonding and the degree of its structural imperfections.

Chemically, a hard material forms extended networks of high density together with a high bonding energy of the covalent bonding [1]. What diamond, cubic boron nitride, and silicon carbide have in common is a highly symmetric extended network of tetrahedrally and singly bonded atoms. In the absence of structural imperfections such as defects and dislocations, such materials are very stiff as they are difficult to deform elastically, and accordingly have large bulk and elastic moduli. These constants are related to the materials' resistance to deformation in volume and along linear directions. Diamond is the hardest material known and as such has the highest hardness and bulk modulus of all materials peaking at 100 GPa and 443 GPa, respectively. [2] It is followed by cubic boron nitride which has a hardness and bulk modulus of about 53 GPa and 369 GPa, respectively. [3,4,5,6].

Understanding hardness from this perspective has led to considerable efforts being made in order to theoretically visualise and empirically synthesise covalently bonded materials which consist of light elements. This is due to their ability to form extended structures consisting of short single covalent bonds just like diamond and cubic boron nitride. Examples of this include: a hexagonal modification of carbonitride known theoretically as β-C_3N_4 [7,8,9] as well as isomorphous to β-Si_3N_4 and more recently, the cubic and stoichiometric modification of boron carbonitride that is known theoretically [10] as c-BNC_2 and which is isomorphous to both diamond and cubic boron nitride. Despite tremendous efforts to synthesise and fabricate β-C_3N_4 in the form of thin films [11,12], as of yet there are no known carbonitrides with a hardness that is anywhere near diamond. In the case of boron carbonitride, it is only recently that hard cubic phases have been realised. These have been fabricated using a high-temperature and high-pressure (HPHT) technique, which yielded a maximum hardness of about 66- 73% of that of diamond and 123-132% of that of cubic boron nitride [13,14,15] however, they still do not exist in the form of a thin film.

The importance attached to chemical bonding has also led to the synthesis of hard materials in another direction, which include a wide range of transition metal oxides and borides that combine high bulk modulus metals and light elements which have the ability to form strong covalent networks [16,17]. Successful examples include RuO_2 [18], $(Os,Ir)B_2$ [19], and ReB_2 [20,21,22] which further expands the list of potential hard materials.

The previous perspective to defining hardness, which helped in understanding the reason for monolithic materials being hard, is commonly referred to as intrinsic hardness [23]. Yet another

definition has emerged in the past two decades following advances in thin films deposition by plasma-assisted vapour deposition methods, which focuses on the micro- and nano-structural reasons for hardness [23, 24, 25]. Such hardness is now commonly referred to as extrinsic hardness. In essence, this approach has been based on the fact that resistance to plastic deformation is also related to the material's ability to suppress the propagation of dislocations that are generated within the material when it is subjected to stresses with loadings that exceed the material's yield strength. This is made possible by the careful control of the material's micro- and nano-structure such that the grains of the material are made to be small enough so that dislocations do not form in them. This also has the effect of suppressing the dislocation movement by forming energy barriers which require more energy to be given to the dislocation in order for it to propagate. Such behaviour has been observed in a form of diamond with ultrafine grains known as "carbonado" [26,27,28]. Early observations of this material revealed that its hardness and toughness exceed those of single crystal diamond [29]. These observations were known even at a time when increasing the material's hardness and resistance to crack generation by refining its micro structure was not fully accessible from a practicable material's synthesis point of view. However, the advent of the nanotechnology era that currently dominates both the research and development of hard thin films, has opened up numerous possibilities which enable the controllable refinement of the material's structure at the nano-level. This has marked the emergence of a central concept, that is, using multi-component nanocomposites in thin film design and fabrication.

1.1.2   Microstructural Design of Hard and Tribological Thin Films

Ever since its initial introduction and particularly during the last two decade, the concept of designing and synthesising multiphase nanocomposite thin films has been a subject of intense research. These nanocomposites usually comprise microstructures with a nanocrystalline phase whereby the crystallite or grain size is less than 100 nm and are subsequently homogenously dispersed in either an amorphous matrix or another nanocrystalline phase. Such nanocomposites are classified according to the class of their basic constitutes as well as to their micro- and nano-structure. One of the widely spread and accepted classifications [30] categorises the materials into two main categories with regards to the crystallinity of their constituent phases. The first describes nanocomposites which are totally crystalline, whereas the second describes a class in which at least one phase takes on an amorphous structure. Several material types have the ability to fall into these two classes, however, the most widely researched include the boride, carbides, nitrides and the oxides of both metals and non-metals.

As previously mentioned, the main reason behind designing materials in this way is to uncover new possibilities which aim to improve the materials' resistance to plastic deformation. This is achieved through the fabrication of materials which not only have high bulk and shear moduli, as well as low defect densities but which also have a heightened ability to resist crack propagation through the refinement of their micro structure. Obtaining such a result depends on being fully cognisant of the mechanisms which act to increase the strength of materials with ultrafine grains. Numerous high resolution microscopy observations have, in fact, provided strong evidence which indicates that nano-sized cracks and dislocations hardly ever exist within grains with sizes less than 40 nm [31]. When considering the Hall-Petch relationship, [32, 176,177] which describes the parabolic dependence of material strength on its grain sizes as the basis for understanding the relationship between materials deformation and grain size, it emerges that there exists a threshold for maximum materials strength. This threshold corresponds to a grain size in the order of 5- 15 nm which also changes with the material type. Grain shape and distribution are other decisive factors which contribute to strength enhancement in nanostructured materials. At grain sizes lower than this threshold, the material behaves in a viscous manner as in the case of amorphous structures. Materials with coarse grains accommodate dislocations generated by the application of stresses as they have plenty of room to propagate thereby leading to plastic deformation. The peculiar enhancement of hardness and strength in nanostructured materials whose grain sizes lie within the aforementioned threshold is understood to be related to the special inter-granular interactions and processes that take place within the materials [33,34,35,36]. At these nano-sized grains, there is a change in material deformation at the microscopic scale whereupon the mechanism ceases to be mediated by the dislocation propagation in grains with large sizes and becomes controlled by grain boundary sliding in nanocrystalline regions.

In view of the above, it becomes evident that considerable benefits can be gained when the materials takes on a nano-sized structure. That said, two main challenges still remain. The first lies in providing a more universal understanding of the actual mechanisms that act to provide this strength enhancement in nanocrystalline materials. The second is related to finding preparation methods which would enable a high degree of structural control of thin films in such a way that materials with well-defined grain sizes within the grain threshold of 5- 15 nm and with controllable shapes can be synthesised.

1.1.3   The Importance of Thin Film Toughness

For a long time, thin film development relied on surface hardness as the central material property when designing surfaces to be wear resistant. This was guided by dominant notions which

postulated that wear is inversely proportional to hardness [37]. Although surface elasticity was believed to be another important factor in determining wear behaviour; indeed a factor which should be taken into consideration when designing thin films, it was for the most part neglected with the exception of a branch of technical science and engineering that was concerned with the development of bearings. Bearing designers used a parameter called the "plasticity index" when attempting to choose a combination of suitable mechanical properties and surface finish that would reduce the degree of plastic deformation which the bearings were subjected to in operation [38]. This parameter included the ratio of hardness to elastic modulus of the material. In fact, these early findings revealed the importance of the relationship of wear to the ratio of hardness to elasticity [39]. However, it was also observed that these two properties (i.e. hardness and elasticity) are interrelated such that high hardness usually means high elastic modulus, and therefore, it was not fully permissible to vary one without the other being fully affected.

It took a long time before thin film design was guided by this parameter (i.e. the ratio of hardness to elastic modulus; H/E) when defining wear resistance. The past decade has witnessed a surge of new research and development aimed at optimising the properties of surfaces to suit wear resistance applications by relying on the mutual control of both hardness and elasticity [40]. These efforts were met with success after advanced thin film preparation methods were introduced which enabled a great deal of control over the films' micro and nano-structure.

The importance of the ratio of hardness to elastic modulus stems from the fact that it defines the elastic strain to material's failure. In a conventional stress-strain diagram, the elastic modulus is the slope of the elastic region of the stress-strain curve. The elastic strain to failure is defined by the yield stress, and the slope that is related to the extent to which a surface can be stretched before it yields. A loaded surface with a high H/E ratio can accommodate more stresses before it deforms plastically.

As previously mentioned, engineered surfaces and thin films form composite structures with the underlying substrate. It is therefore essential to achieve compatibility between both thin films and substrate. Ceramic thin films are stiff by virtue of their high hardness, whereas a great proportion of the technically important substrates are compliant and significantly more elastic metallic materials. The successful mating between a thin film and a substrate involves mediating a range of mechanical and thermal properties between them. Therefore in designing thin films, from a mechanical-properties point of view, the thin film must be able to have a heightened degree of compliancy and be able to stretch with the substrate with reduced or no failure, even if the substrate itself deforms plastically. This may be possible by designing a coating with the appropriate ratio of H/E. Numerous examples in the literature demonstrate advanced hard thin

films that have a high degree of compliancy by flexing with the substrate. These include multilayered and nanostructured thin films.

Another form of the ratio of hardness to elastic modulus can be expressed as H^3/E^2 [41,42,43,40]. This parameter resulted from the consideration that when a hemispherical indenter loading a surface, the load which the surface can accommodate before it yields is defined by H^3/E^2. This means that if the surface has a high degree of elasticity, then the contact area with the indenter increases upon loading. A surface with a high ratio of H^3/E^2 requires much higher loads in order to plastically deform simply because the interfacial contact area will stretch. This shows that by having a proper ratio of these parameters, the surface will absorb the energy elastically and, therefore, is less likely to wear and fret.

In addition, when considering the overall thin film toughness (both elastic and plastic toughness), the ability of a surface to absorb energy and recover elastically, and the degree of its plastic deformation are all important factors which should be taken into account when designing hard thin films for tribological applications. The total toughness of a thin film is not merely defined by the area under the elastic part of the stress-strain curve but by the whole curve. This indicates that in order to increase the compliancy of a hard thin film, it is better in certain cases for it to have a high degree of ductility. For example, results indicate an improved performance when a hard ceramic thin film contains ductile and more elastic constituents as in the case of multilayer thin films which consist of alternating metal/metal nitride layers [44,45]. It is now also commonly accepted and indeed very useful to utilise these ratios in order to rank thin films according to their suitability for specific tribological and wear resistance applications.

This high degree of control over H/E is only permissible when designing nanostructured thin films with an H/E ratio that is greater than 0.1. This value stems from the fact that in most materials, the hardness of a material is about 10% of its elastic modulus. Having an H/E > 0.1 means that the material is less stiff and therefore has a lower elastic modulus. Achieving this ratio is of great value especially when hard thin films have to show a greater degree of elasticity, and it is made possible by controlling the micro- and nano-structure of the thin film during growth [46].

Having discussed the microstructural design of hard thin films, it emerges that the very same structure which contributes to hardness and strength enhancement via grain refinement is indeed responsible for improving film toughness. The mechanisms which act to suppress and hinder the dislocation movements between the nano-sized grains have the result of increasing film toughness in nanocomposite thin films [47]. Accordingly, a design concept was proposed for hard and tough thin films which can also be applied very successfully to ceramic-containing

nanocomposites [23,24, 48] in which the film has a multi-component nanostructure. This structure is composed of different phases which are properly segregated based on thermodynamic and solubility rules. This segregation ensures that the grain boundary sliding of the nano-sized grains with sharp interfaces is lessened [33]. The crystallite or grain size must therefore be controlled such that it remains in the range of 3- 4 nm and is no more than 1 nm apart. There are numerous examples in the literature of hard nanocomposite thin films where their micro- and nano-structures are controlled in such a way so as to enhance their hardness and elastic modulus. This is made possible by carefully choosing the films' chemical composition and microstructure, both of which can be influenced and varied by the implemented deposition method and conditions [49,50,51]. A more comprehensive review of these examples can be found in [52,53]. All this opened up new possibilities for designing hard thin films with prescribed mechanical properties to suit specific applications.

1.1.4   Stress Evolution and Control

From a practical point of view, to surface engineer technical tools which are expected to perform under static or dynamic mechanical and thermal (also chemical) loading conditions, the growth stresses of the coated surfaces need to be kept at a low level. The excessive build-up of residual stresses in thin films is one of the major contributors to film failure and consequently the mechanical failure of the coated surface. It is, therefore, important to understand the origin of film stresses and its relationship to the micro- and nano-structure of the deposited thin films. This fundamental understanding is pivotal to controlling stress when producing successful coatings and coated tools. In polycrystalline thin films which are deposited by energetic plasma-enhanced vapour deposition (CVD and PVD) methods, the resultant residual stresses depend on a number of factors. These include: (i) the deposition temperature and thermal properties of both thin films and substrate as well as the degree of mismatch thereof; (ii) the extent of the incompatibilities in the elastic behaviour of the thin film and substrate; (iii) the degree of film-substrate structural mismatch; (iv) deposition conditions such as nucleation and growth dynamics, ion and atom energies, growing surface temperature and consequently adparticle (i.e. adsorbed particle, atom or ion) mobility. The plasma-enhanced vapour deposition processes (both PECVD and ionised-PVD) can be thought of as being under kinetic control since they are far from equilibrium [54]. As such, the kinetic energy which is imparted to the arrived particles (atoms and/or ions) by the ionising plasma determines various chemical and structural features such as bonding type, densification and the extent to which the defects are incorporated into the grown structures such as point or cluster defects, to name a few. Such effects are well understood

and commonly referred to as "atomic peening" [55] and have a central role in the fabrication of different materials types and microstructures [56].

The thermal stresses which arise from the incompatibilities in film-substrate thermal properties and from high temperature deposition lead to additional compressive contributions to the film's residual stresses. The extent of these types of stresses also depends on whether or not relaxation processes take place at high temperatures. As such, the compressive stresses may decrease or even become tensile due to processes such as grain growth, densification and creep processes [57]. Very often, a combination of all the aforementioned factors come into play giving rise to the film's residual stresses.

1.1.5   High Temperature Coatings Based on the Si-B-C-N System

Demanding technological applications require coated tools surfaces that have a multitude of functionalities (commonly referred to as multi-functional thin films and coatings). Tribological thin films used in wear resistance and tribological applications are not only required to provide adequate support and accommodate a significant proportion of the stresses elastically before deformation, but also have to have outstanding high temperature stability and provide lubricious surfaces to minimise friction and possibly wear. A lot of current research is devoted to designing what is commonly referred to as environmental thin films and surfaces. These are surfaces that trigger a specific functionality at the application conditions once in operation, which usually involves high temperatures, chemical aggressive and abrasive media as well as static and dynamic loadings.

For a hard thin film to achieve these combined characteristics, it should first enjoy a high temperature stability and durability. This means no structural degradation which affects the very same properties that made the film's mechanical behaviour attractive at room temperature. It was recently revealed that a range of transition metals and silicon-containing nanocomposite and amorphous thin films demonstrate outstanding thermal stability. The most comprehensively investigated thin film systems are based on nanocomposite nitrides of silicon and transition metals (nc-MeN/a-Si$_3$N$_4$) which demonstrate attractive stability up to 1000°C [58]. More recently it has been revealed that nanocomposites based on the oxides of silicon and zirconium retain their room temperature mechanical properties even when heated to temperatures as high as 1400°C [59]. In addition, investigations of hard and amorphous thin film systems based on the light elements Si-B-C-N have demonstrated an outstanding thermal stability and oxidation resistance up 1700°C [60]. The thin film does this by incurring no structural changes such as crystallisation, decomposition or degenerative oxidation at high temperature and by passivating

its surface by the build-up of a protective oxidation product that is both adhesive and impermeable; and which works as a diffusion barrier. Such materials continue to arouse significant interest because of their combined attractive properties including high hardness and high thermal stability. Recent investigations have shown how such material are potentially useful in the fabrication of thermally stable fibres [61,62] and in high temperature microelectronics [63].

1.1.6 Smart Tribological Nanocomposite Thin Films

There are strong correlations between the thin film's mechanical properties (H and E) and its tribological behaviour at room temperature. For example, it was found that nanostructured and multilayered thin films based on the Cr-N system demonstrate a sliding friction behaviour that is proportional to the films' elastic strain to failure [64]. Also, in thin films comprising Ti-C and Cu-C nanocomposites, there is a strong correlation between the films' resistance to plastic deformation and their reduced friction coefficients against inert surfaces such as diamond [65,66]. This highlights the importance of controlling the thin film nanostructure and hence mechanical properties when attempting to modify and improve its tribological behaviour.

In addition, the lubricious properties of hard thin films are of paramount importance whenever the thin film comes in contact with counter surfaces other than that of inert diamond such as in machining applications. Under such environments, reactive media which instigate a host of chemical reactions such as oxidation and diffusion define specific tribo-chemical interactions which directly influence the tribological performance of the surfaces. Recent studies on transition metal-containing nanocomposites [67,68,69] which utilise a combination of a hard and a soft phase, have demonstrated a reduced friction and wear as well as a unique tribological behaviour at elevated temperatures [70,71,72]. Such investigations were motivated by the fact that numerous classical lubricants such as graphite and molybdenum disulfide have failed to provide an adequate reduction in friction at elevated temperatures due to rapid oxidation and degradation at temperatures exceeding 350°C [73]. Nanocomposites which contain metals such as sliver and vanadium are among the most heavily researched owing to their ability to form oxides with layered structures upon exposure to high temperature. These layered oxides have been shown to have progressively low friction coefficients as the contact temperature approaches 1000°C. It should be mentioned that it is highly desirable for a hard thin film to trigger such a lubricious functionally at elevated temperatures without undergoing any structural degradation in its bulk. In so doing, the film maintains its mechanical properties and hence suitability for the application while experiencing improved tribo-contact.

1.1.7   Thin Film Deposition and Fabrication Methods

Although the direct implementation of the engineered surface is primarily concerned with the end product, the process with which the surface modification process is brought about is a key technological aspect. Available methods range from well- established techniques, which have long been implemented by the industry to increasingly complicated ones that have just recently come into use, and which are based on recent fundamental research activities. Of particular interest are plasma-assisted or plasma-enhanced chemical and physical vapour deposition methods which modify surfaces at atomistic levels. These techniques have developed to such an extent rendering them an essential part of surface engineering both at research level and at an industrial scale.

One central aspect with regards to these methods is their ability to produce highly energetic atoms and ions through the implementation of high density and highly ionising plasmas. In fully ionised plasma, energy is imparted to the growing films via ion bombardment. Upon arrival at the substrate surface, the high flux of ions and atoms permits chemical reaction pathways to take place that are not accessible under conditions of moderately low temperatures and ambient pressures. A significant proportion of the deposited thin film properties depends on both the energy and flux of plasma- charged particles and neutrals. As previously mentioned, very often the conditions imposed by plasma-enhanced vapour deposition are far from equilibrium which means that the kinetically-controlled pathways are the product-determining routes. Highly energetic ions are required to promote the formation of a strong chemical bonding in the growing surface which is a vital requirement for the synthesis of hard thin films. At the same time, it is also known that high ion energies and fluxes promote the build-up of large compressive macroscopic stresses in the grown films. This, as discussed previously, adversely affects film performance since the build-up of compressive stresses leads to film failure particularly when the surfaces are subjected to harsh thermal and mechanical loading conditions.

The basic relationships between ion energy, flux and stresses in the films mean that in order to produce films with low macroscopic stresses, the deposition method should ensure that the ion energy is maintained at low levels whereas ion flux is high. Selective surface reaction pathways are also central to the stabilisation of a specific chemical bonding in the grown surfaces. This also means that in addition to the importance attached to the ion/atom energies and flux, composition is also crucial. What is, therefore, highly desirable is a low pressure, highly ionising plasma activation with a great deal of flexibility in terms of choice of plasma controlling parameters and chemistry. Nonetheless, although improvements have already been made in the synthesis of these new hard materials, barriers for application still exist. For example, obtaining

high quality and good adhesive thin films still requires moderate to high growth temperatures, which may introduce damages to the substrate or introduce diffusion effects and make it impossible for some applications (e.g. deposition on cutting tools or metallic substrates). Very often, the synthesis parameter window for optimum film growth is too narrow and strict to ensure reliable reproducibility. All this imposes limitations as to the choice of method to be used in order to successfully deposit hard thin film. As such, thin film deposition methods which are enhanced by medium and high frequency low pressure plasmas induced by radio-waves or microwaves are among the best understood and most implemented to engineer hard and nanocomposite thin films.

1.1.8   Combinatorial Approaches to Thin Film Characterisation

The task of investigating and characterising hard thin films is a complicated one. The challenge lies in the wide spectrum of properties which need to be defined and measured in an attempt to successfully understand and control film growth to yield successful applications. Properties which range from: elemental and phase composition, chemical bonding, surface topography, micro- and nano-structure; structural imperfections such as strains and stresses; compositional and structural homogeneity across the thin film thickness; and mechanical as well as tribological properties must all be taken into consideration when fabricating hard thin films. In order to successfully fabricate new hard thin films, most of these properties must be investigated and correlated. In addition, process related parameters such as: the substrate's surface state prior to deposition, plasma characteristics (e.g. plasma chemistry and composition, energy, spatial and temporal distribution), surface temperature, base and working pressures, as well as starting materials (precursor) type and composition before and after plasma activation need to be fully understood and correlated with the aforementioned film properties. All this is necessary in a bid to increase the level of control associated with the deposition process to ensure a reliable and reproducible thin film fabrication.

With regards to compositional characterisation, no one method can be considered universal. For example, there are methods which are best suited for the determination of the chemical composition in the film's upper surface layers but which cannot probe the bulk of the film. The overall behaviour of the thin film is dictated by its surface, bulk and interfacial properties and is dependent on the application. For example, when a hard ceramic thin film which is coating a metallic material comes into tribological contact with another surface, the film's upper layer dictates the frictional and possible wear behaviour of the system. The bulk of the thin film and its thickness determine its load bearing capacity. Variations in the chemical compositions and mechanical properties between the film bulk and interfacial regions with the substrate determine

its fate in terms of a successful balance between rigidity and ductility. All this must be monitored and accounted for if one seeks to understand the complex film behaviour.

In addition, hard thin films can be composed of light elements with a low atomic number and be electrically insulating. This adds additional restrictions on ways of obtaining a full chemical composition. A multitude of surface- and bulk-sensitive spectroscopic and spectrometric methods are therefore required. The type of chemical bonding in the thin film dictates which method will be chosen in order to detect this bonding. For example, vibrational spectroscopy such as infrared and Raman spectroscopy are well-suited to probe a wide range of covalently bonded materials but are dependent on the symmetry of the material's crystal structure. X-ray photoelectron spectroscopy is a method which is sensitive to the compositional information of the film's upper few nano-meters. Its sensitivity and precision supersedes that of the easily accessible energy dispersive X-ray spectroscopy. However, both methods show various degrees of limitations in the detection of very light elements such as hydrogen, an element whose presence is almost always inevitable in PECVD and PVD deposited films and which greatly influences these films' mechanical and tribological properties. On the other hand, due to its depth-resolving capability in the nanometre range together with its sub-micrometer lateral resolution, Time-of-flight Secondary Ion Mass Spectrometry (ToF-SIMS) is particularly well-suited to investigating the chemical changes associated with various pre- and post-deposition processes to which surfaces are subjected. In addition, due to its very high mass resolution, it is highly sensitive to very small variations in the atomic and molecular masses of both very light and very heavy species and is therefore ideal for resolving strong mass interferences. However, it is very difficult to obtain precise quantitative compositional information with ToF-SIMS and its implementation requires using it in combination with other methods. Furthermore, micro- and nanostructural characterisation is also required at both a local scale of a few nanometres as well as at a global scale of a few millimetres in length. Several diffraction methods such as X-ray and electron diffraction form an integral part of film characterisation.

Since the aim is to fabricate hard thin films, mechanical properties are at the heart of all these investigations. Instrumented depth-sensitive indentation with ultra-low loads (nanoindentation) is best suited to gauge the elastic and plastic responses as well as the frictional behaviour of surfaces. Nanoindentation has evolved to be the method of choice for probing the mechanical and tribological properties of surfaces at the nanometre scale. By employing low loads ranging from 10μN up to 10mN, the method is very well- suited and has been recently standardised [74,75] to investigate the mechanical and tribological properties of nanocomposite films at the nanometre scale. In order to aid in the understanding of the interactions between surfaces under

external loading and to establish structure-properties correlations, nanoscale mechanical and tribological investigations are often combined with chemical and microstructural determinations which are assisted by the aforementioned methods. In essence, a proper understanding of thin film properties and behaviour which is necessary to qualify them for application necessitates a combinatorial approach to thin film characterisation.

1.2   Motivation for This Work and Significance of the Research

The quest for new and technically useful hard thin films which demonstrate good adhesion to a wide range of technical substrates and tools remains to this day a topic of keen interest. This growing interest is partly motivated by the desire to fabricate a new class of materials with properties that surpass classical ones, while simultaneously seeking to attain a fundamental understanding of both the acting mechanism behind their formation and their structure-property relationship. Attaining these aims is essential if the performance of coated tools is to have a new dimension, one which is only possible by eliminating existing problems that are associated with various hard thin films.

From a theoretical standpoint, intrinsically hard materials gain their properties as a result of the covalent bonding strength between their constituent elements. It is therefore logical to think of new hard phases based on light elements lying in the second and third periods of the periodic table. As previously mentioned, theoretical verifications have predicted that when such atoms form extended networks of mutually strong single bonds, hardness is a logical consequence. Achieving hardness through practical means is a result of a more complex interplay of numerous parameters: between chemical composition and microstructure on the one hand, and the method used to deposit and grow the materials on the other. To date, there remain numerous experimental efforts to prepare hard material and to verify theoretical predictions. Often these efforts end by a compromise being reaching between the theoretically calculated and predicted hardness and the practically achieved one. The complexity of both the vacuum-based and plasma-based deposition methods poses a major difficulty in the preparation of a hard material as a thin film. In this context, and in the last decade, numerous concerted efforts have concentrated on generating hard phases based on a binary and ternary system of the light elements in the second and third periods of the periodic table. These investigations have spurred this research into the Si-B-C-N system which has been seen to offer an attractive route to synthesising a new type of hard thin films by using a technique operating at extreme preparation conditions.

Research in the area of nanocomposite thin tribological films aims to design materials with the several important characteristics in mind. Firstly, that the materials forming such coatings, which

are subjected to high and abrasive loadings should have a combination of high hardness and an improved fracture toughness and compliance. That said, both these properties lie on the opposite ends of the scale, that is, the higher the hardness of a material, the higher is its stiffness and the lower is its toughness. One of the central concepts which are employed when designing hard but compliant materials relies on making composites of materials that can bring together the advantages of both high hardness and toughness when combined. This approach continues to motivate considerable research that aims to examine the most effective material combination. It is therefore of paramount importance that attention be paid to both the intrinsic properties of the individual constituents that make up the nanocomposites which give rise to the desired properties, and it is equally important to pay heed to the modifications which occur in their structures at the micro- and nano-scale. Attending to these two critical aspects is at the very heart of designing and preparing nanocomposite materials.

Recently a few studies have surfaced which have unveiled novel synthesis schemes as well as interesting properties pertaining to nanocomposites and multilayered systems including that of Mo and N among others. For example, recent research which utilised a combination of a hard and soft phase has demonstrated that tribological PVD coatings including molybdenum nitride, copper, and silver tend to exhibit unique tribological behaviours at elevated temperatures. Although the existing literature is rich with numerous examples of similar kinds of nanocomposite materials, the aforementioned material systems have not received equal attention. This is in spite of the fact that they offer a wide range of promising characteristics. There is, therefore, strong evidence to suggest that multiphase nanocomposites, of the Mo-B-N system can be offered up as promising candidates in the search for tribological hard coatings. Thus, this additional scheme can be included in the ever- growing knowledge base of nanocomposites within the context of hard and tribological surfaces.

Secondly, the material should demonstrate an acceptable level of thermal stability and also preferably oxidation resistance. In industrial applications, these properties together with outstanding adhesion, cohesion, friction, and wear have a direct influence on the performance and life time of the coated parts. In this context, various coating design concepts and architectures have been implemented to overcome classical problems and improve tool performance under severe conditions. Thus, strategies, including the design of nanocrystalline and multifunctional composite coatings have proven successful and demonstrated improved performances.

An increase in the demand for machine parts and technical tools that can perform reliably under harsh environments and which can be manufactured at reasonably low cost dictates that smarter

and more innovative surface engineering concepts are devised. This also sets and defines the current move towards thin films that should perform well under harsh mechanical and thermal conditions. Accordingly, new materials and preparation conditions need to be explored which can then be implemented on technical tools. The controllable deposition of multi-component and multi-functional nanocrystalline composites has paved the way to the preparation of a new generation of hard and tribological coatings capable of transforming tools' performance to the next level.

1.3   Objective of the Thesis

In view of the above, this thesis seeks to explore a range of material systems for implementation as multi-component nanocomposites thin films. These films would aim to take the form of wear-resistant coatings which combine a unique combination of hardness, toughness and elasticity. In doing so, this work strives to seek new synthetic routes to novel hard and tribological thin films based on the following systems: (a) nanocrystalline composites based on the nitrides of Molybdenum and Boron and (b) multi-component films based on the light elements Si-B-C-N-O system, by using the magneto-active (ECR) microwave plasma-enhanced CVD technique.

This work also aims to elucidate both process-property and structure-property correlations in a bid to gain an in-depth understanding of both the deposition process as well as the materials deposited. This will undoubtedly lead to an increase in the fundamental understanding of these systems and will also have the effect of increasing the control levels on the coating processes for potential future applications.

This work also aims to detail the various aspects pertaining to film chemical, compositional and micro-and nano-structural properties and their relationship to the implemented deposition conditions. This work also involves a series of investigations which seek to examine the relationships between the aforementioned film properties and their micro- and macroscopic stresses, thermal stability as well as their oxidation resistance. Furthermore, this work seeks to investigate, in depth, the films' mechanical and tribological properties at ambient conditions, at elevated temperatures, as well as at post-deposition annealing. Thus, these investigations aim to correlate between the films' compositions, micro- and nanostructures and their mechanical and tribological properties.

1.4   Thesis outline

Chapter 1 presents the state-of-the-art in research in the area of thin nanocomposite and hard coatings as well as in the area of microstructural design and concepts pertaining thin tribological films. The chapter then proceeds to state the motivation as well as the research objectives behind this work. The chapter ends by providing a brief outline of the thesis and its structure.

Chapter 2 presents the experimental and methodological parts of the thesis. The deposition systems which are used in the fabrication of the thin films in this work are described in detail, together with the specific preparation conditions implemented. In order to arrive at comprehensive and conclusive characterisations of the thin films produced in this work, a wide range of diagnostic techniques were implemented. These include X-ray photoelectron spectroscopy (XPS), Fourier-transform infrared spectroscopy (FTIR), time-of-flight secondary ion mass spectrometry (ToF-SIMS), X-ray diffraction, transmission and scanning electron microscopy (SEM) together with Energy Dispersive X-ray Spectroscopy (TEM and SEM-EDX), Differential Scanning Calorimetry and Thermogravimetric Analysis in conjunction with Mass Spectrometry (DSC-TGA-MS). In addition, nanomechanical as well as nano-and micro-tribological testing were used in order to investigate the films' mechanical and tribological properties at various levels. The chapter gives a brief background and description of these methods in the context of the investigated materials.

Chapter 3 presents the results obtained in the context of preparing nanocomposite thin films in the Mo-B-N system. Specifically, the chapter details the preparation of a range of molybdenum nitride and molybdenum nitride/boron nitride nanocomposite films which are deposited on silicon and tungsten substrates by electron cyclotron resonance microwave plasma assisted chemical vapour deposition (ECR-MWCVD) in conjunction with *in-situ* ion-beam sputtering of a molybdenum target. This chapter seeks to demonstrate how the aforementioned implemented techniques, which can be considered a hybrid approach to deposition, can be used to control the composition of the nanocomposite films. This chapter illustrates how the use of a reactive gas mixture of BF_3-Ar-H_2-N_2 in He-rich He plasma with controllable ratios together with an *in-situ* sputtering of a molybdenum grid using a He-N_2 plasma, can be used to modify and control the films' composition, phase as well as micro- and nanostructure crystallinity. The chapter presents detailed investigations of the films' composition and chemical bonding in view of the preparation parameters. A combinatorial approach to compositional characterisation is implemented whereby several techniques such as X-ray Photoelectron Spectroscopy, Fourier-transform Infrared Spectroscopy, time-of-flight Secondary Ion Mass Spectrometry as well as X-ray Diffraction are

used. The effect of changing the deposition parameters on the films' crystallinity and microstructure is investigated in depth by means of both local and global diffraction methods, namely: X-ray and electron diffraction. In addition, further details about microstructural features such as the sizes and strains of the diffracting crystallites are investigated by means of a comprehensive line profile analysis of the diffraction data which relies on the double-Voigt method. The macroscopic bi-axial residual film stresses are also investigated by implementing a thin-layer-sensitive technique which relies on measuring the lattice spacing of various diffraction planes at various tilting angles using grazing-incidence geometry. Several correlations between the film microstructure, morphology and composition are explored and investigated. The films' nano-mechanical and tribological properties are investigated in depth by means of nanoindentation and nanoscratching techniques. Several relationships between the films' microstructures and their mechanical and tribological properties are investigated and detailed.

Chapter 4 presents the results obtained in the context of preparing nanocomposite films in the light element Si-B-C-N-O system by means of electron cyclotron resonance microwave plasma assisted chemical vapour deposition (ECR-MWCVD). The chapter details how films with varying composition can be obtained by adjusting the composition of a gas mixture containing $Si(CH_3)_4$, BF_3-Ar, H_2, N_2 and He. Film composition is characterised by employing a range of methods including; X-ray Photoelectron Spectroscopy, Fourier-transform Infrared Spectroscopy, Time-of-Flight Secondary Ion mass Spectrometry, Energy-Dispersive X-ray Spectroscopy as well as X-ray Diffraction. The effect of varying the composition of the gas phase during film deposition on the films' composition and chemical bonding is investigated. In addition, the chemical information pertaining to film composition which is obtained from Time-of-Flight Secondary Ion Mass Spectrometry is investigated in detail. Variations in the spectral data are studied by employing two Multivariate Analysis methods. These include Hierarchal Agglomerate Clustering and Principal Component Analysis and are implemented in order to support the spectral analysis by extracting the most possible chemical information contained in the spectra. Based on this treatment, correlations between chemical composition and ToF-SIMS spectra are established and used to distinguish between the films and to elucidate the complex bonding situation in these materials. In addition, film microstructure is studied using high resolution electron microscopy. The films' mechanical properties are studied by means of nanoindentation and are correlated with composition and microstructure. The high temperature behaviour of the films is examined by means of Thermogravimetric analysis in an inert Helium atmosphere. In addition, the oxidation behaviour of the thermally stable SiCNO and SiBCNO films in ambient air is investigated. A combination of surface and depth sensitive spectroscopic, spectrometric and diffraction characterisation methods are implemented in order to investigate the chemical and compositional

changes which both film types undergo as a result of oxidation. The collated spectral data are further analysed by means of Principal Component Analysis in order to establish the variations in composition of the films' upper layers. Detailed analyses are then used to qualitatively investigate the differences between the chemical compositions of the developed oxide scales on both film types. In addition, Differential Scanning Calorimetry and Thermogravimetric Analysis in conjunction with *in-situ* Mass Spectrometry as well as High Resolution Transmission and Scanning Electron Microscopy are used to study the variations in the films' thermal stability, possible oxidation and decomposition routes, and to investigate changes to film morphology and microstructure during the oxidative annealing treatment. The chapter details various relationships and correlations between film composition and behaviour at high temperatures in ambient air.

In Chapter 5, the tribological behaviour of the SiCNO and SiBCNO films is investigated in various tribological contact conditions. Both nano- and micro-starching tests are carried out at various loads ranging from 10 μN up to 1 N with various counter bodies in order to investigate the tribological behaviour of these films in a multitude of conditions. The films' frictional behaviour against diamond indenters is also investigated after these films are subjected to thermal annealing in the temperature range 100- 400°C. In addition, the films' frictional and wear behaviours are investigated at high contact loads against alumina indenters at elevated temperatures. Correlations are established between the films' tribological performances and their mechanical properties as well as the changes to their chemical composition as a result of the annealing treatment. This attempts to shed more light on the different tribo-chemical processes acting in the contact zone in various conditions.

Chapter 6 presents a summary of the thesis. It also provides suggestions and recommendations for future related research work.

All abbreviations and symbols used in this work are clarified and listed under the headings *Abbreviations* and *Symbols*, respectively. All cited references in this work have been numbered and arranged in the order of their appearance in the main text under the heading *References*. The implemented citation styles for journal articles and paper is: Authors names, *Journal name*, **Volume and issue number**, (Publication year), Starting page number or article number. The citation style for books, Authors names, *Book name*, Editors names, Publisher, (Publication year), Starting page- Ending page whenever applicable. All mathematical equations, figures and table are numbered sequentially according to their appearance in the text. The numbering starts from 1 in each chapter and is preceded by the chapter number. The appendix contains additional information related to the work which is not included in the text.

2   Experimentation and Methodology

2.1   Film deposition using Electron Cyclotron Resonance Microwave Plasma-Assisted Chemical Vapour Deposition (ECR-MWCVD)

An Electron Cyclotron Resonance Microwave Plasma-Assisted Chemical Vapour Deposition (ECR-MPECVD) system was used in this study to deposit the thin film systems: (i) The Si-B-C-N and (ii) The Mo-B-N. The reactor was originally an ASTEX-type microwave magnetised plasma source CVD system, which was modified to incorporate a second large recipient underneath the plasma chamber. By using this technique, 2.45 GHz microwaves were guided into the ECR excitation chamber via a quartz window. To maintain the ECR condition, an 87.5 mT magnetic field was required The magnetic field was configured in such a way that the ECR point matches the substrate surface. This is essential to obtain the maximum ionisation in the vicinity of the substrate surface. A schematic diagram of the deposition reactor and the distribution of the magnetic field along the deposition chamber are shown in Figure 2.1. When required, the substrate was negatively DC-biased to assist film growth.

The thin films investigated in this study were deposited on a range of substrates including Si (100) wafers, hardmetal substrates (WC-10%Co), and tungsten metal substrates. A gas mixture of BF_3–N_2–Ar–He was fed into the ECR excitation zone while H_2 and $Si(CH_3)_4$ were introduced into the elastomer-sealed reaction chamber underneath the ECR zone. Prior to deposition, the reactor was pumped to a base pressure of about 5×10^{-3} Pa and the substrates were resistively heated to about 800- 900°C.

The reactor was evacuated using a combination of mechanical and turbo-molecular pumps, which were connected in series to the reaction chamber. The mechanical pump was a D65BCS Leybold rotary pump that provided a low vacuum of around 8×10^{-2} Pa, which was required as an initial pressure for the turbo-molecular pump. The turbo-molecular pump was a Turbovac Leybold Turbotronic NT20 with a pumping speed of 1100 L/s as measured for N_2. When operating together, both pumps could maintain a base pressure of about 5×10^{-3} Pa. The quality of the vacuum in this reactor could not have been improved owing to the fact that the reaction chamber underneath the ECR zone was elastomer-sealed. The system had several pressure gauges, which include: two capacitance manometers working in the pressure ranges 1.3×10^{5}–1.3×10^{2} Pa and 1.3×10^{2}– 1.3×10^{-2} Pa and a cold cathode vacuum gauge (1.3×10^{-2} – 1.3×10^{-8} Pa) that connected to the reaction chamber. A fourth Pirani gauge (10^{2} - 1.3×10^{-2} Pa) was connected to the turbo-molecular pump to measure the pressure at the inlet to the pump.

The substrate stage was modified from its original form that consisted of a graphite-based induction heater to include a DC-resistive heating unit. The unit consisted of a thin graphite sheet sandwiched between a pressed hexagonal BN mould that was capable of reaching temperatures up to 1100°C (Boralectric® from GE). A Molybdenum plate assembly was placed on top of the heater in order to introduce additional substrate bias when needed. Due to the inevitable heat losses arising from this arrangement, the maximum attainable temperature at a gas pressure of about 1.3 Pa was about 900°C. A feedback thermocouple that extended into a hole on the side of the Molybdenum plate was used to monitor the substrate temperature during temperature calibration.

Additionally, in order to obtain substrate surface temperature information during the deposition experiment, an infrared optical pyrometer was focused on the substrate from two viewing windows. The first was located on the upper part of the symmetric plasma coupler and the second was located on a side window. The stage height could be adjusted in both chambers of the reactor in a range of 110 mm with the aid of a step motor.

Various types of precursors, both vapours and gases, were introduced into the reaction chamber via two ports. The first was just beneath the microwave-transparent quartz window in the ECR-chamber which delivered the gaseous stream in a shower-head manner. The second port was placed in the vicinity of the substrate and took the form of a circular stainless steel cannula. The second delivery port was used in various experiments in order to investigate the influence of gas decomposition and fragmentation on the deposition process as well as to avoid poisoning some of the DC-biased metal stages, which were introduced in certain experiments. More details about this as will be given later in this section. The gas flow was controlled using mass flow controllers (MFCs) along with shut-off pneumatic valves. Leak-proof VCR® and Swagelock® fittings were used for gas delivery and to ensure easy maintenance of the gas lines. The various gases that were used included: boron trifluoride (10% in argon), tetramethyl silane (1.15% in hydrogen), hydrogen (99.999%), nitrogen (99.999% and 99.97%) and methane (99.9%).
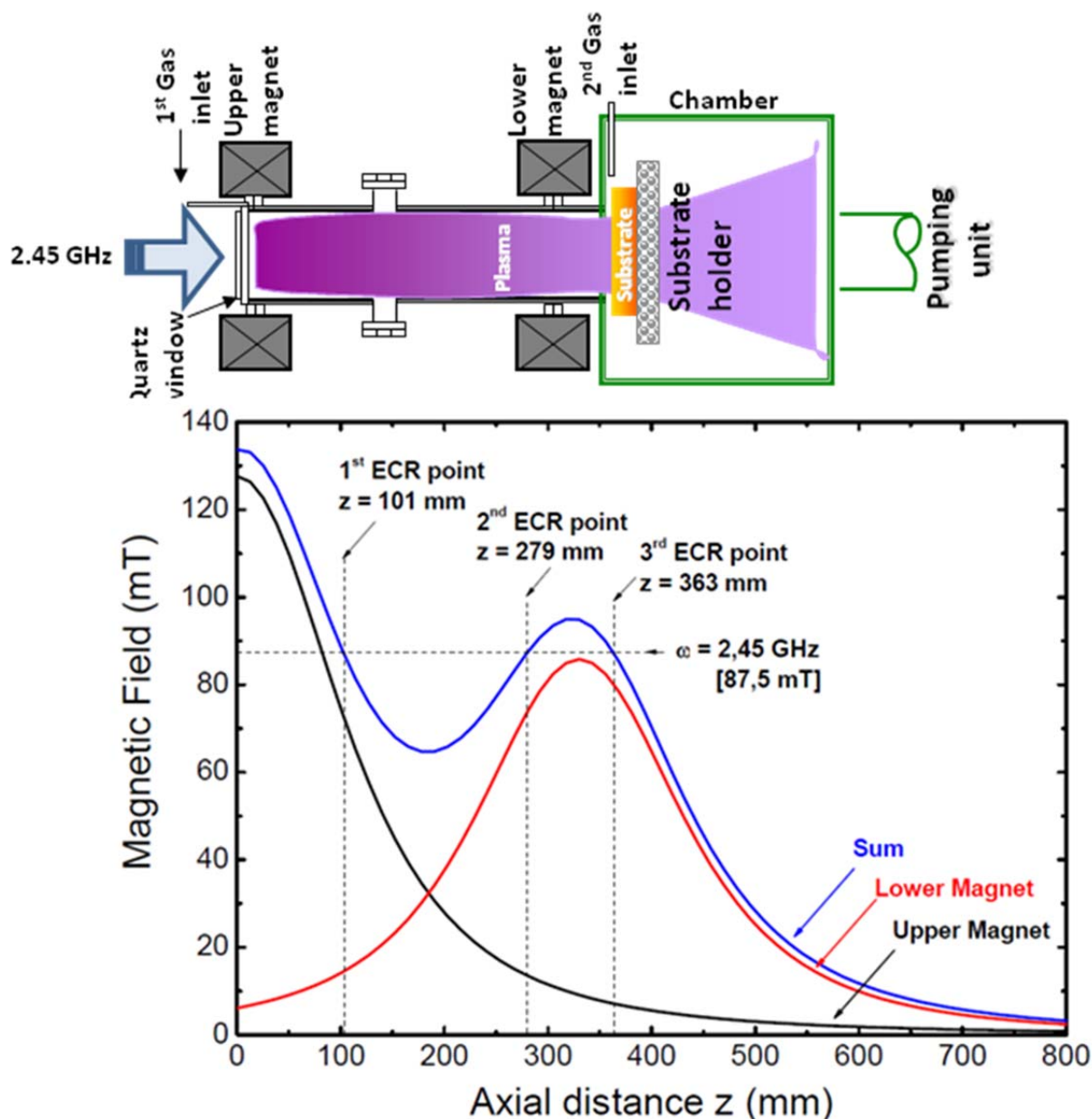
Figure 2.1: (Top) a schematic of the deposition reactor. (Bottom) shows the distribution of the magnetic field across the reactor and indicates the position of the ECR point in relation to the substrate.

2.1.1 Procedure for Deposition of SiBCNO Films

Films with various compositions were deposited on silicon (100) wafers using the ECR-MWCVD reactor described earlier. Microwave of the frequency 2.45 GHz with powers of 200, 300 and 1400 watts were guided into the ECR excitation chamber via a quartz window. Two DC-powered magnetic coils which were placed coaxially with the ECR chamber axis at specific locations were employed to generate a combined magnetic field of about 132mT. The configuration of the magnetic field can be controlled by varying both the distance between the upper and lower magnets as well as the DC power imparted to each magnet. The upper and lower magnetic coils

operated at 183 A and 122 A, respectively, to ensure maximum ionisation of plasma. In order to achieve the ECR effect with exciting microwaves of 2.45GHz, the magnetic field strength should be 87.5mT which generates an electron gyration frequency equal to that of the microwaves. The implemented setup forms three locations within the ECR chamber where the above condition is met. The substrate was placed in a second chamber such that its height matches the axial position corresponding to a magnetic field strength of 87.5 mT (i.e. 3rd ECR point at z = 363mm) as can be seen in Figure 2.1. The substrate was heated resistively using a boron nitride heater. The substrate was negatively DC-biased at low 30 V to assist film growth.

In all experiments, 100 sccm of 1.15 % $Si(CH_3)_4$ in H_2 was introduced into the reaction chamber underneath the ECR zone where the substrate is placed. When required CH_4 was also added near the substrate, whereas, a gas mixture of 10% BF_3 in Ar, He and N_2 was fed into the ECR excitation zone. The reflected microwave power was always monitored and maintained below 10% of the forwarded power at low powers and below 50 watts at high forwarded powers. This was done by continuously adjusting two of the three stub antennas affixed to the microwave guide and maintaining the flow rate of He between 20- 30 sccm to ensure a stable ignition of the plasma. Prior to deposition, the reactor was pumped to a base pressure of between 5- 10 $\times 10^{-3}$ Pa, and the substrates were resistively heated to about 900°C based on measurements using a thermocouple beneath the substrate and additional optical pyrometer. It was found that the reactor assembly and gas fixture arrangements contributed to nitrogen and oxygen inclusions in the films as was later determined by EDS and XPS measurements. This was in fact always detected in the films even when no N_2 was flown in the reactor, a fact which can be considered a drawback in the implemented conditions. Although the exact origin of this contamination was unclear, it is thought to be attributed to the unavoidable high base pressure and leak rates in the old and elastomer-sealed reactor.

Films with various compositions were obtained by implementing the deposition parameters listed in Table 2.1. The chemical formulae which are used to describe the film are expressed in atomic per cent as obtained from XPS and EDS analysis and include all detectable elements.

Film	Formula (at.%)	Gas flow rates (sccm)						MW power (watts)	Thickness (nm)
		$Si(CH_3)_4$	H_2	BF_3	Ar	CH_4	N_2		
SiBCNO1	$Si_{14}B_{24}C_{29}N_{22}O_{11}$	1.15	98.85	1.15	10.35	5.75	0	1400	1300
SiBCNO2	$Si_{19}B_{21}C_{23}N_{25}O_{12}$	1.15	98.85	1.15	10.35	1.15	0	1400	740
SiBCNO3	$Si_{33}B_8C_{19}N_{27}O_{13}$	1.15	98.85	0.3	2.7	0	0	1400	470
SiBCNO4	$Si_{15}B_{25}C_{15}N_{33}O_{10}$	1.15	98.85	1.15	10.35	0	0	1400	848
SiBCNO5	$Si_6B_{22}C_{39}N_{20}O_8$	1.15	98.85	0.3	2.7	0.58	0	300	1300
SiCNO1	$Si_{36}C_{22}N_{25}O_{16}$	1.15	98.85	0	0	1.15	0	1400	430
SiCNO2	$Si_{40}C_{16}N_{27}O_{15}$	1.15	98.85	0	0	0	0	1400	500
SiCNO3	$Si_{39}C_8N_{42}O_{10}$	1.15	98.85	0	0	0	8	1400	600
SiCNO4	$Si_{32}C_{17}N_{26}O_9$	1.15	98.85	0	0	0.58	2.3	300	445
SiCNO5	$Si_{33}C_{38}N_7O_{12}$	1.15	98.85	0	0	0.58	0	300	567

Table 2.1: The parameters implemented in the deposition of the SiBCNO films.

2.1.2   Procedure for Deposition of MoBN Films

For the deposition of Mo-B-N thin films, a hybrid approach to film deposition was adopted by utilising *in-situ* sputtering of Mo via the ECR ion beam. This was done using an additional unit consisting of a DC-biased double Mo-grid as a sputter source. The unit was assembled in a hierarchal manner on top of the substrate heating stage as shown in

Figure **2.2**. In these experiments, 1400 watts of the 2.45 GHz microwaves were used and the two magnetic coils operated at 183 A and 122 A generating the required 87.5 mT magnetic field to maintain the ECR condition. The magnetic field was controlled in such a way as to guide the ion-beam stream towards the DC-biased Molybdenum grids and the substrate, which were placed in the second reaction chamber under the ECR zone. The grid assembly consisted of double Mo-grids separated at a distance of 30 mm and were negatively DC-biased at 150 V. Here, a gas mixture of 10% BF_3 in Ar, He and N_2 was fed into the ECR excitation zone while H_2 was introduced into the reaction chamber. This was a necessary step to minimise the poisoning of the Mo-grids. This arrangement ensured that the biased Mo-grids were continuously bombarded with the plasma stream, and that the sputtered Mo arrived at the substrate to undergo a surface reaction with the reactive BF_3, N_2 and H_2 gases. Prior to deposition, the reactor was pumped to a base pressure of about 5×10^{-3} Pa and the substrates were resistively heated in a high vacuum to about 900°C.

In these experiments, both single crystal silicon (100) wafers as well as 1-mm thick mirror polished tungsten plates were used as model substrates. At the start of each experiment, the ECR plasma was ignited with a mixture of He and N_2. In all the experiments, the flow rates of He and N_2 were kept constant at 140 and 30 sccm, respectively. After the plasma stabilisation stage, the reactive gases were introduced at the desired flow rate marking the beginning of deposition. The total pressure was kept constant in the range of 0.5- 0.6 Pa. Such a pressure range still satisfies the ECR condition. All the deposition experiments were carried out continuously for six hours. Upon completion, the reactive gases and the grid bias were turned off. The He/N_2 plasma was left on for several minutes until the other gases were pumped out of the system. Finally, the plasma and substrate heating were turned off, and the system was allowed to cool down in rough vacuum. The reactor was then vented with nitrogen for sample exchange. A summary of synthesis conditions is listed in Table 2.2.
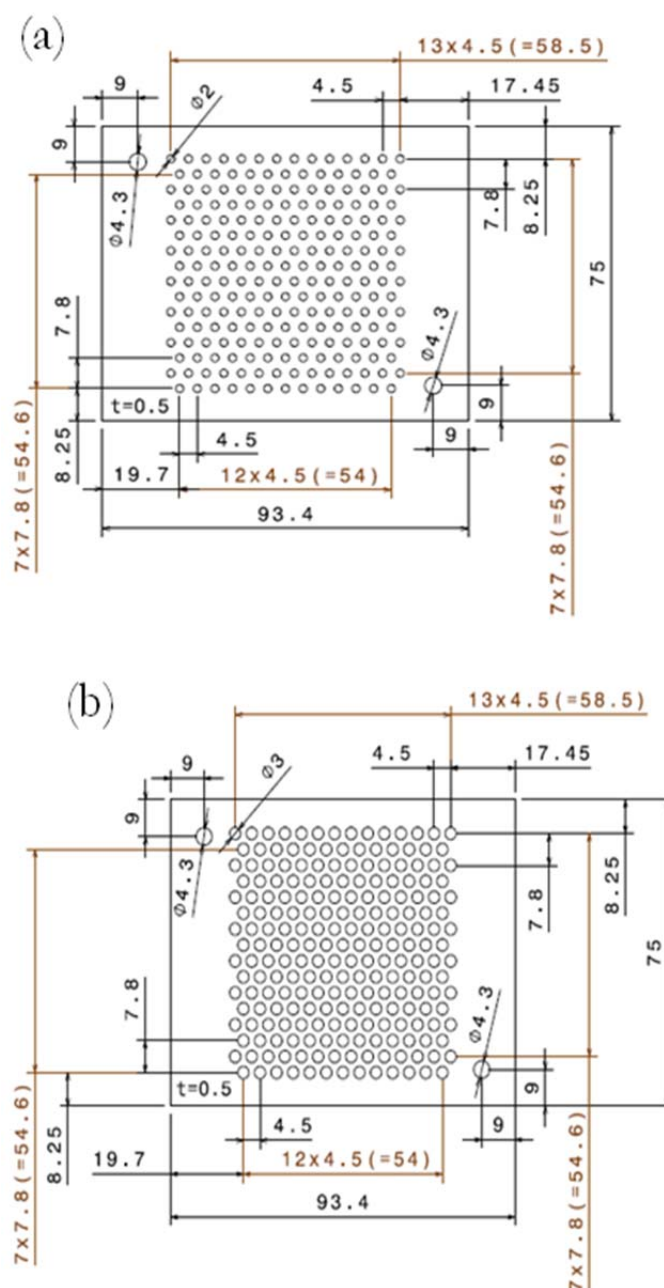
Figure 2.2: A technical drawing showing the (a) upper and (b) lower molybdenum grids used for the in-situ sputtering.

film		flow rate [sccm]				Film thickness [nm]
	H_2	BF_3 (10% in Ar)	Ar	He	N_2	
A	0	0	0	140	30	400
B	0	0.45	4.05	140	30	466
C	3.3	0.45	4.05	140	30	412
D	3.3	0.9	8.1	140	30	380
E	3.3	1.8	16.2	140	30	375

Table 2.2: A summary of the Mo-B-N films deposition parameters.

2.2   Material Characterisation

2.2.1   Visual Inspection and Optical Microscopy

Prior to their removal from the deposition reactor, the coated surfaces were allowed to cool down to room temperature slowly in vacuum in order to avoid rapid temperature gradients, which could lead to possible film delamination and flaking-off. The reactor was vented with N_2 (99.97%) before the coated samples were removed. Inspecting the coated surfaces both with the unaided eye and with a low resolution optical microscope was a very important initial step in examining the coated material. Other observations such as the colour of the surface after deposition were found to be equally important, as this served to indicate the nature of the coating material, thickness and homogeneity. A heterogeneous film thickness is common observation particularly in the case of film which was deposited by ECR-MWCVD. Thus due attention must be given in order to ensure a proper comparison between surfaces coated at different parameters is carried out.

2.2.2   High Resolution Microscopy

2.2.2.1   *Scanning Electron Microscopy*

Scanning Electron microscopy is a technique which is widely used in the characterisation of surfaces owing to its high resolution capabilities and ease of sample preparation. When coupled with Energy Dispersive X-ray Spectroscopy (EDS), the technique is ideally suited to investigate both surface morphological features as well as chemical composition [76]. An ultra high resolution Field Emission Scanning Electron Microscope (FESEM) (Ultra55-ZEISS), which used a range of detectors including: a standard Eberhart-Thornley secondary electrons (SE) detector, an In-Lens SE detector and an energy and angle selective backscattered electrons (EsB) detector. The microscope was capable of reaching a magnification up to 900 thousand. With a spatial resolution in the order of 1 nm at an accelerating voltage of only 1 kV, the microscope was capable of providing high quality and high resolution imagery. Images obtained from purely secondary electrons were particularity useful for high resolution imaging, whereas those obtained from the backscattered electrons provided material contrast imaging based on the atomic numbers of the elements making up a certain phase. While surface conductivity is a prerequisite for imaging, gold-sputtering is necessary to image insulating films. Finally, fractured or polished cross-section micrographs were used to calculate the thickness of the various films in this work.

2.2.2.2 Transmission Electron Microscopy

High Resolution Transmission Electron microscopy (HRTEM) together with selected area electron diffraction (SAED) are powerful techniques, which are capable of elucidating detailed microstructural information about the thin films that were produced in this work. These techniques proved invaluable in determining the phase composition, structure, film morphology, crystallite and grain sizes as well as grain boundary structure and texture. Further information about microstrains can also be revealed through the measurement of the individual fringe spacings and angles in the material. While this type of information is obtained at micro- and nano-levels in a localised manner, it is necessary as it complements other data obtained from large areas using techniques such as X-ray diffraction, and vibrational spectroscopy. When combined, such information provides a more accurate description of the complex evolution of film microstructure.

Sample preparation for TEM investigations is lengthy procedure which requires a great deal of experience and dexterity. It involves a series of steps that aim to produce an electron-transparent specimen of the material that is to be investigated. An ideal specimen would have the following characteristics: be of high-quality, uniformly thin, electrically conductive, non-magnetic, stable both in the laboratory environment and during transport and inside the microscope under the electron beam. Specimens were prepared in two forms: plan-view and cross-section. In this work, selected samples were investigated using HRTEM in order to determine the crystal structure of the phases in the films as well as the crystallite and grain sizes distribution function and their boundary structures. In addition, selected area electron diffractions (SAED), which were obtained from the material were used for the phase identification. Such information can be revealed through the measurement of individual fringe spacing in the SAED patterns. In order to index the diffraction pattern, the measured diffraction ring diameter was used to calculate the interplanar spacing (d_{hkl}) though the expression:

$$r \cdot d_{hkl} = L \cdot \lambda \qquad \qquad \textbf{2-1}$$

Where r is the measured ring diameter; λ the wavelength of the electron used as determined by de Broglie's equation; the product $L \cdot \lambda$ the camera constant; and d_{hkl} the interplanar distance corresponding to the crystallographic plane with the Miller indices (*hkl*). The calculated d_{hkl} values were then compared with the data in the Inorganic Crystal Structure Database (ICSD).

2.2.2.3 *Atomic Force Microscopy*

Atomic force microscopy (AFM) was used to perform topographic characterisation including both surface morphology and roughness on the films which were prepared in this work. The scanning probe microscopy of the type XE-100 (PSIA) was operated in the non-contact AFM mode to obtain detailed surface topography. The samples were imaged using commercial tips of silicon nitride (Si_3N_4), which featured a nominal tip radius of 10 nm in a feedback controlled mode on all three axes (x, y and z). Each surface was measured at least five times in different surface positions and in each case, areas of 5×5 μm^2 or 10×10 μm^2 with a pixel resolution of 512×512 $pixel^2$ and 1024×1024 $pixel^2$, respectively, were scanned to extract the corresponding root-mean-square surface roughness (R_{rms}).

2.2.3 Spectroscopy and Spectrometry

2.2.3.1 *X-ray Photoelectron Spectroscopy*

X-ray Photoelectron Spectroscopy (XPS) [122,123] is a surface analytical technique which is sensitive to the atomic composition of the uppermost 10 nm of the film's surface. The technique yields both quantitative and qualitative information about the elemental composition of the surface. When the surface which is to be analysed is irradiated with X-rays of a suitable energy in ultrahigh vacuum, photoelectron spectra are obtained through the simultaneous measurement of the kinetic energy of a number of core electrons which escape from the uppermost 10 nm layer of the analysed surface. In XPS, the measured binding energies (BE's) of the core electrons depend on the attractive and repulsive forces which they experience from both the nucleus and the valence-shell electrons, respectively. Thus, the binding energies of core electrons are sensitive to changes in the local chemical environment and can, therefore, be used to study the chemical structure.

In the XPS investigations which were carried out in this work, all the surfaces were sputtered by an Argon beam at an energy of 1 KeV until a significant amount of the upper surface layers were removed in order to ensure surface contaminants were removed. In the case of Si-B-C-N-O films, oxygen and nitrogen were always found even after very long sputtering times leading to the conclusion that they are one of the main chemical species and not just contaminants. The sputtering time was calibrated such that no variation in the amount of oxygen detected was measured. Typically, a 5×5 mm^2 area required about 60 min. of sputtering, a procedure that was repeated on different area of the sample in order to clean a 12×4 mm^2 area, which is necessary for a reliable XPS study. Preliminary Auger Electron Spectroscopy (AES) analysis was attempted, but strong charging effects made these measurements difficult or in some cases impossible, so

that no reliable AES spectra could be performed. In the case of Mo-B-N films, a preliminary check with Auger technique (probed area of about 0.5×0.5 mm²) verified that the analysed surfaces did show contaminations of oxygen and atmospheric carbon. Nevertheless, the residual carbon and oxygen signals which were seen in the XPS survey spectra are likely to have been originating from non-sputtered zones on the analysed surfaces or from the sample holder.

Photoemission analyses of the core levels were carried out using a non-monochromatised Mg X-ray anode source, where K_α = 1253.6 eV. Two types of spectra were collected: the first type was a survey spectrum which was obtained at a low energy resolution (Pass Energy, PE = 100 eV) and used to obtain quantitative compositional data of the surface layers. The relative atomic percentage of an element is calculated using the following expression:

$$C_x = \frac{A_x / XSF_x}{\sum A_i / XSF_i} \times 100\%$$

2-2

Where C_x is the atomic concentration of element x; A_x the integral area of the core level spectrum which should be normalised to the element's X-ray photoelectron sensitivity factor (XSF_x); and $\sum A_i$ the sum of the integral areas of the core level spectra of all other detected elements normalised to their corresponding sensitivity factors XSF_i. The XSF values were adopted from published data [77].

The second type was a detailed analysis of the core level spectra, which were carried out at a higher energy resolution (Pass Energy, PE = 25 eV). During the measurements carried out on insulating films, such as SiBCNO films, strong surface charging effects were encountered, which were to be expected owing to the materials' large band-gaps. This resulted in the measured binding energies shifting to higher values than those of the standard ones which needed to be corrected. The line profile of a core level spectrum was fitted to a combination of Cauchy (Lorentzian, which accounts for the lifetime broadening) and Gaussian functions (which accounts for the instrumental resolution). The profile background was fitted to a Shirley background which represents the secondary electron background.

2.2.3.2 *Vibrational Spectroscopy (Fourier Transform Infrared (FTIR) Spectroscopy)*

Fourier Transform Infrared (FTIR) spectroscopy forms an essential part of material characterisation that is non-destructive and require little to no sample preparation. In this work, the technique was routinely used to analyse the deposited films. FTIR is suitable for measuring

films with phases that have various IR active bonds and phonons. It enables the extraction of qualitative information about the quality, crystallinity and mass fraction of such phases by performing either absorption or reflection measurements. In essence, basic infrared analysis involves monitoring the changes in the intensity of an incident polychromatic electromagnetic radiation as a function of the wavelength after its interaction with an absorbing medium. In this work, FTIR measurements in both absorption and reflection modes were performed. The reflection mode was especially useful as it enabled further phase identification those strongly absorbing films which did not permit a high intensity IR radiation to pass through.

As it is sensitive to surface structure, the reflection mode was also beneficial as it helped in gathering more information pertaining to specific film surface chemical bonding structure. In reflection mode, FTIR measurements yield spectral features which include both imaginary and real parts which should be separated before using the high intensity spectral positions for the correlations bond vibrations or phonons. One way of separating both real and imaginary parts is to use the formalism of Kramer-Krönig [78,79] in order to derive the films' extinction coefficients in the respective spectral range. In addition, reflection mode measurements work best with perfect reflectors (e.g. gold-coated substrates with reflection of about 99%) which yield the highest intensities possible. Therefore, the main difference between the measurements of the reflection mode and those of the absorption mode is that the reflection mode spectra do not give absolute intensities and that their intensities should be scaled relative to that of a gold-coated substrate so as to maintain reproducible measurements with lower systematic errors.

The FTIR Nicolet-6700 spectrometer (Thermo-Fischer, Germany) was used in these investigations to collect the spectra in the mid-IR region of the electromagnetic spectrum (400-4000 cm^{-1}) in both the transmission and reflection modes. Up to 200 spectra were collected from each film at various locations on the surface with a spectral resolution of 1.98 cm^{-1}. The reflection measurements were performed at near normal-incidence with an angle of 16°. The transmission spectra were background corrected while those of the reflection were analysed according to the Kramers-Krönig method in order to derive the films' extinction coefficients in the respective spectral range. The spectrometer was not purged with dry air or nitrogen during the measurements leading to the ubiquitous appearance of signals from carbon dioxide and water vibrations whose intensities were reduced significantly by subsequent background subtraction.

2.2.3.3 Time-of-Flight Secondary Ion Mass Spectroscopy

Due to its depth-resolving capability in the nanometre range together with its sub-micrometer lateral resolution, Time-of-flight Secondary Ion Mass Spectrometry (ToF-SIMS) [145] is

particularly well-suited for investigating the chemical changes to film surfaces which are associated with various pre- and post-deposition processes. In addition, due to its very high mass resolution, it is highly sensitive to very small variations in atomic and molecular masses and is therefore ideal for resolving strong mass interferences.

In short, this method is based on sputtering the surface of the sample which is to be analysed by means of an energetic beam of ions, often referred to as a primary ion beam. This primary beam has energies ranging from hundreds to several tens of thousands of eV, which upon bombardment of the surface, results in the production of ionised secondary mono- and poly-atomic species under ultra-high vacuum conditions. These species then arrive at the detector at different times due to their various arrival rates dictated by their respective masses which gives rise to the term time-of-flight. The angle of incidence that the primary ion beam makes with the surface is a parameter that influences the momentum transfer into the surface and is therefore important to control. Upon incidence, the primary ion beam loses part of its energy in the form of a collision cascade resulting in imparting this energy to the atoms of the surface which break their chemical bonds and sputter off the surface as secondary species. Theses secondary species originate from the uppermost surface layers and consist of intrinsic surface material as well as sub-implanted ions brought about by the primary ion beam. While the great majority of the secondary species which are formed as a result of the primary ion beam-surface interaction are neutral, the ones which are charged positively and negatively are those which are of interest for SIMS detection.

In Time-of-Flight SIMS analysis, the ejected pulses of secondary ions are then accelerated by a potential that renders all ions possess approximately the same kinetic energy. They are then allowed to drift through a fixed-length space called "flight tube" which is free from any field before arriving at the detector. As such the heavier ions travel more slowly through the space and therefore require longer flight time to the detector. A mass spectrum is then collected by measuring the flight time of the secondary ions. Finally, the technique can operate in a depth resolved mode wherein two separate ion beams operate in a so-called "Dual Beam Mode": with one beam sputtering materials off the surface to be analysed and the second beam analysing the resultant surface after a short delay. Detailed description of the method can found in [80,81,82].

In this work, Time-of-Flight Secondary Ion Mass Spectrometry TOF-SIMS (ION-TOF, Münster, Germany) was implemented in order to obtain depth-sensitive compositional details of the deposited films. An area of 300×300 μm^2 of the film's surface was sputtered with a 5kV/200nA primary O_2^+ ion-beam. The depth profile spectra were obtained by scanning an area of ca. 70×70 μm^2 with a Bi^+ ion-beam. This area was chosen to be in the middle of the sputter

square in order to reduce any interference effects from the crater edges during the measurements. Collating these profiles involved carrying out an initial sputtering with primary O_2^+ ion-beam for 10 s followed by a Bi^+ ion-beam that is used to analyse the rest of the layer. The analysis time was kept constant at 300 ms. This method proved more effective in overcoming the extensive charging effect, which is commonly encountered with such wide band-gap materials and is deemed advantageous as it is capable of detecting the chemical composition of a greater proportion of the annealed films in a speedy fashion. The Bi^+ ion-beam was adjusted under optimum fine focus conditions to achieve a primary beam diameter of ca. 2 μm. This along with the film's surface roughness dictated the lateral resolution of the scan measurements. In the investigations carried out in this work, the ToF-SIMS data were obtained by using a reasonably low dose density in the order of 2.79×10^{13} primary ions per square centimetre (also referred to as ion fluence). This is done to minimise the probability that the detected secondary ions are a result of damaged materials (i.e. material that has undergone structural rearrangements), which in turn ensured the most intact secondary ion emission [80]. The mass spectra were collected in both negative- and positive-ion modes. At least three different spots on the surface were probed. In the case of insulating surfaces such as those of SiCNO and SiBCNO films, a low-energy electron flood gun was directed to the surface in order to neutralise the surface during the analysis[83].

The mass scale was calibrated using peaks from C^-, O^-, C_2^- and C_3^- for data collected in the negative ion mode, whereas peaks from H^+, B^+, CH_3^+ and $C_2H_5^+$ were used in the calibration of the positive mode. The error in peak selection was maintained at a value lower than 10 ppm. The mass resolution ($m/\varDelta m$) of the negative secondary ion spectra was typically in the range 3000-6500 for amu/z = 26.

2.2.3.4 Multivariate Analysis (Principal Components Analysis)

Classically, the handling of ToF-SIMS spectral data involves the manual selection of what is deemed to be important emitted secondary ions. The procedure has the drawback of being both time consuming and of introducing specific assumptions about the data. This may lead to a particular bias which may be reflected in the analysis. While at a simplistic level, such a univariate analysis, may lead to satisfactory interpretations, it is considered a huge reduction in the abundant chemical information which the ToF-SIMS spectra contain and may yield. Therefore, manual univariate analysis is not only significantly time consuming as it requires a significant amount of data work-up time, but it also leads to the frequent neglect of important and hidden spectral information. Alternatively, the use of Multivariate Analysis (MVA) has gathered enormous momentum and received increasing attention from the scientific community in the context of

extracting the most possible chemical information contained within the ToF-SIMS spectra. Several recent reviews on this topic in the context of implementing it in ToF-SIMS measurements are found in [84,85,86].

Essentially, the approach is based on the simultaneous analysis of the effects which several statistical variables have on the parameters of interest. Here, analysis of the ToF-SIMS data proceeded by using two multivariate analyses: the first is based on partitioning the spectral data in a hierarchal agglomerate clustering (HAC), whereas the second uses Principal Component Analysis (PCA). In this work, these analyses were performed by using two pieces of user-friendly software, Tanagra® [87] and the Visual Statistic system ViSTa® [88], which are available for use as freeware for academic and research purposes.

In Hierarchal agglomerate clustering analysis (HAC), all the collated ToF-SIMS spectra were grouped into sub-classes (commonly referred to as clusters), such that the spectra belonging to every sub-class bore significant similarities. This is referred to as an unsupervised data mining process, which is based on the calculation of the variances between the individual spectra. The sub-classes are constructed based on the maximum variance possible between each sub-class. In this context, two types of data variances are considered: the first is the variance between the spectra in each sub-class (cluster) while the second represents the variance between the various resulting clusters. The latter may be thought of as a measure of the variation between clusters.

In this treatment, the aim is to look for hierarchal clustering which maximises the variance between the sub-classes based solely on the dataset and without any prior assumptions about the spectral data (commonly referred to as supervised selection of data). Hierarchical clustering was used in this treatment in order to re-group the surfaces (films) in order to rank them according to their spectral similarities. The HAC analysis implemented the agglomerative type of clustering which is a "bottom-up" approach in which each spectrum starts by forming a cluster on its own. Then the individual spectra are compared with respect to their variances and are consequently grouped into bigger clusters which are merged upwards. The algorithm which forms the basis of hierarchal clustering analysis is based on Ward's criterion. This criterion is based on minimising the variance between the sub-classes (clusters). Each two clusters which have the smallest difference are grouped into a new higher sub-class or cluster [89].

In PCA, the relationships between variables and similarities (or dissimilarities) between the individual spectra are explored. In doing so, the collected spectral data are expressed in one matrix (or table) (X) which is conventionally constructed such that its rows represent the individual observations (or samples), whereas its columns represent the measurable quantities (or

variables). Here, the matrix, X, has the dimension of $i \times j$, where i = the individual spectra (i.e. measurements or observations or samples) and j = the spectral features (i.e. measurable, variables, the intensities of mass/charge value) as follows:

$$X = \begin{bmatrix} d_{11} & \cdots & d_{i1} \\ \vdots & & \vdots \\ d1j & \cdots & dij \end{bmatrix} \qquad \textbf{2-3}$$

The basic equation that describes PCA models the dataset X as the product of two matrices one of which is transposed plus an additional matrix which represents the residuals.

$$X = T \times P^T + E \qquad \textbf{2-4}$$

Where X is the matrix which contains the dataset to be analysed by PCA; T a matrix which contains the scores; P^T a transposed matrix which contains the loadings; and E a matrix which contains the residuals that make up the unexplained part of the data.

Graphically, if the original matrix, X, which contains the observations and variables, can be represented as [84]:
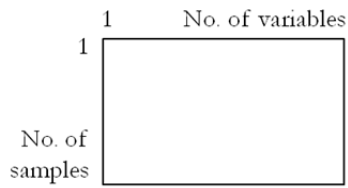
Then, the expression above may be represented as:

Here, the matrices $\mathbf{T}$ and $\mathbf{P^T}$ are referred to as the scores and loadings, respectively. A parameter F is chosen to represent the number of components in the PCA model such that F forms the columns in the scores matrix, whereas it forms the rows in the loadings matrix. For example, in a three component model (F = 3 i.e. three Principal Components), the scores matrix (T) will have three columns whereas the loadings matrix ($\mathbf{P^T}$) will have three rows. The size of the residual matrix will be the same as that of the original dataset matrix (X). Both matrices, T and P^T are determined by an approach which is based on the least squares. The purpose of this treatment is

to describe the original matrix by projecting it in a space or coordinate system with a reduced dimensionality. These new coordinates form a set of vectors whose directions are the ones with the highest possible variance in the data. The number of new coordinates that are chosen to describe the variance in the data is represented by F. Each new coordinate is called a Principal Component (PC) and consists of one score and one loading vector.

A newly constructed axis (i.e. a PC) spans the data to describe its variance. The first Principal Component is the one which captures the highest possible variance in the dataset and is denoted by PC1. The scores on this PC are the values which describe the spatial position of each observable (sample) in relation to it (i.e. distance between the observable and the PC). The second Principal Component, denoted by PC2, is perpendicular to PC1 and has the next highest possible variance. Similarly, its scores describe the distance between it and each observable. Each additional PC will be perpendicular to the previous PC's and capture progressively less variance in the data.

In theory, the total number of PC's can be equal to the total number of variables, however, since the aim of PCA is to reduce the dimensionality of the data, a specific number of PC's is chosen such that most of the variance in the data is described by the least possible number of PC's. The amount of variance which a PC captures is given as a percentile of the total variance and is written between brackets after the symbol PC. For example, if the first Principal Component captures 90% of the variance in the data, the suitable designation would be PC1(90%). In this manner, it is then possible to display the patterns in the data by plotting the scores of each data point on the respective PC.

Preparing the ToF-SIMS data for PCA is a central to the analysis and is commonly referred to as data treatment. As previously mentioned, a matrix (X) whose dimension is $X = i \times j$ is constructed such that the columns (j) are formed by the ToF-SIMS spectra which belong to samples forming the rows (i). These spectra (j) are collated either sequentially as in depth-profiling with each spectrum being obtained after (i) sputtering time (which corresponds to sputtering depths) or discretely from various (i) samples (e.g. various compositions, various annealing treatment, various spatial position on the film's surface). Because ToF-SIMS measurements are very sensitive to surface topography and homogeneity, it is important to compare the spectra which are obtained from surfaces with similar origins. This is commonly referred to as "matrix effects", where the word "matrix" in this instance, refers to the probed sample volume during ToF-SIMS measurements and carries a different meaning to that associated with matrix (X) that is constructed for PCA.

The spectral information, which was used to construct X, was chosen in the mass range 0- 200 amu/z based on the condition that their signal:noise ratio is greater than 3 (S/N >3). Each spectrum was normalised to the sum of the total intensities. This treatment could be used to establish the spectral features which are responsible for distinguishing between different samples (either different sputtering depths or different films). Furthermore, each matrix is mean-centred by subtracting the column mean from each of the data points in the column. When the PCA model is determined from the mean-centred data, the focus is shifted away from variation within one sample towards variations between the samples [90].

Finally, it should be mentioned here that the main source of variance within each ToF-SIMS spectrum arose from changes in the surface chemical composition. This was either due to changes in composition during film deposition or to post-deposition surface treatment such as surface cleaning or annealing. In the former case, the treatment was used to rank films according to their elemental composition, whereas the latter used the variation in the spectra to identify the changes in chemical composition as a result of heat treatment and locate the position of the newly formed interfaces.

2.2.4   X-ray Diffraction

In this work, X-ray diffraction (XRD) was used for phase analysis and microstructural characterisation of all deposited films. The diffraction measurements were carried out by using two diffractometer systems, which included a 4-axis Seifert XRD3000PTS and a Philips X'Pert. The equipment is illustrated in Figure 2.3. In the XRD3000PTS system, the X-ray source is fixed whereas the specimen and the scintillating detector are rotated through the angles θ and 2θ, respectively, in either a symmetric θ-2θ or an asymmetric (ω-2θ) geometry. In order to carry out thin film measurements using grazing incidence in an asymmetric fashion, the only part that was allowed to rotate was the detector which was rotated at an angle of 2θ, whereas the angle between the specimen and the X-ray source was fixed at a specific grazing incidence angle, α.

The XRD3000PTS diffractometer, being a 4-axis system, is equipped with an Eulerian cradle which permits additional rotation along a set of two orthogonal axes. The first enables a symmetric rotation and is called (Φ) whereas the second enabled a symmetric tilting of the specimen and is called (Ψ). Therefore, this system can be used to carry out residual stress measurements on both symmetric θ-2θ and asymmetric ω-2θ grazing-incidence geometries. The latter proved very useful in gauging the residual stresses from thin films owing to the almost constant and shallow X-ray penetration depths. This was used to carry out specific residual stress

measurements for some films. The two X-ray sources that were employed used point-source Cu- and Cr-anodes and allowed the generation of either circular or line beams of various sizes by employing suitable masks. The diffracted beam side included a flat graphite monochromator. It also had either soller slits coupled with receiving slits or parallel beam collimators for use with the symmetric θ-2θ and asymmetric ω-2θ grazing-incidence geometries, respectively. Finally a proportional counter detector was used for signal collection. A schematic diagram of the principal diffractometer's set of axes is show in Figure 2.3. The numbered components in the diagram correspond to: 1: X-ray anode with K_β filters, 2: attachment for auto-absorber or additional slit optics for channel-cut monochromator; 3: primary slit optic attachment or mirror and channel-cut monochromator accessory; 4: specimen holder; 5: secondary slit optic attachment; and 6: detector and secondary monochromator. The precision in the Ω, Φ, and X axis movement is $\pm 5 \times 10^{-5}$ °, $\pm 5 \times 10^{-3}$ °, and $\pm 5 \times 10^{-3}$ °, respectively. The centre of the diffractometer is represented by point C in the diagram and is used as the universal reference for both axes alignment and measurements. Prior to carrying out any measurements, a rigorous and extensive calibration procedure was conducted, which involved axes alignment, instrument-related systematic errors and line profile broadening determination.
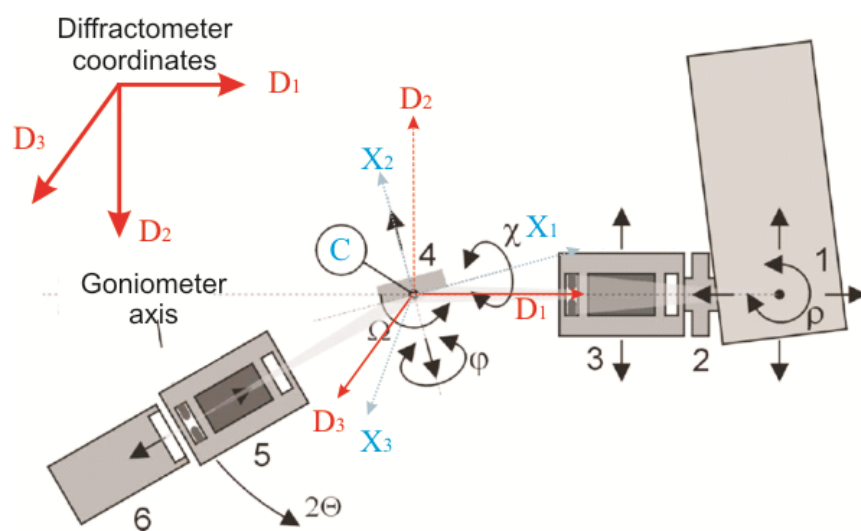

Figure 2.3: A schematic illustration of the Photographs of the 4-axis Seifert XRD3000PTS diffractometer used in this investigation. The definition of the diffractometer and specimen sets of axes are superimposed on the images.

2.2.4.1   X-ray Line Profile Analysis

The quest for new materials which are synthesised for the purpose of serving specific applications under improved conditions requires both a deep understanding and an increased level of control over the structure-property-performance relationships. To that end, a more sophisticated approach to materials characterisation is required. The mere fact that the nanocomposite thin films, which were prepared in this work, are as their name suggests,

composites, implies that they are by no means perfect. Instead, they have structures with varying levels of complexity at the micro and nano-level (commonly referred to as microstructure).

It is well established that diffraction methods such as X-ray and electron diffraction are particularly well suited to investigate the material's microstructure owing to their combined ability to probe the structure both locally and at a large spatial resolution. In the case of microstructural characterisation by X-ray diffraction, the amount of information contained within a diffractogram goes beyond the mere determination of interplanar spacing for the purpose of phase identification. Although this approach remains a central part in material characterisation, much more can be gained by a careful and quantitative examination of the diffraction line profile. Because the microstructure of most materials deviate from the ideal defect-free single crystals, their diffraction profiles (also referred to as reflections) suffer a number of irregularities, which can be used to describe the originating defective microstructure. More specifically, any changes occurring to the shape and breadth of the diffraction line helps to reveal the changes that occurred to the size of the crystalline domains which cause the diffraction. By quantifying the magnitude of the diffraction line broadening, quantitative information about the sizes of the diffracting crystallites (also called coherently crystallite domains, CDD) can be obtained.

Additionally, any angular shift in the position of the broadened diffraction profile with respect to its position based on a perfect single crystal will provide useful information about the degree of distortion that the diffracting crystallites are subjected to in the material. More specifically, information about lattice strains as well as the presence of dislocations and stacking faults can be revealed by measuring the shift in the diffraction line positions and relating then to those of unstrained and prefect crystals. All this is possible when the diffraction line shape is adequately described by a physical model that unmasks the sources of structural imperfections.

Although the procedures involved are complex, lengthy and require an accurate determination of the instrumental contribution to diffraction line broadening, the benefits gained from microstructure determination are enormous given the fact that such methods are in essence non-destructive by nature and do not require extensive efforts in sample preparation. This is in stark contrast to microstructural characterisation by means of high resolution electron diffraction, which offers other advantages and drawbacks. For details see section 2.2.2.

In practice, in order to be able to extract quantitative information about the sizes and disorder (also simplified as microstrains) pertaining to the coherently diffracting domains from XRD measurements, it is vital that the instrumental contribution to the diffraction line shape broadening be determined. This instrumental contribution is commonly referred to as an

instrumental profile and can be obtained by measuring the diffraction lines from a carefully prepared reference powdered material. This material must possess a number of characteristics including being chemically stable and non-hygroscopic. It should also be in the form of finely divided powdered materials which ensures a completely random orientation of the poly-crystals without any preferred orientation or textural effects. In addition, their crystallites sizes should be precisely quantified and/or large enough in order to eliminate their contribution to line broadening.

In this work, several reference materials were used to calibrate and define the instrumental functions of all the diffractometres used in this investigation. Figure 2.4, shows the variation of the integral breadths of all detected reflections as a function of the diffraction angles (2θ). The diffractogram spans the entire 2θ range which will be used in the measurement of all the materials in this investigation. These measured reflections must be correctly fitted to a (split) pseudo-Voigt function in order to determine the angular dependencies of the line widths and shapes parameters precisely. It has been shown that such a formalism can be used to express the variation in line shape parameters as a function of 2θ for a diffraction measurement by using monochromatised radiation in the Bragg-Brentano geometry [91]. A central part of this treatment is to adequately fit the variations in the line shape parameter (integral breadths and mixing factor, η) throughout the entire 2θ range. This fit function will form the basis for the treatment of the measured profiles of the unknown samples whose microstructure is to be investigated. In order to ensure a precise evaluation of the instrument's contribution to the measured diffraction data, the variation in the instrumental integral breadths has to be fitted to a quadratic *tan*θ function with adequate accuracy over the entire 2θ range. According to the implemented fitting procedure, the fitting function and its parameters are as follows:

Gaussian: $\Gamma^2_G = U \tan^2\theta + V \tan\theta + W + Z/\cos\theta,$ **2-5**

Lorentzian: $\Gamma_L = X \tan\theta + Q + Y/\cos\theta$ **2-6**

The values of the parameters A, B, C and D for the various diffractometers used in this investigation are listed in Table 2.3.

Parameter	U	V	W	Z	X	Y	Q
Philips X'Pert	0.00125	-0.00741	0.02408	0	0.08108	- 0.07396	0.06985
XRD3003PTS	0.00306	0.05211	0.03373	0			

Table 2.3: Fitting parameters of the Caglioti functions for the two diffractometer types used in this investigation.
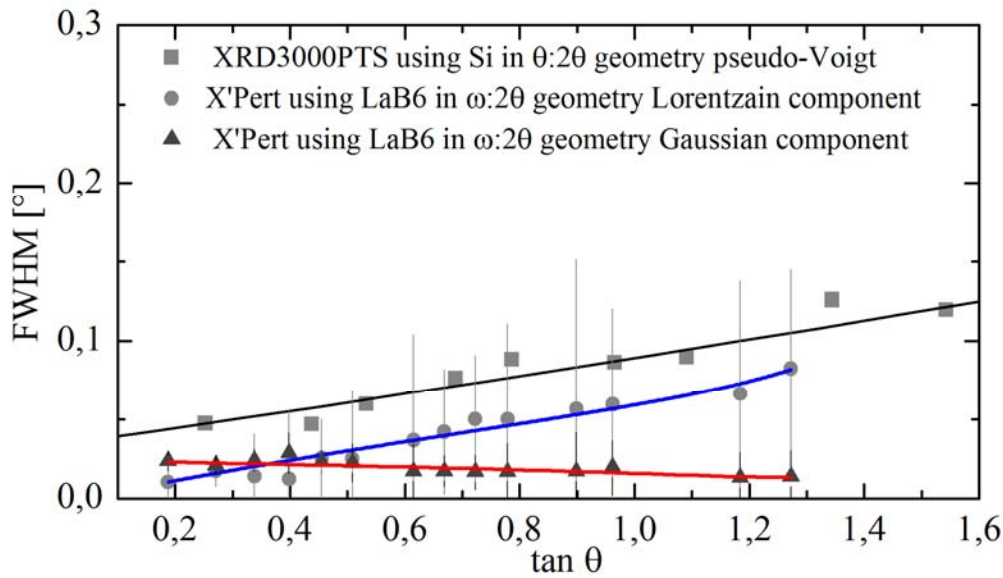
Figure 2.4: The change in the measured and fitted instrumental line profile parameter (FWHM) as a function of tanθ for Silicon by using XRD3000PTS (black) and LaB$_6$ by using Philips X'Pert (blue and red). Both Si and LaB$_6$ are NIST SRM standards.

2.2.4.2 Determination of Film's Residual Biaxial Macrostresses

X-ray diffraction is the method of choice when it comes to determining the stresses of crystalline materials [92, 93]. It is particularly well suited to determining the material's micro- and macroscopic strains owing to its ability to measure the crystallites' lattice spacing with very high accuracy. The build-up of growth and thermal stresses in thin films is inevitable especially when such films are grown at high temperatures and on substrates which may have mismatching crystal structures, lattice spacing as well as mechanical and thermal properties. The resulting stress state can be of a bi- or tri-axial nature. The latter reflects the stress normal to the film's growth direction. When considering the biaxial stress state in the plane of the film, the stresses in the individual phases of the film can be measured by determining the spacing of a particular crystallographic plane (*hkl*) of a crystalline phase as a function of its orientation. In the stress-free state, a particular crystallographic plane (*hkl*) has a spacing of d$_{hkl}$ which is invariable in all directions. In contrast, the lattice spacing of randomly oriented crystallites of a stressed phase will vary depending on the crystallites' orientation. For example, in a single phase film which is in an isotropic tensile biaxial stress state, the spacing of the crystallographic planes that are aligned parallel to the film will increase while that of those aligned perpendicularly will decrease. This means that in a stressed crystallite, there is a directional character to the variations in the measured lattice spacing, which can be used to determine the crystallites' strain. The stresses can be determined from these strains when the interplanar spacing values in the stress-free state are known. Figure 2.5 illustrates schematically how the variation of the lattice spacing of the same crystallographic plane is dependent on the film's stress state and the orientation of the crystallographic direction with respect to the specimen's coordinates.

In this work, the films' residual stress measurements were carried out by employing the $sin^2\Psi$ method [92,93], which is based on the precise measurements of the interplanar spacing values of a crystallographic plane, d_{hkl}, at various tilting angles (Ψ). This angle is defined as the angle between the specimen's normal and that of the diffractometre's. Bragg's equation is then used to calculate the d_{hkl} values of a crystallographic plane (hkl) by using the formula:

$$d_{hkl} = \frac{\lambda}{2 \sin \theta}$$ 2-7

Where d_{hkl} is the spacing of the crystallographic plane (hkl); λ the wavelength of Cu-$K_{\alpha_{1,2}}$ (1.541874 Å) radiation; and θ the Bragg's diffraction angle.

Under an isotropic biaxial stress state, the strain can be obtained by measuring the spacing of a particular crystallographic plane at a specific tilt angle (ψ) according to the following expression:

$$\varepsilon_{\varphi\psi} = \frac{d_{\varphi\psi,hkl} - d_{0,hkl}}{d_{0,hkl}} [\frac{1}{2} s_2(hkl) \cdot sin^2\psi \cdot \sigma_\varphi + s_1(hkl) \cdot (\sigma_1 + \sigma_2)]$$ 2-8

Where $\varepsilon_{\varphi\psi}$ is the strain at the rotation angle (φ) and the tilt angle (ψ); $d_{\varphi\psi,hkl}$ the measured interplanar spacing (hkl) at the rotation angle (φ) and the tilt angle (ψ); and $d_{0,hkl}$ the value of the un-stressed interplanar spacing of the crystallographic plane (hkl). The constants ½ s_2 (hkl) and s_1 (hkl) are the X-ray elastic constants of the crystallographic plane (hkl) which can be expressed in terms of the plane's mechanical constants. ½ $s_2 = [(1+\upsilon)/E]$ and $s_1 = [-\upsilon/E]$ where υ is the Poisson's constant and E is the elastic modulus. The values σ_1 and σ_2 are equal based on the assumption that an isotropic biaxial stress state exists and correspond to the orthogonal stress components in the specimen's surface. σ_φ corresponds to the stress component at the rotation angle (φ).
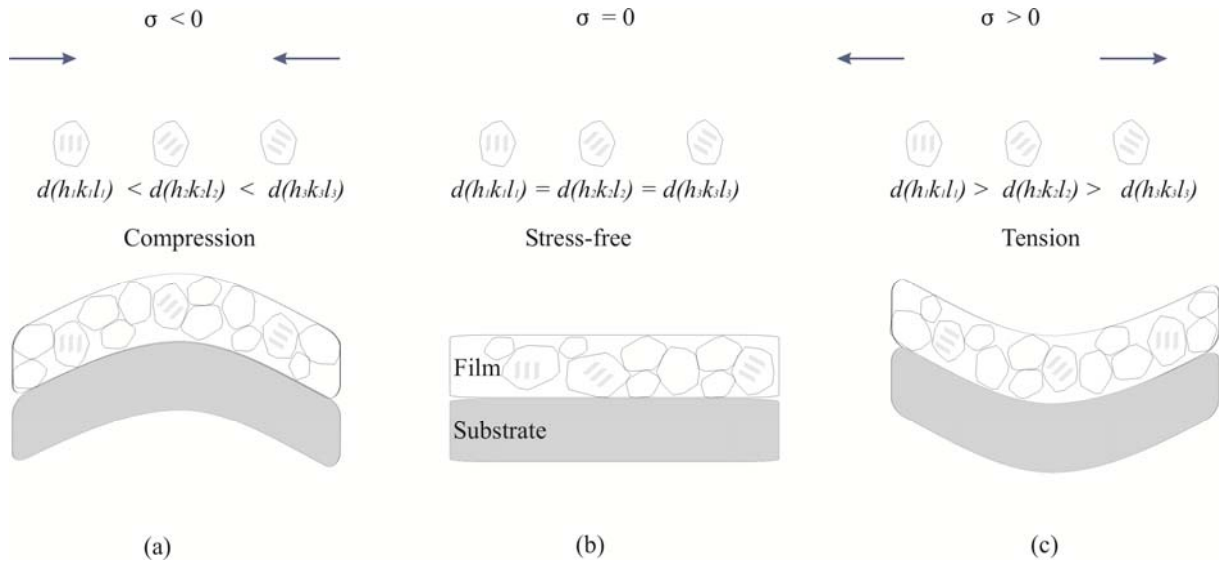
Figure 2.5: The variation of lattice spacing of the same crystallographic plane depending on the film's stress state and the orientation of the crystallographic direction with respect to the specimens coordinates.

According to the expression above, if the d-spacing of the crystallographic plane (*hkl*) is determined at various tilting angles (ψ), the stress may be calculated from the slope of the plot of $d_{\varphi\psi,(hkl)}$ vs $\sin^2\psi$, hence, the method is conventionally referred to as the $\sin^2\psi$-method. In order to minimise the errors in the calculated slopes (and stresses), the measurement of several crystallographic planes as a function of the tilt angle (ψ) are carried out and the variations in the calculated stresses among these planes is considered. It can be seen that the determination of the d-spacing of the unstressed (*hkl*) crystallographic plane is essential in order to calculate the biaxial stress with reasonable accuracy. Figure 2.6 is a schematic diagram of the axis geometry which should be implemented when performing the stress measurement by the $\sin^2\psi$-method. In this measurement, the specimen is at first tilted by an angle (ψ) around the diffractometer axis D_3 before the diffracted beam intensity is collected around the Bragg angle (θ). The specimen and detector rotate symmetrically around the diffractometer D_2 axis by the angels θ and 2θ, respectively.
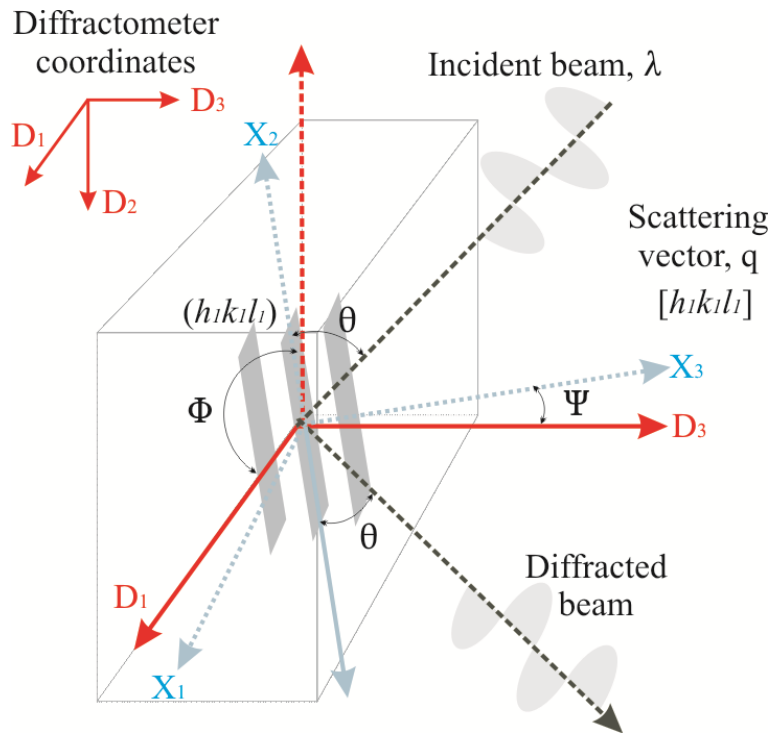
Figure 2.6: A schematic diagram of the residual stress measurement by the symmetrical rotation and tilting of the specimen and detector. D_1, D_2 and D_3 represent the diffractometer's coordinates, whereas X_1, X_2 and X_3 represent the specimen's coordinates. The incident and diffracted angles correspond to the Bragg-angle of the (hkl) diffraction plane. The rotation angles; Φ, is achieved by rotation around D_3 whereas the tilt angle; Ψ, is achieved by rotation around D_1.

Despite the fact that performing this type of measurement is a straightforward matter, it may become unattractive as it is extremely time consuming and requires a long measurement time. Additionally, because measurements in this work were carried out on thin films whose thicknesses do not exceed 500 nm, applying this type of tilt measurements led to significantly reduced intensities from the required Bragg reflections. This is due to the film's much smaller diffracting volume as compared to that of the substrate whose reflections became more dominant. In turn, the significantly reduced intensities from the thin film resulted in the introduction of significant errors when determining the plane spacing which subsequently impacted the stress calculations.

Alternatively, measurements in this work were carried out at a fixed grazing incidence, in which the incident X-ray beam is kept at a constant angle (α) of 2.00° with the specimen surface [93]. In turn, the specimen did not rotate with the detector at half its rotation angle (2θ). This had the advantage of eliminating the diffraction from the substrate while at the same time increasing the diffracting volume to include the entire film. This was made possible because the incident X-rays were spread over a much larger area of the sample, which in turn led to an increase in the diffracted beam intensity. In this manner, the rotation of the specimen and detector no longer proceeded in a symmetrical fashion which limited the choice of which tilt angle (ψ) to use. In the grazing-incidence geometry, the tilt angle (ψ) is restricted to the difference between the grazing incidence and the Bragg angles (α - θ) and cannot exceed (α - θ) - 90° which leads to larger

errors in calculated stresses. Figure 3.28 illustrates the geometry of the diffractometer when determining the biaxial residual stresses at a fixed grazing incident angle. In order to obtain the biaxial residual stress according to equation 2-8, the interplanar spacing of several Bragg reflections must be measured at their corresponding tilt angles (ψ). Choosing several Bragg reflections is essential to obtain a plot of $d_{\psi,hkl}$ vs. $\sin^2(\alpha - \theta)$ whose slope is least-squares fitted on order to obtain the biaxial residual stress. Finally, the residual biaxial stress values were calculated using the averaged X-ray elastic constants (XEC), which are either obtained from the single-crystal compliance according to Reuss's or Voigt's models or by using the isotropic materials' mechanical constants [92,93].

2.2.5 Mechanical and Tribological Properties

Known for its ability to gauge both elastic-plastic responses as well as the frictional behaviour of surfaces, instrumented depth-sensitive Nanoindentation has become the method of choice for probing the mechanical and tribological properties of surfaces at the nanometre scale. By employing low loads ranging from 10 μN up to 10 mN, the method is very well suited and has been recently standardised [74,75] to investigate the mechanical and tribological properties of nanocomposite thin films at the nanometre scale. In order to better understand the interactions between surfaces under external loading and establish structure-property correlations, nanoscale mechanical and tribological investigations are often combined with chemical and microstructural determination which are assisted by other methods. These include surface structure characterisation by AFM, GI-XRD and high resolution electron diffraction as well as the chemical compositional analysis of the interfaces by XPS, EDX, FTIR, and ToF-SIMS to name a few.

Mechanical and tribological characterisations in this work were carried out in two main load regimes. The first was at an ultralow-to-low load in the range of 10 μN- 10 mN and was performed using Nanoindentation. The second was at a high load of 1 N using a home-made laboratory setup. This was performed in order to investigate the film's tribological behaviour at elevated temperatures in the range RT- 400°C. The following sections detail the implemented experimental conditions.

2.2.5.1 Nanoindentation Tests

Measurements of the films' mechanical properties were carried out by a transducer-based scanning nanoindenter (TriboIndenter, Hysitron Inc.) in a laboratory environment (RT and RH of about 50%). Indentations were carried out using a Berkovich indenter with a total included

angle of 142.3° and a radius of curvature of about 100 nm. The indenter was loaded in a quasi-static manner to various final loads up to a maximum of 10mN. The area function of the indenter was calibrated using a standard procedure, which was based on a series of indentations of various loads performed on a fused silica standard with known mechanical properties. This procedure entailed alternating between indenting the films and the fused silica standard. This was carried out repeatedly in order to monitor any possible changes to the tip geometry during indentations. All indentation tests were performed in a force-control mode where the applied load was controlled according to a programmed loading function, and the displacement was continuously monitored throughout the process. The loading function of the quasi-static indentations comprised a 250 µN/s loading and unloading rate segments with a dwell time in the range of 2 to 10s at the peak load, which was used to reduce the influence of the creeping effect [94]. The maximum load was decided by the maximum indentation depth in the films, which was set around 10% of the total film thickness in order to reduce the influence of the substrate. The samples were probed at three different spots. In each spot, a total of 25 indents was placed in a grid pattern composed of 5×5 indents which are 20 µm spaced apart and were obtained from various final loads that ranged from 200 µN to 10 mN. Finally, the mechanical properties of the films were evaluated following the procedure proposed by Oliver and Pharr [95,96].

2.2.5.2   Sliding/ Scratch Tests
A   Nanosliding/ Nanoscratching

Tribological friction tests are an important part of characterising the surface properties of the various hard and protective films fabricated in this work. The transducer-based scanning Nanoindenter which was used to evaluate the films' nanohardness and reduced modulus is also capable of performing nanosliding or nanoscratch tests under constant or incremental ramped loads, pre-selected scratch length and other control parameters. Depending on the indenter's load and the variation in mechanical properties between both counter bodies, the mechanical response of the surface may result merely in elastic deformation (sufficiently low loads where sliding occurs) or combined elastic and plastic deformation (sufficiently high loads where scratching and material removal occurs). In the discussions that will follow, the generalised term nanoscratching will be used to describe the process of nanosliding. In the Tribo-Indenter mode, two conical diamond tips were used which had a 90° cone opening angle and nominal tip radii of 1 µm and 20 µm, respectively. The corresponding real tip radii were 0.7 µm and 4.5 µm, respectively, as determined by fitting a Hertzian contact to low load indents which were made into fused quartz. Nanoscratches with a constant normal load of 500 µN as well as a linearly increasing load from

10 µN to 100 µN were performed. A typical load and lateral displacement profile of an implemented nanoscratch segment is shown in Figure 2.7. In all nanoscratch tests, the scratch speed, minimum distance between two nanoscratches, and the number of nanoscratches for a particular load were set to 1 µm/s, 20 µm, and 10, respectively.

During a nanoscratch, four parameters were collected as a function of scratching time, these are: normal force (F_N), normal displacement (h_N), lateral (tangential) force (F_L), and lateral displacement (h_L). Comprehensive information relating to the films' tribological behaviour against the indenter could be obtained from these parameters. Friction data were extracted from both scratch types by examining the change to the lateral forces as a function of scratch time. Preliminary testing confirmed that the scratches were not influenced by the load ramping manner (i.e. increasing or decreasing the load during scratching). Therefore, the results presented here were confined to uni-directional scratch tests with either constant or linearly increasing loads. The lateral force, F_T, is an important parameter when characterising the surface's frictional behaviour and deformation. It is dependent on the applied normal force as well as the film's mechanical properties and microstructural characteristics.

In the case of nanoscratching with constant normal loads, the friction coefficient was calculated based on the ratio of the measured lateral force to the applied normal force and is denoted as "measured friction coefficient". A typical curve of such a measured friction coefficient versus time is shown in Figure 2.7(c). For scratches with linearly increasing loads, the friction coefficient was calculated from the slope of a linear fit of the change in lateral versus normal forces [97]. The slope is an average value of the steady state scratching and is considered to be the "effective friction coefficient". This procedure is commonly adopted [98] and which account for any non-zero measured lateral forces that are naturally present at a normal load of zero. These non-zero values may be attributed to intrinsic adhesive forces between the surface and the counter body (diamond indenter) and/or equipment-generated artifacts. It is widely accepted that the adhesion forces' contribution consist of various attractive forces such as capillary, electrostatic, and van der Waals. All conducted scratches showed these lateral forces at a normal load of zero. According to Amonton's law, the frictional force (lateral force) can be thought of as:

$$F_L = \mu \cdot (F_N + F_0)$$
<div align="right">2-9</div>

Where F_L is the frictional or lateral force; F_N the normal force (load); F_0 a constant which may be attributed to intrinsic adhesive forces between the counter bodies and/or equipment-generated artifacts; and µ the friction coefficient as obtained from slope of the linear fit of F_L vs. F_N.
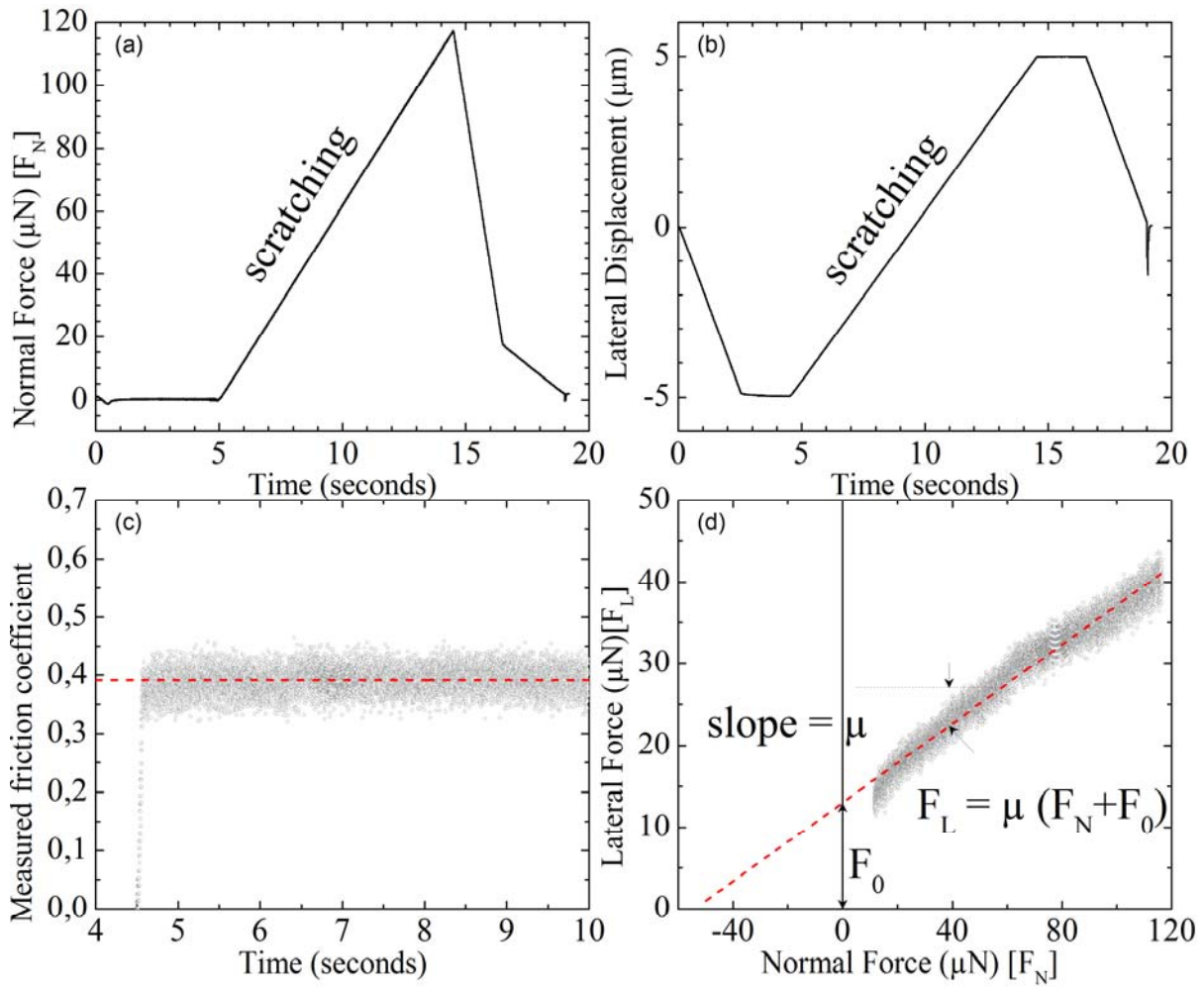
Figure 2.7: Exemplary (a) load and (b) displacement profiles of an individual scratch segment implemented in this work. (c) The variation in the measured friction coefficient as a function of scratching time of amorphous BN with a load of 500 μN. (d) Lateral force vs. normal force diagram for a film in contact with a 1 μm conical diamond indenter where the effective friction coefficient is calculated from the linear fitting procedure.

B   Reciprocating Dry Sliding

In the micro-tribological tests at high loads, a reciprocal friction testing apparatus was used with a modified specimen stage to enable *in-situ* heating during sliding tests. The temperature of the specimen surface was continuously monitored with a set of thermocouples. A load of 1 N was applied perpendicularly via an alumina ball (commercially available grade with a 6 mm diameter). During testing, the specimen was moved reciprocally along the X-direction at a constant speed of 37.7 mm/min while the loaded alumina counter ball remained stationary. At room temperature, the relative humidity was about 50%. Preliminary tests confirmed that the actuator had different sensitivities in the pull and push directions and that the accuracy of the recorded tangential forces were more sensitive to the slide direction. The friction data were generated from the more accurate forward sliding direction with all friction tests being performed in ambient air in the

temperature range 20- 400°C. All data were corrected for the tribometer's responses without the use of specimens at all testing temperatures and the indentation load was calibrated several times throughout the scratching procedure. Further tribological characterisation involved the determination of the coefficients of friction (COF), wear coefficient (k) in units of mm³/Nm and the investigation of the wear tracks by SEM in conjunction with energy dispersive X-ray spectroscopy (EDS). A schematic diagram of the specimen holding and heating stage is illustrated in Figure 2.8.
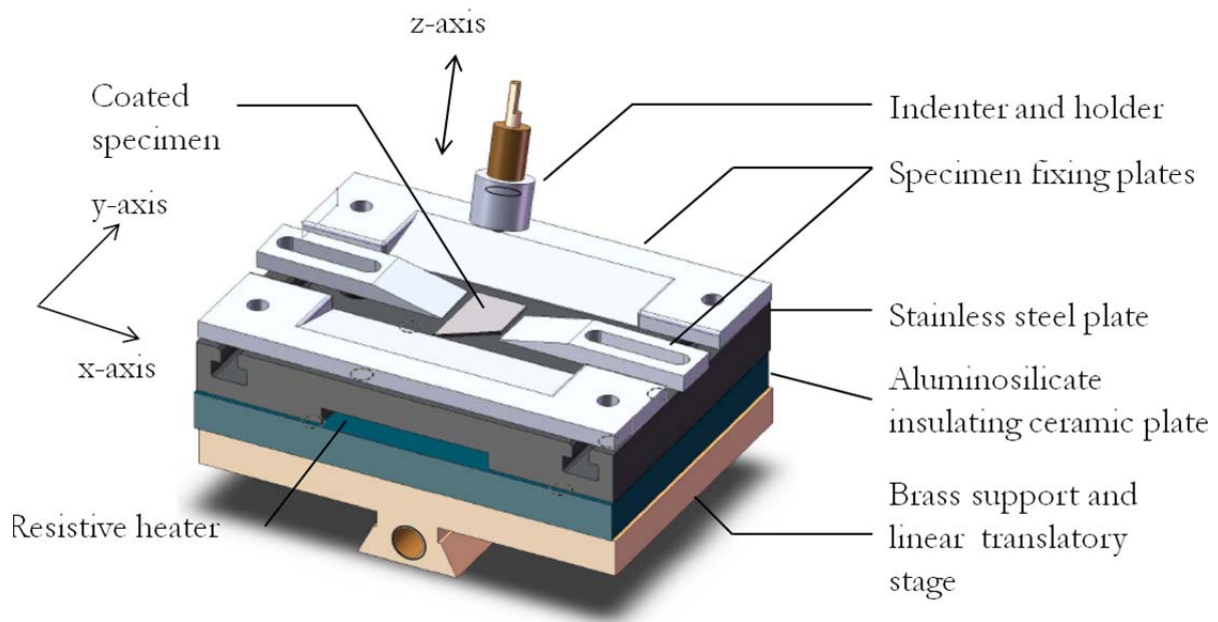
Figure 2.8: Schematic illustration of the specimen stage in the reciprocal sliding testing apparatus.

The temperature control and feedback was performed by using several thermocouples attached to the sample's surface and at various other locations on the stage. It was found that when the temperature of the specimen reached 400°C, the rest of the specimen stage had also heated up to about 150°C, despite the fact that an insulating aluminosilicate ceramic plate with a very low specific thermal conductivity, according to manufacturer's instructions [99], was used. While this did not hinder conducting the sliding test experiments, it imposed a limit to the upper surface temperature that could be attained. Test temperatures that are higher than 400°C would adversely affect the performance of the double bearing rack.

2.2.6   Differential Scanning Calorimetry and Thermogravimetric Analysis

The thermal and oxidation behaviour of selected SiCNO and SiBCNO films were investigated using Differential Scanning Calorimetry (DSC) and Thermo-Gravimetric Analysis (TGA) in conjunction with Mass Spectrometry (MS) in the temperature range RT- 1350°C. A simultaneous thermo-analyser of the type NETZSCH STA 449C (from Netzsch, Selb) allowed the determination of DSC signals and TG curves under a controlled atmosphere. Measurements were carried out in an inert atmosphere under a constant flow of Helium as well as in open ambient air with a relative humidity of about 55%. The instrument was connected to a quadruple mass spectrometer via a heated steel cannula which enabled the simultaneous detection of the effluent gas species that ensued during the annealing process. The mass spectra were collected at a time interval of 20 s in the mass range 10- 100 amu/z. The upper temperature was limited to avoid melting the silicon substrate (melting temperature of 1414°C). Specimens weighting ca. 6.4- 12 mg consisted of film/substrate fragments (ca. 500 nm film adhered to the silicon substrate) were loaded to an alumina crucible where only the film is exposed to the air or He flow. A heating rate of 5°C/min starting from room temperature up to 1350°C was implemented. At 1350°C, the samples were held at this temperature for 180min before they were allowed to cool down slowly to room temperature at a similar rate of 5°C/min as is shown in Figure 2.9. This was a necessary step to avoid possible film delamination. Finally, the samples which were subjected to heat treatment were analysed by X-ray diffraction to determine the phase changes that ensued as a result of the annealing treatment.
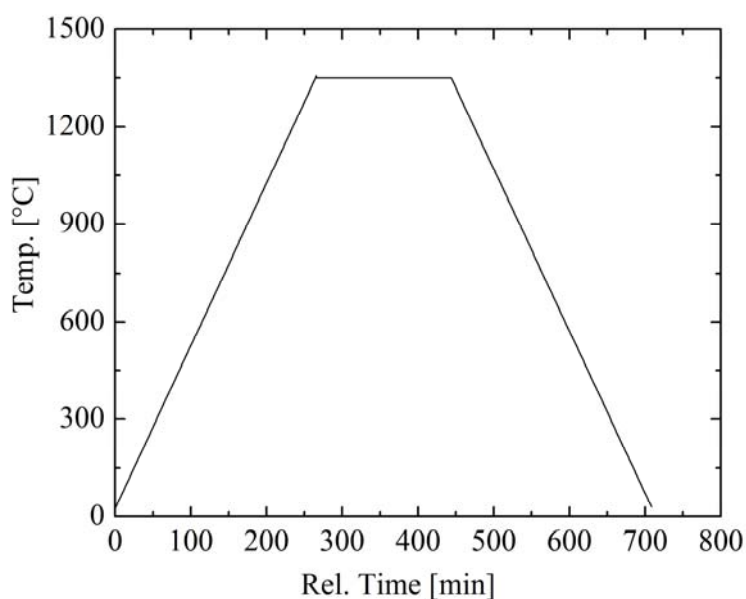

Figure 2.9: Heating cycle which is implemented in the DSC/TGA analysis

3   Nanocomposite Films in the Mo-B-N System

3.1   Introduction

Little is known about Mo-B-N thin films [100], despite the considerable attention which similar thin films based on other refractory metals such as W [101, 102, 103], Cr [104, 105],Ta [106,107,108,109], Zr [110,111,112], Hf [113] and Ti [114,121] have received and in particular those which are sputter and cathode-arc deposited. In bulk form, previous work [115] on the Mo-B-N system under argon atmosphere and in the absence of additional gaseous nitrogen revealed a complex set of high temperature phase diagrams (1200- 1600°C) which constitute several phases including chiefly stoichiometric and sub-stoichiometric molybdenum boride Mo_xB_y phases in addition to hexagonal BN. No presence of any molybdenum nitrides such as MoN or Mo_2N were detected (cf. Figure 3.1). Unfortunately, experimental or calculated phase diagrams of this system are not available in published literature.

Each of these phases demonstrates a different bonding structure and hence varying mechanical properties. The boron nitride phase which exists in three main modifications: hexagonal, wurtzitic and cubic, exhibits a contrast in mechanical properties. While the cubic phase, which is iso-electronic with diamond, is superhard and demonstrates attractive properties as an abrasive, hexagonal BN is a soft lubricant with low shear strength and is universally used as lubricant in most dry sliding applications. Its low friction of coefficient and lubricious properties particularly at temperatures in the range of 400- 800°C make it the material of choice in a number of high temperature tribological applications [116, 117, 118, 119]. As a thin film designed for wear resistance applications, the cubic phase is often sought after, particularly for its work as an abrasive in the presence of iron-, cobalt-, and nickel-based alloys. Nonetheless, boron nitride in multi-phase nanostructured thin films often exists in an amorphous form [120,121]. In addition, Molybdenum nitrides thin films are being investigated for use in wear resistance and tribological applications, as they demonstrate attractive performances in sliding contact owing to their ability to form lubricious layered oxides and sub-oxides particularly at elevated temperatures.

The process of arriving at novel design concepts and implementing new methods of making nanocomposites has always followed one central approach. This approach relies on predicting the performance of the new nanocomposite based on projections regarding the behaviour of its individual constituent phases. It is important to study and evaluate the microstructure of these nanocomposites and understand the relationships between its constituents, their composition and micro- and nanostructures. Nanocomposites films are sought after as they promise to have improved performance as opposed to single phase materials.
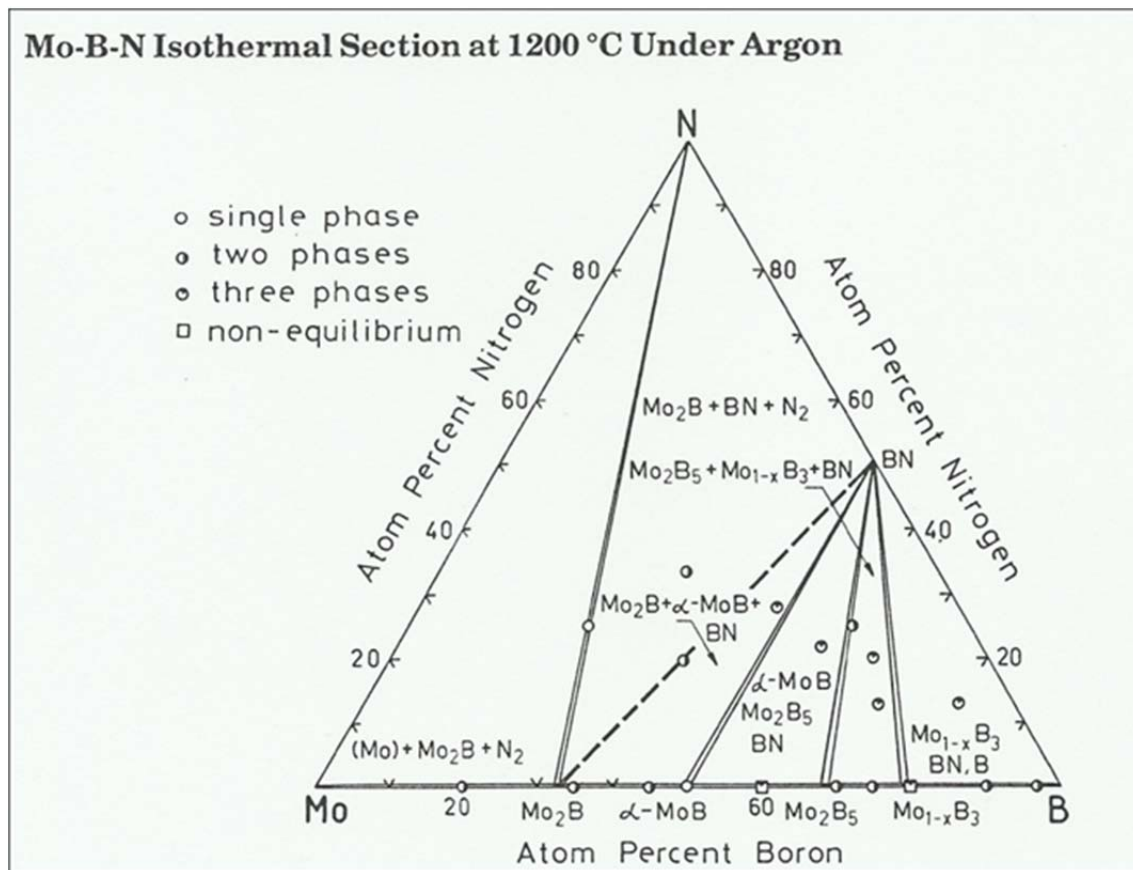
Figure 3.1: High temperature phases in the Mo-B-N in the absence of external nitrogen obtained from [115].

In the context tribological thin films which can have wear resistance characteristics, the success of the application depends on the degree at which the integrity of the film-substrate system is upheld during service conditions. These service conditions very often include thermal and mechanical loadings in conjunction with corrosive chemical media. The most catastrophic film failure results from the accumulation of residual stresses, both intrinsic (growth) and thermal, which lead to film de-bonding and delamination. Thermal stresses become very relevant when depositing nanocomposites at high temperatures during growth. Depending on the materials which make up the substrate and the film, differences in the thermal properties (mainly the thermal expansion coefficients) dictate the nature of the thermal stresses. During high temperature growth, the films tend to develop compressive stresses as well as thermal stress which are compressive during heating up. Some of the compressive growth stresses may be reduced by relaxation processes such as creep and crystallite growth leading to densification. Upon completion of the high temperature deposition process, the resultant residual stresses may either be compressive or tensile depending on the differences in thermal and mechanical properties of the film-substrate system. It is therefore of paramount importance to characterise the nanocomposites' microstructure and seek to evaluate their residual stresses in an attempt to

obtain a better understanding of the relationship between the deposition parameters and the film properties. This will lead to an increase in the degree of control over the deposition process and improve the performance of the nanocomposite under real service conditions.

In this chapter, details of the deposition of nanocomposite films in the Mo-B-N system are presented. The correlations between the chemical composition and mechanical and tribological properties are discussed in depth. In addition, the chapter aims to study the nanocomposites' micro- and nanostructure and to establish correlations between their compositions, and their mechanical and tribological behaviour in the light of their microstructure.

3.2   Film Composition

3.2.1   X-ray Photoelectron Spectroscopy Analysis

X-ray Photoelectron Spectroscopy (XPS) analysis [122] was used to determine film composition, which is expressed in terms of atomic concentrations and displayed in Table 1. The analysis was performed on Ar sputtered surfaces so as to avoid most of the contamination contributions resulting from exposure to air. Film compositions were calculated based on the ratio of the core level intensities of the corresponding elements, which were corrected using the theoretical sensitivity factors based on Scofield's photoionisation cross-sections [123,124].. The survey XPS spectra shown in Figure 3.2 indicate the presence of six elements Mo, B, N, C, O and Ar. The level of impurities in the Mo–B–N films such as O, and C does not exceed a total of 0.5 at% for either, a value which is comparable to the detection limit of the method used. With respect to their main constituents, the films can be divided into three groups. The first group is made up of films which are synthesised in an N_2-He gas mixture and are represented by film **A**. In these films the Mo/N atomic ratio is equal to 2.4. The second group which is represented by film **B** comprises films which were synthesised in the presence of a small fraction of BF_3, but without the addition of H_2 in the gas phase. These films are entirely composed of Molybdenum and nitrogen and do not include any Boron as one of their constituent elements. The Mo/N ratio in these films is higher than that in the first group and amounts to 3.0. The third group represents nanocrystalline composites films in the Mo-B-N system, which are synthesised in the presence of both H_2 and BF_3 gases. Films containing boron are grown by controlling the molefraction of BF_3 in the gas mixture such that if the film's boron-content were to be increased, a higher flow rate of BF_3 would have to be used. As a result, subsequent analysis reveals the presence of the elements Mo, B, and N along with Ar. The latter is due to the sputtering procedure which is performed prior to the spectra being recorded. A summary of the films' elemental composition is listed Table 3.1.

According to the XPS composition data, the flow rates of both BF_3 and H_2 have a direct influence on film composition. Figure 3.3 illustrates the variation in film composition as a function of changing the flow rate of the reactive gases during deposition. By increasing the flow rate of BF_3 during deposition, the film's B-content increases steadily. In the presence of H_2, increasing the flow rate of BF_3 from 0.45 to 1.8 sccm leads to an increase in the boron concentration from 17.6 ± 0.9 to 38.5 ± 1.9 at.%. Although the film's nitrogen content remains between 29.1 ± 1.5 and 36.0 ± 1.8 at.% and is not as greatly affected by the increase in the molefraction of BF_3 in the gas phase, the concentration of molybdenum then drops significantly from 70.9 ± 3.5 to 25.5 ± 1.3 at.% in a manner that is almost a mirror image to that of boron. The results indicate that there is a synergetic effect caused by the addition of boron to the film which causes the variation in the concentrations of boron and molybdenum. The films which are deposited in the absence of H_2, but with the slight addition of 0.45 sccm of BF_3 do not contain boron and are predominantly Mo-N-containing. This is marked by the solid data points in Figure 3.3. Furthermore, XPS analysis was not only used to determine the films' stoichiometry but also to characterise the chemical states of all the constituent elements in order to investigate the relationship between film composition and chemical bonding. To this end, the core level spectra obtained from all elements were evaluated and analysed within an uncertainty range in binding energy values (BE) being in the order of ±0.1 eV.
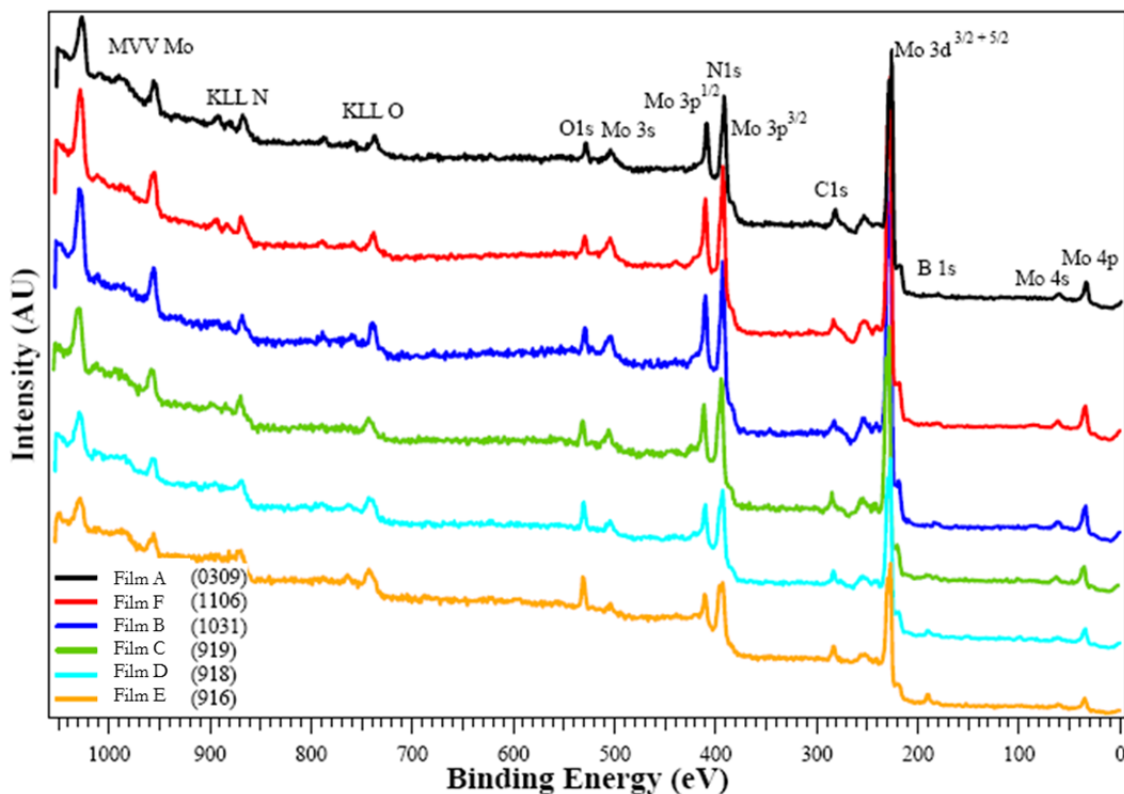

Figure 3.2: Survey XPS spectra obtained from various Mo-B-N films

	Elemental composition (at %)		
Film	Mo	B	N
A	70.9±3.5	0.0±0.0	29.1±1.5
B	74.9±3.7	0.0±0.0	25.1±1.3
C	52.5±2.6	17.6±0.9	30.0±1.5
D	37.0±1.8	30.5±1.5	32.5±1.6
E	25.5±1.3	38.5±1.9	36.0±1.8

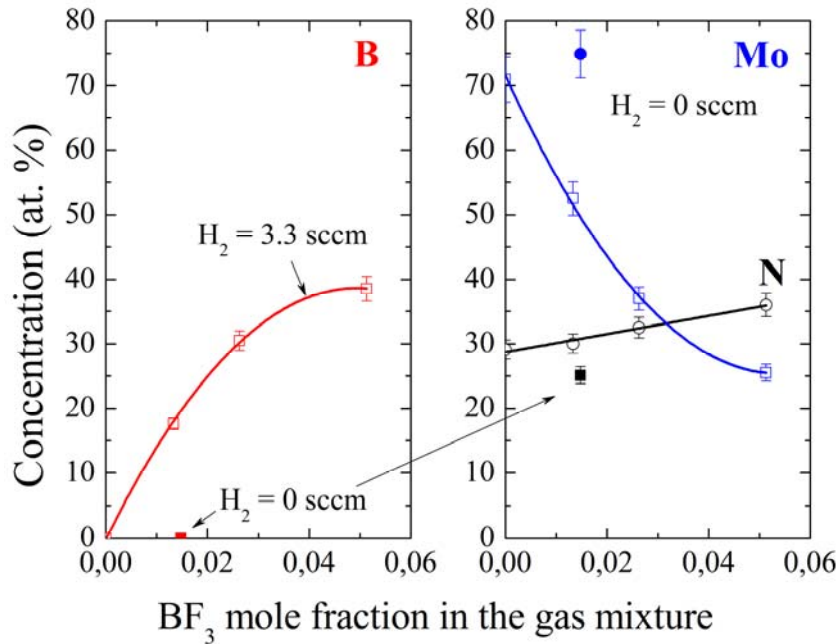**Table 3.1: A summary of the films' elemental and phase composition.**

Figure 3.3: The change in film composition as a function of varying the flow rate of the reactive gases BF$_3$ and H$_2$ during deposition. The solid data points correspond to films deposited in the absence of H$_2$.

According to the binary Mo-N phase diagram [126], no reactions take place between nitrogen and molybdenum at ambient pressure. The solubility of nitrogen in metallic molybdenum is very low at temperatures lower than 1200°C and a solid solution Mo(N) containing 1 at% of nitrogen is only permissible at considerably high pressures reaching up to 385 bar leading to [125]. According the binary phase diagram, at pressures as low as 100mbar a nitrogen content between 28at% would result in formation of a sub-nitride of molybdenum in both tetragonal (α) and a cubic (γ) modification of Mo$_2$N at temperatures above 900°C. Increasing the nitrogen content to levels ranging between 28- 35at% gives rise to the high temperature cubic (γ) phase. At the same temperature and pressure, the stoichiometric MoN phase forms when the nitrogen content is 50 at%. Clearly the films which are deposited at 900°C but at much lower pressures don't produce phases which either conform to or can be predicted by the aforementioned phase diagram. The Mo-N film deposition conditions are far from equilibrium. There are even less data available in published literature for the case of the Mo-B-N system. The only available data are of high temperature phases at temperatures in the range 1200- 1600°C [115] which cannot be used to

predict the phase formation at lower temperatures. Nonetheless, there is no appreciable solubility of boron in either molybdenum or molybdenum nitride at the deposition temperature and the high temperature ternary phase diagram clearly marks the absence of any ternary compounds. The respective positions of these films within the ternary Mo-B-N phase diagram are shown in Figure 3.5. The positions of these films suggest the possibilities of the existence of multiple phases particularly those with high boron content. Under the implemented deposition conditions, the formation of non-equilibrium phases cannot be excluded.
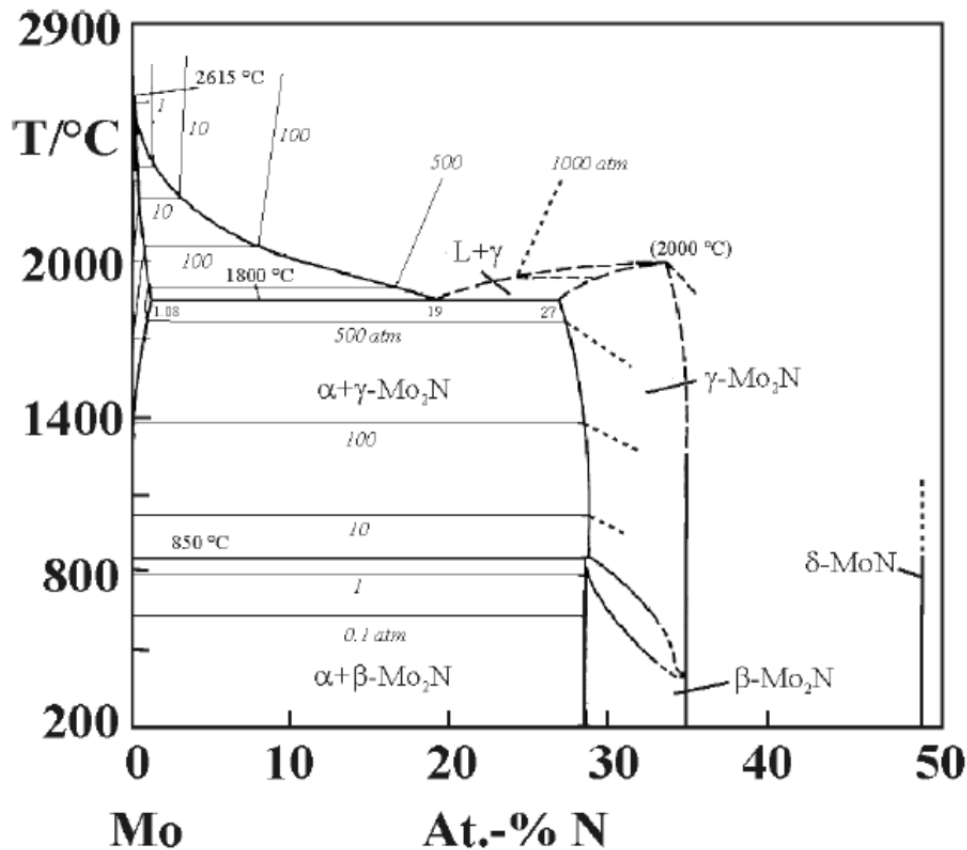
Figure 3.4: The binary Mo-N phase diagram including various pressure isobars after [126].
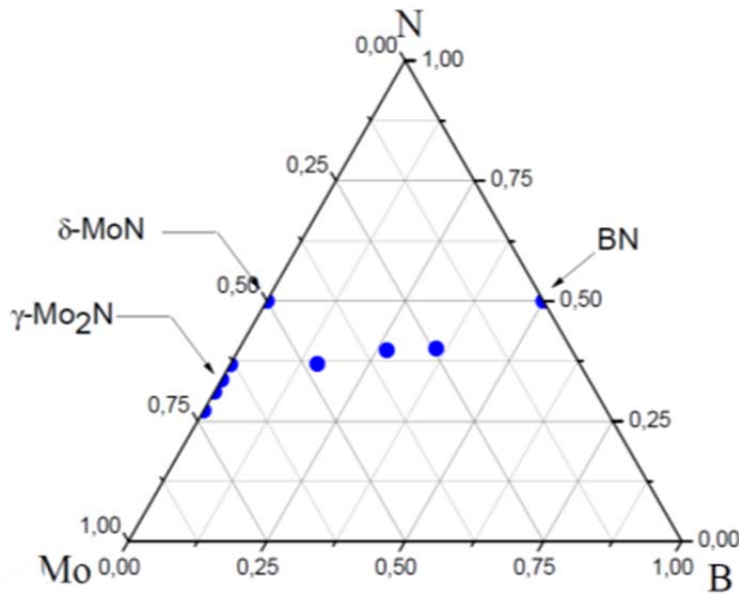
Figure 3.5: Composition of various deposited films as determined by XPS with respect to the simplified ternary Mo-B-N phase diagram.

Furthermore, the high resolution XPS core level spectra were used to obtain detailed information about the chemical bonding in the films. Figure 3.6 (a) and (b) show the XPS core level spectra of Mo $3d$ and Mo $3p$- N $1s$ of molybdenum nitride films **A** and **B**. The Mo $3d$ doublets of all films indicate the presence of a nitride with a complex oxidation state. The binding energies of the Mo $3d_{5/2}$ and Mo $3d_{3/2}$ electrons are found to be 228.4 ± 0.1 eV and 231.4 ± 0.1 eV, respectively. The energy difference between these two states remains at a constant value of 3.0eV for all films and is consistent with the theoretical value [127]. It is evident that both peaks are a superimposition of several peaks which indicates several bonding states of Mo in the films. Peak de-convolution of the asymmetric Mo $3d$ doublets reveals the presence of two major components in the spectra of **A** and **B**, while three components were required to give a satisfactory fit in the case of the core level spectra obtained from **C**, **D** and **F**. The strongest component in the Mo $3d_{3/2}$ spectrum of **A** and **B** centres at 231.6eV and 231.4eV, respectively, whereas that of the Mo $3d_{5/2}$ spectrum of the same films centres at 228.4eV and 228.3eV, respectively. This strong component corresponds to a low oxidation state of Mo and is similar to the values which are obtained from Mo$_2$N. This is in good agreement with previously reported values for the Mo $3d_{5/2}$ binding energies for the stoichiometric Mo$_2$N, which are found to be around 228.4 eV [128] and 228.5 eV [129].

In contrast, the minor and broad components in the Mo $3d_{3/2}$ and Mo $3d_{5/2}$ spectra at 232.9eV and 229.7eV, respectively, in the case of film **A**, and at 232.5eV and 229.3eV, respectively in the case of film **B** indicate the presence of a higher oxidation state of Mo. The position of these maxima is directly related to the oxidation state of molybdenum. For example, in MoO$_2$ in which molybdenum has the oxidation state +4, the Mo $3d_{5/2}$ peak is reported to be centred at 230.0eV [130]. A carefully prepared molybdenum oxide standard MoO$_3$, in which molybdenum has the

oxidation state of +6 was used in the calibration process during the XPS analysis. The result indicated a Mo $3d_{5/2}$ peak position at 232.4eV that is consistent with literature values [130]. All this suggests that both de-convoluted components in the Mo $3d$ doublets result from Mo with an oxidation state that is less than +4 but higher than that of Mo which contributes to the more intense lower energy of the spectra. Thus, it can be inferred that Mo exhibits a mixed valance state, one which originates from a mixture of both a stoichiometric Mo_2N and MoN and possibly from a non-stoichiometric $Mo_2N_{1\pm x}$. In fact, X-ray diffraction patterns of **A** and **B** (see section 3.3.2) supports this observation by confirming the presence of both hexagonal MoN and cubic Mo_2N phases.

Figure 3.6(b) shows the XPS spectra of Mo $3p_{3/2}$ and N $1s$ core levels obtained from films **A** and **B**. Due to the very close binding energy values from both levels, there is quite a large superimposition of both Mo $3p_{3/2}$ and N $1s$ signals. In both spectra, the Mo $3p_{3/2}$ peak appears at 394.0eV, however, as in the Mo $3d$ doublet peak de-convolution, a satisfactory fit of the Mo $3p$ doublets is best obtained by fitting with two components. These components correspond to a mixed valent Mo in the nitride and are similar to previously published values [131]. The N $1s$ line centres on 397.5eV which is close to previously reported binding energies in Mo_2N at 397.2eV [128].

The chemical binding states of the Mo-B-N nanocomposite films (**C**, **D** and **E**), which were grown with various boron contents were also characterised by analysing their XPS spectra. The core level spectra of Mo $3d$, Mo $3p$, N $1s$, and B $1s$ which are obtained from these films are presented in Figure 3.7(a- c). In the Mo $3d$ spectra (cf. Figure 3.7(a)), film **C** with a boron content of 17.6±0.9 at.% B exhibited similar Mo $3d_{3/2}$ and Mo $3d_{5/2}$ spectra peaking at 231.5 and 228.4 eV, respectively. Both peaks are, however, largely asymmetric and peak de-convolution resulted in a satisfactory fit with three components. These binding energies (BEs) indicate that Mo atoms are bonded to both N and B atoms due to the close values of Mo–N (BE = 231.4/ 228.4 eV) [128] and Mo–B (BE = 231.0/ 227.9 eV) binding energies (the first and second value in the bracket correspond to the Mo $3d_{3/2}$ and Mo $3d_{5/2}$, respectively) [122]. While there is no discernible shift in the binding energies of the Mo $3d$ doublet as a results of increasing the B% in the films, there is a gradual increase in the ratio of the Mo-B and Mo-N components obtained from both Mo $3d_{3/2}$ and Mo $3d_{5/2}$ peaks. The peak area ratio of the fitted Mo-B and the Mo-N components increases by a factor of three from 0.04 to 0.12 as a result of increasing the film's boron content from 17.6±0.9 to 38.5±1.9 at.% B, which confirms that an increase in the proportion of Mo-B bonds in the films has taken place.
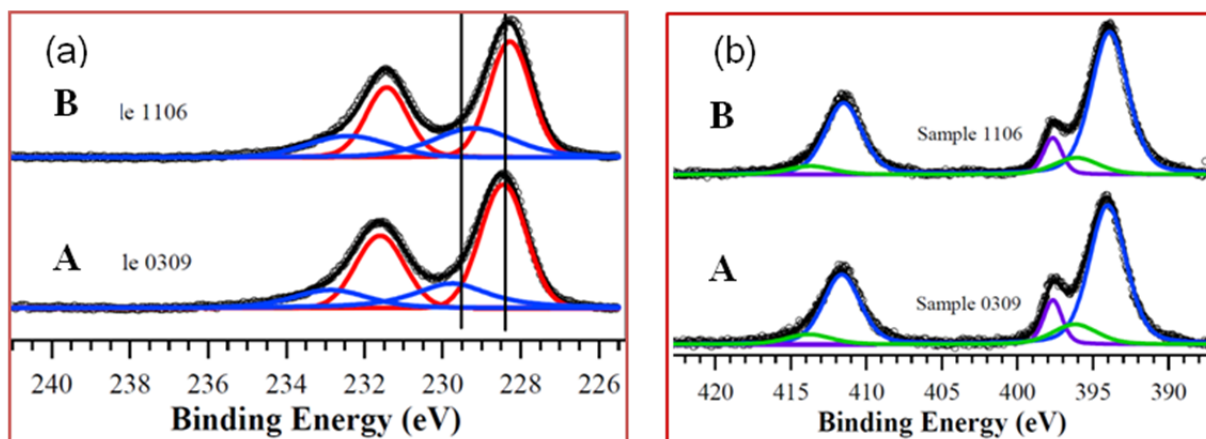
Figure 3.6: XPS Spectra of as deposited Mo-N films (A and B): (a) Mo $3d_{3/2}$ and Mo $3d_{5/2}$ core levels and (b) Mo $3p_{1/2}$ and Mo $3p_{3/2}$ and N $1s$ core levels.
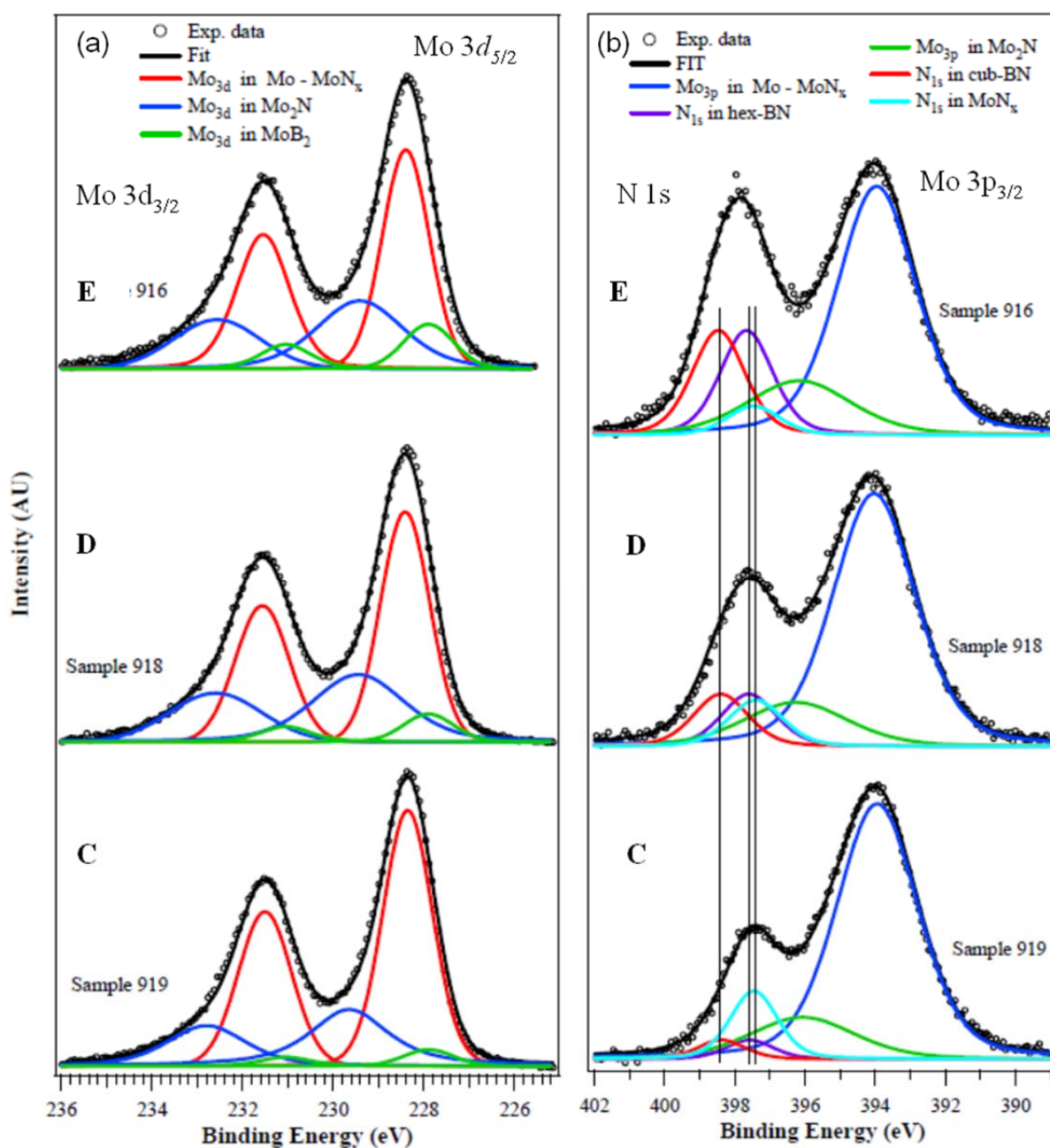

Figure 3.7: XPS Spectra of Mo-B-N nanocomposite films with various B content (C, D and E): (a) Mo $3d_{3/2}$ and Mo $3d_{5/2}$ core levels and (b) Mo $3p_{3/2}$ and N $1s$ core levels.

The N $1s$ spectra (Figure 3.7(b)) are both asymmetric and strongly superimposed on the Mo $3p_{3/2}$ peak. The N $1s$ binding energy centres around 397.4eV for film **C** and gradually shifts to higher binding energies as the film's boron content increases in films **D** and **E**. Peak de-convolution reveals the presence of three components which could be attributed to N-Mo (BE = 397.4eV), and to two types of N-B bonds. The latter could be fitted by de-convoluting at least two possible peaks centred at 397.6 and 398.6 eV, which correspond to both sp^2- and sp^3-bonded N-B, respectively. This is in agreement with previously reported values for B-N bonds [132] although higher values have been reported of BN compounds as well [133,134]. In addition, the relative peak area ratio of the components which are related to N-Mo and N-B bonds diminishes steadily as the films' boron content increases. This indicates that the N-B bonds become predominant at higher B-contents and that the additional boron binds primarily with nitrogen, which decreases the proportion of N-Mo bonds. This is also evident by the 0.5 eV shift in the binding energy to higher energies which is attributed to an increased proportion of the B-N bonds in the nanocomposite as can be seen from Figure 3.8(a).

The B $1s$ spectra (cf. Figure 3.9) of the nanocomposites reveal a more complex bonding situation. Evidence from their XPS spectra reveals that molybdenum nitride films: **A** and **B**, are free of any boron-related characteristic peaks. In films **C**, **D** and **E**, two symmetrical features are seen to be centred at 188.0 eV and 191.2 eV, which can be attributed to B-Mo and B-N bonds, respectively. The separation between these two peaks is sufficiently large to enable the identification of their chemical states. A comparison with the binding energies of B(sp^3)-N, B(sp^2)-N, and B–O bonds, which are reported at 190.7 [135], 191.2 [136] and 193.6 eV [137], respectively, suggests that the measured binding energy corresponds to both sp^2 and sp^3 B-N bonds. While it is difficult to unambiguously distinguish between sp^2 and sp^3 B-N bonds, the large peak width (FWHM ~ 1.2 eV) may be compatible with the presence of these two features which are very close in energy. The high peak symmetry eliminates the presence of any detectable B-O bonds in these films. Furthermore, the peak at 188.0 eV is related to MoB_2 (BE = 188.1 eV) [138,139] and its de-convolution with one component gives good line shape reproducibility. In addition, the intensity of this peak decreases steadily as the film's B-content increases from 17.6±0.9 at% to 38.5±1.9 at.%. Figure 3.8(b) illustrates how the peak area ratio of the B $1s$ photoemission that related to the B-N and B-Mo bonds increases linearly as a function of the film B-content. This change is attributed to the decrease in the proportion of Mo-B bonds, and to the fact that the boron in the nanocomposite binds predominantly to nitrogen. This observation is well correlated with the systematic shift towards higher energies in the N $1s$ photoemission spectra as seen in Figure 3.8(a).
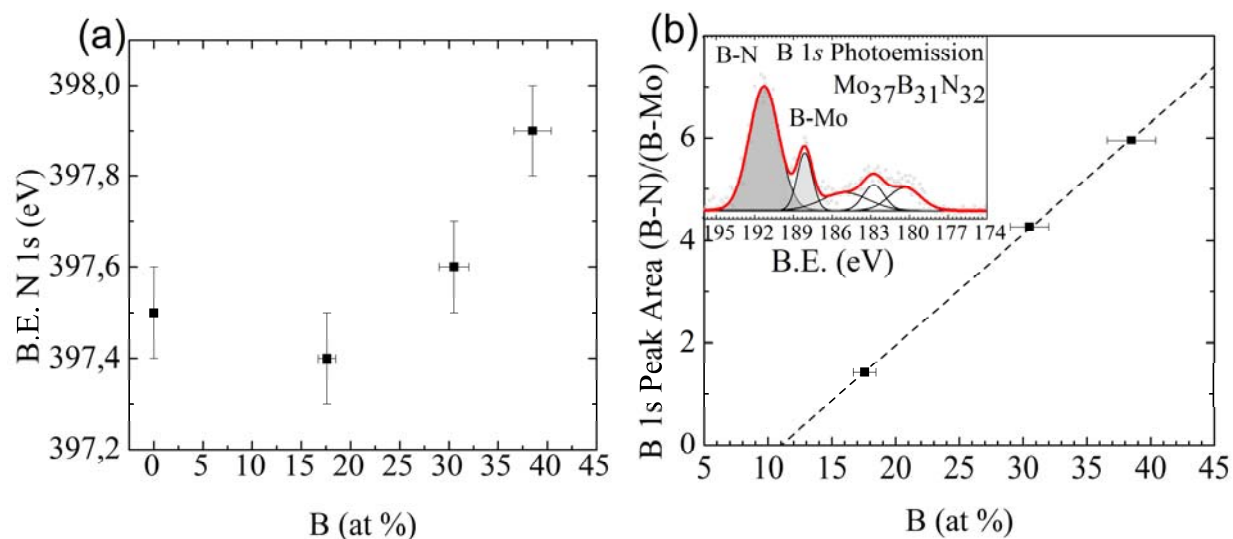
Figure 3.8: (a) N 1s photoemission energy as a function of nanocomposite boron content. (b) The relative peak area of the B 1s photoemission of B–N and B–Mo bonds. Inset shows an example of the respective fitted photoemission B 1s peaks and of film D.
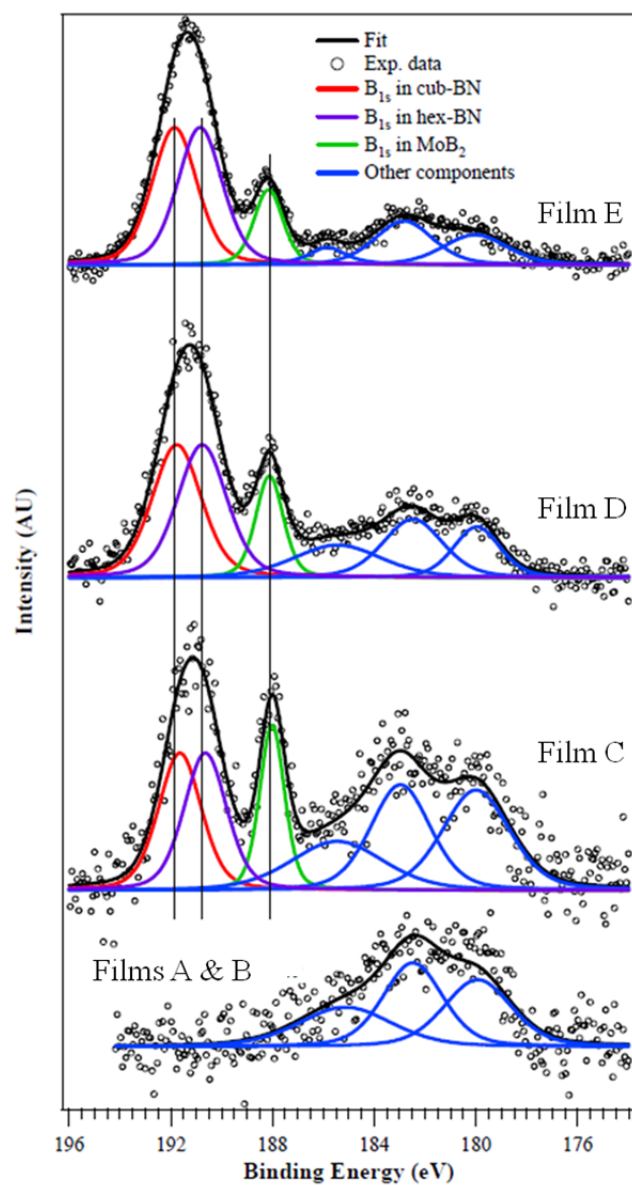

Figure 3.9: The B *1s* core level XPS spectra of films A- E.

3.2.2   FTIR and ToF-SIMS Analysis

FTIR spectroscopy is particularity useful in detecting the bond B-N, B-O and B-C which may be present in the nanocomposites. Figure 3.10(a) and (b) show the FTIR absorption spectra of the films which were collected in both transmission and reflection modes. Films **A** which was prepared without the addition of either BF_3 or H_2 shows absorption at all the spectral range 400-4000 cm^{-1}. Similar spectra are also obtained from film **B** in which BF_3 was used during deposition but not H_2. The absence of any B-N related vibrational bands is evident in films **A** and **B**. This is because hydrogen, which is crucial to the formation of BN under such plasma conditions, was not part of the deposition gases as will be explained in section 3.9.1. In films **C**- **E,** the strong absorption bands which are located around 1374 and 775 cm^{-1} can be attributed to the Transverse Optical (TO) stretching and bending vibrations of the B-N bond, respectively. These bands are always found to dominate the absorption spectra of hexagonal boron nitride (h-BN) and therefore, they provide evidence of the existence of the boron nitride phase in these films. The shoulder band which is located at around 1285 cm^{-1} could be attributed to the wurtzite modification of BN [140].

With a measured band width of over 200 cm^{-1}, these vibrations reflect a the high defect density of the BN phase and suggest that it exists in a largely disordered form and has considerably small and disordered grains [141 , 142]. The intensities of both BN bands appear to increase systematically with increasing the flow rate of BF_3 during deposition. This is a clear indication of the increasing fraction of the BN phase in the films. Films **D** and **E** which were deposited at 0.9 and 1.8sccm BF_3, respectively, show the most intense BN bands and therefore have the highest BN content. In contrast, the intensity of the TO stretching vibration in films prepared with 0.45 sccm BF_3 dropped sharply and broadened significantly. This change can be traced more clearly in the reflectance spectra (cf. Figure 3.10(b)). Such a significantly broad feature which centres around 1330 cm^{-1} in film **C** has also been observed in amorphous hydrogenated boron nitride [143] and can therefore be attributed to an amorphous sp^2-bonded BN. In addition, the bands appear to be shifted to lower wavenumbers in **C** as opposed to **D** and **E** which can be expected from the highly defective and distorted BN phase [144].

Figure 3.11 reveals the elemental distribution in all the films as obtained by ToF-SIMS depth-profile analyses. Films **C**- **E** show a relatively uniform and homogeneous distribution of Mo, N and B across the film thickness as marked by the constant intensity profiles of the B^+(11.0057 amu/z), Mo^+ (97.9187 amu/z) and MoN^+ (111.9145 amu/z) secondary cations. The species

MoN^{+-} was chosen to represent the nitrogen incorporation instead of N$^+$ due to the considerably low secondary ion yield of atomic N which is a common observation in SIMS measurements [145]. The profile of the Si$^+$ (27.9705 amu/z) is also shown to indicate when sputtering of the entire film occurs. In film **A**, a slight increase in the intensity of Mo$^+$ and MoN$^+$ near the interface region can be attributed to the denser film structure in the early growth stages. The relative intensities of B$^+$ species follows a pattern which corresponds to the amount of BF$_3$ used during deposition and hence the film's B- content.
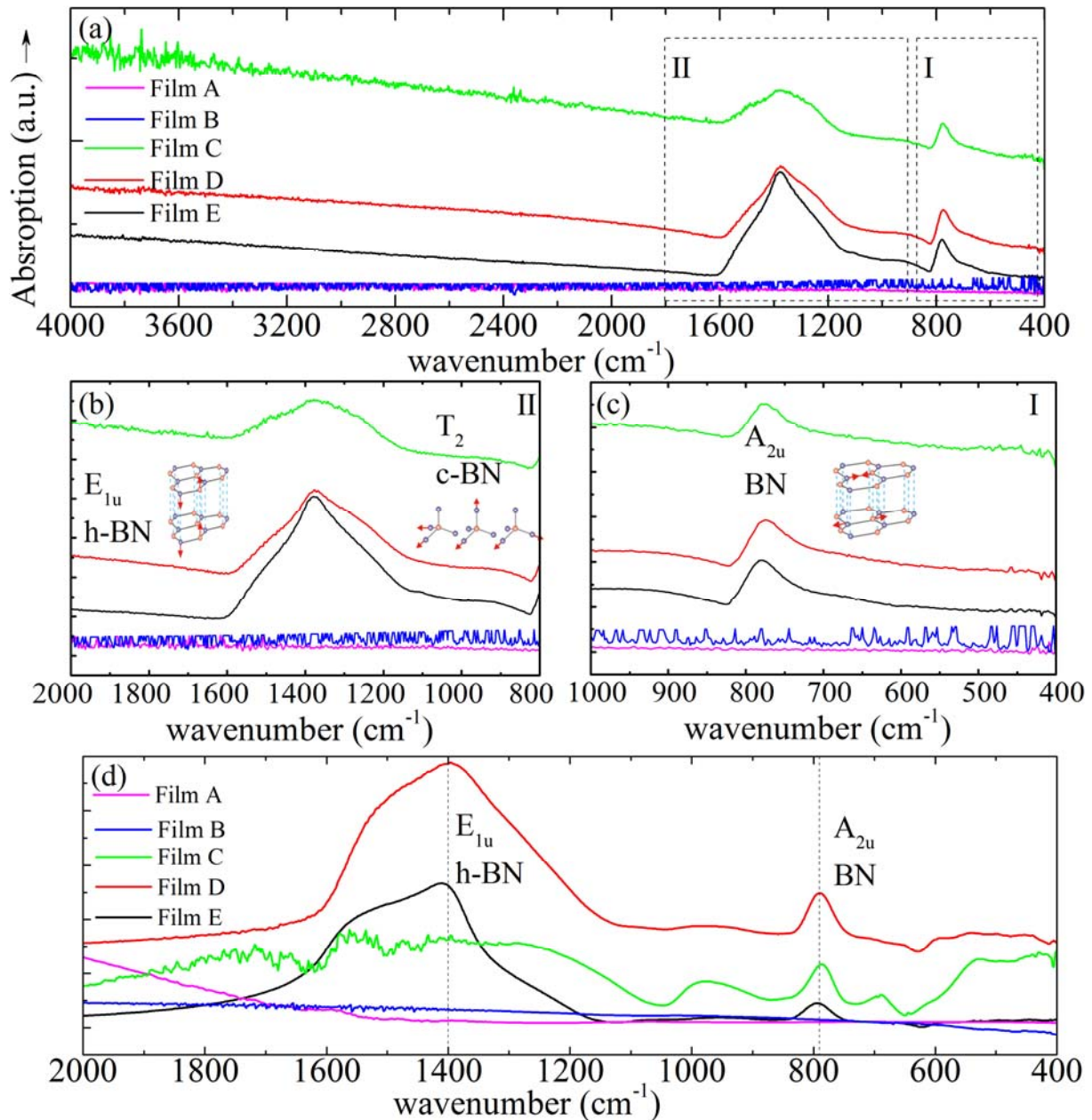

Figure 3.10: (a- c) Absorption FTIR spectra of films synthesised at various flow rates of BF₃ which were collected in transmission mode. In (b) the spectra were collected in near-normal reflection mode and were also Kramer-Krönig analysed in order to extract the films' extension coefficient.
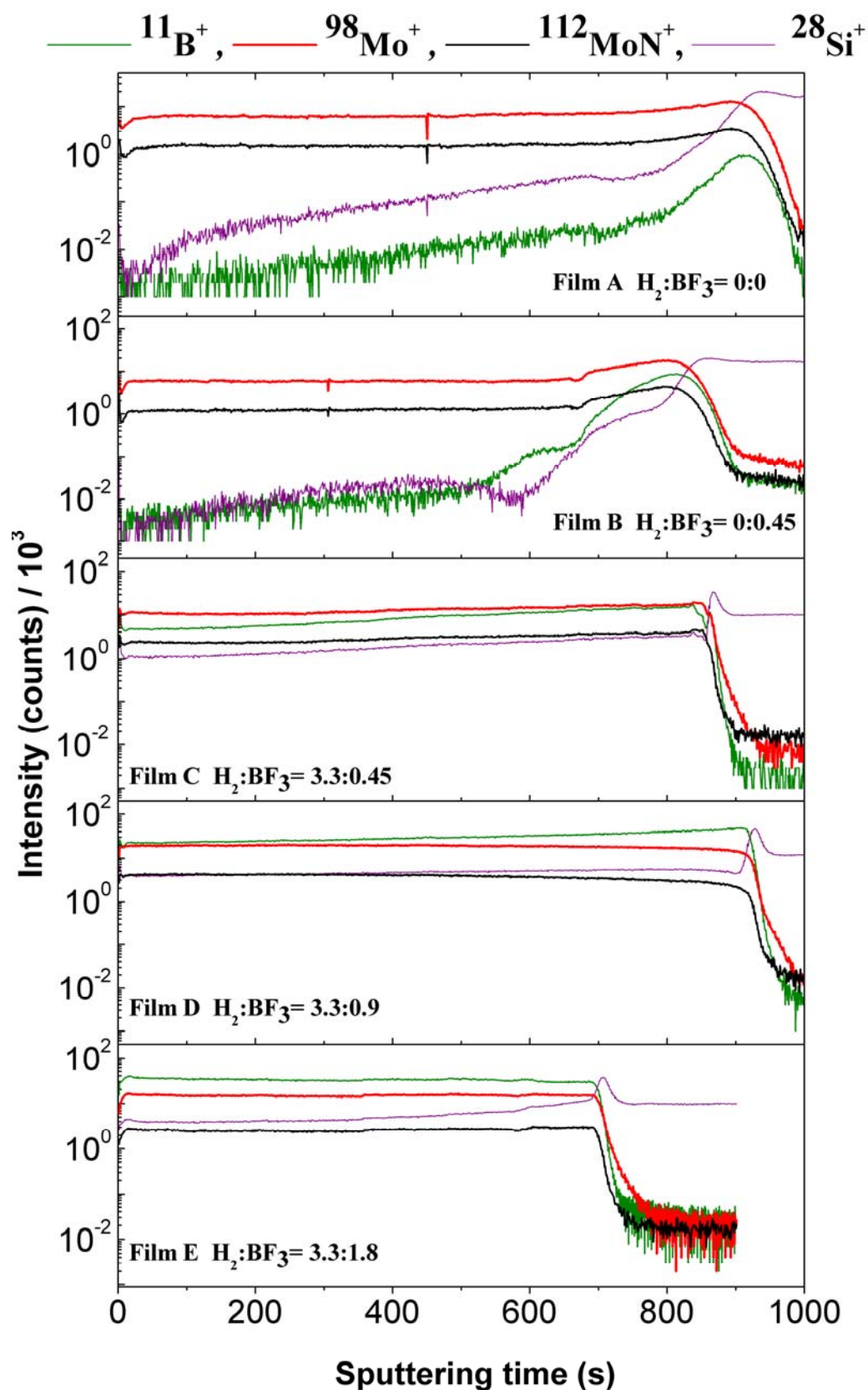
Figure 3.11: The evolution of ToF-SIMS signal intensities of secondary anions related to the elements: molybdenum, nitrogen and boron for various nanocomposites films.

3.3   Structure and Morphology

3.3.1   SEM Observations

After deposition the films exhibited a range of colours ranging from silver-greyish for those films deposited only in N_2/He to dark violet-black for those deposited with BF_3 and H_2. Plan-view and cross-section SEM micrographs of films **A**-**E** are presented in Figure 3.12 and Figure 3.13, respectively. These films were prepared at increasing flow rates of BF_3 from 0 to 1.8 sccm and depict marked morphological changes associated with increasing the BF_3 flow rate during deposition. Polycrystalline molybdenum nitride films (**A** and **B**) show faceted grains with a uniform grain size of more than 80 nm. The slight addition of 0.45 sccm of BF_3 during the depositing of film **C** changes the polycrystalline grains into smaller spherical grains mostly of sizes of well below 15 nm. By further increasing the BF_3 flow rate, the films' morphology becomes entirely different: consisting of spherical grains, of notably smaller sizes which appear in brighter contrast and are embedded in a finer matrix which appears in dark contrast. The fracture micrographs of films **A** and **B** show a columnar-like growth of the molybdenum nitride with rough surfaces reflecting this growth morphology. It appears that the lower section of the film near the silicon substrate is much finer than the upper sections of the film indicating that the grains increase in size as the film grows. On the other hand, the nanocomposite films **C**, **D**, and **E** show more homogenous structure throughout the entire thickness with much finer grains which are similar in size to the surface grains which are observed in the plan-view micrographs. In all cases, there are no signs of any delaminated sections in these films even after substrate fracture indicating strong adhesion to the silicon substrates.
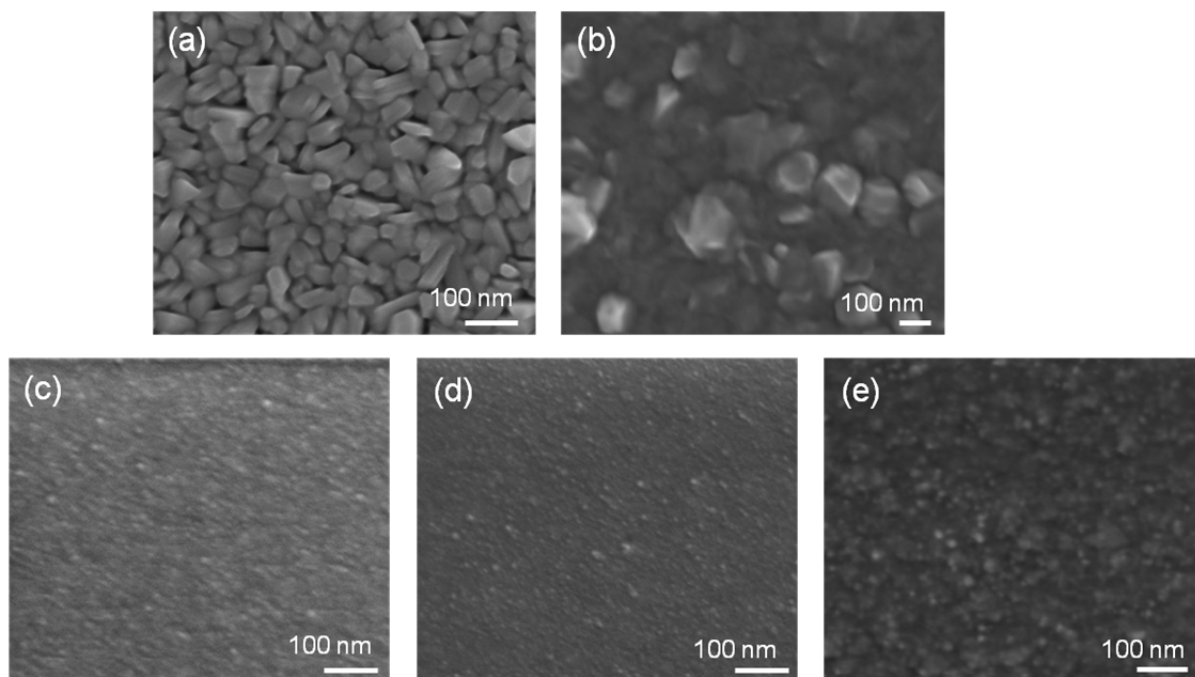
Figure 3.12: Plan-view SEM micrographs of films (a) A, (b) B, (c) C, (d) D, and (e) E.
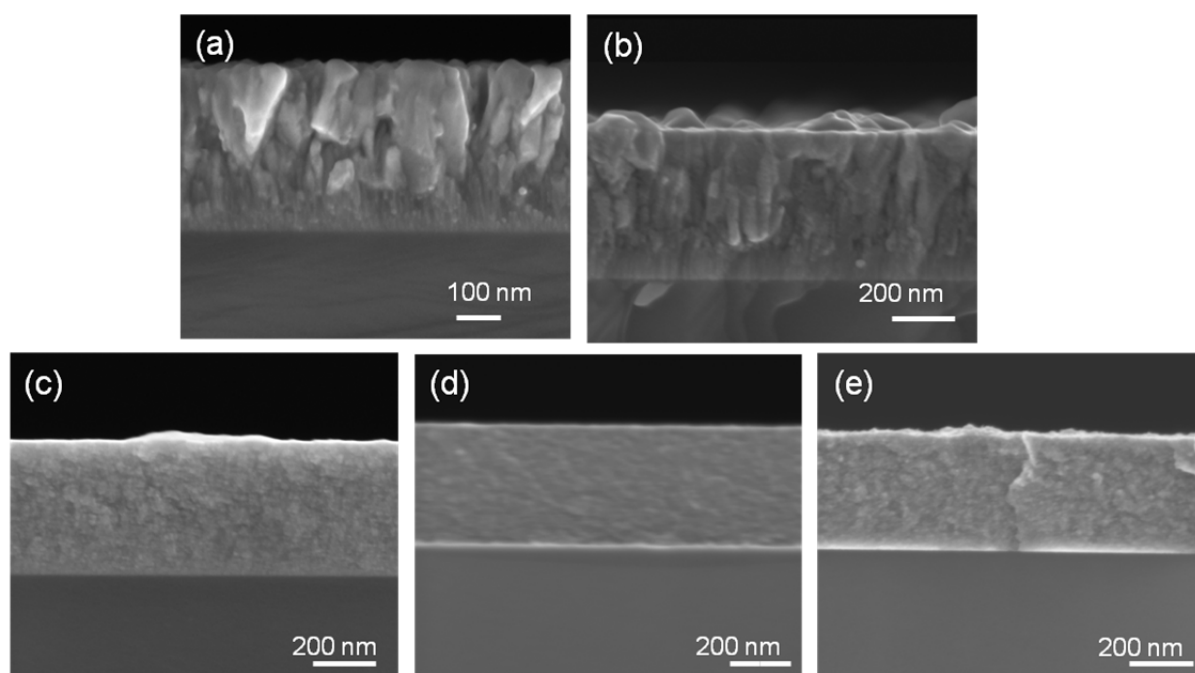

Figure 3.13: Cross-section SEM micrographs of films (a) A, (b) B, (c) C, (d) D, and (e) E.

3.3.2 XRD Analysis

Figure 3.14 shows the grazing-incidence X-ray diffraction (GI-XRD) patterns of the films deposited on silicon (100) single crystals at various flow rates of H_2 and BF_3, which were recorded at an incident angle of 2.0°. For film **A,** which was deposited in a N_2/He plasma mixture, without

the addition of either BF_3 or H_2, the diffraction pattern reveals the presence of a mixture of two nitride phases of molybdenum. The first is a hexagonal modification known as δ-MoN, which crystallises in the space group: $P6_3/mmc$ (JCPDS: 25-1367) and the second is a face centred cubic (*fcc*) modification known as γ-Mo_2N which crystallises in the space group: $Pm3m$ (JCPDS: 25-1366). The observed reflections in the pattern of this film correspond well to the δ-MoN and γ-Mo_2N phases. No evidence of crystalline molybdenum or other crystalline molybdenum nitride phases can be detected and the pattern suggests the absence of any obvious film texture as the relative intensities of the all reflections are close to those of the referenced powdered phases. The film's phase structure did not vary significantly in the case of film **B** which was deposited under identical conditions to film **A,** but with the addition of 0.45 sccm of BF_3. As previously mentioned, the addition of minute amounts of the boron precursor did not result in boron inclusion in the film as confirmed by XPS. The diffraction pattern of film **B** resembles that of **A** greatly, a fact which indicates that only hexagonal δ-MoN and cubic γ-Mo_2N make up the film structure. As in film **A,** there is no indication for the presence of metallic molybdenum or any preferred growth orientation or texture. Additionally, there are no detected reflections which can be ascribed to any molybdenum borides which corroborate the results obtained by XPS.

The film's phase structure has changed drastically by introducing 0.45 sccm of BF_3 in the presence of H_2 (3.3 sccm) during deposition as in the case of film **C**. The intense reflections of δ-MoN are totally diminished, while those of the (*fcc*) γ-Mo_2N phase dominate the diffraction pattern. The detected reflections can be indexed to the (111), (200), (220), (311) and (222) of the γ-Mo_2N phase. Besides, no detectable reflections related to molybdenum boride or boron nitride could be observed. Similar patterns were observed with the nanocomposite films (**D** and **E**) which were synthesised by increasing the BF_3 flow rate. In addition, the diffraction patterns of the Mo-B-N nanocomposites feature significantly broadened reflections of the γ-Mo_2N phase. This indicates a clear shift towards a nanocrystalline character of this phase. Although the increasingly broad reflections of this phase made it especially difficult to render a definitive interpretation with regards the presence of other nanocrystalline phases in the film, the negligible asymmetry obtained by the peak fitting procedure conducted on these reflections suggested that it is most likely that the only detectable nanocrystallites are those of the γ-Mo_2N phase.

While no reflections of other crystalline phases could be detected in the measured pattern, the results suggest that the (*fcc*) γ-Mo_2N phase is the dominant crystalline phase. Furthermore, as with film **B**, no reflections associated with crystalline molybdenum boride or boron nitride phases were detectable in the measured patterns of these films. Despite the fact that both XPS and FTIR spectra provided clear evidence of the presence of increasing amounts of the BN phase in films

C- **E**, the absence of evident reflections pertaining to this phase in the measured diffraction patterns implies that it is rather x-ray amorphous.
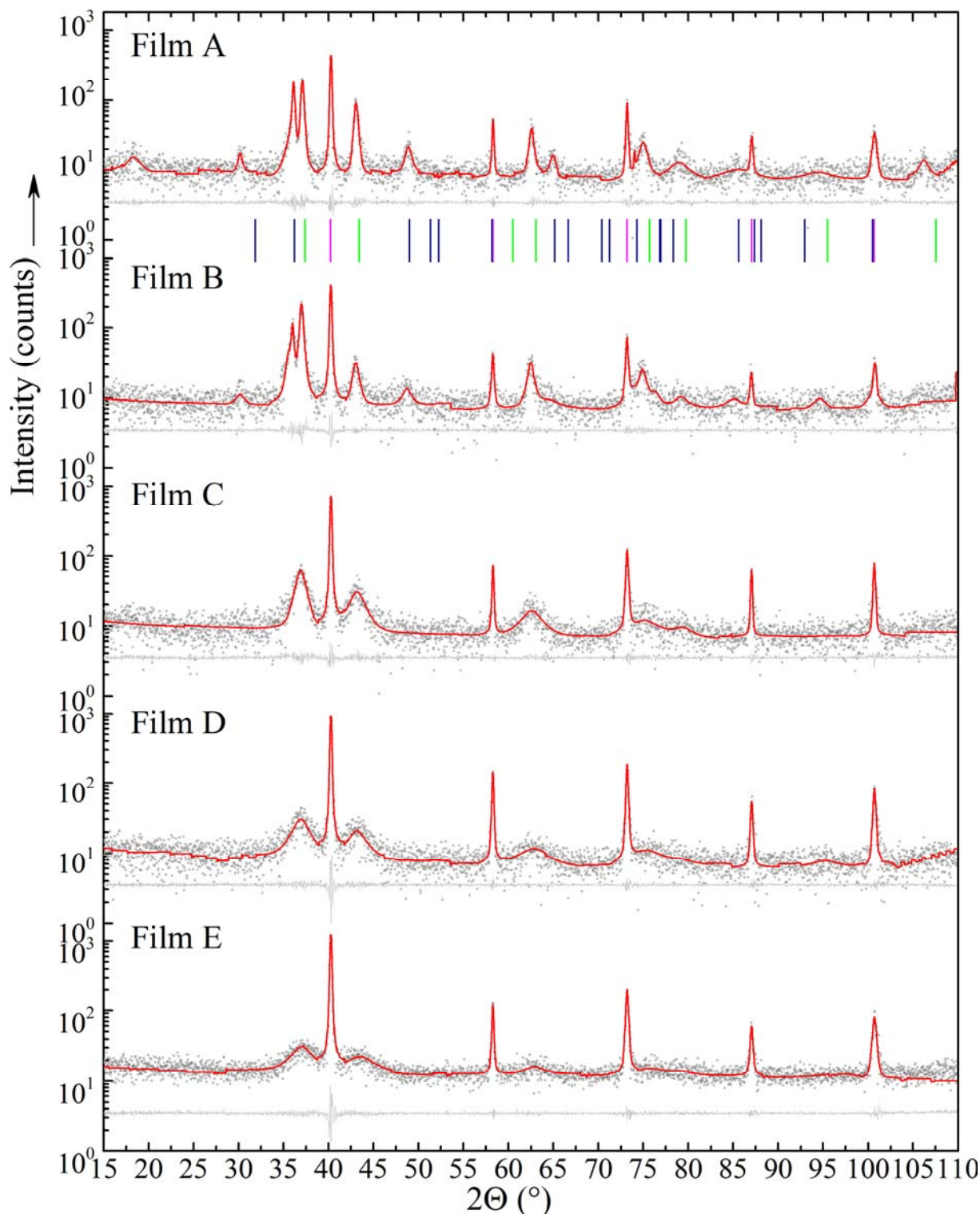

Figure 3.14: Measured and fitted grazing-incidence XRD patterns of the nanocomposite films on tungsten substrates. The position of the diffraction lines from γ-Mo₂N (JCPDS: 25-1366), δ-MoN (JCPDS: 25-1367) and W (JCPDS: 04-0806) are indicated by the lines in green, blue and magenta, respectively.

Furthermore, the diffraction patterns were used to calculate the lattice parameters of the crystalline phases in all films.

Figure 3.15 shows the variation in the lattice constant of cubic (*fcc*) γ-Mo_2N in these films which have varying compositions. It was observed that an increase in the film's total B-content leads to a simultaneous decrease in the Mo content which will have a direct influence on the stoichiometry of the deposited nitride. It is evident that the lattice constant decreases steadily as the B-content in the films increases from about 4.19(5) Å in film **A** (boron-free) to 4.17(6) Å in film **E** (boron-rich). Although this change may be deemed too small to render definitive statements about the structural changes in the cubic phase in these films, it is very likely that these variations are due to changes in the stoichiometry of molybdenum nitride. Due to the fact that the BN phase is amorphous, it is not possible to deduce its formula from the XPS composition data which in turn makes deductions about the stoichiometry of molybdenum nitride equally difficult. However, it is known from other kinds of experiments that the stoichiometry of molybdenum nitride can vary widely depending on the amount of nitrogen which is available to fill interstitial sites in the Mo lattice. Therefore, the nitride's unit cell size will be determined by its stoichiometry. The lattice parameters of the cubic molybdenum nitride phase, which were obtained from several reports, are included in

Figure 3.15. Despite the large scatter in these values, it can be seen that the higher the nitrogen content in the nitride (or the lower the Mo/N ratio) the larger the cubic unit cell. Lattice constants as large as 4.242(3) Å and 4.223(2) Å were reported in the case of near stoichiometric MoN, which have adopted the B1-structure type and have Mo/N ratios of 0.97 and 1.05, respectively [146]. Other values appear to be conflicting for sub-nitrides with Mo/N ratios 1.45-1.32, which have measured lattice parameters lying in a large range between 4.145 Å- 4.217 Å [147,146,148]. Nonetheless, the measured lattice parameters in this work seem to be in good agreement with some of the previously reported values. The trend observed suggests that there is a slight change in the stoichiometry of the Mo_2N towards decreasing the lattice constant with decreasing Mo/N.
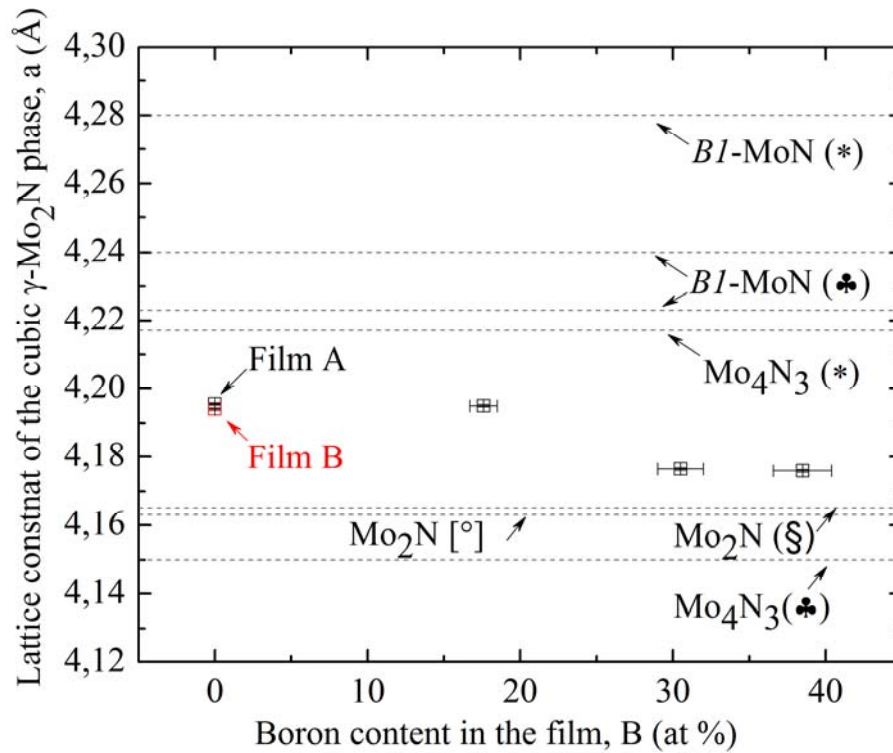
Figure 3.15: The change in the lattice parameter of the (fcc) γ-Mo₂N phase in nanocomposite films of various composition (i.e. B-content and Mo/N ratios). The lattice constant which are obtained from other reports are marked as follows: (*) from [147], (♣) from [146], (°) from [JCPDS: 25-1366], and (§) from [148].

3.3.3 AFM Analysis

Three dimensional AFM micrographs (on a 5×5 μm^2 except for film **C** imaged at a 10×10 μm^2) of the surface morphology of various nanocomposites are shown in Figure 3.16. The Z-values which are indicated in the micrographs correspond to the highest scanned peak-to-trough feature in the film at the given scale. It can be seen from these images that the B-free molybdenum nitride film (**A**), which exhibits a morphology of faceted grains with a uniform grain size of more than 80 nm has a noticeably high roughness peaking at 7.37±0.46 nm. The morphology of the nanocrystalline Mo₂N/BN composite films deposited at different flow rates of BF₃ (i.e. contain various amounts of boron) is drastically different. Those films have surfaces with much smaller spherical grains whose sizes are well below 15 nm and have average root-mean-square roughness (R_rms) values that are less than 1 nm and ranging between 0.52±0.09 and 0.90±0.07 nm for films **C** and **D**, respectively. A further increase in the film's boron content increases the RMS roughness slightly to 3.43±0.28 nm as is the case with film **E**. Despite this slight increase in surface roughness, the surfaces of the Mo-B-N nanocomposites remain somewhat similar and the AFM images reflect a topography which is similar to that observed in the plan-view SEM

micrographs (cf. Figure 3.12) of the same films. The R_{rms} values which are calculated from at least five different scans of each surface at various locations are given in Figure 3.17.
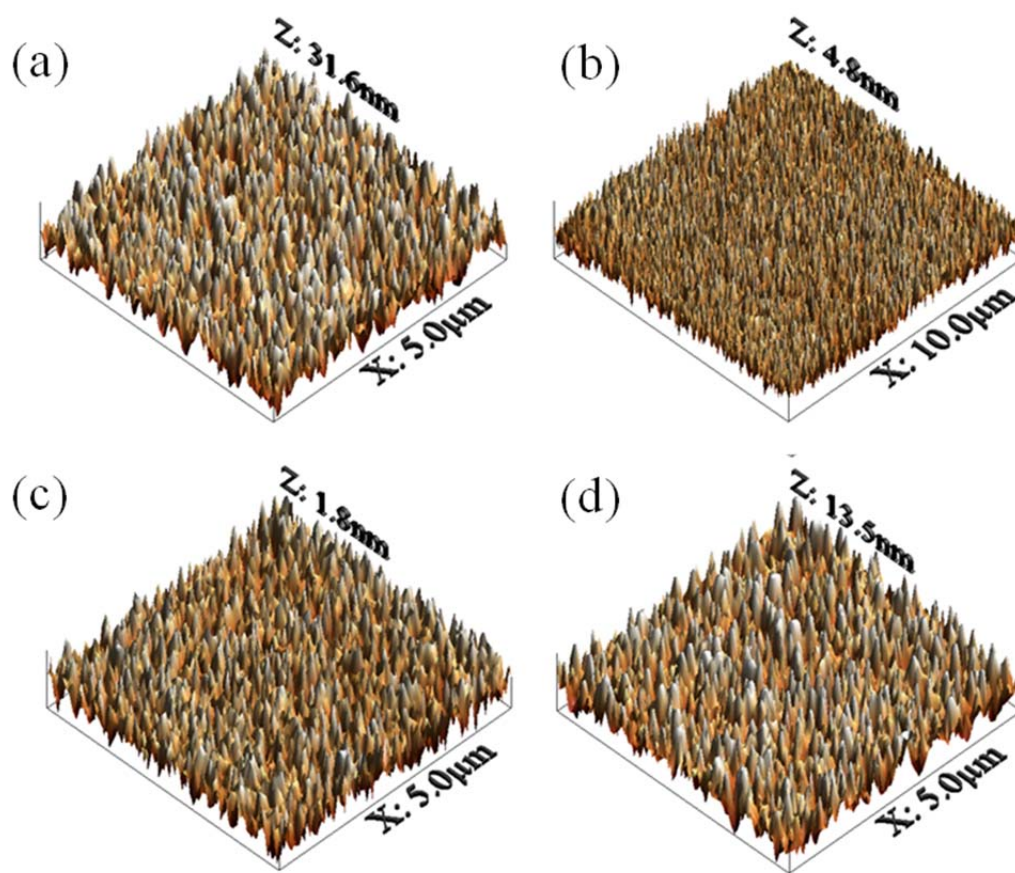

Figure 3.16: Three dimensional AFM micrographs (on a 5×5 µm² except for film C imaged at a 10×10 µm²) showing the surface morphology of the Mo-N and Mo-B-N films synthesised at different $H_2:BF_3$ flow rate ratios: (a) 0:0 sccm, (b) 3.3:0.45 sccm, (c) 3.3:0.9 sccm, and (d) 3.3:1.8 sccm. The Z values correspond to the maximum peak-to-trough amplitude difference of each surface. The corresponding calculated R_{rms} values are given in Figure 3.17.
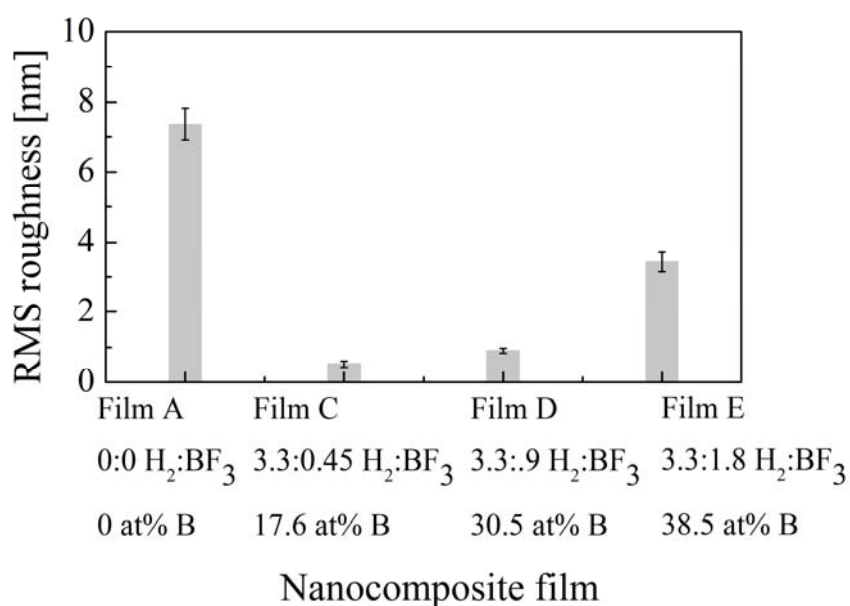

Figure 3.17: RMS roughness calculated on a lateral scale of 5×5µm² of Mo-N and Mo-B-N nanocomposite films which were synthesised at different $H_2:BF_3$ flow rate ratios.

3.3.4   HRTEM Analysis

The bright field HRTEM micrographs of films **A**, **C** and **E** are shown in Figure 3.18(a), (c) and (e), respectively, together with their corresponding selected area electron diffraction (SAED) rings, (b), (d) and (f), respectively, which reveal marked microstructural differences between the films. Film **A** which was deposited without the addition of boron, consists of the nitrides MoN and Mo_2N, which show grain sizes in the range of 20-30nm. The low resolution micrographs show a homogenous distribution of randomly oriented grains.

The corresponding SAED pattern shows two sets of diffraction rings, which correspond to two different phases of molybdenum nitride: a δ-MoN phase (JCPDS 25-1367) and a face-centred cubic γ-Mo_2N phase (JCPDS 25-1366). The δ-MoN phase crystallises in a hexagonal structure and belong to the space group $P6_3/mmc$ with lattice parameters a and c equal to 5.7250 Å and 5.6080 Å, respectively. The micrographs (c) and (e) in Figure 3.18 show the effect that the addition of BF_3 during deposition has on the film's nanostructure. In films **C**, which was prepared by the addition of 0.45 and 1.8 sccm of BF_3 and H_2, respectively, the micrograph clearly shows grains with an average size of about 4 to 7 nm. The micrograph clearly illustrates the random orientation of similarly-sized grains. In addition, the second brighter phase seems to exist along the grain boundaries and between the darker grains which is believed to correspond to the amorphous boron nitride phase. The diffraction rings in the SAED pattern of the film shown in Figure 3.18(b) correspond to lattice spacing values which are in agreement with γ-Mo_2N (JCPDS 25-1366) with the space group $Pm3m$ and a unit-cell dimension of 4.111 Å. The lattice spacing values are listed in

This values is less than the one reported for the reference powder phase (JCPDS 25-1366) and is more likely to be a result of accumulating compressive stresses in the γ-Mo_2N crystallites. The nanograins sizes in film **E** are noticeably smaller with average sizes in the order of 2 nm. The great majority of the nanograins are equally sized and appear homogenous and randomly distributed and surrounded by what appears to be a brighter phase. Based on this initial examination of HRTEM observations, it can be deduced that the nano-sized grains represent (*fcc*) γ-Mo_2N nanocrystals while the phase which appears to have a brighter contrast may be attributed to the amorphous BN occupying the region in between these nanocrystals.

In order to confirm the identity of the crystalline phases which appear in the micrographs, it is necessary to examine several high resolution micrographs and their corresponding diffraction patterns. The Debye–Scherrer rings of the selected area electron diffraction (SAED) pattern of films **A**, **C** and **E** are shown in Figure 3.18(b), (d) and (f), respectively.

Table 3.2 summarises the measured d-values of all high intensity rings and compares the obtained values with those measured in the JCPDS data. In the case of film **A**, the SAED patterns, which were obtained from various positions in the film show two sets of diffraction rings, which can be ascribed to the δ-MoN and γ-Mo$_2$N phases. They are in good agreement with the XRD results obtained for the same films (cf. Figure 3.14) and from those in the JCPDS data. Indexing the lattice fringes also confirms the formation of δ-MoN and γ-Mo$_2$N as nanocrystalline phases. Figure 3.19 shows a high resolution micrograph of some selected crystallites in film **A** together with Fast Fourier Transform (FFT) of the indicated selected regions, which were obtained from image calculation.

Despite the presence of a few regions which do not exhibit sufficient contrast to show the lattice fringes of the crystallites, nanograins which correspond to both δ-MoN and γ-Mo$_2$N crystallites can be identified based on the measurement of lattice fringes. In this micrograph, at least two δ-MoN crystallites are seen which show lattice fringes spaced at 1.97±0.04Å and 2.44±0.04Å and correspond to the (202) and (200) crystallographic planes, respectively. Several other γ-Mo$_2$N nanocrystallites can also be observed, which reveal dominant lattice fringes of the (111) and (200) crystallographic planes with average lattice spacing values of 2.37±0.04Å and 2.10±0.02Å, respectively. Due to limitations in lateral resolution, the observations based on the micrograph shows no evidence of the presence of nanograins or crystallites with smaller lattice fringes that would indicate other crystallographic orientations. Instead the images reveal that there is no indication of any preferential orientation adopted by the nanograins with all crystallites being randomly orientated. In addition, the calculated FFT images show distinct diffraction points with no interference from other crystallographic planes, which indicates that the selected areas belongs to a perfect crystallite.
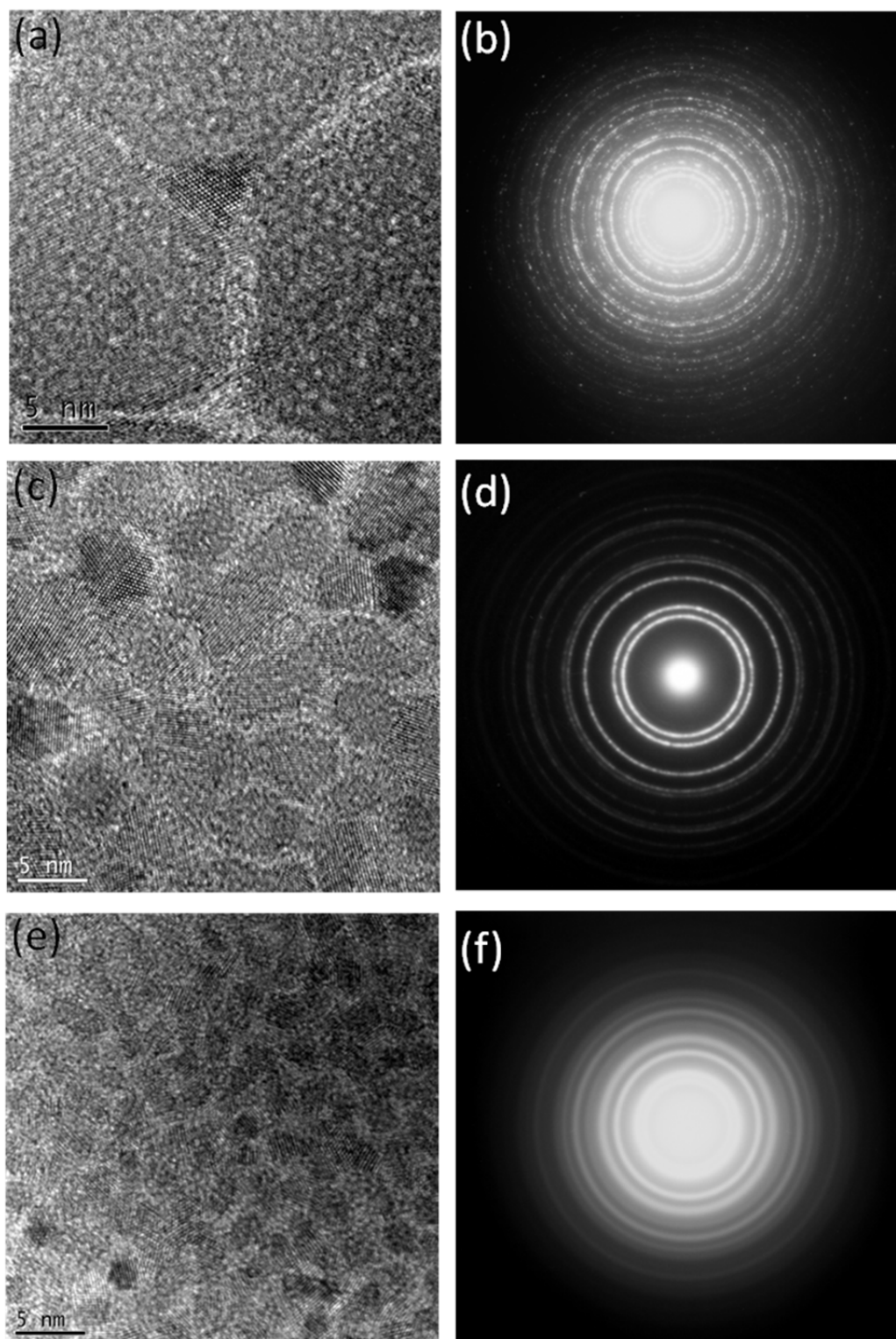
Figure 3.18: Bright field HRTEM micrographs of films (a) A, (c) C and (e) E together with their corresponding selected area electron diffraction (SAED) pattern in (b), (d) and (e), respectively.

In Films **C** and **E**, only one set of diffraction rings related to the γ-Mo_2N phase can be observed, which confirms that molybdenum nitride is the only crystalline phase in the nanocomposite. The pattern demonstrates continuous diffraction rings indicative of a random orientation and a

nanocrystalline character. There are no diffraction rings or lattice fringes in the HRTEM bright field micrographs, which may be ascribed to other phases such as molybdenum, molybdenum boride and boron nitride. Although the observed d-values are in good agreement with those reported for the cubic γ-Mo_2N phase, they are up to 6% smaller than the values recoded in the JCPDS data.
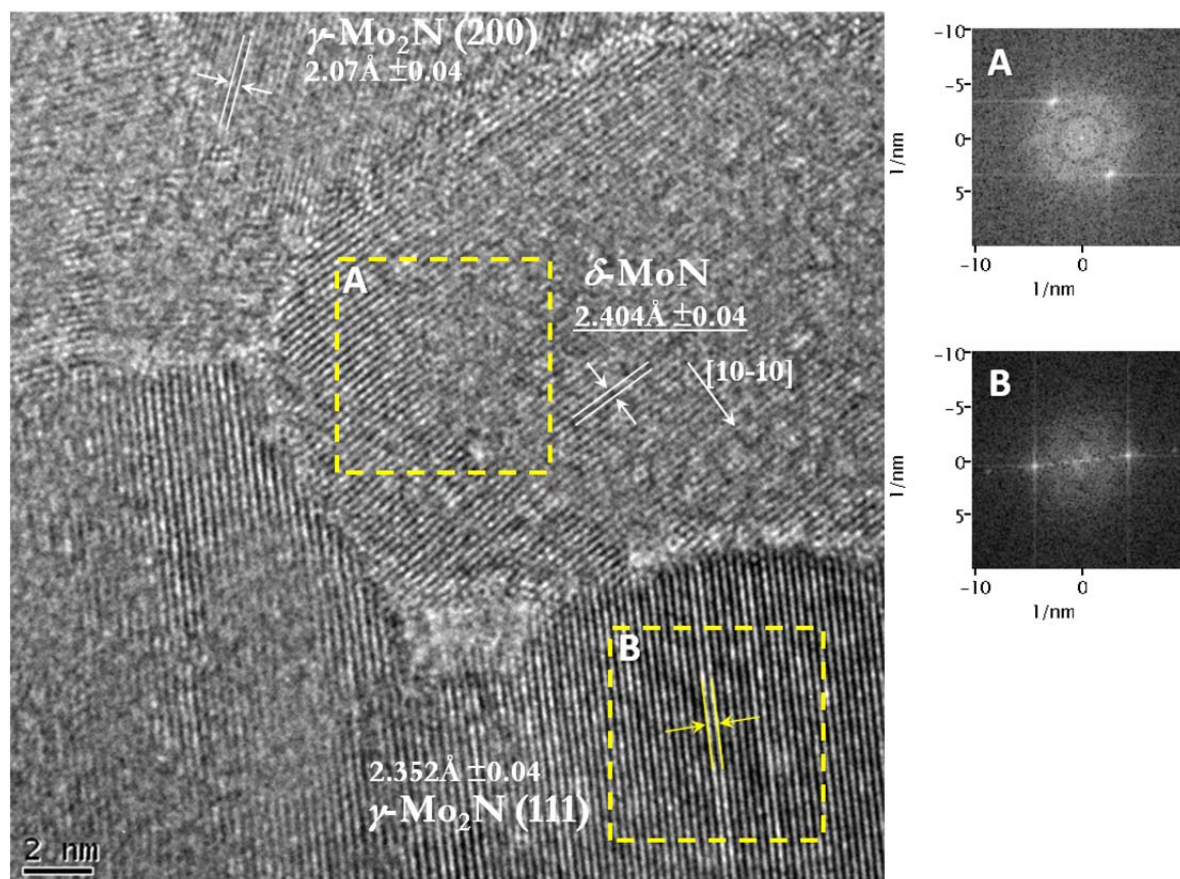

Figure 3.19: HRTEM micrographs taken from film A. The insets (A) and (B) are the FFT's of the highlighted areas A and B which correspond to nanocrystallites of hexagonal δ-MoN and (fcc) γ-Mo_2N, respectively.

In addition, the HRTEM micrograph of film **C** (cf. Figure 3.20) clearly shows that the nanocrystalline γ-Mo_2N grains, which are well-separated, are distribute quite homogeneously in the a-BN phase (or in the amorphous phase). A closer look at the HRTEM micrographs reveals that in the case of film **C** the embedded γ-Mo_2N grains have a uniform size with an average diameter of 4-7 nm and are set apart by an average minimum distance of 5 nm. In contrast, the nanograins in film **E** (cf. Figure 3.21) are on average 2 nm large and at a an average minimum separation distance of 3 nm. This calculation was statistically based on 50 nano-sized grains in each film, which were observed with HRTEM. In both cases, the individual nano-sized grains are

almost always γ-Mo₂N single crystals, which are well separated and evenly distributed in the nanocrystalline composite films. The lattice spacing values of some selected crystallites from films **C** and **E** correspond well with those calculated from the Debye–Scherrer rings of the selected area electron diffraction (SAED) pattern from both samples. In film **C**, (cf. Figure 3.20), the high resolution micrograph reveals that certain areas between the nanograins are totally amorphous. The Fast Fourier Transform (FFT) and image calculation obtained from the areas highlighted as (I) and (II) reveal the diffraction spots which can be ascribed to diffraction along the (111) crystallographic plane. In the FFT image (I), the angle between spots 1 and 1 is approximately 71°, whereas that between spots 2 and 3 is 56° indicating that this image is taken from a crystallite whose axis is oriented near the zone axis. It also evident that the γ-Mo₂N (111) lattice fringes are the most discernible with interplanar spacing measured at 2.37±0.04Å, which is very close to the value calculated from the diffraction rings in Figure 3.18(d). The second highlighted area (II) is totally amorphous as appears from the diffused halo of the FFT image, which is likely to correspond to the boron nitride phase.
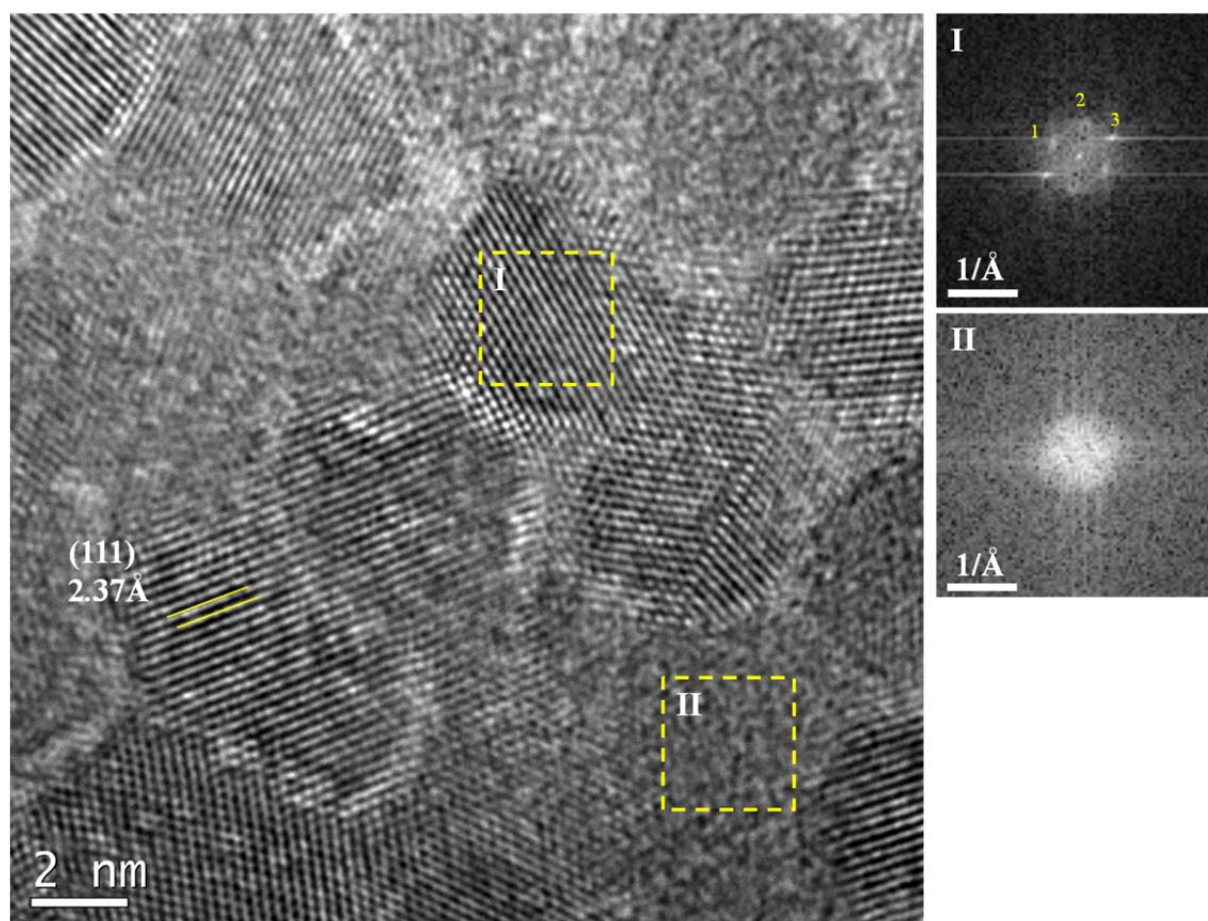
Figure 3.20: HRTEM micrographs taken from C. The insets (I) and (II) are the FFT of the highlighted areas I and II, respectively, and correspond to randomly oriented nanocrystallites of (fcc) γ-Mo₂N showing the (111) plane and an amorphous region, respectively. In the FFT inset the angle between spots 1 and 2 is 71° and between 2 and 3 is 56° which indicates that the (111) diffracting planes is oriented close to the zone axis.

Figure 3.21: (a) HRTEM micrographs taken from film E. The regions which are marked with the letter A correspond to amorphous structures surrounding the γ-Mo₂N crystallites. (b) A 400% magnified section of the micrograph in (a). The FFT in the insets belong to the highlighted fields (I), (II) and (III).

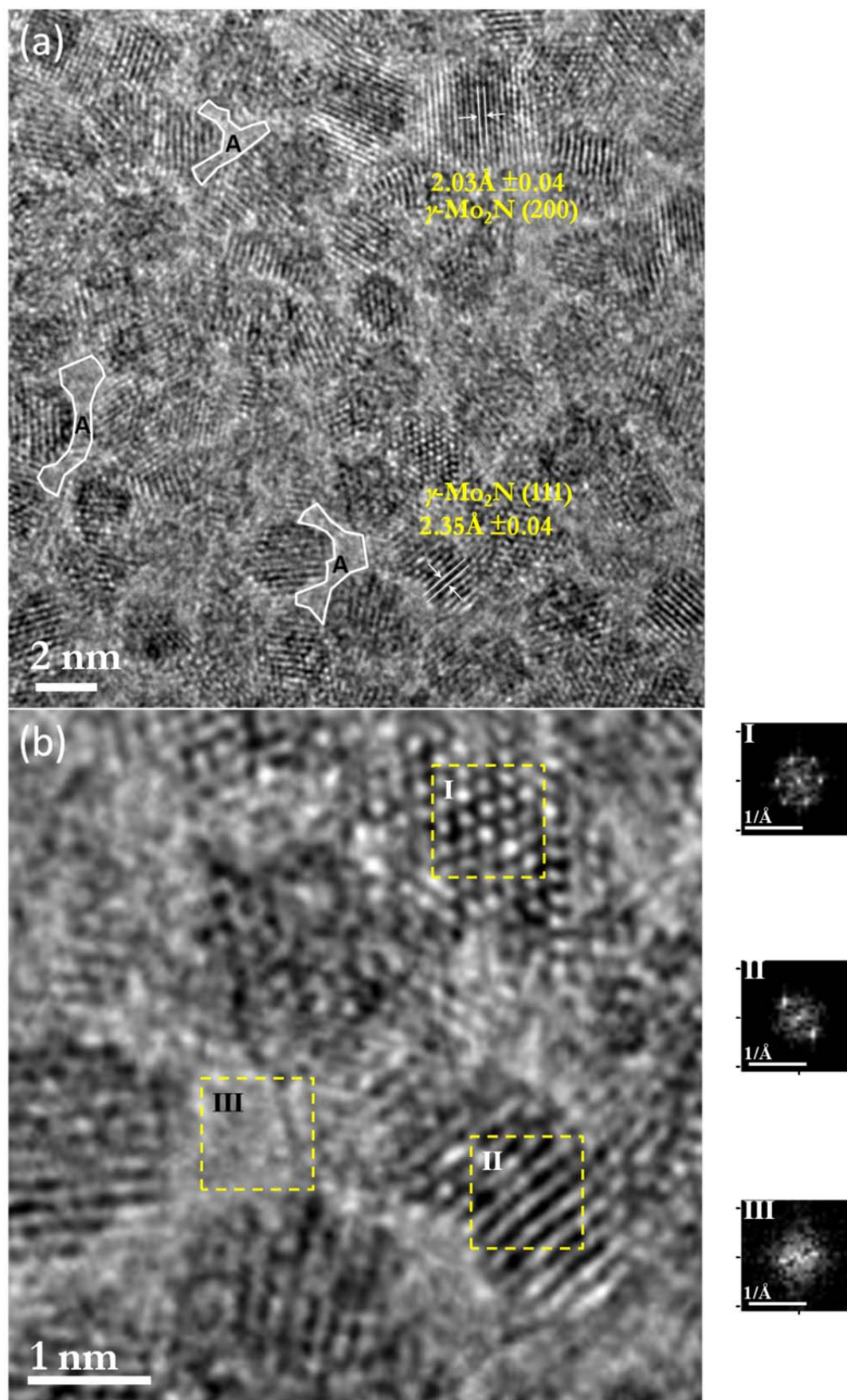Figure 3.21 illustrates that film **E** consists of smaller γ-Mo$_2$N crystallites, which are roughly half the size of those found in film **C**. Areas which are clearly amorphous can be seen between the nanograins. The discernible lattice fringes correspond to the (111) and (200) crystallographic planes of γ-Mo$_2$N, which are measured to be 2.35±0.04Å and 2.03±0.04Å, respectively. These values are similar to the ones calculated from the diffraction rings in Figure 3.18(e). The insets in (b) are the Fast Fourier Transform (FFT) image calculations obtained from the areas highlighted as (I) and (II), which reveal the diffraction spots which can be ascribed to the diffraction along the (100) and (111) planes. It is also evident that the FFT of area (III) corresponds to an amorphous region as marked by the diffused halo. Similar to Film **C**, the nanograins appear to be randomly oriented γ-Mo$_2$N single crystallites. Based on HRTEM imagery and electron diffraction, it can be seen that an increase in the nanocomposite's boron content is associated with the formation of finer γ-Mo$_2$N crystallites. Upon increasing the B-content from 17.6 to 38.5 at% B, the average diameter is observed to decrease from 5 nm to about 2.5 nm, respectively. In order to obtain statistical information with regards to the sizes and distribution of the γ-Mo2N phase, several HRTEM micrographs of films **C** and **E** were analysed. In each film, the distribution of the grain sizes was calculated based on a minimum of 50 nano-sized grains whose area projections were obtained directly from the micrographs. The grain diameter was obtained from the calculated equivalent area assuming that the grains are spherical. The grain diameters were arithmetically grouped into at least 11 classes. Figure 3.22 shows the frequency histograms of nanocomposites **C** and **E**, which correspond to the absolute count of the nanograins and are fitted to a log-normal function whose expression is as follows:

$$P(D) = \frac{A}{\sqrt{2\pi}\sigma \cdot D} \cdot \exp\left[\frac{-(\ln\frac{D}{D_o})^2}{2\sigma^2}\right] \qquad \text{3-1}$$

Where $\boldsymbol{D}$ represents the equivalent area diameter of the nano-sized grains, $\boldsymbol{D_o}$ is the median of the distribution, and $\boldsymbol{\sigma}$ is a shape parameter which corresponds to the standard deviation of the Gaussian distribution of log $\boldsymbol{D}$.

Based on the Log-Normal distribution, the median diameter ($\boldsymbol{D_o}$) of γ-Mo$_2$N nanograins approximates at 6.04±0.21 and 2.33±0.02 nm in films **C** and **E**, respectively. In view of the above, there is a marked difference in nanostructure between those films which contain boron nitride and those which do not. Molybdenum nitride films have much larger crystallite sizes as opposed to Mo-B-N nanocomposites. The drastic reduction in crystallite size of the γ-Mo$_2$N is only a result of increasing the film' boron content, which consequently leads to the growth of a

second BN phase. In Mo-B-N nanocomposites, the increase in the amount of the BN phase does not allow the γ-Mo$_2$N crystallites to grow further, which results in increasingly smaller γ-Mo$_2$N nanograins. There is no indication that BN takes on a crystalline form nor is there any indication of the presence of other boride or metallic phases.
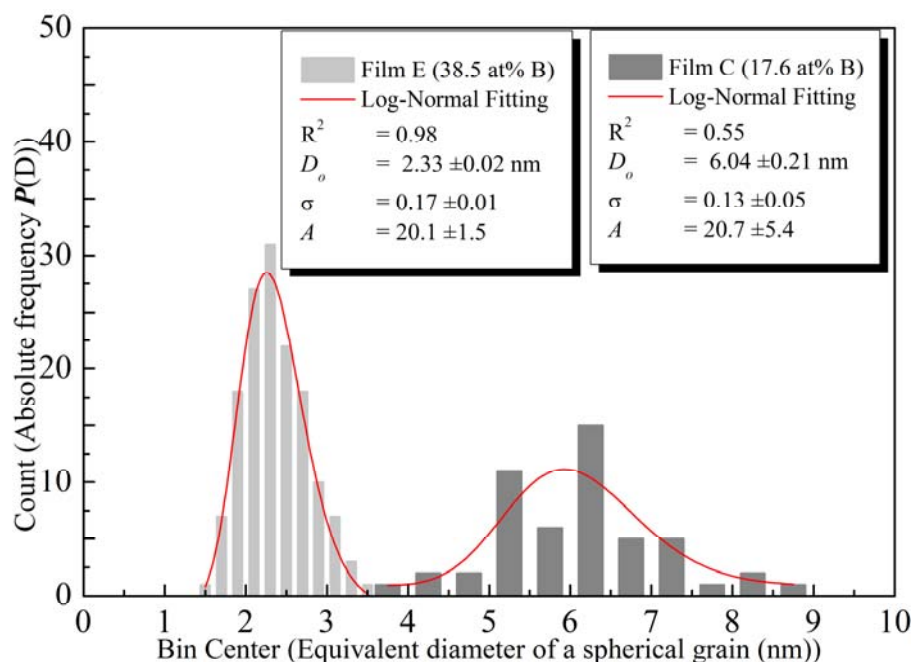

Figure 3.22: The grain size distribution of the γ-Mo$_2$N phase in nanocomposites C and E. The quality of the log-normal fitting is given as R^2 values.

Lattice spacing values (d$_{hkl}$) in Å							
Film A		**Film C**	**Film E**	**γ-Mo$_2$N**		**δ-MoN**	
				(JCPDS 25-1366)		**(JCPDS 25-1367)**	
Set 1	**Set 2**			**d$_{hkl}$**	**(hkl)**	**d$_{hkl}$**	**(hkl)**
3.278	2.319	2.378	2.237	2.404	(111)	3.714	(101)
2.71	2.050	2.058	1.931	2.081	(200)	2.804	(002)
2.543	1.399	1.452	1.393	1.472	(220)	2.479	(200)
1.639	1.252	1.243	1.181	1.255	(311)	1.857	(202)
1.737	1.163	1.191	1.133	1.202	(222)	1.777	(211)
1.639	1.035	1.025	0.984	1.041	(400)	1.749	(103)
1.511	0.944	0.942	0.891	0.955	(331)	1.585	(301)
1.334	0.890	0.925	0.794	0.931	(420)	1.402	(004)
1.271		0.838				1.24	(400)

Table 3.2: A summary of the lattice spacing values which are obtained from SAED of films A, C, and E. The d-values from the δ-MoN phase (JCPDS 25-1367) and a face-centred cubic γ-Mo$_2$N (JCPDS 25-1366) are also included to aid comparison.

3.4 Microscopic Strains and Grain Sizes

As was previously discussed in section 2.2.4.1, in order to be able to describe the microstructure of the nanocomposite based on the diffraction data, it is necessary to use a model which has a physical basis to adequately describe the diffraction line profile in a quantitative manner, which would aid in extracting the required parameters. Information about the size of the coherent diffracting domains (<D>), of the γ-Mo$_2$N phase and possible microscopic strains (ε), occurring in the crystallised state are obtained from the integral line breadth of multiple γ-Mo$_2$N broadened reflections. The line profile of every measured reflection was fitted to a model based on the least-squares fitting to a Voigt function and was analysed according to the double-Voigt formalism [149]. This model proved to be satisfactory when describing line shape parameters [150] and is described as being general, in the sense that it is not materials- and microstructure-dependent [151,152]. The Voigt function itself is a folding of two components: a Cauchy (or Lorentzian) component and a Gaussian one.

$$I(2\theta) = I_0 + A \frac{2\ln 2}{\pi^{3/2}} \frac{\Gamma_C}{\Gamma_G^2} \int \frac{e^{-t^2}}{\left[\frac{\Gamma_C}{\Gamma_G^2}\sqrt{\ln 2}\right]^2 + \left[\sqrt{4\ln 2}\frac{2\theta_t - 2\theta_{max}}{\Gamma_G}\right]^2} \cdot dt \qquad \textbf{3-2}$$

Where $I(2\theta)$ is the observed intensity, I_0 the background intensity, A the peak area, θ_{max} the Bragg angle, Γ_C and Γ_G the integral breadths of the Cauchy (or Lorentzian) and Gaussian components, respectively.

The choice of the symmetric Voigt function is justified by the negligible asymmetry of the measured line profile given the implemented diffractometer geometry and optics described in section 2.2.4. The quality of the fit is demonstrated in Figure 3.23. It should be noted that the adopted procedure for fitting the reflections from the films also allows for reflections from the substrate. In fact, neglecting the contribution of the substrate can lead to an erroneous determination of the peak profile particularity when a slight overlapping between the reflections occurs. This has the effect of underestimating the domain sizes.

According to the double Voigt method, the Cauchy and Gaussian integral breadths are related and can be written as expressions of the line broadening effects, which are due to the coherently diffracting crystallites' sizes and the degree of distortion (i.e. microstrains and other defects such as dislocations and stacking faults) as follows:

$$\Gamma_C = \Gamma_{CS} + \Gamma_{CD}\frac{s^2}{s_0^2} \qquad\qquad 3\text{-}3$$

$$\Gamma_G = \Gamma_{GS} + \Gamma_{GD}\frac{s^2}{s_0^2} \qquad\qquad 3\text{-}4$$

Where $s_{hkl} = 2\sin\theta/\lambda = 1/d_{hkl}$ is the reciprocal space coordinate; Γ_C, Γ_G the integral breadths of the Cauchy and Gauss components; and Γ_{CS}, Γ_{GS}, Γ_{CD}, Γ_{GD} the integral breadths of the Cauchy (C) and Gauss (G) functions, corresponding to the size (S) and distortion (D) broadening, respectively. Additionally, the size coefficient of a Voigt size-broadened line profile can be given as the Fourier transform $A_S(L) = \exp(-2L\Gamma_{CS} - \pi L^2 \Gamma_{GS}^2)$, where $L = n|a_3|$ is the length of columns of cells along a direction which is normal to the diffracting planes (commonly referred to as a_3). The size distribution function $p_V(L) \propto L\dfrac{d^2 A(L)}{dL^2}$ is determined from the second derivative of the size coefficient,

$$\frac{d^2 A(L)}{dL^2} = [(2\pi L\Gamma_{GS}^2 + 2\Gamma_{LS})^2 - 2\pi\Gamma_{GS}^2]A_S(L) \qquad\qquad \textbf{3-5}$$

The respective mean values for the area-weighted and volume-weighted coherently diffracting domain sizes are given, respectively, as:

$$<\overline{D}>_S = \frac{1}{2\Gamma_{CS}} \qquad\qquad \textbf{3-6}$$

$$<\overline{D}>_V = \frac{\displaystyle\int_0^\infty L p_V(L)dL}{\displaystyle\int_0^\infty p_V(L)dL} = \frac{\exp(k_S^2)}{\Gamma_{GS}}erfc(k_S) \qquad\qquad \textbf{3-7}$$

where $k = \dfrac{\Gamma_{CS}}{\sqrt{\pi}\cdot\Gamma_{GS}}$ corresponds to the characteristic integral-breadth ratio of a Voigt function.

Similarly, the strain coefficient of a Voigt size-broadened line profile can be given as the Fourier transform $A_D(L) = \exp(-2L\Gamma_{CD} - \pi L^2 \Gamma_{GD}^2)$ and the mean-square-strain $(\varepsilon^2(L))$ that is normal to the diffraction plane is

$$<\varepsilon^2(L)> = \frac{1}{s_o}\exp\left(\frac{\Gamma_{GD}^2}{2\pi} + \frac{1}{L}\frac{\Gamma_{CD}}{\pi^2}\right) \qquad\qquad \textbf{3-8}$$

The user-friendly program BREADTH [152], developed by Davor Balzer, was used to determinate of the area-weighted and volume-weighted coherently diffracting domain sizes. In the line-broadening analysis described above, all the measured Bragg reflections of the crystalline phases; (fcc) γ-Mo_2N in the nanocomposites **C- E** and both (fcc) γ-Mo_2N and the (hex) δ-MoN phases in the case of molybdenum nitride films **A** and **B** were fitted and analysed. An iterative Levenberg-Marquardt non-linear least-squares fit (LM-fit) was used to model analytical Voigt functions which considered both Cu $K\alpha_1$ and Cu $K\alpha_2$ components. The Rachinger correction [153] was then performed to remove the contribution of Cu $K\alpha_2$ from the data. The LM-fitting procedure included adjustable parameters to describe the area (A), position (2θ), integral breadths of the Cauchy and Gauss components (Γ_C and Γ_G), and shape (modelled by the mixing parameter of the Voigt function) of all the Bragg reflections, together with two additional parameters used to model a linear background common to all the phases in the same fit. The quality of the fit was evaluated in terms of adjusted R^2.

Figure 3.23 and Figure 3.24 illustrate the Voigt fits to the (111), (200), (220) and (311) diffraction profiles of all the nanocomposite films. The difference patterns and R^2 indicating the quality of the fitting procedure is also included. As previously mentioned, the Voigt function represents the measured diffraction profiles quite well due to the negligible peak asymmetry. Despite its qualitative nature, an initial examination of the integral breadth trends of these five reflections from each film (i.e. Williamson-Hall plots of the integral line broadening versus the reciprocal vector of each reflection that are constructed from the fitted data) can reveal useful trends pertaining to the microstructural features of the crystalline molybdenum nitride phase. Figure 3.25 shows higher slopes in the case of boron containing nanocomposites, which in turn appear to increase progressively as a function of the film's Boron content (Films C- E). The distortion and microstrain contributions to the line broadening in these films are more dominant than those contributed by the crystallite size. On the other hand, the size contribution to the microstructure of the crystalline γ-Mo_2N phase is higher when the slopes are small such as in film A. Despite the ease with which such graphs are constructed, quantitative information about the microstructure may only be drawn when the instrument-corrected diffraction line shapes are de-convoluted into Cauchy (Lorentzian) and Gaussian components which leads to the separation of both the size and distortion (microstrain) components [154].

The distributions of volume-weighted column lengths for all investigated nanocomposites are presented in Figure 3.26. It can be seen that both films **A** and **B** have quite broad distributions with maxima around 2340 Å and 342 Å, respectively. They also show much larger column lengths of the γ-Mo_2N phase, which are at least two to three orders of magnitude higher than the

rest of the films. In contrast, the distributions in the nanocomposites **C**, **D** and **E** are much sharper with maxima ranging between 20- 40 Å. By assuming that the diffracting crystallites have a spherical geometry, the diameters which correspond to averages of surface-area-weighted ($<D_S>$) and volume-weighted average contributions, ($<D_V>$) can be calculated using equations 4-6 and 4-7 and It should be noted that this assumption can be supported by two physical observations: the first is that the absence of any texture or preferred orientation effects in the diffraction data. The second is based on results obtained from high resolution electron microscopy. FESEM micrographs (cf. section 3.3.1) do not show any columnar growth features in films (**C**- **E**) but show homogeneous round grains. In addition, HRTEM (cf. section 3.3.4) micrographs reveal spherical grains of the crystalline γ-Mo_2N phase. Table 3.3 summarises the calculated mean surface-weighted and volume-weighted coherently diffracting domain (CCD) sizes of γ-Mo_2N and their microscopic strain.

Both average CDD diameters and microstrains tend to change systematically as a function of the films' B-content. The δ-Mo_2N/γ-Mo_2N films **A** and **B** have the largest volume-weighted CDD diameters at 690±164 and 4722±248 Å, respectively. The large percentage errors amounting to 24% are due to the fact that such sizes border on the upper limits which may be detected using the implemented diffraction measurements. The inclusion of boron in the Mo-B-N nanocomposites is accompanied by a marked decrease in volume-weighted CDD diameters with values at least two to three orders of magnitude smaller. These values also decrease monotonously as increasing amounts of boron are added. Volume-weighted domain diameters of the γ-Mo_2N phase decrease from about 82±8 to 41±2 Å for films containing 30 at% to 36 at% boron, respectively. On the other hand, a reversed pattern is demonstrated by the γ-Mo_2N crystallites' microstrains. The smaller crystallite sizes found in all the nanocomposite films exhibit an increasing built-up microscopic stresses. The γ-Mo_2N phase in film **B** has the highest root-mean-square microstrain reaching a value of 3.4%, whereas that of film **A** amounts to about a third of that value (ca. 1.3%). A closer look at the development of the Cauchy component of the line shapes in the reciprocal space coordinate reveals steadily increasing integral breadths, which indicates the accumulation of tensile microstresses in both of those films. In contrast, nanocomposite films (**C**- **E**) show a tendency towards building compressive microstresses, which are most considerable in those films with the highest B-content. Despite the error margins in the absolute values of the root-mean-square microstrains in film **D** and **E**, which are due to larger errors in determining the line shapes of large angle reflections, it was evident from the development of the Cauchy integral breadths against the reciprocal space coordinate that the line sloped downward and that compressive microstrains did build up in the γ-Mo_2N phase.

Based on these observations, it can be unambiguously stated that smaller crystallites of γ-Mo$_2$N tend to exhibit higher compressive stresses and that this change is monotonous as a function of the film's boron content, which is a result of increasing the BF$_3$ flow rate during deposition. The variation in CCD diameters and root-mean-square microstrains as a function of film composition is shown in Figure 3.27.
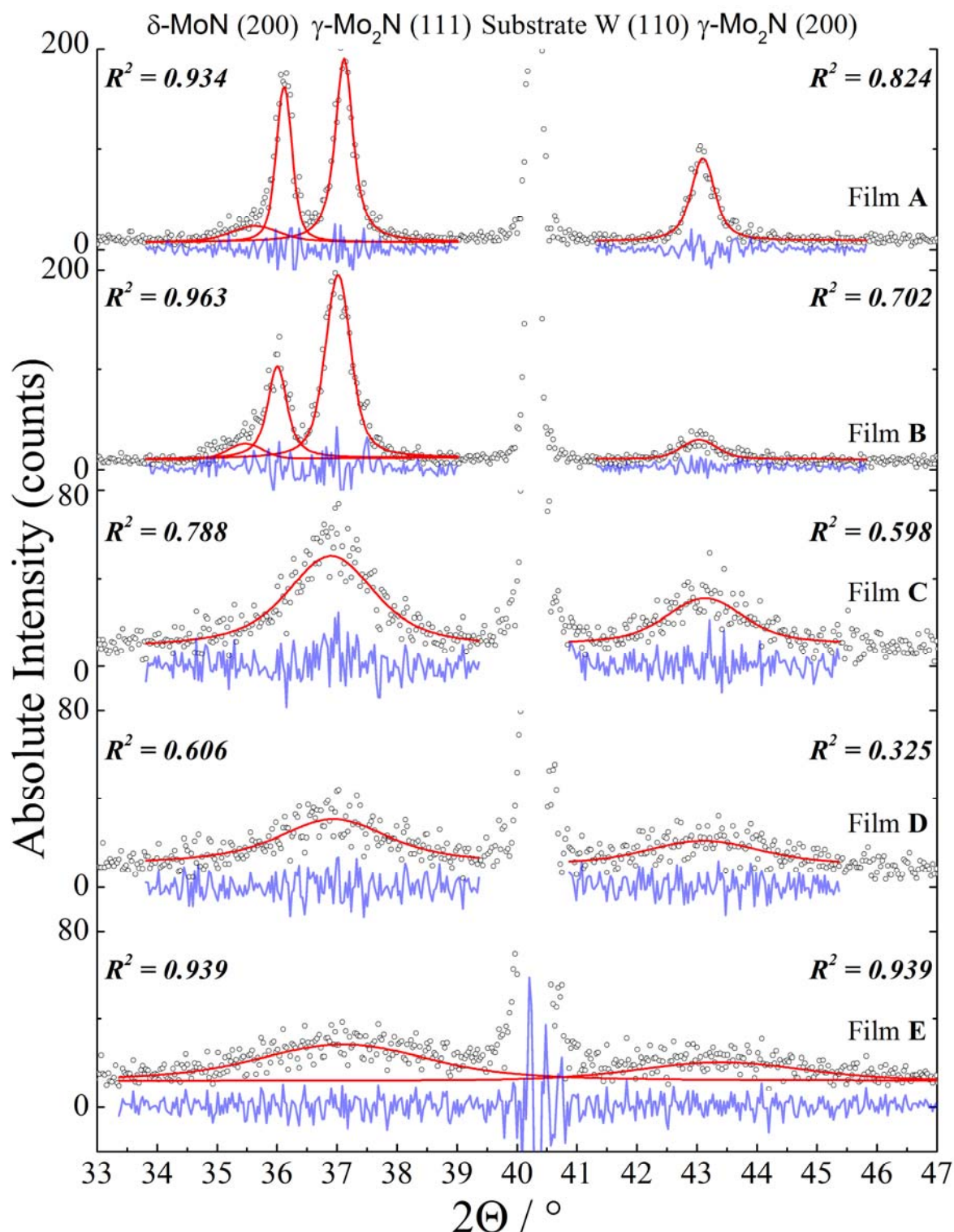

Figure 3.23: Measured and Voigt-fitted diffraction patterns of nanocomposite films in the lower 2θ range 33- 47°. The difference patterns and R² indicate the quality of the fitting procedure.
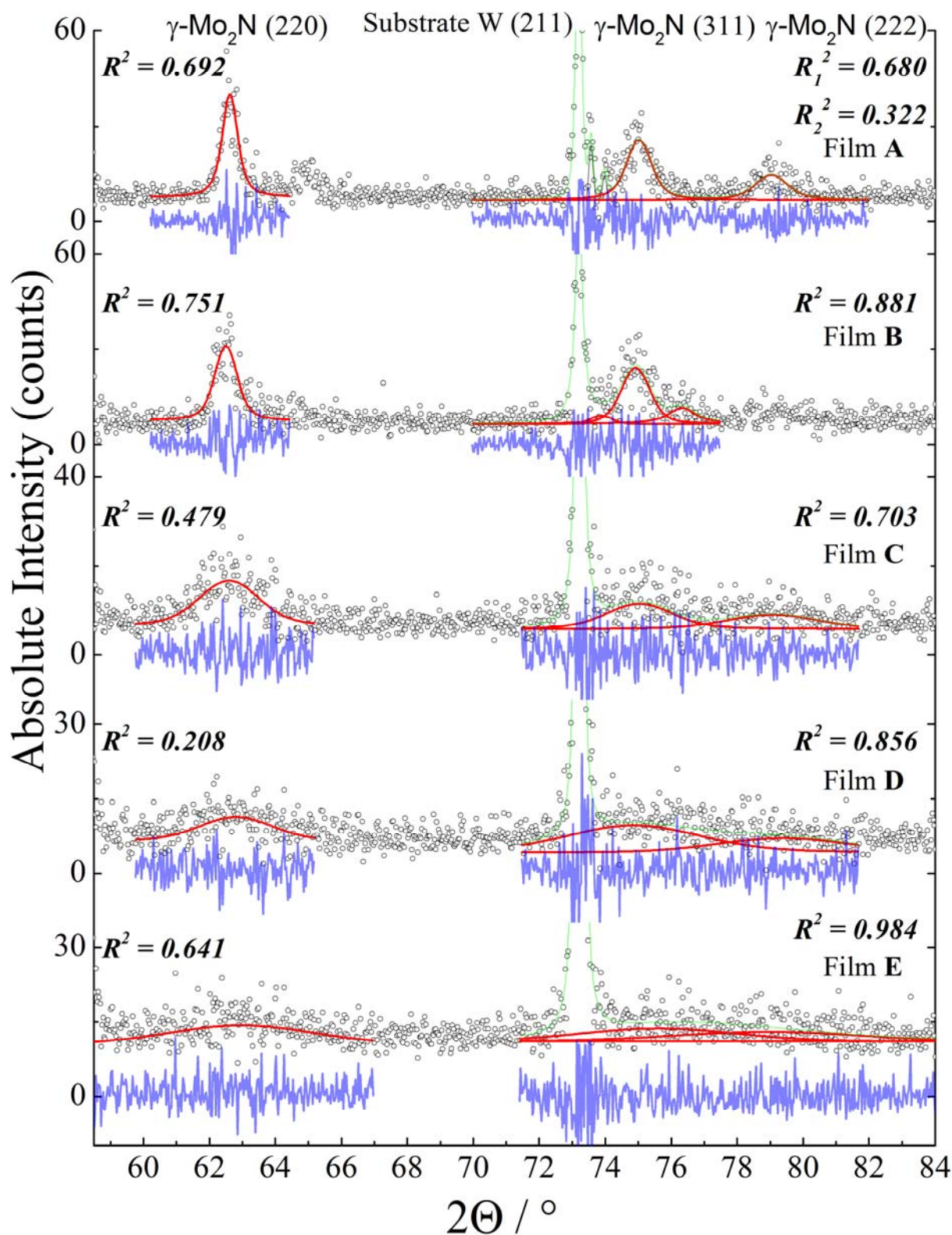
Figure 3.24: Measured and Voigt-fitted diffraction patterns of nanocomposite films in the higher 2θ range 59- 84°. The difference patterns and R² indicate the quality of the fitting procedure.
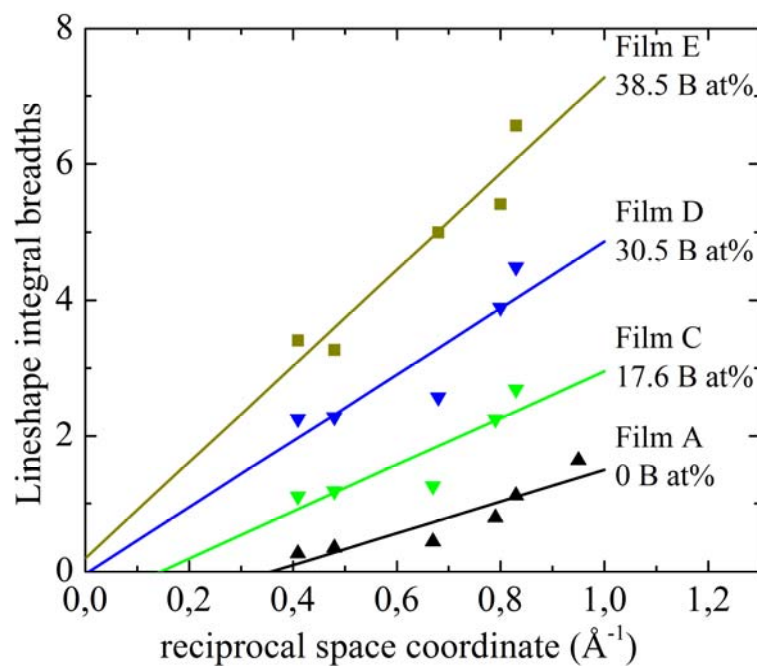
Figure 3.25: Williamson-Hall Plots of the nanocomposite films indicating the contribution of each Bragg reflection.
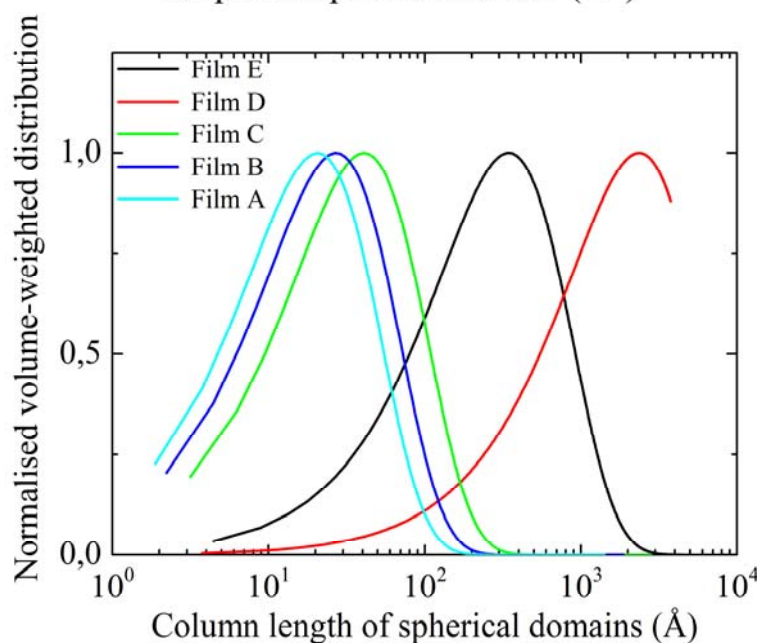

Figure 3.26: Volume-weighted distributions as a function of domain sizes for various nanocomposites

Film	Mo [at.%]	N [at.%]	B [at.%]	$\langle D_S \rangle$ [Å]	$\langle D_V \rangle$ [Å]	$(\varepsilon^2(L))^{1/2}$
A	70.9	0	29.1	345($\pm$82)	690($\pm$164)	1.25×10^{-2} ($\pm8.8\times10^{-4}$)
B	74.9	0	25.1	2361($\pm$124)	4722($\pm$248)	3.42×10^{-2} ($\pm6.81\times10^{-4}$)
C	52.5	17.6	30.0	41($\pm$4)	82($\pm$8)	1.23×10^{-2} ($\pm2,.24\times10^{-4}$)
D	37.0	30.5	32.5	27($\pm$1)	54($\pm$2)	1.56×10^{-2} ($\pm1.04\times10^{-3}$)
F	25.5	38.5	36.0	21($\pm$1)	41($\pm$2)	2.80×10^{-2} ($\pm4.63\times10^{-4}$)

Table 3.3: The mean surface-area and volume-weighted coherently diffracting domain (CCD) sizes as well as microscopic strains of γ-Mo₂N in several nanocomposites.
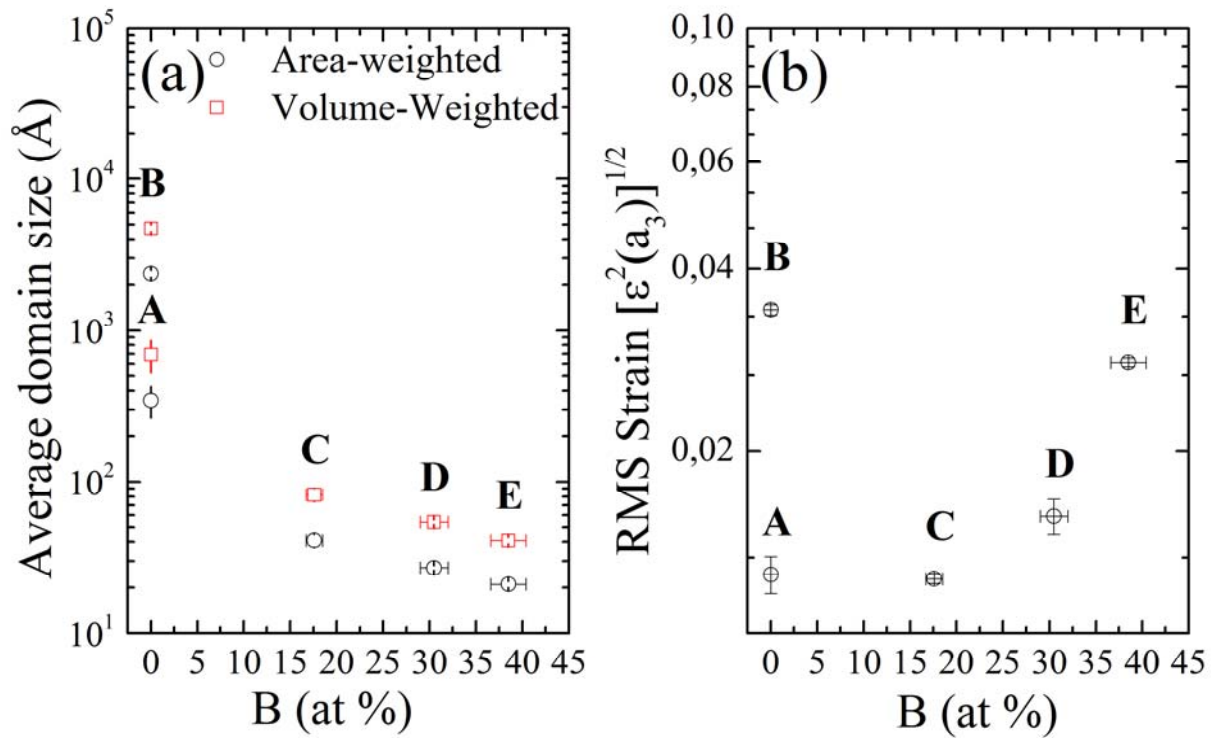
Figure 3.27: The variation of (a) mean surface-area- and volume-weighted coherently diffracting domain (CCD) sizes, and (b) root-mean-square microscopic strains averaged over the column length in real space of the γ-Mo$_2$N phase in the nanocomposites as a function of the films' boron content.

3.5 Isotropic Biaxial Residual Stress

Information about the microscopic strains which accumulate in the nanocomposite films as a result of the deposition process can be obtained by measuring the changes which occurr to the lattice spacing values of the crystalline phases as a function of film tilt and rotation. As was previously discussed in section 2.2.4.2, the films' residual strains are measured by employing the grazing incidence $\sin^2\Psi$ methods in which (Ψ) refers to the tilting angle between the specimen's normal and the diffractometer axis D_3 as shown in Figure 3.28. In this method, the incident X-rays illuminate the film's surface at a fixed and grazing (i.e. small angle, $\alpha = 2.0°$) incidence. This kind of measurement poses certain geometrical constraints on the degree of freedom with which the specimen tilts about the diffractometer's axis D_1 which restricts the tile angle (Ψ) such that it cannot exceed ($\alpha - \theta$) - 90°. However, the small angle of incidence offers the advantage of limiting the diffraction to the thin films and thereby minimises the interference effects of the crystalline substrate. In addition, due to the small film thickness, a fixed grazing incidence of $\alpha = 2.0°$ ensures that the entire thickness is gauged based on the absorption coefficients of the nitrides of molybdenum and boron. In addition, this technique becomes the method of choice

when there is a large degree of overlap between the reflections of the film and that of the substrate.

However, there are a number of issues that must be carefully monitored during such measurements. Firstly, in order to reduce the usually large errors incurred by this method with regards the lattice strain determination, measurements of the interplanar spacing of a large number of reflections at the corresponding tilt angles are required. Secondly, due to the geometrical restrictions imposed, large tilt angles are not permissible, which leads to certain degree of restriction with respect to evaluating the residual strains. Thirdly, because macrostrains in the lattice spacing are calculated from several diffraction lines, the material's anisotropy becomes more critical. Very often, the material's bulk mechanical or elastic constants are used in the calculations of the residual stresses from strains based on Hook's law. However, anisotropy in the material's elastic behaviour leads to varying elastic constants as a function of the crystallographic orientation which yields greater errors in stress determination. Despite the aforementioned constraints associated with this method, it remains particularly attractive for analysing macroscopic strains of thin films.

The investigated films have thicknesses in the order of 400- 500 nm and are deposited on tungsten substrates which were produced by high temperature sintering. The crystalline phases in the films included the nitrides of molybdenum γ-Mo_2N and δ-MoN which showed at least five reflections in the 2θ range 30- 120°. Particular difficulties were encountered in the case of δ-MoN due to strongly overlapping reflections, many of which have low intensities. Therefore, only three reflections were used to determine the lattice spacing in the case of δ-MoN. In Mo-B-N nanocomposites (**C**- **E**), the film's residual macrostrain is expressed only in terms of the crystalline phase (i.e. γ-Mo_2N) since the BN phase is totally X-ray amorphous. Table **3.4** lists the diffraction lines that are measured from each phase and the corresponding tilt angles at which the interplanar spacings are measured. Low intensity and strongly overlapping reflections were left out. Accordingly, the d_{hkl} values of the measured and then fitted reflections will be used to construct the $\sin^2\Psi$ plot whose slope is a direct measure of the macrostrain of the respective crystalline phase.

In this analysis, all the measured Bragg reflections of the crystalline phases: (fcc) γ-Mo_2N in the nanocomposites **C**- **E** and both (fcc) γ-Mo_2N and the (hex) δ-MoN phases in the case of molybdenum nitride films **A** and **B** were fitted and analysed. After using a linear background correction, an iterative Levenberg-Marquardt non-linear least-squares fit (LM-fit) was used to model the analytical split PearsonVII functions [155] which accounted for both Cu $K\alpha_1$ and Cu

$K\alpha_2$ components. After peak fitting, a Rachinger correction [153] was then performed to remove the contribution of Cu $K\alpha_2$ from the diffraction data before re-fitting the residual peak. In the fitting procedure, the parameters which correspond to peak area (A), position (2θ), integral breadths (ω), and shape parameter (m) were all adjusted for best fit. Adjusted R^2 was used as a measure to evaluate the fitting quality.
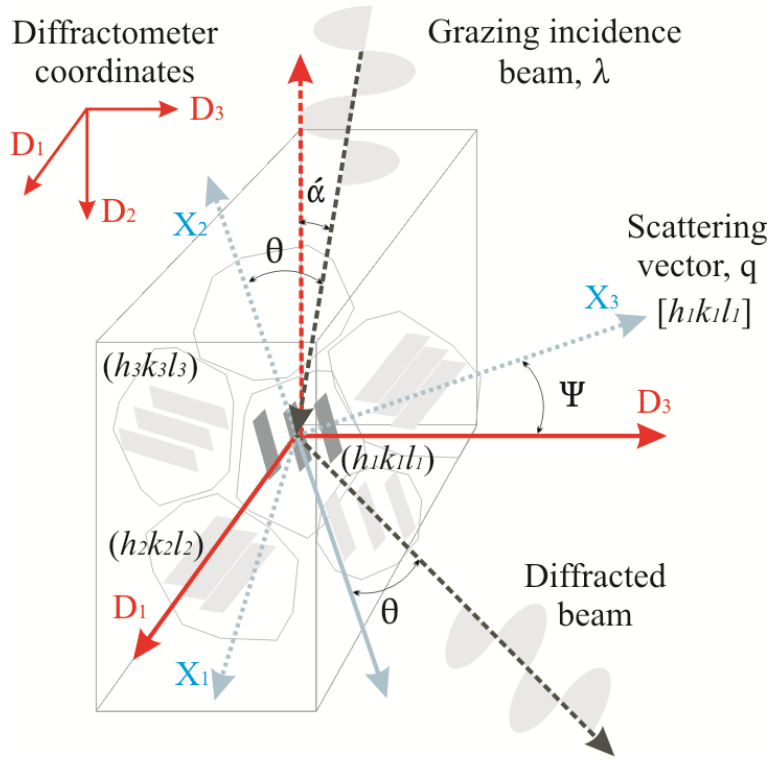

Figure 3.28: A schematic diagram of the diffractometer in residual stress measurements at asymmetric grazing-incidence geometry. D_1, D_2 and D_3 represent the diffractometer's coordinates, whereas X_1, X_2 and X_3 represent the specimen's coordinates. The grazing incident angle is α whereas θ and Ψ correspond to a Bragg-angle rotation and specimen tilt, respectively.

γ-Mo₂N			δ-MoN		
(*hkl*)	*2θ (K$_{α1}$line)*	$\Psi = 2.0°$ -θ_{Bragg}	(*hkl*)	*2θ (K$_{α1}$line)*	$\Psi = 2.0°$ -θ_{Bragg}
(111)	37.0215°	-16.689°	(002)	30.0587°	-12.788°
(200)	43.0010°	-19.726°	(200)	36.0063°	-16.103°
(220)	62.4743°	-29.554°	(202)	48.7715°	-22.508°
(311)	74.8480°	-35.864°	(220)	64.8638°	-30.568°
(222)	78.7533°	-37.855°	(222)	74.33°	-35.165°
(400)	94.2704°	-45.728°			
(331)	105.9146°	-51.765°			
(420)	110.029°	-53.832°			

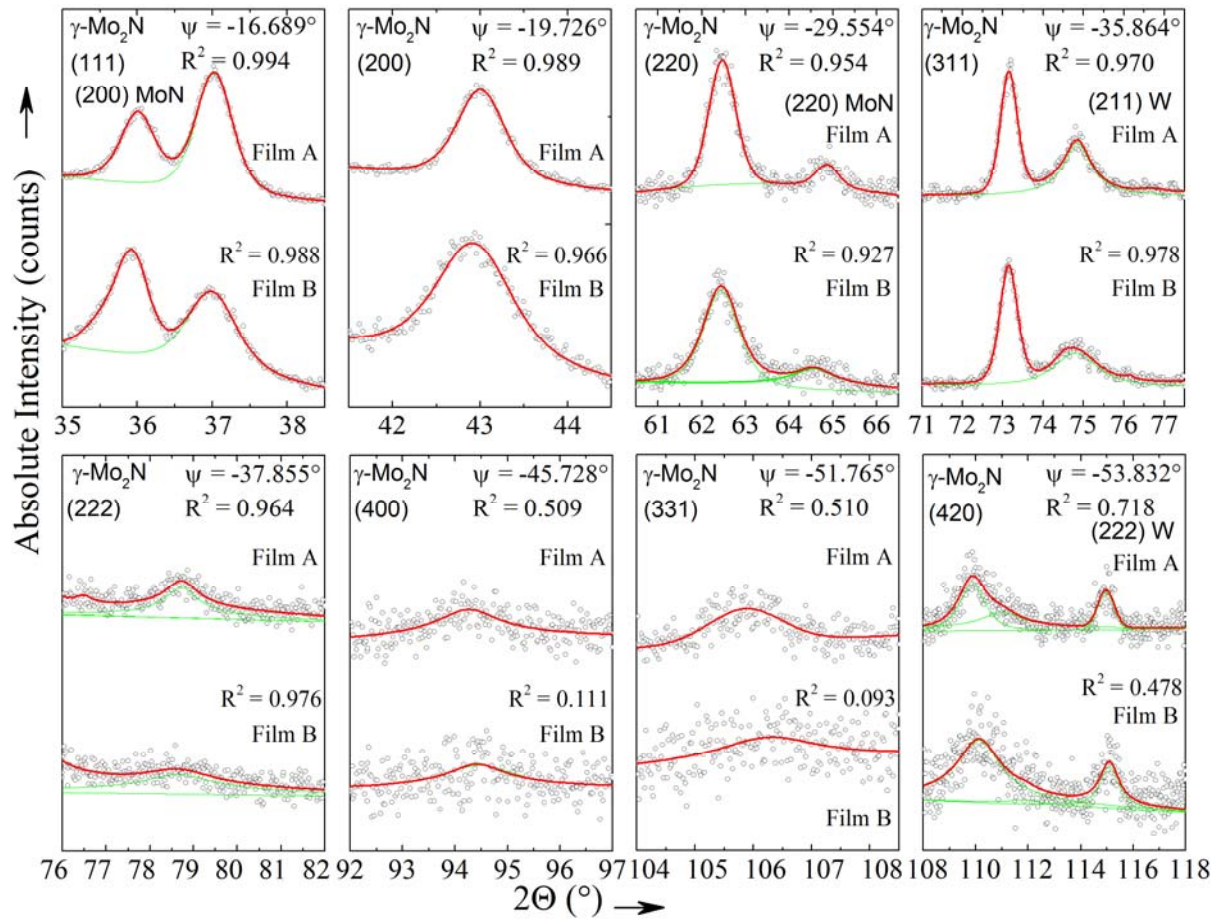**Table 3.4: The measured diffraction lines of γ-Mo₂N and δ-MoN and the corresponding tilt angles (Ψ)**

Figure 3.29: The fitted diffraction lines of the crystalline molybdenum nitrides (fcc) γ-Mo₂N phase in films A and B. The quality of the fit in terms of R² and the tilt angles at which each reflection is collected are also indicated.
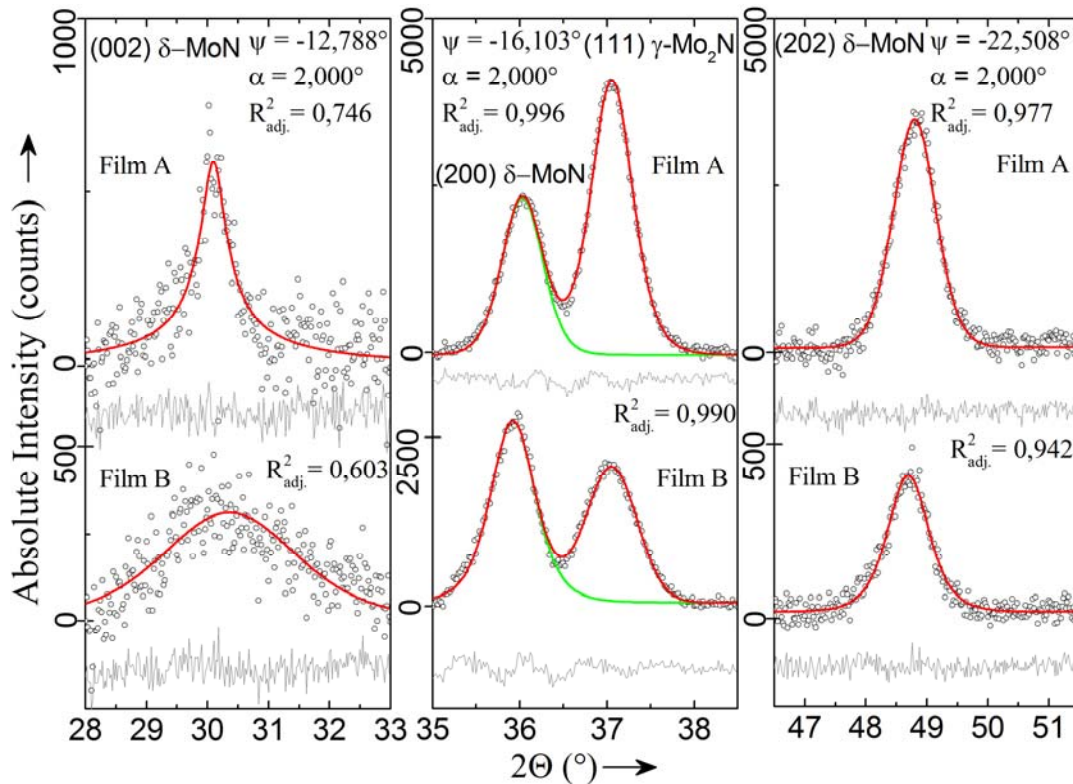

Figure 3.30: The fitted diffraction lines of the crystalline molybdenum nitrides (hex) δ-MoN phase films A and B. The quality of the fit in terms of R² and the tilt angles at which each reflection is collected are also indicated.
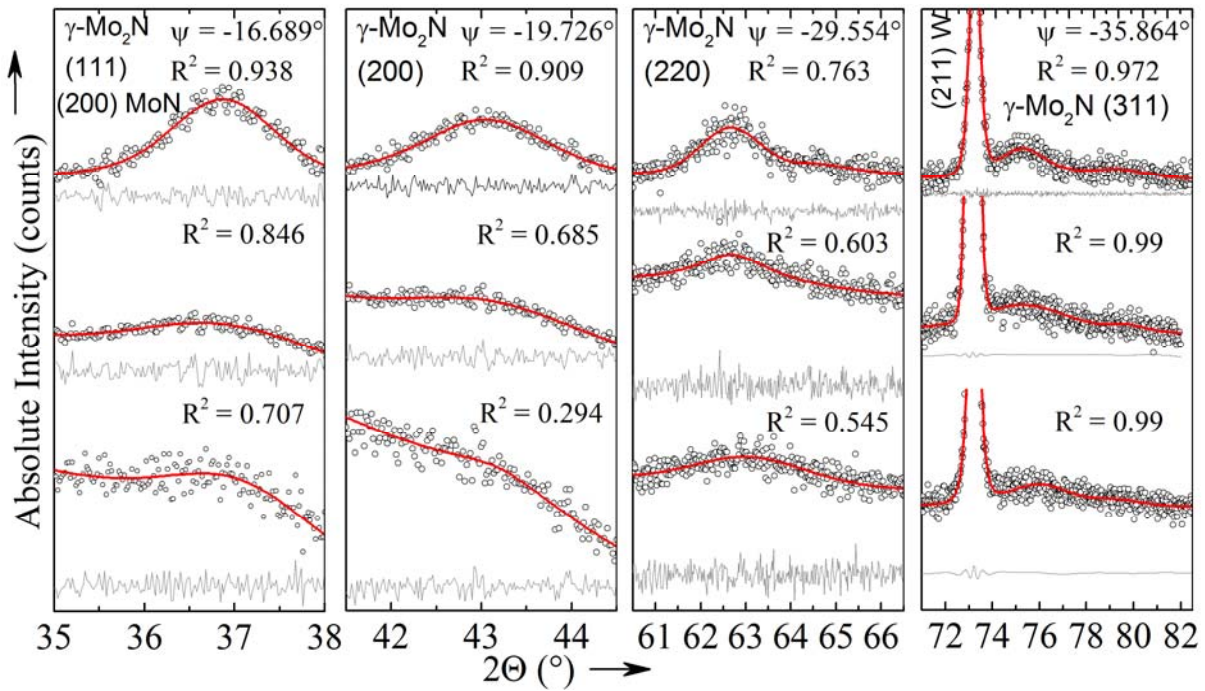
Figure 3.31: The fitted diffraction lines of the (fcc) γ-Mo₂N phase in the nanocomposites C, D and E. The quality of the fit in terms of R² and the tilt angles at which each reflection is collected are also indicated.

Figure 3.29 and Figure 3.31 show the fitted diffraction lines of (fcc) γ-Mo₂N phase in all of the nanocomposites. The macrostrains of these films were evaluated by monitoring the variation in the interplanar spacings of the various (*hkl*) reflections (expressed in terms of γ-Mo₂N lattice constant) as a function of the tilt angle. In order to calculate the film's residual stress with respect to each crystalline phase, the elastic constants which are based on the materials' Young's modulus and Poisson's constant as well as XEC's $s_1 = - v/E$ and $\frac{1}{2} s_2 = (v+1)/E$ [93] are used. These values for (fcc) γ-Mo₂N and δ-MoN are given in Table 3.5 a were adopted from previously published data [147,161]. It should be noted that although using these values helps to quantify the macrostress of each film, the obtained values are in fact approximate values, since the central assumption was based on the invariability of these constants with only minute changes occurring in the stoichiometry of the nitrides. However rough this approximation is, it can provide useful information that will help rank the films, which were prepared with various mass fraction of the amorphous BN phase, with respect to their residual stresses. If one is concerned with the absolute values of these stresses, then it becomes essential that the elastic constants for each film be determined in-situ by other methods [156,157].

Material	Lattice Parameters [Å]	*E* [GPa]	v	½ s₂ [TPa⁻¹]	s₁ [TPa⁻¹]	Reference
γ-Mo₂N	a = 4.1630	370	0.3	3.514	- 0.8108	JCPDS: 25-1366, [161]
δ-MoN	a = 5.7250 c= 5.6080	450	0.3	2.889	- 0.6667	JCPDS: 25-1366, [161]

Table 3.5: The elastic constants of γ-Mo₂N and δ-MoN. The number in brackets is the references from which these values are obtained.

The changes to the lattice parameter as a function of $\sin^2\psi$ for all films which is shown in Figure 3.32 suggest a linear variation of the lattice parameters. This points to the fact that the stress gradation in the direction normal to the film growth is either absent or negligibly small and that there are no changes in the stoichiometry of the nitride present in the normal direction. The biaxial residual stress values, which are obtained from the slope of the $\sin^2\psi$-plot are listed in Table 3.6 together with the fitting quality in term of R^2 values which are shown in Figure 3.33 as a function of the films Mo/N ratio. Ideally, as far as the absolute value of the residual stress is concerned, one should use the lattice constant of the same film in an unstressed state which may be difficult to achieve practically. Nonetheless, residual stress values of the γ-Mo$_2$N phase in each film are calculated based on both: the lattice parameter from the standard powder diffraction data (JCPDS: 25-1633) and the intercept of the $\sin^2\psi$-plot. These are very close indeed indicating that only a small error is introduced in the residual stress value by adopting the standard lattice constant.

In molybdenum nitride films, the biaxial residual stress in the γ-Mo$_2$N phase is relatively small and slightly tensile (0.64±0.19GPa) in film **A** and compressive (-1.11±0.51GPa) in film **B**. The δ-MoN phase in both films is significantly more compressively stressed in the order of -3.12±0.14GPa and -9.66±0.60GPa for films **A** and **B**, respectively. On the other hand, the magnitudes of the residual stress are significantly higher in the B-containing nanocomposites. The residual stress appears compressive in all Mo-B-N nanocomposites and increase monotonously with increasing the films' B-content from -2.51±0.86GPa in film **C** up to an order of magnitude higher bordering at -11.75±2.37GPa in film **E**.

In order to understand these values, the origin of such stresses needs to be considered. A film's residual stresses are a combination of intrinsic growth stresses and thermal stresses. While the former is directly dependent on the deposition method being used and more particularly on the bombarding ion energy of the plasma, the latter is due to incompatibilities in the thermal properties of both film and substrate and are directly dependent on the deposition temperature. To evaluate the effect of thermal stresses, one should consider the differences in the thermal properties between the film and substrate. After carrying the deposition at 900°C, and upon cooling, both the Mo$_2$N and tungsten substrate contract to different extents owing to the differences in their thermal expansion coefficients. However, by virtue of their complex electronic bonding system that comprises metallic, covalent, and ionic characters; interstitial nitrides such as Mo$_2$N and MoN have similar thermal and electrical conductivities to those of the metals. The following expression is used when quantifying the magnitude of thermal stresses ($\sigma_{thermal}$) which build-up in the films:

$$\sigma_{thermal} = \frac{E_{film}}{1 - \upsilon_{film}} \int_{T1}^{T1} (\alpha(T)_{Substrate} - \alpha(T)_{film}) \cdot dT \qquad \textbf{3-9}$$

Where the film's $E_{film}/(1-\upsilon_{film})$ in the case of γ-Mo$_2$N is approximately 526 GPa, $\alpha(T)_{substrate}$ and $\alpha(T)_{film}$ are the thermal expansion coefficients of the tungsten substrate and γ-Mo$_2$N film, respectively. While $\alpha(25°C)_W = 4.57×10^{-6}$ K^{-1} [158], surprisingly that of γ-Mo$_2$N or δ-MoN is not available in published literature. These values, however, should not depart much from the thermal expansion coefficients of other interstitial nitrides with similar radii of ions and interstitials and accordingly crystal structure such as those of tungsten [159]. For example, the thermal expansion coefficients of cubic WN$_{x=0.43}$ thin films is equal to $5.8×10^{-6}$ K^{-1} [160]. Using these approximations the expression above yields thermal stresses in the order of 1 GPa in compression. The calculation of thermal stresses in the case of the Mo-B-N nanocomposites is understandably more complex not only due to the absence of $\alpha(T)$ values for both amorphous BN and γ-Mo$_2$N, but also because the final value will depend on the mass fraction of each phase which is not available. However simplistic, the previous discussion suggests that the thermal stresses have a relatively small contribution to the film's total residual stress. This is particularly more evident in the case molybdenum nitride films, leaving the majority of the residual stresses to be attributed to intrinsic growth stresses. The presence of large compressive stresses in vapour deposited molybdenum nitrides (γ-Mo$_2$N or δ-MoN) is not surprising since such films are deposited under high ion-bombardment energy. Similarly compressed molybdenum nitride films were reported to accumulate stresses between 4- 11 GPa [161].

Film	σ_{macro} in γ-Mo$_2$N [GPa] using a = 4.163 Å	using the intercept of sin$^2\Psi$-plot	σ_{macro} in δ-MoN [GPa] using the slope	using the intercept of sin$^2\Psi$-plot
A	+0.64±0.19	+0.64±0.19	-3.12±0.14	-4.53±0.06
B	-1.12±0.52	-1.10±0.51	-9.66±0.60	-8.09±0.28
C	-2.54±0.86	-2.51±0.85		
D	-9.10±1.62	-8.96±1.60		
E	-11.83±2.38	-11.75±2.37		

Table 3.6: A summary of the biaxial residual stresses accumulated in the cubic γ-Mo$_2$N phase as calculated from the slopes of the sin$^2\psi$-plot.
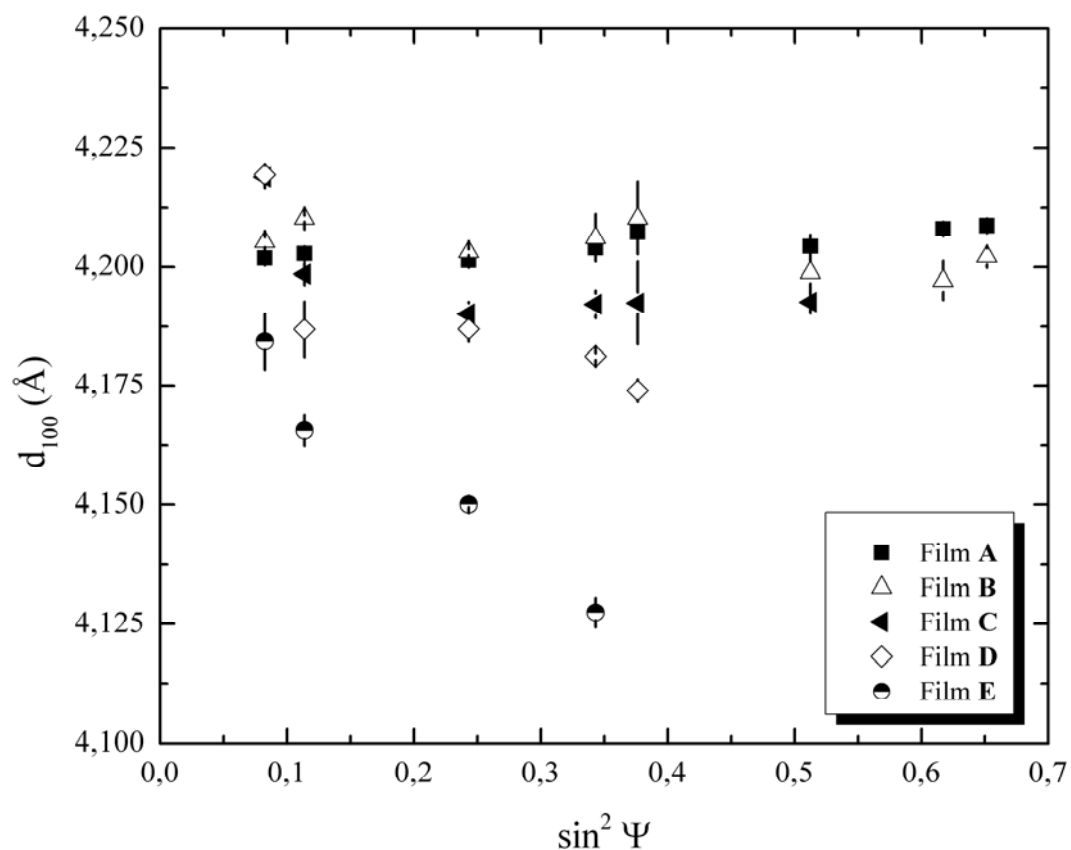
Figure 3.32: The sin$^2\psi$-plot for γ-Mo$_2$N in films A to E.
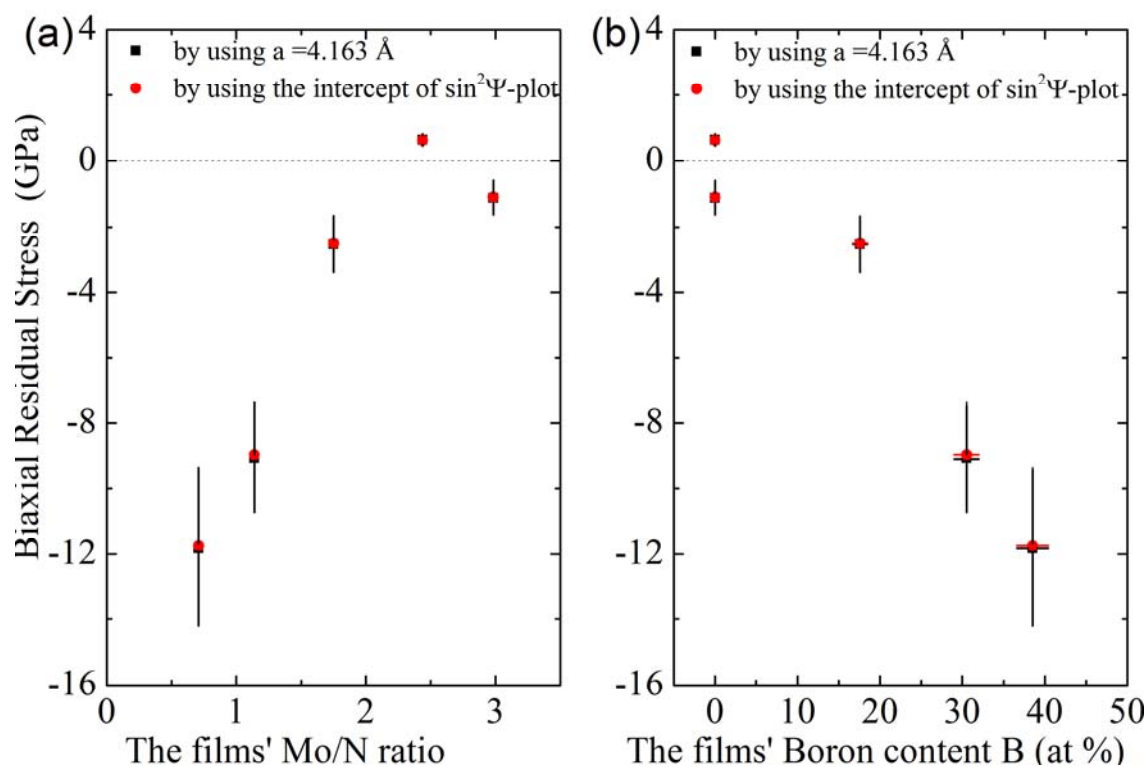

Figure 3.33: The biaxial residual stress of films A-E as a function of the films' (a) Mo/N ratio and (b) boron content.

3.6   Correlation between Micro- and Macro-Strains

Micro structural characterization by XRD affords a much deeper insight into the evolution of the film's microstructure during deposition. It has the added advantage of probing the material's microstructure at a much larger scale compared to that probed by other methods such as HRTEM. The combination of diffraction line profile analysis and biaxial residual stress measurements proves very useful in shedding more light on the interaction between the microscopic and macroscopic strains in the deposited materials. With regard to the crystalline phase in the nanocomposite: γ-Mo$_2$N, the microscopic strains in the diffracting crystallite domains change linearly with the isotropic biaxial residual macroscopic strains. Figure 3.34 shows the relationship between the films' macro- and microscopic strains. It can be seen that the γ-Mo$_2$N phase in films which have a large B-content (and consequently a larger mass fraction of the amorphous BN phase) tend to have large compressive macrostrains whose diffracting crystallite domains are progressively smaller and are hugely disordered and microstrained. All of this is associated with the growth of a second amorphous phase (i.e. a-BN) ensued by controlling the flow rates of the reactive gases H$_2$ and BF$_3$.

From the point of view that the macroscopic stresses in the film should be balanced, the presence of large compressive stresses in γ-Mo$_2$N means that the second phase is under a tensile stress. Although it was not possible in this investigation to measure the magnitude of the stress in the a-BN phase owing to its amorphous nature, the progressively large compressive strains building up in Mo$_2$N is an indirect indication that the tensile strains in a-BN increase with increasing its mass fraction. It may be possible to measure the overall stress in the film by the substrate bending method and applying the Stoney' relationship [162] to quantify the residual stresses in a-BN by subtracting the macroscopic stresses of γ-Mo$_2$N, which are evaluated by X-ray diffraction. However appealing this approach may be, applying it in the present investigation was not feasible for a number of reasons. Firstly, it requires a precise knowledge of the volume fractions of the constituent phases and their elastic constants which is particularly difficult for the amorphous BN phase. Secondly, much higher film thicknesses would be required to bend the 1-mm thick tungsten substrates to a measurable extent. This was not implemented due to the fact that much longer deposition times would have been required which was not only infeasible, but also meant that the stress state of the thicker films would be more likely to become more complicated with the possibility of introducing a stress gradation in the direction normal to film growth.
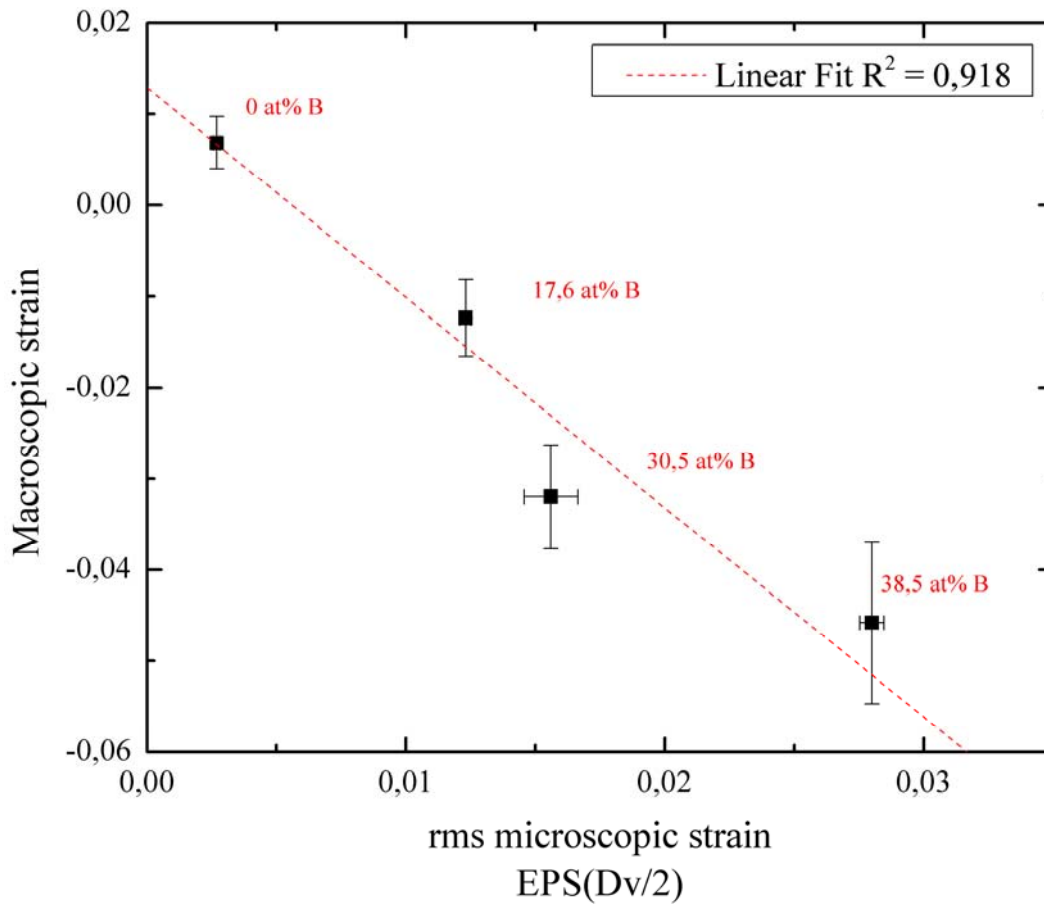
Figure 3.34: The change in micro- and macroscopic strains of nanocomposite films. The numbers in brackets indicate the film's B-content in at%. R^2 shows the quality of the linear slope.

3.7 Mechanical Properties Due to Microstructure.

Figure 3.35 illustrates that δ-Mo_2N/γ-Mo_2N of films **A** and **B** nanocomposites have hardness of 18.1±2.4GPa and 19.2±0.4GPa, respectively. Film hardness continues to stay at around this value for films prepared with 0.45sccm BF_3 (Film **C**) which showed a maximum of 18.5±0.5GPa before it decreases monotonously at further BF_3 addition. A minimum hardness of 10.3±1.1GPa corresponds to the nanocomposite **E** prepared at 1.8 sccm BF_3 and has a boron content of 38.5 at%. E_r values decrease from 220±22GPa and 210±3GPa for polycrystalline δ-Mo_2N/γ-Mo_2N in **A** and **B**, respectively, to 157.0±21,0GPa for the nanocomposites deposited 0.45sccm BF_3 (Film **C**). The values continue to decrease monotonously to 117.0±5.3GPa and 93.9±1.1GPa by increasing the BF_3 flow rates to 0.9 and 1.8sccm respectively. In order to assess the coatings suitability for tribological applications, the ratio H^3/E_r^2 was calculated based nanoindentation results. Both molybdenum nitride films **A** and **B** have ratios of 0.12 and 0.16 GPa, respectively. Similarly low values of 0.18 and 0.12GPa were obtained for films deposited at 0.9 and 1.8sccm BF_3, respectively. However, the nanocomposites which were deposited 0.45sccm BF_3 has highest elastic strain to failure and resistance to plastic deformation among the nanocomposites with

H/E_r and H^3/E_r^2 values reaching 0.118 and 0.26 GPa, respectively. A summary of the films' mechanical properties as determined by Nanoindentation is given in Table 3.7.
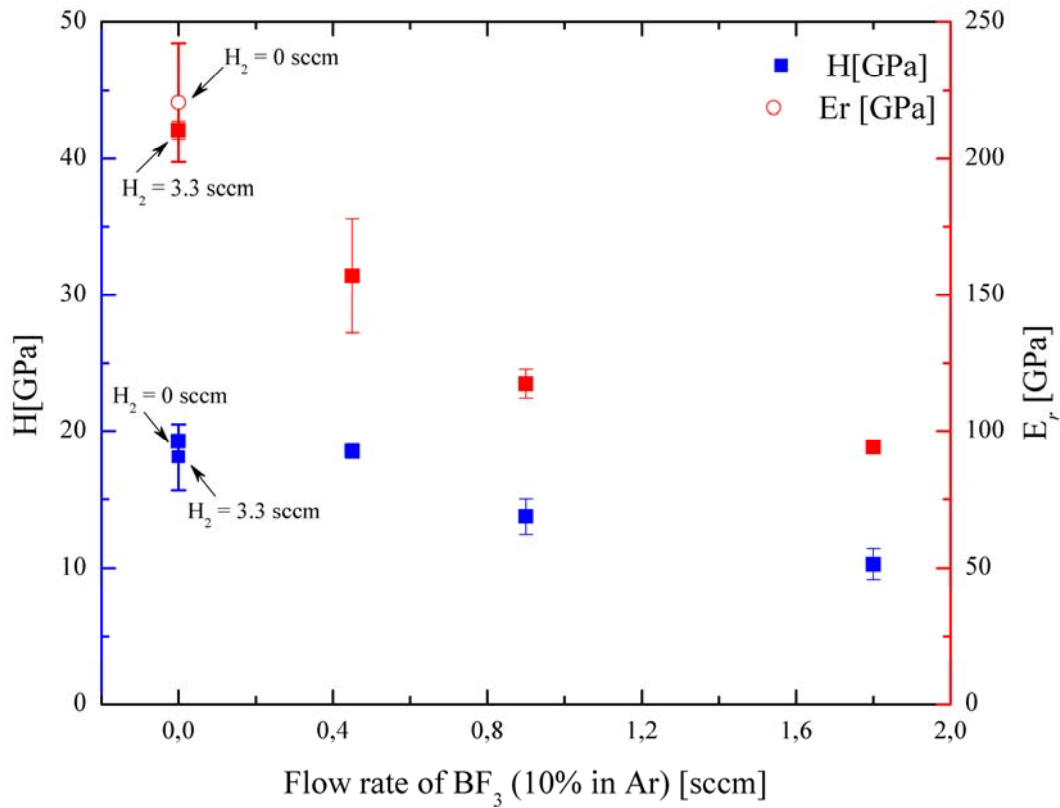

Figure 3.35: Nanoindentation hardness and reduced elastic modulus for films as a function of BF₃ flow rate.

3.8   Tribological Investigation of Mo-B-N films.

3.8.1   Nanoscratching at Ultralow Loads (10 μN – 500 μN)

The frictional behaviour of the nanocomposite films was assessed by performing two types of scratches against the diamond indenter. The first involves ramping the scratching load in the range 10 μN to 100 μN, whereas the second is carried out at a constant load of 500 μN. Figure 3.36 (a) and (b) show typical lateral force curves of nanoscratches on various nanocomposite films at incremental and constant normal loading, respectively. In incremental loading, Apart from the initial increase in the lateral force at the onset of the scratch, this force increases linearly as a function of normal load in the incremental scratch mode. The product of the friction coefficient and the non-zero lateral forces (μF_0) was found to vary between 1.3 and 2.3 μN in all measured nanocomposites. These non-zero values may be attributed to intrinsic adhesive forces between the surface and the counter body (diamond indenter) and/or equipment-generated artifacts.

The calculated friction coefficients of all nanocomposites in the load range 10- 100 μN are shown in Figure 3.37. Generally, low coefficients of friction are observed in B-containing nanocomposites. All B-containing films have friction coefficients which are lower than 0.21 with film D which contains 30.5 at.% B having noticeably the lowest friction coefficient of 0.13. This does not apply to molybdenum nitride (A), which has the highest friction coefficient reaching up to 0.34. A similar trend is also observed with scratches that are performed at the constant load of 500μN. In this case the values of the measured friction coefficients are very close to those calculated from the liner fitting of ramped scratches. The friction data which are obtained from amorphous boron nitride (a-BN) are just as low as those of Mo-B-N nanocomposites.

Film	H [GPa]	E_r [GPa]	H/E_r	H^3/E_r^2	R_{rms} [nm]	Friction Coefficient at $F_N=$	
						10- 100 μN	500 μN
A	18.1±2.4	221±22	0.082	0.121	7.37±0.46	0.348±0.006	0.285±0.008
C	18.5±0.5	157±21	0.118	0.257	0.52±0.09	0.181±0.002	0.166±0.003
D	13.7±1.3	117±5	0.117	0.187	0.90±0.07	0.133±0.005	0.167±0.003
E	10.3±1.1	94±1	0.109	0.122	3.43 ±0.28	0.209±0.006	0.216±0.002
a-BN	5.8±1.3	42±6	0.11	0.114	4.49±0.25	0.186±0.006	0.160±0.012

Table 3.7: A summary of the mechanical and tribological properties of Mo-N and Mo-B-N nanocomposite films. The values which were obtained from amorphous boron nitride films are added to aid comparison.
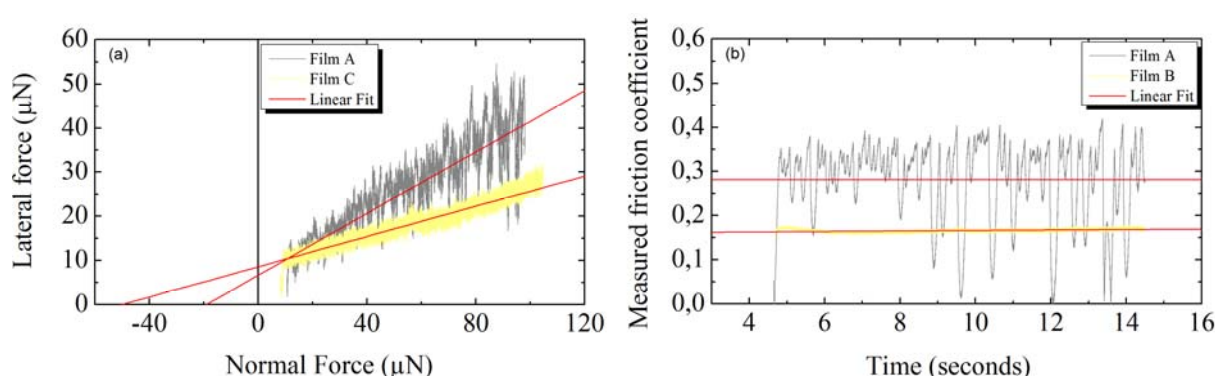

Figure 3.36: The change in the lateral force during scratching Mo-N and Mo-B-N nanocomposites at (a) incrementally increasing normal load from 10 μN to 100 μN and (b) constant normal load of 500 μN.

In constant-loading scratches at 500 μN, after an initial increase in the friction coefficient, which corresponds to the loading portion of the scratching curve, a constant value is maintained throughout the constant loading which lasts 10s. This constant friction corresponds to a steady

state friction. It is evident that during the course of scratching, all Mo-B-N nanocomposites (films **C**- **E**) and amorphous boron nitride (a-BN) nanoscratches are smooth, showing no abrupt changes. This indicates that both materials are structurally homogenous at the scratch length, and that neither slip-stick effects nor pop-ins are present. The larger fluctuation in the nanoscratch of film **A** is representative of its surface topography, since film **A** has a rougher surface in comparison with the rest of the films. Nonetheless, no indications of delaminations or cracking events can be seen to take place during scratching as would be expected from such low loads. A summary of the films' tribological properties as determined by Nanoindentation is given in Table 3.7.

An initial examination into the relationship between variations in film composition and variations in the friction coefficient does not render a clearly discernible correlation between the two. What can be clearly ascertained is that the B-containing nanocomposites seem to have a somewhat lower friction coefficient than that of the molybdenum nitride films suggesting that the key to the relationship between these two variations: composition and friction coefficient lies elsewhere.
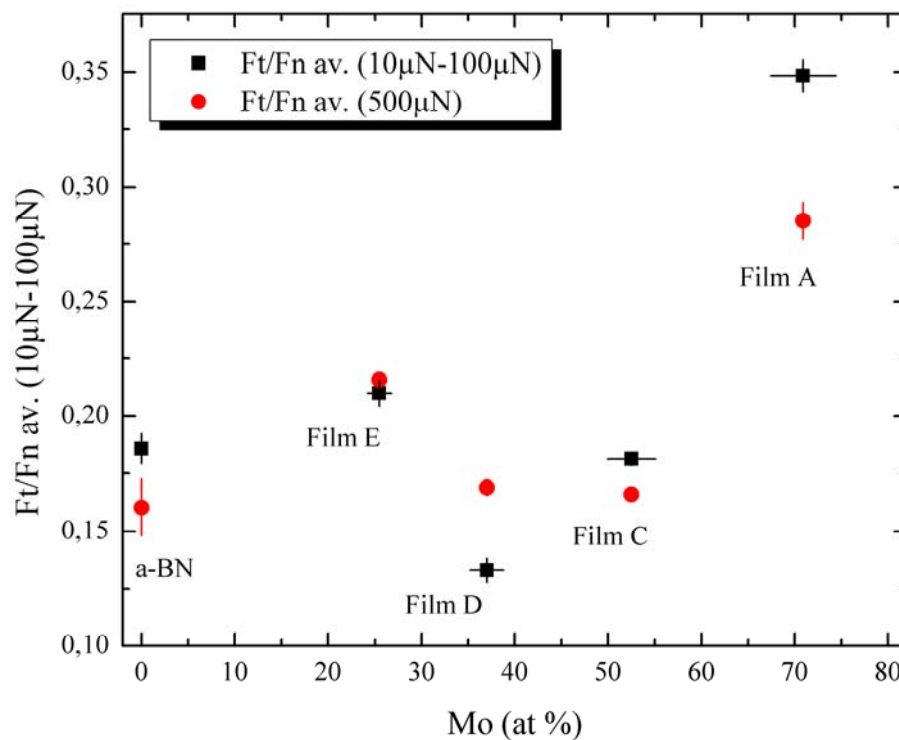

Figure 3.37: The friction coefficient of all tested coatings as obtained from nanoscratch testing against a 20 μm conical diamond indenter in the load range 10- 100 μN (black squares) and at a constant load of 500 μN (red squares) vs. film composition.

In order to examine the friction data in more depth, other mechanical properties of the films are considered. Previous studies have suggested that the friction coefficient may be directly linked to both hardness and elastic modulus [163]. Figure 3.38 (a) and (b) illustrate the variation in the

friction coefficient obtained from both nanoscratches as a function of the films' reduced elastic moduli (E_r) and their ratio of hardness to reduced modulus (H/E_r), respectively. The trend shows how both friction coefficient values increase steadily with increasing the reduced elastic modulus, while it decreases almost exponentially with increasing H/E_r ratios. This trend suggests that films with a lower reduced elastic modulus tend to have lower friction coefficients. In fact, this trend appears to be contradictory to a previously proposed model [164], which suggests based on AFM friction studies that in sliding elastic contact regimes, the nanoscale friction coefficient increases linearly with the inverse of the effective elastic modulus ($1/E_{eff}$). The data which are presented in Figure 3.38 follow an opposite trend revealing that both measured and calculated friction coefficients increase with increasing the film's reduced elastic modulus.

The explanation for this behaviour may lie in a previously observed the pile-up and sink-in effects which occur during Nanoindentation. When an indenter is loaded against a surface such that the contact is elastic, the surface underneath the indenter is typically pulled away from the indenter leading to a sinking-in behaviour. Once the contact load increases to a level which involves plastic deformation, the surface will either sink-in or pile-up around the indenter depending on its mechanical property, namely; the ratio of the effective elastic modulus to the yield stress (E_{eff}/σ_y). A material with a high (E_{eff}/σ_y) ratio and with little to no tendency for work hardening tends to pile-up largely [165,166]. (For example, compare glass with E_{eff}/H in the order of 12 which deforms plastically with a sink-in to that of aluminium with E_{eff}/H approaching 117.5 which exhibit a strong pile-up behaviour). Provided the high hardness of the films investigated in this work (i.e. E_r/H ratios between $9 - 12$), sinking-in upon loading is always expected.

The sinking-in behaviour ensures that the contact area which the indenter makes with the film is reduced as a result of the film drifting inwards away from the indenter. In addition, the magnitude of the sinking in is proportional to the reduction in the E_r/H ratio. Since the friction coefficient is directly proportional to the contact area, a decrease in the latter has the effect of reducing the friction coefficient which is exactly what is observed in the case of scratching the nanocomposite films under these low loads. These observations have been confirmed experimentally in the nanoscratching of hydrogen-containing amorphous carbon (a-C:H) films in the elastic regime with ultralow loads (150μN) [167]. These experiments demonstrated that upon scratching various (a-C:H) films on silicon single crystals with varying hardnesses and reduced elastic moduli, a decrease in the friction coefficient was observed for the more elastic films. The same explanation may be used to account for the decrease in the friction coefficient observed in

Figure 3.38(a). The more elastic films reduce the overall elasticity of the film/substrate system leading to a decrease in the friction coefficient.

It is also important to consider the H/E_r and H^3/E^2_r ratios as they are indicative of the surface's ability to absorb energy elastically [40]. Previous tribological sliding tests of Cr-N surfaces which are coated on a set of compliant and elastic interlayers forming a multilayered system with controllable H/E ratios have demonstrated that the H/E_r ratio plays an important role in determining the sliding friction coefficient [64]. Based on these experiments, which were conducted under high loading conditions (i.e. loading under plastic regimes), a model was constructed [64,168,163] which showed that, in fact, the ratio of hardness to reduced elastic modulus is more relevant to the friction behaviour than the elastic modulus alone.

Based on the above, the importance of the H/E ratio stems from the following: (i) H/E ratio affects the contact area between the counter bodies which influences friction. (ii) H/E ratio is related to the amount of energy absorbed elastically in contact and the degree to which a surface accommodates contact stresses and therefore responds to deformation. As such H/E can lend itself as a useful predictor to gauge the film's tribological performance.

In the scratch tests presented here, the data appear to follow the trend of decreasing the friction coefficient for films with higher H/E_r ratios under both low loading conditions in the range 10μN to 100μN as well as under higher loading (500μN). It can be seen from Figure 3.38(b) that the B-containing nanocomposites films, which have H/E_r ratios in the range 0.109 to 0.118 also have the lowest friction coefficients. While the stiffer Mo-N nanocomposites with an H/E_r ratio hovering around 0.082 have the highest friction coefficient. Thus, it is evident that the material with a higher H/E_r ratio can absorb more of the deforming energy elastically. During low loads (10- 100 μN) nano-scratching of surfaces with high H/E_r ratios, as in films **C**- **E**, the film (or more precisely the film/substrate system) tends to be more compliant and exhibit sink-in behaviour. This leads to a decrease in the contact area with the indenter which in turn reduces the friction coefficient since the friction coefficient depends on the contact area as follows: F = τ×A where τ is the shear stress.

Despite the fact that the aforementioned model has been previously applied to sliding experiments under high loading which ultimately led to plastic deformation (these conditions are not applicable to the experiments in this work which were conducted at low loads), it does not account for the fact that the change in the H^3/E^2_r ratio is another interesting parameter which may correlate with the friction data. Figure 3.39 shows how both measured and calculated friction coefficients change with the H^3/E^2_r ratio of a large number of nanocomposite films in

the Mo-B-N system, which were deposited with various compositions. Clearly, those nanocomposites with a higher H^3/E_r^2 ratio tended to have a lower friction coefficient against the diamond indenter. This may be interpreted as follows: as the surface's H^3/E_r^2 ratio increases, so does the threshold for plastic deformation. Accordingly, the material requires more stress to deform plastically since it absorbs more of the deforming energy elastically. The Nanoindentation loading regime, which is implemented here, can be considered as largely elastic as marked by the exponential decaying in the measured friction coefficient with increasing normal load [167]. Therefore, as the film is indented, the degree of its compliance and elastic deformability determine how it (or more precisely the film/substrate system) behaves beneath the indenter. Films with a high H^3/E_r^2 ratio feature reduced contact area with the counter body which results in a lower friction coefficient.

These results point to a very important conclusion with regards to the relationship between the material's design and its tribological behaviour. By depositing films which have the proper H^3/E_r^2 ratio, the surface will absorb the energy (or the force) elastically, and therefore it is less likely to be adversely affected by contact tribology causing wear and fret. These results indicate that it is possible to control the film's mechanical properties and tribological behaviour by carefully controlling film composition and consequently its structure and mechanical properties. Nanocomposite films with improved elasticity and reduced friction can be obtained for a composition which corresponds to high H^3/E_r^2 ratios. These were shown to be the ones with a specific boron content.
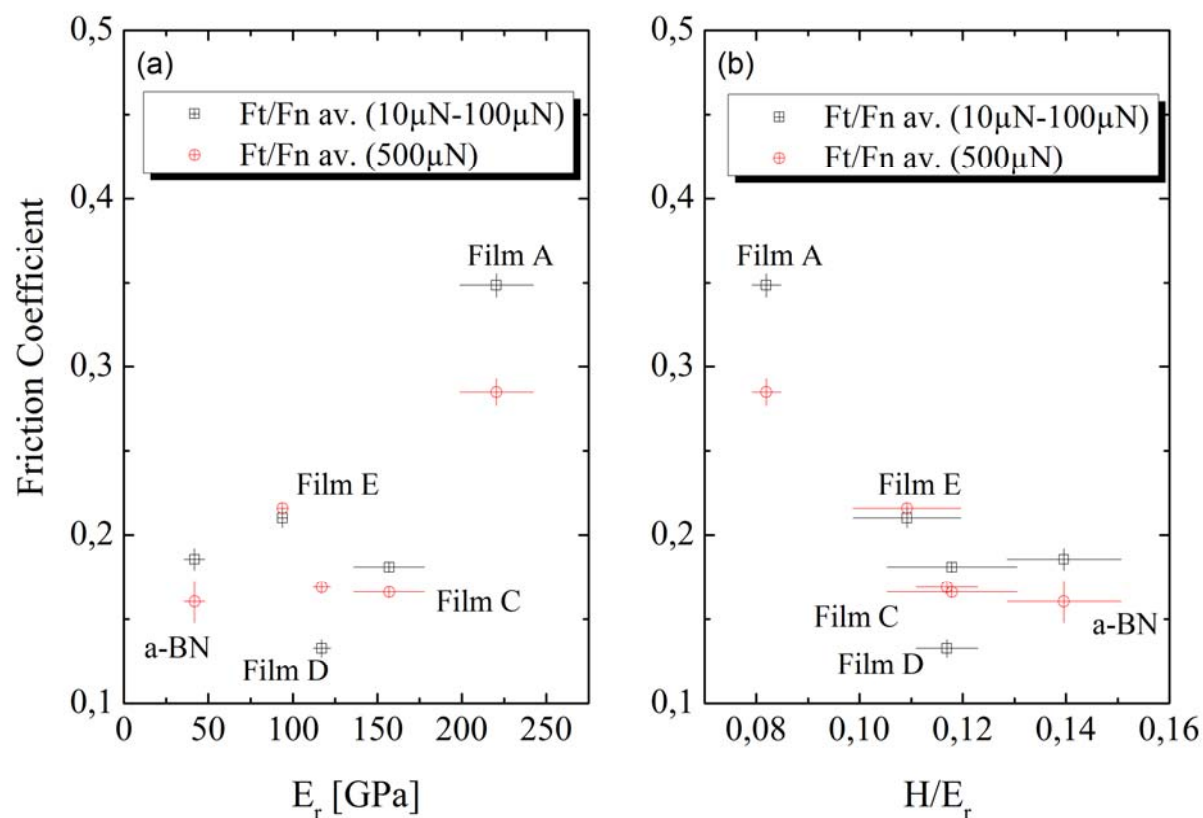
Figure 3.38: The change in friction coefficient for both types of scratches as a function of the film's (a) reduced elastic constant and (b) H/E$_r$ ratio.
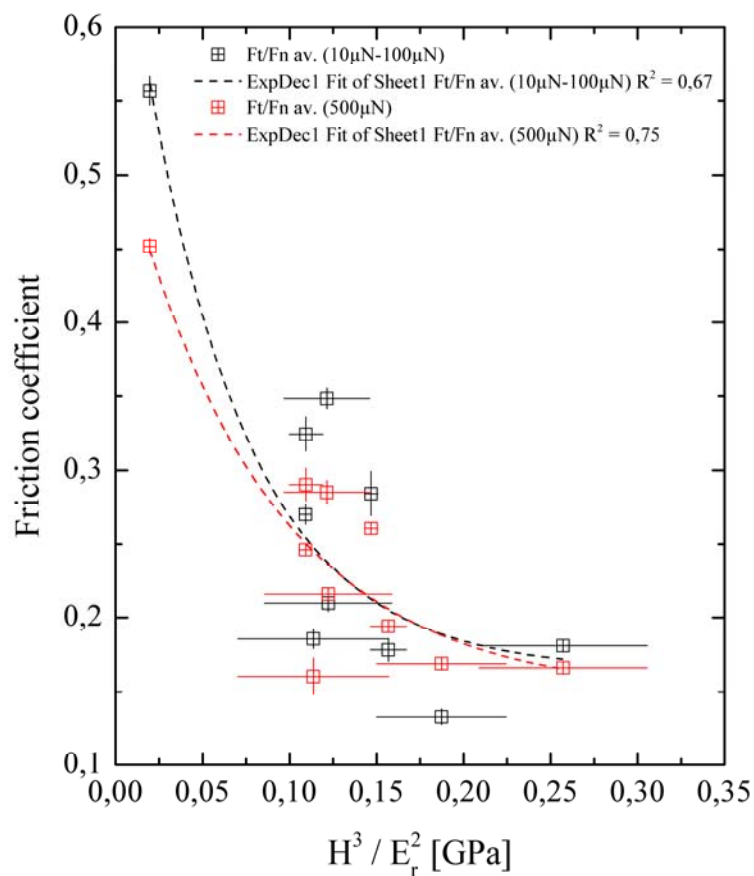

Figure 3.39: The change in the friction coefficient of various nanocomposite films as a function of the films' H^3/E^2_r ratio.

3.9 Discussion

3.9.1 Influence of BF$_3$ Flow Rate on Film Composition and Structure.

The flow rates of both BF$_3$ and H$_2$ effect both the film's phase composition and microstructure significantly. XPS results shows that in the presence of H$_2$, the film's boron content increases steadily with the addition of BF$_3$ whereas its molybdenum content is almost mirror imaged with decreasing content. FTIR and XRD results show that the film deposited in the N$_2$/He plasma mixture without the addition of both BF$_3$ and H$_2$ consisted merely of δ-MoN and γ-Mo$_2$N. In N$_2$/He plasma, a surface reaction takes place between the sputtered Mo species and N$_2^+$ which are produced by the strongly ionising ECR plasma [169]. It is only possible to grow the BN phase by allowing both the BF$_x$ and H species to react in the presence of excessive amounts of N$_2^+$ ions. The net reactions which take place can be summarised as follows:

$$2Mo + N_2 \rightarrow Mo_2N \tag{1}$$

$$BF_3 + \tfrac{1}{2}N_2 + 1\tfrac{1}{2}H_2 \rightarrow BN + 3HF \tag{2}$$

A key feature in the implemented deposition conditions is that reaction (2) takes place only in the presence of H$_2$. While reaction (1) is mainly controlled by the sputtering rate of Mo atoms in excess of N$_2^+$ and at a given bias voltage, the extent of reaction (2) is determined by the amount of BF$_3$ (or more precisely on the ratio of BF$_3$/H$_2$) used during film growth, which controls the BN fraction. This is confirmed by the systematic increase in the intensities of both the stretching and bending vibrations of B-N bonds.

It should be mentioned that the absence of BN in films deposited by BF$_3$ containing gas phase and without H$_2$ can be attributed to the following: (i) In the absence of hydrogen, the strong etching effect of fluorine of solid BN lessens its growth as previously observed when BF$_x$ gas chemistry was used to deposit BN [244(a)-(b)]. (ii) Theoretical observations and predictions which highlighted that hydrogen species have been described to be very effective in stabilising the growth of BN [244(c)].

Detailed XPS core level spectra reveals a complex picture of the chemical bonding state in molybdenum nitride films. Molybdenum shows mixed low oxidation states which are indicative of at least two nitrides without the presence of metallic molybdenum. This means that all molybdenum atoms have undergone a chemical reaction with nitrogen leading to the formation of molybdenum nitride. Because of the presence of multiple oxidation states of Mo, it can be concluded that there are two possible pathways for reaction (1) which results in either nitride: Mo$_2$N and MoN. It is known from deposition experiments carried out by PVD [170,171,172] that the stoichiometry of molybdenum nitride depends on the N$_2$ molefraction in the gas phase, in such a way that high partial pressures of N$_2$ are always required to achieve the stoichiometry of

Mo:N = 1:1. With regards the deposition carried out in this work, no major difference in film composition and chemical bonding could be determined despite the fact that film deposition is carried out both with and without BF_3 as in the case of films **B** and **A**, respectively. This would be expected from depositions in abundant N_2. However, it may be concluded that for a single phase molybdenum nitride film, a higher nitrogen flow rate would be necessary.

The addition of BF_3 during deposition can only lead to the formation of boron nitride when hydrogen is present as clarified earlier. XPS data do not give a clear indication of whether the formed boron nitride takes on the form of sp^2 or sp^3-bonding. This is due to the very close binding energies of the B $1s$ and N $1s$ electrons in both bonding types, which are difficult to resolve using this technique. However, in the light of FTIR data there is a clear indication that the BN phase is largely sp^2-bonded and significantly disordered as marked by the very large band widths of the corresponding vibrations. Increasing the flow rate of BF_3 has the effect of increasing the mass fraction of BN in the film, while simultaneously increasing the amount of Mo-B bonds in the nanocomposite. Although the proportion of B-N bonds is clearly much more than that of Mo-B as was judged based on the area ratios of the corresponding de-convoluted peaks, other spectroscopic and diffraction methods do not give any measurable sign of the presence of molybdenum borides. This indicates the peculiarity of the Mo-B bonds in the nanocomposites.

Furthermore, diffraction data obtained from both XRD and SAED patterns show that γ-Mo_2N is the only detectable crystalline phase in the nanocomposite, while BN appears to be x-ray amorphous. The co-deposition of the BN phase greatly suppresses the growth of the γ-Mo_2N, whose mean crystallite size drop continuously to about 2 nm according to both XRD line profile and HRTEM analyses. In light of the above, the nanocomposites' composition and chemical bonding can be described as resulting from changes in the deposition reaction conditions. A nanocomposite which comprises two different nitrides; that of molybdenum and boron can only be grown in the presence of H_2 and BF_3. The growth of the amorphous BN phase suppresses the crystal growth of molybdenum nitride, which leads to the formation of very fine nanograins that are randomly oriented in the film. The detection of Mo-B bonds by XPS suggests that these bonds are the result of bonding between Mo atoms in Mo_2N nanocrystals and the surrounding BN amorphous layers. This is also in agreement with the thermodynamic data of the Mo-B-N system. Although the phase diagrams available in published literature describe only the high temperature phases (1200- 1600°C) [115], the data clearly show that there is neither an appreciable solubility of B in Mo-metal at temperatures lower than 1100°C, nor are there any detectable ternary Mo-B-N compounds. The XRD and HRTEM findings corroborate this by marking the absence of any molybdenum borides. Therefore, the peculiar situation with regards

to the Mo-B bonding can be understood in the light of the nanocomposite nanostructure. Because of their nano-metric size, there are significant proportions of Mo and N atoms at the surface of the Mo_2N grains compared to that in their bulk. This gives rise to a greater chance for Mo-B bonds to form across the interfaces between the nanograins and the surrounding amorphous BN network.

3.9.2   Influence of Film Microstructure on Mechanical Properties.

Both the film's composition and the nature of its microstructure have a direct bearing on it mechanical and tribological behaviour. The material's hardness and elasticity are intrinsically a direct consequence of the nature of the chemical bonds between the constituent atoms, and extrinsically due to its micro- and nanostructure. The stark micro- and nano-structural changes associated with changing the reactants' ratios during film deposition greatly affect the films' response to plastic deformation. As the films move from a pronounced polycrystalline columnar microstructure with faceted grains to a dense, fine-grained nanostructure, their hardness values tends to decrease monotonously. Polycrystalline δ-MoN/γ-Mo_2N films have hardness values of about 18.0($\pm$2.4) GPa, which are similar to previously reported values for magnetron sputtered γ-Mo_2N [173,174,175], whereas, nanocomposite **C** shows a maximum hardness of 18.5($\pm$0.5) GPa. The structure of film **C** corresponds to a microstructure comprising γ-Mo_2N with a mean grain size of 8 nm (according to $<D_V>$ extracted from XRD line profile analysis) which are dispersed in a small amount of sp^2-bonded amorphous BN. The result suggests that such a microstructure shows a certain degree of microstructure-induced enhancement to the resistance of plastic deformation. Nanocomposites **D** and **E**, which have a higher fraction of the BN phase, reveal sharply dropping values of hardness and reduced elastic modulus due to the formation of an increasing fraction of the softening BN phase.

A careful examination of the relationship between the film's hardness and its elasticity, which is carried out by computing the ratio H^3/E_r^2 reveals the effect which the film's micro- and nanostructure have on its mechanical properties. The results reveal that by controlling the volume fraction of both nitrides, the grain sizes of the crystalline phase can also be controlled, which results in films with H^3/E_r^2 values ranging between 0.12 and 0.26. The decrease in Mo and the consequent increase in the softening amorphous BN phase leads to an increase in plasticity and consequently a decrease in resilience. However, the nanocomposites which exhibit a sufficient degree of elasticity and strain tolerance are the ones with the highest H^3/E_r^2 ratios. These nanocomposites do not vary much in composition. In fact, the difference in the Mo content between films **A** and **C** does not exceed 20 at.%, and the B-content in nanocomposites **A**- **C** varies by only 21 at.%. Nonetheless, the variation in their H^3/E_r^2 ratios is high. This

signifies the extrinsic effects of microstructure on the mechanical properties. At the nanometre scale, the film whose structure is made up of γ-Mo$_2$N crystallites with an average size of no more than 4- 8 nm, which are randomly dispersed in the amorphous BN matrix is the one with the highest degree of elasticity and strain tolerance. When the size of the randomly oriented crystallites falls below this 4 nm, as is the case with the nanocomposite with the highest boron content (or least Mo), the distance separating the grains is large enough to include more of the softening a-BN phase. The result is a nanostructure, which is defiant to the prevention of dislocation propagation induced by loading; and which is as a consequence less resilient.

This may suggest a specific strengthening mechanism that is related to the microstructure, which acts to increase the film's resistance to plastic deformation. In order to understand this effect, the mechanism of strengthening materials needs to be highlighted. Under the influence of external stresses, plastic deformation is mediated by the generation and propagation of dislocations. When obstructed, these dislocations can only propagate further when sufficient additional stresses are applied. Such obstructions can be brought about by reducing the grain sizes in a material. More grain boundaries exist in a material as a result of reducing its grain sizes, which act as a form of hindrance to the dislocation movement. It is well established that an increase in the density of grain boundaries causes an increase in the amount of stresses that are required to propagate dislocations. This is because the stress increases with decreasing the distance between the dislocations, which is commonly described as the Hall-Petch effect [176,177]. This effect is also used as a strategy to strengthen materials by reducing their grains size to values lower than 100 nm, and is usually referred to as grain refinement. In this relationship, the yield stress (σ_{yield}) of a material changes parabolically with d$^{-\frac{1}{2}}$ as follows:

$$\sigma_{yield} = \sigma_{lattice} + k \cdot d^{-\frac{1}{2}}$$

3-10

Where $\sigma_{lattice}$ is a stress threshold that is commonly referred to as lattice friction stress, which required to move individual dislocations; and k a constant that is dependent on the material's stress intensity factor. This relationship does not imply, however, that the continuous refining of grains leads to progressive strengthening. In fact, there is always a critical grain size under which the resistance to the dislocation movement is impeded leading to material softening [179]. The nanocomposites prepared in this work show that the aforementioned relationship maybe be applied. Increasing the film's B-content decreases the γ-Mo$_2$N crystallite sizes monotonously. Despite limited statistical data shown in Figure 3.40, nanocomposites with spherical CCD diameters in the order of 8 nm show the highest elasticity and strain tolerance, and therefore the

highest resilience. The latter tends to drop by either increasing or decreasing the crystallite sizes. It can therefore be argued that the critical domain or grain size is in the order of 8 nm. Although, there are ample examples in published literature which supports the findings in this work (i.e. a further decrease in grain sizes leads to a softening effect), it is still unclear why this inverse effect takes place.
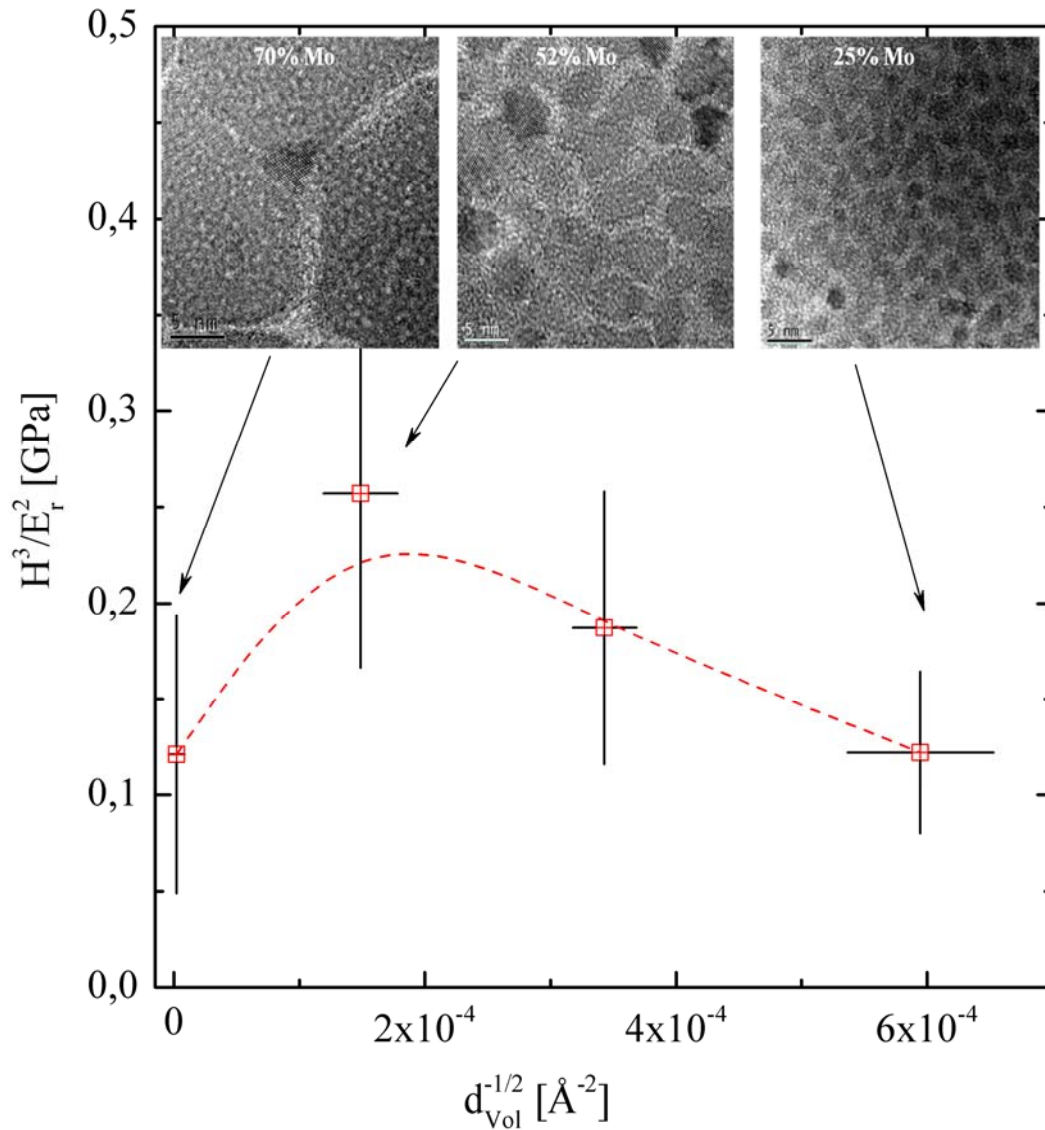

Figure 3.40: The change in the films' resilience expressed in terms of the ratio H^3/E_r^2 as a function of the size of coherently diffracting γ-Mo$_2$N domains in various nanocomposites. The sizes are obtained from XRD line profile analysis. The HRTEM micrographs show the corresponding nanostructures of the nanocomposites which contain 25%, 52% and 70%at. of Molybdenum. The scale bar in all micrographs is equal to 5 nm.

Many arguments [33,178,179] aim to provide an explanation that is based on the notion that due to the nanoscale size of the grains, the probability of moving dislocations within the grain is hugely lessened, which directs the movement towards the grain boundaries. Upon reaching a specific stress threshold, the dislocation movement forces the atoms which form the grain

boundaries to slide on top of each other leading to material softening. At a given stress threshold, this softening effect occurs at a specific critical grain size which marks the transition from plastic deformation that is mediated by the propagation of dislocations into one which is controlled by grain boundary sliding.

On the other hand, the variations in the nanocomposites' macrostresses (expressed in terms of γ-Mo_2N) show that the film with the highest H^3/E_r^2 ratio is the one where the γ-Mo_2N is only slightly compressed. Highly stressed films are not favoured from a practical point of view, as they tend to fail rather quickly under static or alternating mechanical loading conditions.

In view of the above, these results demonstrate that these nanocomposites can be engineered as wear-resistant coatings demonstrating a unique combination of hardness, toughness and elasticity. This could potentially qualify these coatings to become the materials of choice, which would suit a wider range of substrate materials and tribological applications.

3.9.3   Influence of Film Microstructure on Tribological Properties.

Tribological properties of thin films and surface coatings are system properties which not only depend on the material and morphology of the thin film and counter body material, but also on the test environment and the nature of wear which takes place during tribological contact. The latter affects the nature of tribological behaviour since wear determines the third body type and the nature of its involvement in the tribological contact. Although from an application point of view, some may argue that testing the tribological and frictional properties of thin films by nanoindentation under ambient atmospheres has limited applications, it is still a means of understanding material behaviour at the nanoscale. Evaluating the tribological properties of nanocomposites by using a chemically inert diamond indenter at ultralow loads is a very useful tool. Although this type of tribological contact is only encountered in specific environments such as in micro- and electro-mechanical systems (MEMS), the very small sub-micron contact areas generate considerable Hertzian contact pressures at maximum contact depths that do not exceed several tens of nanometre. This makes nanoindentation particularity well-suited to probe the "real" mechanical and frictional properties of nanocomposite thin films.

The effect of changing the film composition on the frictional behaviour of the nanocomposite against the diamond indenter under low loading conditions was very pronounced in the case of B-containing nanocomposites. There are specific film compositions which correspond to the highest elastic deformability as quantified by the H^3/E_r^2 ratio. It is previously mentioned, increasing the film's B-content does not always increase this ratio and that the relationship is

somewhat parabolic. When properly controlled, films with the highest H^3/E^2_r ratio can be synthesised. These show improved tribological properties with regards to their friction behaviour against diamond under an ambient atmosphere. Nanocomposites with high H/E_r and H^3/E^2_r ratios can absorb more loading stresses elastically due to their heightened threshold for plastic deformation. This means that these nanocomposites can accommodate more stresses and feature reduced friction coefficients. This can be seen, for example, by comparing films **A** and **C** which have 0 at.% and 17.6 at.% of boron, respectively. Although both films have similar hardness values, film **C** is more elastic and therefore more compliant resulting in a film that has a higher ability to accommodate stresses elastically before yielding. Under contact loading, such a film demonstrates lower friction not only in the elastic regime as shown by the nanoscratches in the load range 10- 100 μN, but also under plastic deformations due to its more compliant character. This means that larger stresses (forces) are required for this kind of film to fail provided that no major topographic changes are introduced as is the case here. While it might be beneficial to increase the proportion of the softer phase in the nanocomposite in an attempt to increase its elasticity, this change has an adverse effect in the sense that the films' hardness will decrease as well. As a result both H/E_r and H^3/E^2_r ratios drop and the film losses its resilience and consequently tends to demonstrate worse tribological behaviour. The key is to design a film with enhanced H and reduced E_r aided by proper microstructural control.

3.10 Conclusions

The results obtained in this system demonstrate how it is possible to modify the mechanical and tribological properties of Mo-B-N nanocomposite films through changes to their nanostructure and chemical composition, which can give rise to new behaviour. By using a hybrid method employing ECR-MWCVD and the *in-situ* sputtering of Mo using the gas mixture BF_3–Ar–H_2-N_2– He, specific reaction conditions were established. This entailed controlling the ratio of the reactant gases, which leads to the formation of nanocomposite films consisting of two different phases: γ-Mo_2N and BN. The mass fraction of either phase can be varied by controlling the ratio of BF_3/H_2 and the bias voltage of the Mo sputtering source. Films prepared in N_2/He plasma consist solely of a polycrystalline mixture of δ-MoN and γ-Mo_2N. Increasing the BF_3/H_2 ratio leads to the formation of a γ-Mo_2N/a-BN nanocomposite with increasing amounts of BN. The BN phase remains X-ray amorphous at all deposition parameters and suppresses the growth of γ-Mo_2N which takes the form of nanocrystals with mean grain sizes of less than 10 nm. Both HRTEM an XRD line profile analysis reveal γ-Mo_2N crystallites of 4- 8 nm at 0.9 sccm BF_3. The γ-Mo_2N crystallites continue to decrease in size as the mass fraction of BN increases. The γ-Mo_2N phase is under compressive macro- and microstresses whose extent increases as the film's

BN fraction increases. With no molybdenum borides being detected in all the nanocomposites, the presence of Mo-B bonds as revealed by XPS suggests that such bonds are formed only across the grain boundaries. A fact, which is also supported by the very low solubility of B in both Mo and MoN and the absence of known ternary Mo-B-N compounds. ToF-SIMS depth profile measurements reveal a generally homogenous distribution of the Mo, N and B throughout the nanocomposite films. Nanocomposite films which were synthesised at 0.9 and 3.3 sccm of BF_3 and H_2, respectively, showed a slight increase in film hardness to 18.5($\pm$0.5) GPa when compared to polycrystalline δ-MoN/γ-Mo_2N films. A further increase in the mass fraction of the BN phase leads to a sharp drop in both hardness and reduced elastic modulus values. Additionally, by depositing films which have the proper H^3/E_r^2 ratio, the surface will absorb the energy (or the force) elastically, and therefore it is less likely to be adversely affected by contact tribology causing wear and fret. These results indicate that it is possible to control the film's mechanical properties and tribological behaviour by carefully controlling film composition and consequently its structure and mechanical properties. Nanocomposite films with improved elasticity and reduced friction can be obtained for a composition which corresponds to high H^3/E_r^2 ratios. These were shown to be the ones with a specific boron content and microstructure.

4   Hard Films in the Si-B-C-N-O System

4.1   Introduction

The development of multi-component hard-films is essential in order to develop a new generation of technically important and versatile hard films. Recently, ternary and quaternary ceramics, such as nitrides and carbonitrides of silicon and boron were shown to demonstrate attractive qualities such as corrosion resistance and hardness which make them suitable for high-temperature abrasive applications. While such ceramics have been intensively investigated over the past two decades when prepared in bulk form [1,136] via polymer pyrolysis synthetic routes, it is only very recently when that this class of materials were successfully realised in thin film form. Recent work has demonstrated that amorphous thin films in the system Si-B-C-N can be realised by magnetron sputtering techniques [180,181] under medium to high substrate bias with reduced growth stresses in contrast to other hard ceramics such amorphous carbon and boron nitride.

In the context of developing new compounds based on the light elements Si-B-C-N system, early investigations [182], which relied on a high pressure/high temperature process, have demonstrated the possibility of forming a solid solution based on this system. For example, at a temperature of 2600°C and pressures up to 700 MPa, a compound composed of 20 mol.% SiC and 80 mol.% BN was synthesised that had a maximum hardness of 36 GPa. Other work which has been carried out on hot-pressed SiC ceramics [183] revealed that the addition of small amounts of boron can lead to increasing the hardness of the cubic 3C-SiC phase by more than 80% reaching 40GPa, by forming a composite ceramic with strong grain boundaries. One of the hardest compounds is based on a system which can be thought of as primarily a B-C system which is alloyed with small amounts of Si as in $B_{1.2}C_{2.88}Si_{0.35}$ [184]. In crystalline form, this compound is reported to have a hardness reaching 63 GPa. Similarly, a B-free crystalline SiCNO compound with the empirical formula $Si_3N_{2.2}C_{2.16}$ have demonstrated a hardness of 65 GPa [184]. The chemical routes which have been used to synthesise such films have proven to be particularly attractive for a number of reasons which include: the simplicity of preparation and the ease of up-scaling. Nanocrystalline SiBCN (nc-SiBCN) ceramics [185] can also be prepared by poly-condensation of precursors such as polysilazanes which are functionalised with boron alkyl amides. Upon subsequent high temperature annealing in an inert atmosphere, which is commonly referred to as pyrolysis, a dense network of the ceramic is formed which essentially contains the same covalent bonds which are present in the starting materials (also referred to as a polymer precursor). Not only does nc-SiBCN have a high hardness, but it also possesses a range of other

attractive properties such as enhanced thermal-shock, chemical, and oxidation resistance. These are the beneficial outcomes of including (doping or alloying) as well as the high temperatures annealing. Nonetheless, during pyrolysis, these ceramics revealed a number of issues which may be considered problematic with regards their applicability. The fact that the ceramics produced by this method were porous and had a high-hydrogen content meant that there were limitations to their structural and thermal stability. This in turn motivated considerable research not only to try to overcome these problems from a precursor-design perspective, but to also seek other synthesis routes. For example, due to the fact that such preparation routes are not fully capable of producing the same material in thin film form, researchers have had to explore other means to achieve the same materials. These findings have spurred on a large number of investigations which aim to unearth new possibilities of synthesising such hard ceramics specifically by means of vapour deposition techniques. A range of Si–B–N–C compounds can be achieved as thin films by different synthesis methods such as pyrolysis, chemical vapour deposition (CVD), and physical vapour deposition (PVD). In vapour deposition, the choice of a suitable precursor is crucial to ensure a specific film composition and chemical structure. Considerable work aimed at developing target specific precursors has shown that a large number of precursors can be used. For example, in thermal CVD [186] which was used to deposit SiBCN thin films, borosilazane and its derivatives were considered suitable precursors as they liquefy at high deposition temperatures (ca. 900°C). These resulting films acted as oxidation barriers for carbon fibres as they are able to withstand temperatures in excess of 1000°C. The films have a chemical composition of approximately $SiB_{1.0}C_{2.6}N_{1.4}:O_{0.7}$ at the surface, revealing a large amount of SiO_2 by XPS analysis. Another important property which influenced the precursor choice is the fact that these experiments aimed at depositing a ceramic that contained the same kind of strong single covalent bonds which could be repeated in a network. This would ultimately ensure the synthesis of a strong and thermally stable material. The degree of sophistication in precursor-design has increased so as to include a precursor such as Tri(dimethylamino)silylamino-di(dimethylamino)boran; (TDADB) $[(CH_3)_2N]_3Si-NH-B[N(CH_3)_2]_2$, which was to be implemented in a CVD process. The precursor contained the desired Si-N and B-N single bonds needed to form the bone structure of the ceramic upon proper thermal annealing. In fact, at temperatures as high as 1000°C, the ceramic which was obtained from this precursor [187] was a transparent thin film with the composition $SiB_{1.1}C_{1.6}N_{1.1}(O_{0.1})$. The films were X-ray amorphous and the ratio of B to Si in the precursor was conveyed to the amorphous ceramic.

Plasma-assisted CVD was also extensively used as a synthesis method for such complex compounds owing to its strongly ionising character. Early work using radio-frequency (RF)

plasma-enhanced chemical vapour deposition (PECVD) has shown how $SiBC_{2.8}N$ films with a hardness of 22 GPa can be obtained from a single-source silylamino-boran precursor (TDADB) [188] in an $Ar-N_2$ RF-Plasma. Furthermore, magnetoactive plasmas such ECR-MW-plasma-enhanced CVD has long been implemented to develop dielectric silicon carbide and silicon nitride thin layers for implementation in III-V semiconductor applications [189,190,191,192]. The development of SiCNO film by this method was also motivated by the move towards high temperature electronics [193,194,195]. The attractiveness of this technique lies in its ability to generate high-density plasmas which motivated work to produce such ceramics at relatively low substrate temperatures. Furthermore, ion-implantation routes to the synthesis of Si-B-C-N thin layers have also been examined. For example, silicon single crystals were implanted with the elements N, B and C by using high doses of N^+, C^+ and BF_2^+ ions accelerated at several ten thousands of eV towards the substrate to yield both amorphous and crystalline layers that consist mainly of SiC bonding network [196,197] at substrate moderate to high temperatures. PVD techniques employing RF [198] and DC magnetron sputtering [180] were also used to produce a range of hard Si-B-C-N coatings. Perhaps, the most comprehensive work on this class of material was performed by using DC-magnetron sputtering of Si-C-B targets under a controllable N_2 atmosphere [199,181,200,201,202] and reported a hardness up to 47 GPa of thin films which also demonstrated very attractive thermal stability properties with oxidation resistance temperature of more than 1500°C [60,203].

The goal of this study is to investigate the chemical bonding, structure, morphology, as well as the, mechanical and tribological properties of a range of amorphous films in the Si-B-C-N-O system. As such, all the films were prepared by electron cyclotron resonance (ECR) microwave plasma assisted chemical vapour deposition (MWCVD). Attempts were made to correlate film composition with deposition conditions. This was achieved by employing a range of diagnostic methods which probed both the surface and bulk compositions of these materials. Owing to the fact that these materials demonstrated very attractive mechanical properties, further correlations between film composition and mechanical properties were also studied in depth. The thermal stability of these amorphous ceramics was also investigated by means of Thermogravimetric analysis and the results were discussed in relation to their composition. These dense, pore-free and nearly stress-free films can be deposited with a range of varying compositions and possess potentially useful mechanical properties, including: high hardness, very large elastic recovery and good adhesion to the substrates. The preparation of such films will undoubtedly pave the way to the introduction of a new class of films which could even rival existing state-of-the-art hard amorphous ceramics.

4.2 Film composition

After their removal from the deposition chamber, all substrates which were prepared without the addition of BF_3 had a mirror-like black appearance, which became dark violet-black with increasing the BF_3 flow rate during synthesis. The film deposition rate was estimated based on the film's thickness as obtained from fracture SEM micrographs as well as the deposition time, and was found to change from about 1.5- 4.3 nm/min at 300 W to 4.2- 9.5 nm/min at 1400 W. Summaries of film deposition parameters and composition are listed in Table 2.1 and Table 4.1, respectively.

Film	Formula	Atomic composition (in at.%)				
		Si	B	C	N	O
SiBCNO1	$Si_{14}B_{24}C_{29}N_{22}O_{11}$	14.0±0.7	23.±1.1	28.±1.4	22.±1.0	11.±0.5
SiBCNO2	$Si_{19}B_{21}C_{23}N_{25}O_{12}$	19.±1.0	21.±1.0	22.±1.1	24.±1.2	12.±0.6
SiBCNO3	$Si_{33}B_8C_{19}N_{27}O_{13}$	32.±1.5	8.1±0.4	19.±2.0	27.±1.3	13.±0.6
SiBCNO4	$Si_{15}B_{25}C_{15}N_{33}O_{10}$ (*)	15.	25.	15.	33.	10.
SiBCNO5	$Si_6B_{22}C_{39}N_{20}O_8$ (*)	6.	22.	39.	20.	8.
SiCNO1	$Si_{36}C_{22}N_{25}O_{16}$	36.±1.8	1.1±0.5	21.±1.1	24.±1.2	16.±0.8
SiCNO2	$Si_{40}C_{16}N_{27}O_{15}$	40.±2.0	1.5±0.1	16.±0.7	26.±1.3	15.±0.7
SiCNO3	$Si_{39}C_8N_{42}O_{10}$	38.±2.0	1.0±0.1	8.2±0.4	41.±2.0	10.±0.5
SiCNO4	$Si_{32}C_{17}N_{26}O_9$	32.±	0.±0.	17.±	25.±	9.±
SiCNO5	$Si_{33}C_{38}N_7O_{12}$	33.±	0.±0.	38.±	7.±	12.±

Table 4.1: A summary of film composition. The chemical composition of the film with the asterisk is determined by EDS analysis and has a significantly larger error margin.

4.2.1 X-ray Photoelectron Spectroscopy Analysis

X-ray Photoelectron Spectroscopy (XPS) analysis [122,123,124] was used to determine film composition, which is expressed in terms of atomic concentrations and displayed in Table 4.1. The films' chemical composition was obtained from the low resolution survey spectra and the average atomic percentages were calculated from at least three analysis spots for each film type. The analysis was performed on Ar sputtered surfaces, and thereby avoided most of the contamination contributions resulting from exposure to air. The strong charging effects, which were encountered during the analysis, are due to the wide band-gap characteristic of these films. These effects were reliably evaluated and accounted for using suitably prepared standards. As a result, an increased uncertainty in the absolute binding energy (BE) values was taken into account, i.e. ±0.2 eV instead of the typical ±0.1 eV. The stoichiometry and chemical states of all

film forming elements were evaluated from the core level analysis. The survey XPS spectra in Figure 4.1 clearly shows the presence of six elements Si, B, C, N, O along with Ar. The latter is likely to be a product of the sputtering procedure which took place prior to recording the spectra. Film compositions were calculated based on the ratio of the core level intensities of the corresponding elements, which were corrected using the theoretical sensitivity factors based on Scofield's photoionisation cross-sections [123]. All prepared films showed a significant amount of oxygen and nitrogen even in those prepared without the intentional use of N_2 gas. Owing to the fact that a cleaning sputtering procedure took place which removed a significant proportion of the films' surface, these elements were considered as constituents of the synthesised material, not only as a contaminant resulting from air exposure. As a result film stoichiometry is described in terms of the concentration of all constituting elements.
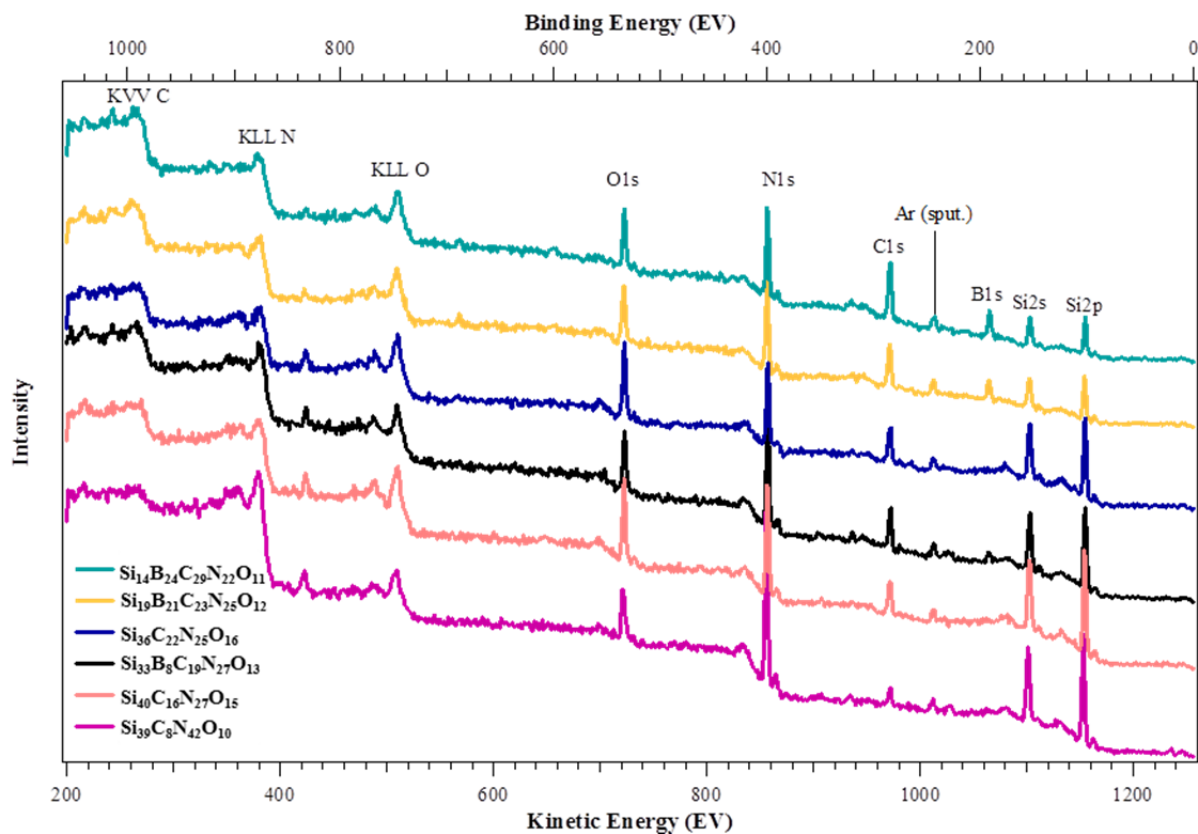

Figure 4.1: XPS Survey spectra of several Si-B-C-N-O films.

The high resolution XPS core level spectra were used to obtain detailed information about the chemical bonding in the films. Figure 4.2(a)-(d) shows the core level spectra of Si $2p$, B $1s$, C $1s$ and N $1s$ from all B-containing films, which were obtained by increasing the BF_3 flow rate during growth; whereas, Figure 4.3(a)-(c) presents the core level spectra of Si $2p$, C $1s$ and N $1s$ obtained from the boron-free SiCNO films. The Si $2p$ core level spectra have full width at half maximum (FWHM) that ranges between 2.5 and 2.8 eV, which is much larger than that obtained from

stoichiometric Si_3N_4 and SiC (1.79 eV and 1.84 eV, respectively [204]). Such a wide lineshape can be expected from silicon atoms which exhibit varying electronic states (i.e. oxidation states). Peak de-convolution revealed the presence of two major components representing the Si-C and Si-N bonding states located around 100.8 eV [205] and 102.2 eV [206], respectively, which is in agreement with literature values. These components correspond to silicon atoms which form SiC_xN_y units such as those present in a Si_3N_4 and SiC bonding environment. In the case of SiCNO films, increasing the carbon content from 8 to 22 at.% clearly shifted the Si $2p$ lineshape to lower energies by about 1.4 eV. This shift could be attributed to an increased proportion of Si-C bonds since additional carbon tends to compete with nitrogen to bond with existing silicon atoms. Also, a correlation with the N $1s$ spectra (cf. Figure 4.3(c)) showed that this addition carbon tends to bond with Si rather than with N as marked by the shift in the N $1s$ spectrum to lower energies, whereby nitrogen forms N-Si bonds almost exclusively.

A smaller contribution to the Si $2p$ spectra comes from Si-O bonds which have been reported to be located at 103.4 eV [207] and which become more evident for those samples deposited at increasing B-content. Finally, there was no clear evidence for Si-Si and Si-B bonds in all spectra. In the case of B $1s$ spectra (Figure 4.2b), the peaks were symmetrical and centred at 190.9 eV and 190.5 eV for films containing 8 and 21 at.%, respectively. Peak de-convolution was performed with one main component leading to a satisfactory reproducibility of the lineashape. A comparison with the peak binding energies of B–C, $B(sp^3)$-N, $B(sp^2)$-N, and B–O bonds, which have been reported to be 188.4 [208], 190.7 [135], 191.2 [136] and 193.6 eV [137], respectively, suggests that this major component corresponds to $B(sp^2)$-N bonds. A film with the composition $Si_{14}B_{24}C_{29}N_{22}O_{11}$ contains the highest amount of boron, whereby the peak remained symmetrical but shifted to a higher value of 191.3 eV. While it was not possible to distinguish between sp^2 and sp^3 B-N bonds, the fairly large peak width (FWHM = 2.6 eV) could be compatible with the presence of these two bonds which are very close in energy. While this shift to higher BE's for the film with 24 at.% of boron may suggest an increased proportion of sp^3 bonded boron, it is more likely to be a result of increased proportion of B-O bonds.

The C $1s$ spectra of SiBCNO films (cf. Figure 4.2(c)) were clearly asymmetric and very broad which indicates various carbon bonding environments. The characteristic binding energies of C-Si, $C(sp^2)$-C, C-B, C-C, C-H, and $C(sp^2)$-N bonds have been reported to be 283.4 [209,210], 284.5 [137], 284.1 [208], 285.0 [137], 285.0 [137] and 286.0 eV [211,212,213], respectively. The dominant contributions could be attributed to C-Si (component P1) while the minor ones to $C(sp^2)$-C (component P2). The absence of a pronounced feature in the B $1s$ spectra (cf. Figure 4.2(b)) corresponding to B-C bonds suggests that the contribution in C $1s$ spectra is more likely

to be a result of the $C(sp^2)$-C rather than C-B bonds. The tail of the lineshape at about 286.2 eV, which became more prominent in films with higher a B-content points to an increase in the contribution from either $C(sp^2)$-N [211,212,213] and C-O bonds at about 286.2 eV [214].
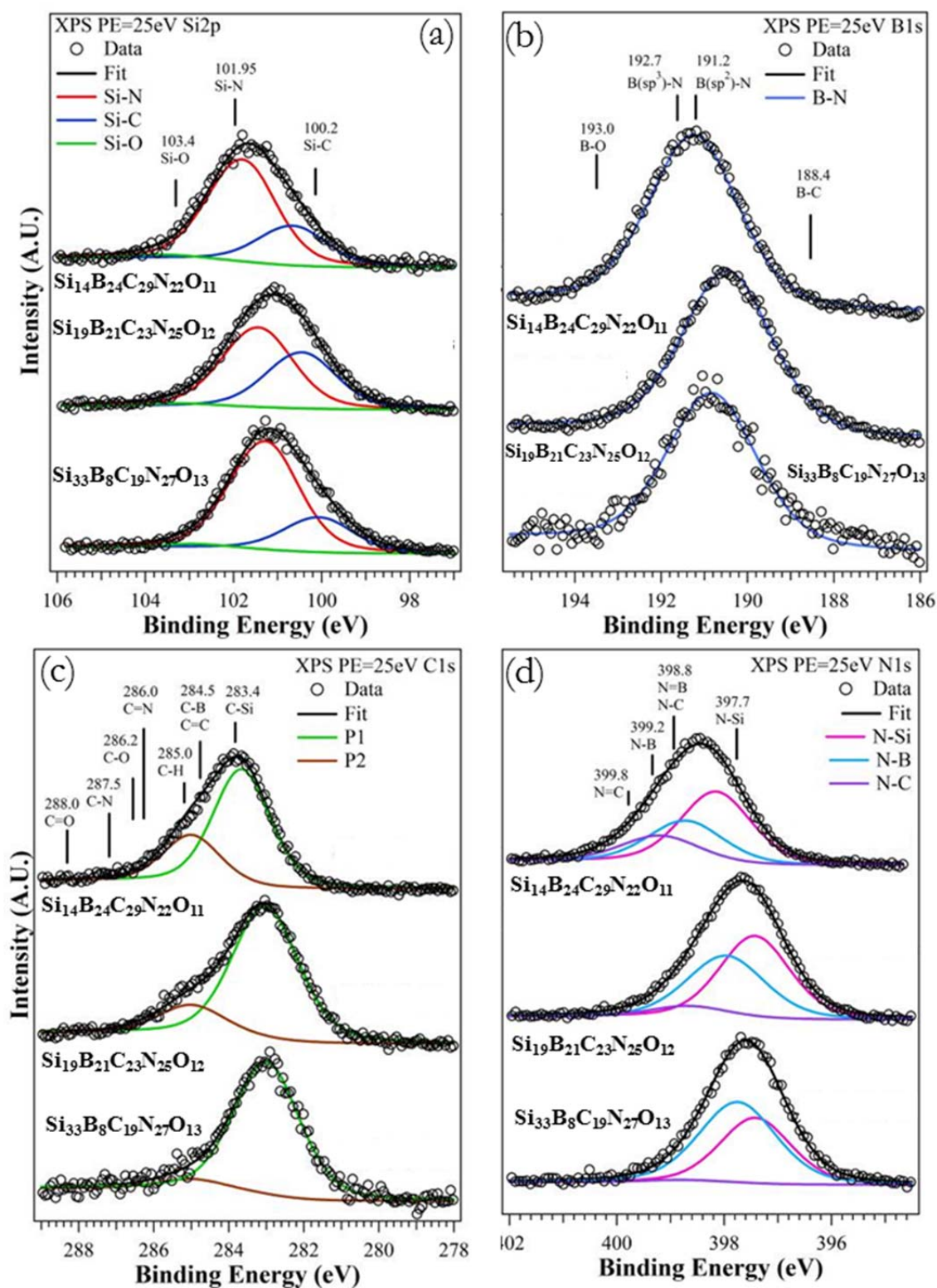

Figure 4.2: XPS photoelectron spectra from the (a) Si 2p, (b) B 1s, (c) C 1s and (d) N1s core levels of three B-containing SiBCNO films with various compositions. Asymmetric peaks are de-convoluted into their constituents.

Similarly, in the boron-free $Si_{40}C_{16}N_{27}O_{13}$ and $Si_{36}C_{22}N_{25}O_{12}$ which were prepared at 1.15 and 5.75 sccm CH_4, respectively, the C 1s peak were centred at 283.45 eV, and were shifted by 1.0 eV to higher energies when compared the carbon-poor $Si_{40}C_8N_{27}O_{10}$ film. This clearly indicates that the majority of carbon in the former two films forms mutual bonds with silicon, while only a minor amount forms graphite-like bonds. While the C 1s peaks maxima in SiCNO films are slightly shifted to a lower energy, indicating increased proportion of C-Si bonds, further additions of CH_4 during film growth clearly moved the binding energy to higher values as can be seen in Figure 4.3(b). This suggests an increased amount of $C(sp^2)$-C multiple bonds in the carbon bonding network.

In the N 1s spectra (cf. Figure 4.2(d) and Figure 4.3(c)), five important bonding states were identified. These were N–Si, $N(sp^3)$–C, $N(sp^2)$–B, $N(sp^3)$–B, $N(sp^2)$–C at 397.7 [209,211,215], 398.8 [208], 398.8 [208], 399.2 [135,208] and 399.8 eV [211,213,216], respectively. It is evident that nitrogen is preferentially bonded to Si and C in all SiCNO and in the boron-poor $Si_{23}B_8C_{19}N_{27}O_{13}$ films. Peak de-convolution of the symmetric N 1s lineshape in these films suggests the presence of two main bonding states with regards to Si and C atoms. Furthermore, films with 21 at.% B featured an N 1s peak which is slightly shifted to a higher energy corresponding to an increased amount of N-B bonding. In contrast, $Si_{23}B_{24}C_{29}N_{22}O_{11}$ with the highest B- and C-content of 24 and 29 at.%, respectively, showed an N 1s lineshape which was shifted by about 1.0 eV to higher energies and was centred at 398.6 eV (cf. Figure 4.3(d)). This indicates a markedly different nitrogen environment to that of the other films, which can characterised by having a significant increase in the proportions of N-B and N-C as opposed to N-Si bonds.

Finally, Figure 4.4 shows that all the measured O 1s spectra can be satisfactorily fitted with a single peak located in the binding energy range 531.6- 532.6 eV. These values are close to the Si-O bonds in silicon oxynitrides at 532.6 eV [206,217] and were shifted to lower binding energies with regards to the Si-O bond in stoichiometric SiO_2 at 532.9 eV [218,219]. In SiCNO films, this binding energy shifted gradually to lower values as the films' carbon content increased. It is also likely for a small amount of B-O to exist in the B-containing film since the binding energy of the O 1s electron in these bonds range between 533.0 eV [220] and 533.5 eV [221], which coincided with the tail of the O 1s peak. However, the absence of strong contributions from these bonds in the B 1s spectra suggests that if these bonds exist, they only form a small part of the oxide bonds. The very small contribution which appears in some of the films at 529.7 eV can also be attributed to adventitious contaminations. The absence of strong evidence of the formation of B-O and C-

O bonds from the corresponding spectra suggests that oxygen can be incorporated in the bonding network mainly via the formation of Si-O bonds.
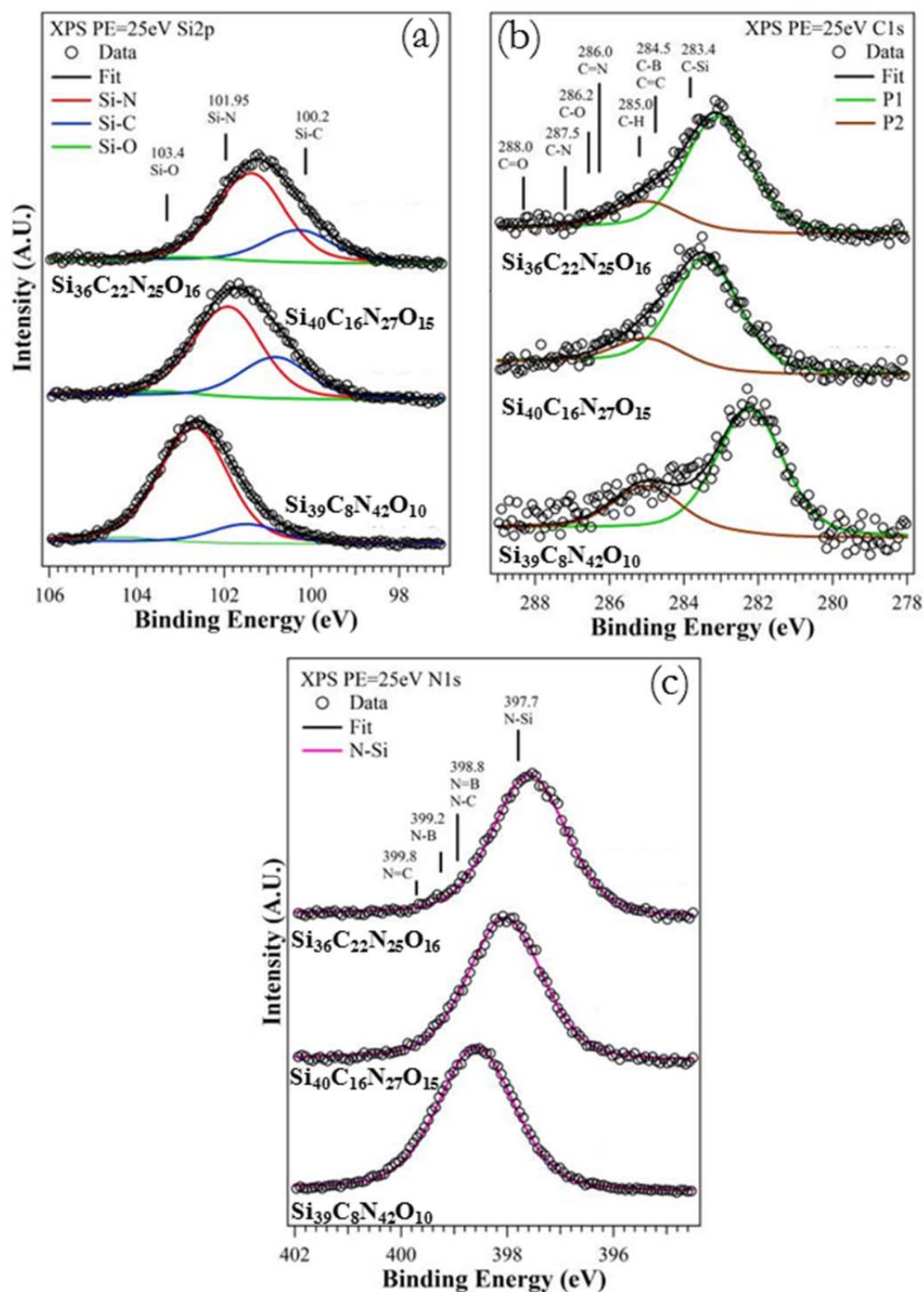

Figure 4.3: XPS photoelectron spectra from the (a) Si 2*p*, (b) C 1*s*, and (c) N 1*s* core levels of three B-free SiCNO films with various compositions. Asymmetric peaks are de-convoluted into their constituents.
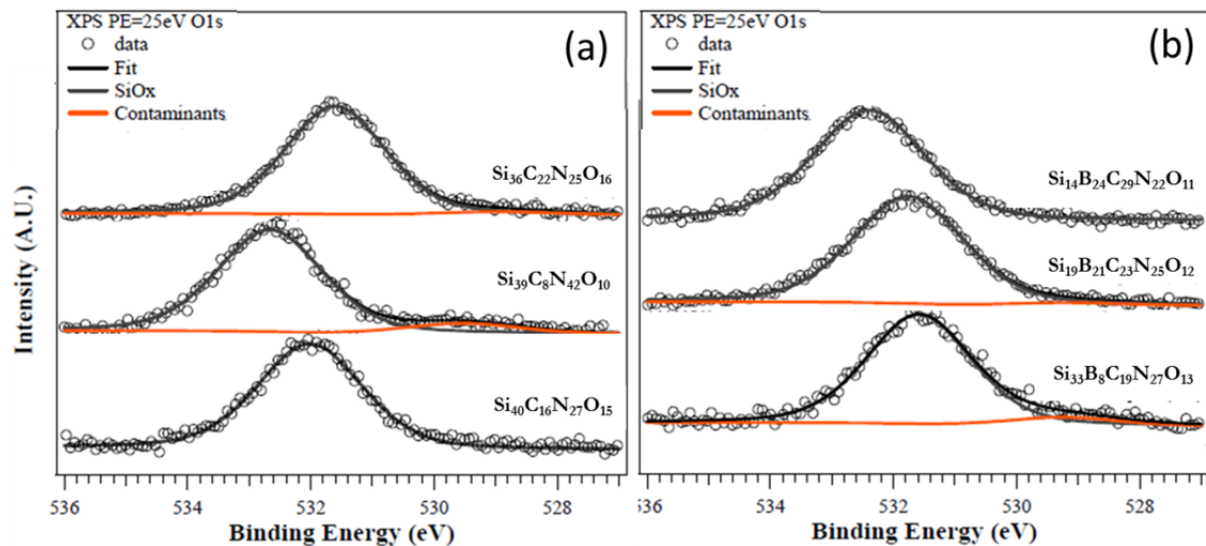
Figure 4.4: XPS photoelectron O 1*s* spectra obtained from (a) SiCNO and (b) SiBCNO films with various compositions.

4.2.2   Fourier-Transform Infrared Spectroscopy

Absorption FTIR measurements were performed in order to further characterise the chemical bonding structure of the films. The FTIR absorption spectra were corrected by subtracting the absorption of a bare silicon wafer substrate. Figure 4.5(a) illustrates that the absorption spectra of SiCNO films consist of one main strong broad absorption band in the region 600- 1050 cm^{-1} as well as a minor and weak band at about 2200 cm^{-1}. The main feature is typical for both Si-C and Si-N bond vibrations which are commonly observed in SiC (796 cm^{-1}) [222] and Si$_3$N$_4$ (846, 947 and 1021 cm^{-1}) [223]. The high intensity of this band suggests that the aforementioned bonds dominate the film structure. However, this band has quite a large FWHM of about 230- 300 cm^{-1} when compared to that of Si-C in SiC and Si-N in Si$_3$N$_4$, which are reported to be about 40 cm^{-1} [224] and 140 cm^{-1}[225], respectively. Such significantly broad absorptions are expected due to the films' amorphous state and the consequent bond-angle distortions [211] as well as the presence of possible contributions from Si$-$CH$_3$ rocking or wagging modes [135,209,211,215], all of which makes it difficult to give an unambiguous peak assignment. Nonetheless, Figure 4.6(a) shows that the main absorption band for the C-poor Si$_{39}$C$_8$N$_{42}$O$_{10}$ is located at 886 cm^{-1} as opposed to 861 and 851 cm^{-1} for Si$_{40}$C$_{16}$N$_{27}$O$_{15}$ and Si$_{36}$C$_{22}$N$_{25}$O$_{16}$, respectively. This systematic red-shift to lower frequencies correlates well with increasing the films' carbon content which indicates an increasing proportion of Si-C bonds. On the other hand, two shoulders can be observed in the higher frequency side at about 1098 and 1296 cm^{-1}. While the first can be assigned to the Si$-$O stretching band [261-267], bonds of the type (CH$_{2-3}$)C$_{1-3}$-Si can also have

contributions in this region [135,209,211, 226 , 227]. The second shoulder at 1296 cm^{-1} corresponds to the stretching vibrations of C-N bonds [227].

The absorption spectra of SiBCNO films, which were grown by increasing the film's B-content are shown in Figure 4.5b. Two strong and broad absorption bands in the regions 600- 1050 cm^{-1} and 1100- 1700 cm^{-1} can be observed. The former band corresponds to mainly Si-C and Si-N stretching vibrations similar to those detected in SiCNO films. Two peaks can be distinguished in this region at about 845 and 970 cm^{-1}. The relative intensity of the latter increases for films with higher B-content and may be associated with Si-N modes. The 1100- 1700 cm^{-1} region is common for B-C bond vibrations at around 1200 cm^{-1} [228,229] and for both C-N [230] and B-N [231] bond vibrations in the region 1300-1500 cm^{-1}. There is a systematic increase in the intensity of the absorption bands in around 1300 cm^{-1} which is proportional to the increase in both B-N and B-C bonds fraction. Such a broad band (FWHM ~ 260- 340 cm^{-1}) was observed in amorphous hydrogenated boron nitride [232] and can therefore be attributed to an amorphous sp^2-bonded BN. Besides, the absorption maxima, which were red-shifted by about 70 cm^{-1} in comparison to h-BN are to be expected from a highly defective and distorted BN phase [233].
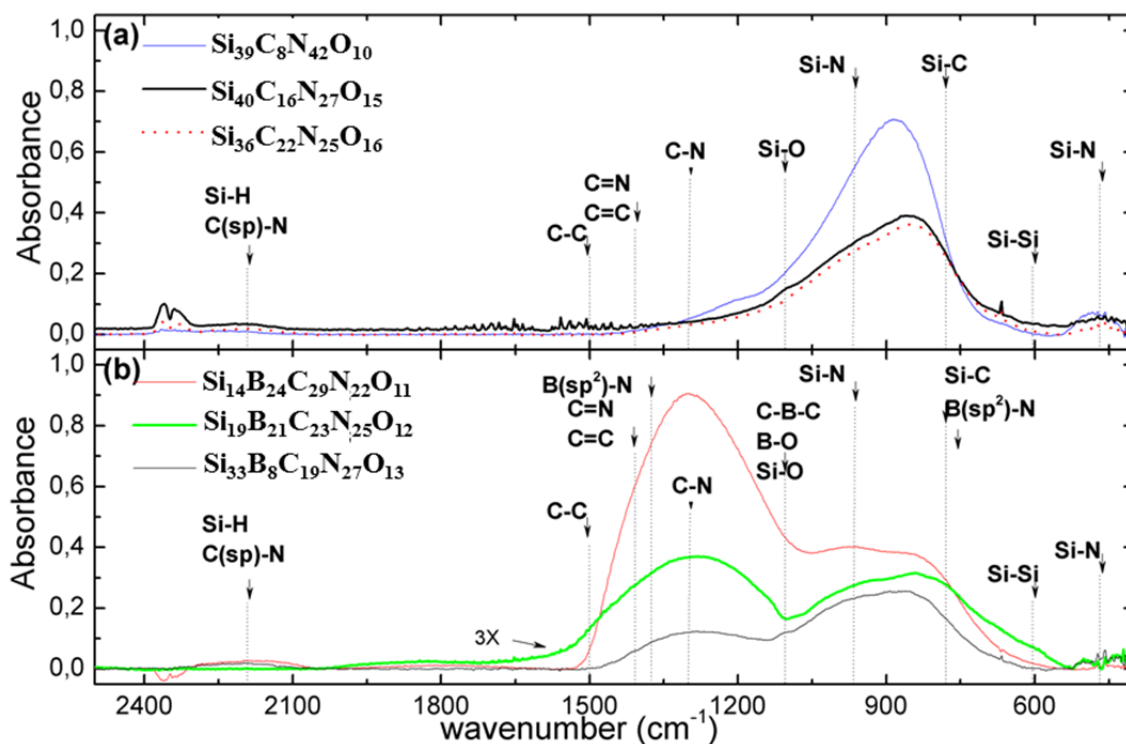

Figure 4.5: FTIR absorption spectra in the spectral range 400- 2500 cm^{-1} of various (a) SiCNO and (b) SiBCNO films with various compositions.
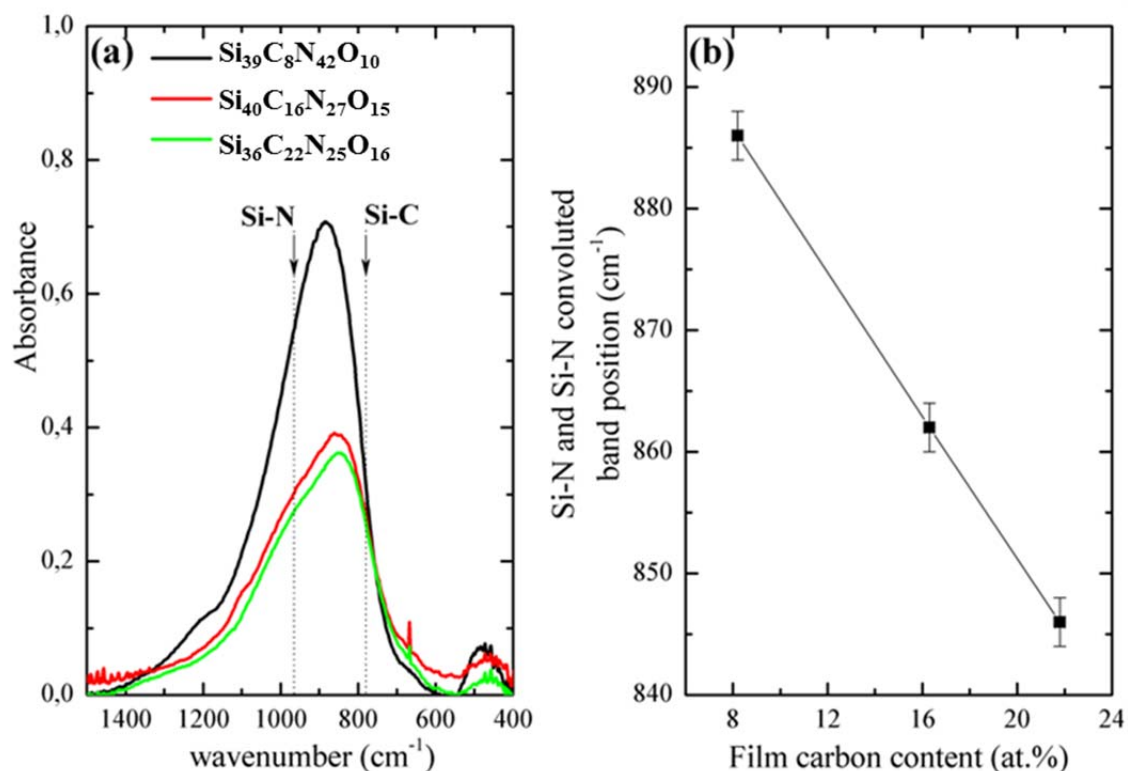
Figure 4.6: (a) The spectral region 500- 1500 cm⁻¹ in the FTIR absorption spectra of SiCNO films with various carbon content. (b) The shift in the convoluted absorption band which corresponds to Si-N and Si-C bonds as a function of the film carbon content as determined by XPS.

Finally, the weak and broad absorption observed at 2200 cm⁻¹ in all spectra can be assigned to sp-bonded C≡N [213,234, 235]., asymmetric stretching modes of N=C=N bonds as well as Si-H (2180 cm⁻¹) [236,237]. However, the presence of weak and broad absorption around 3700 cm⁻¹ and 3330 cm⁻¹ that are typical for bonds of the type Si-O-H [238,239] and N-H [240], respectively, may suggest that these films contain a certain amount of hydrogen. This hydrogen could either be in the bulk of the film or in the form of surface contaminations that could result from the residuals of the silicon precursor which was used in the deposition. No absorptions that could be related to C-H bonds around 2900 cm⁻¹ [239]. Although the amount of hydrogen inclusions in these films could not be quantified, it is likely that they are small due to the fact that the films were deposited at elevated temperatures (~ 900°C), a fact which was indeed confirmed upon examining the respective regions of all spectra (cf. Figure 4.7).
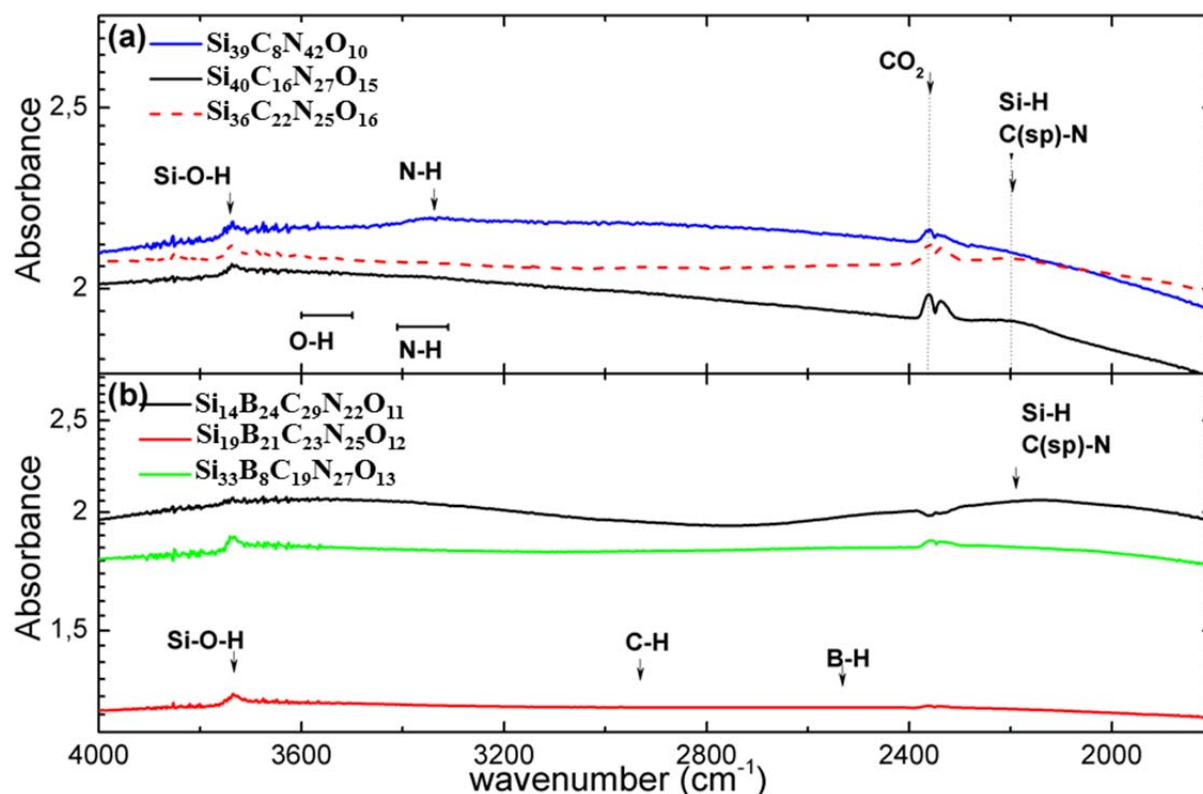
Figure 4.7: FTIR absorption spectra in the spectral range 1800- 4000 cm^{-1} of various (a) SiCNO and (b) SiBCNO films with various compositions.

4.2.3 Time-of-Flight Secondary Ion Mass Spectrometry

Qualitative ToF-SIMS analyses are particularly useful in revealing the compositional characteristics of surfaces, and in identifying variation trends in chemical composition as a result of changes in film deposition parameters. With this in mind, both surface spectra and depth profiles were collected and variations in signal intensities of a large number of secondary anions, which were generated as a result of sputtering with a Bi^+-primary ion beam were recorded. Here, two sets of films consisting of three SiCNO films (**SiCNO1**, **SiCNO2**, and **SiCNO3**) and three SiBCNO films (**SiBCNO1**, **SiBCNO2**, and **SiBCNO3**) of various compositions were studied. An initial examination of the collated ToF-SIMS spectra reveals that the vast majority of the resultant secondary ions are detected in the range of 1- 200 amu/z and that very little information can be gathered from the high mass number fragments. The intense peak at 209 amu/z corresponds to Bi^+ ions emanating from ion implantation in the surface as a result of the direct current (DC) cleaning stage of the surface prior to collecting the spectra. While both surfaces mostly share the same kind of species, which appear as secondary ions, the most noticeable difference lies in the B-containing species.

Although the spectra appear to be complex as they contain a large number of fragment peaks, there are distinct differences that can be seen at specific major peaks. Figure 4.8 shows selected portions obtained from the negative ToF–SIMS spectra of six films with various compositions. The peaks at 26.002, 39.976, 41.98, 42, and 69.957 amu/z, which correspond to the secondary anions: CN^-, SiC^-, SiN^-, CNO^- and Si_2N^-, respectively, are clearly more abundant in all SiCNO films. The intensities of all Si-containing secondary anions are noticeably higher in SiCNO films than with in their B-containing counterparts. Unlike in SiBCNO, the spectra from B-free films have no signals related to B-containing anions with both spectra showing clearly distinct patterns. The peaks at 21.02, 23.009, 25.012, 35.008, 36.021, 41.008, 42.999, and 61.03 amu/z, which correspond to the secondary anions: B_2^-, CB^-, BN^-, BC_2, BNC^-, BNO^-, BO_2^-, and BNC_3^-, respectively, are distinctly found in the three SiBCNO films. Despite their low intensities, high mass fragments prove particularly useful in highlighting the differences between both film types. Figure 4.8 shows that peaks at 66.0222, 68.0131, 75.025, 77.0298, 103.03, 110.05, and 115.03 amu/z are unique to the SiBCNO films. These peaks are related to the BN species and represent the secondary molecular anion: $SiCBNH^-$, $B_4N_2^-$, $(BN)_3^-$, SiC_2BN^-, $(BN)_3N_2^-$, $(BN)_3BC_2^-$, and $(BN)_3CN_2^-$, respectively. An additional set of peaks, which are unique to SiBCNO films are located at 91.0321, 92.0321 and 93.0311 amu/z. These correspond to the oxygen containing $(BN)_3O^-$, $(BN)_3OH^-$, $(BN)_3OH_2^-$ secondary anions. Signal intensity variations in the obtained ToF-SIMS spectra were also in accordance with the elemental composition of the film, whereby the intensities of the former peaks are highest in the B-rich films (**SiBCNO1** and **SiBCNO2**). Figure 4.9 shows how the signal intensities of a number of secondary anions increase linearly with increasing the film's C-content. It is also interesting to observe that the signals intensities of $SiOH^-$ and BNO^- are lower with films having higher C-content.
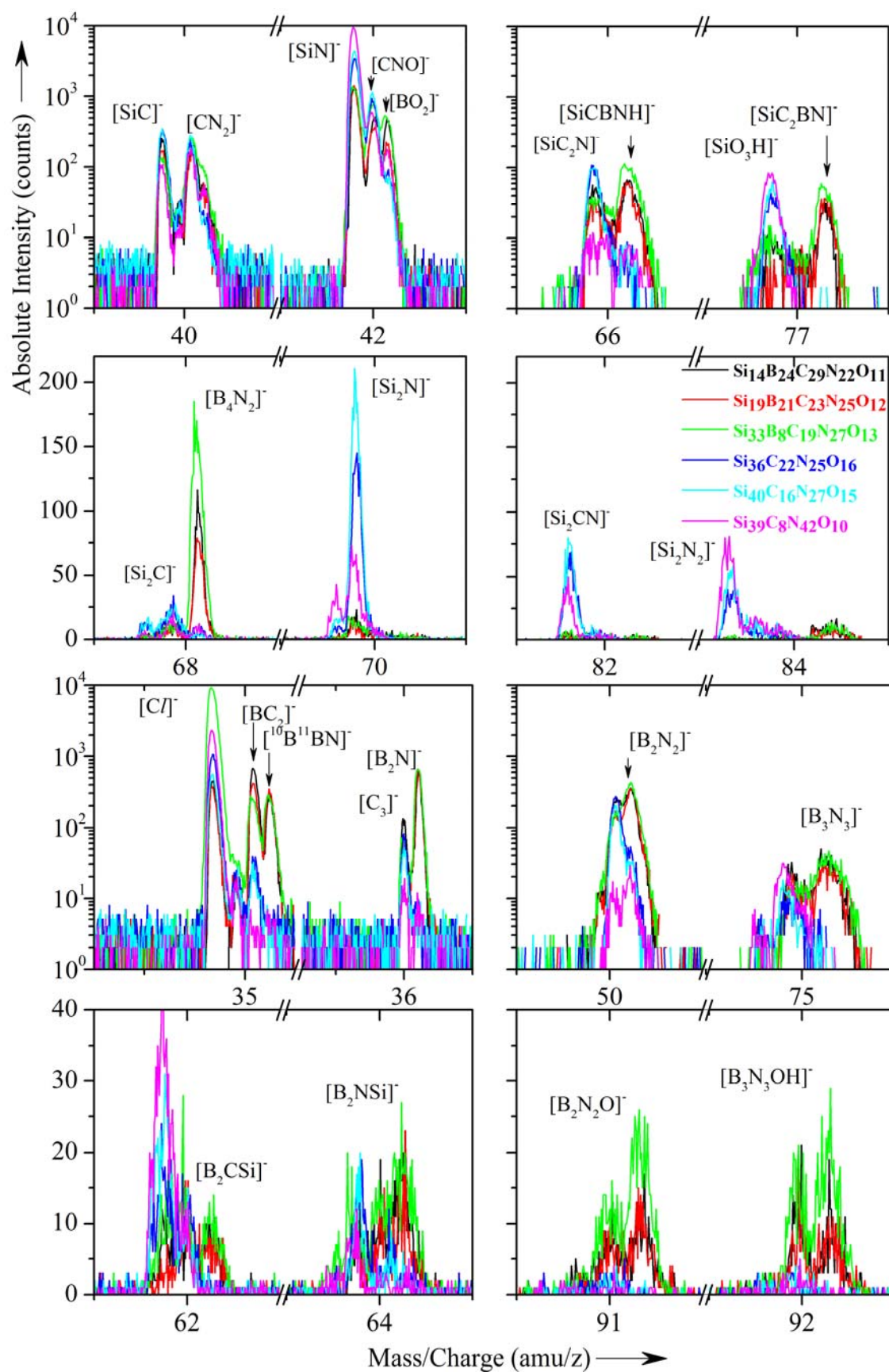
Figure 4.8: Selected portions of the negative ToF-SIMS spectra obtained from SiCNO and SiBCNO films.

It was also observed that the fragmentation pattern of the film was in agreement with the chemical bonding information obtained from both XPS and FTIR spectroscopy. The B-containing secondary anions which were observed in the ToF-SIMS spectra of the three SiBCNO films (**SiBCNO1**, **SiBCNO2**, and **SiBCNO3**) such as BN^-, $(BN)_3^-$, $(BN)_3N_2^-$ were correlated with the BN bonds represented by XPS (BE B $1s$ 190.5- 191.3 eV) and FTIR bands in the region of 1300- 1400 cm^{-1} (cf. Figure 4.5(b)). On the other hand, the secondary anion fragments at 41.0135, 51.977, 53.98, 54.98, 63.97, 65.98684, 67.95, 69.9587, 79.95673, and 81.9605 amu/z which are attributed to CN_2H^-, SiC_2^-, $SiCN^-$, $SiCNH^-$, SiC_3^-, SiC_2N^-, Si_2C^-, Si_2N^-, $Si_2C_2^-$, and Si_2CN^-, respectively, appeared to be most considerable with the two C-rich SiCNO films (**SiCNO1**, **SiCNO2**). These correlate well with the IR bands in the region of 780- 990 cm^{-1}, where Si-C and Si-N stretching vibrations are seen (cf. Figure 4.5(a)). Additionally, the ToF-SIMS spectra that were obtained from the C-poor SiCNO films (**SiCNO3**) revealed that peaks relating to Si_xN_y and $Si_xN_yO_z$ secondary anions were the most prominent. The intensity at 15.011, 29.996, 41.9802, 42.98, 43.97, 44.97995, 57.977, 58.9829, 59.99416, 86.95866, and 100.96988 amu/z, which are attributed to NH^-, NO^-, SiN^-, $SiNH^-$, SiO^-, $SiOH^-$, $SiNO^-$, $SiNOH^-$, $SiNOH_2^-$, Si_2NOH^-, and $Si_2N_2OH^-$, respectively, are highest in $Si_{39}C_8N_{42}O_{10}$ (**SiCNO3**). Thus, it is clear that the C-containing secondary anions appear to be minor in comparison to the C-rich SiCNO films. Consequently, FTIR spectra from these films showed a clear bias of the band at around 900 cm^{-1} towards higher frequencies as would be expected from silicon nitride.
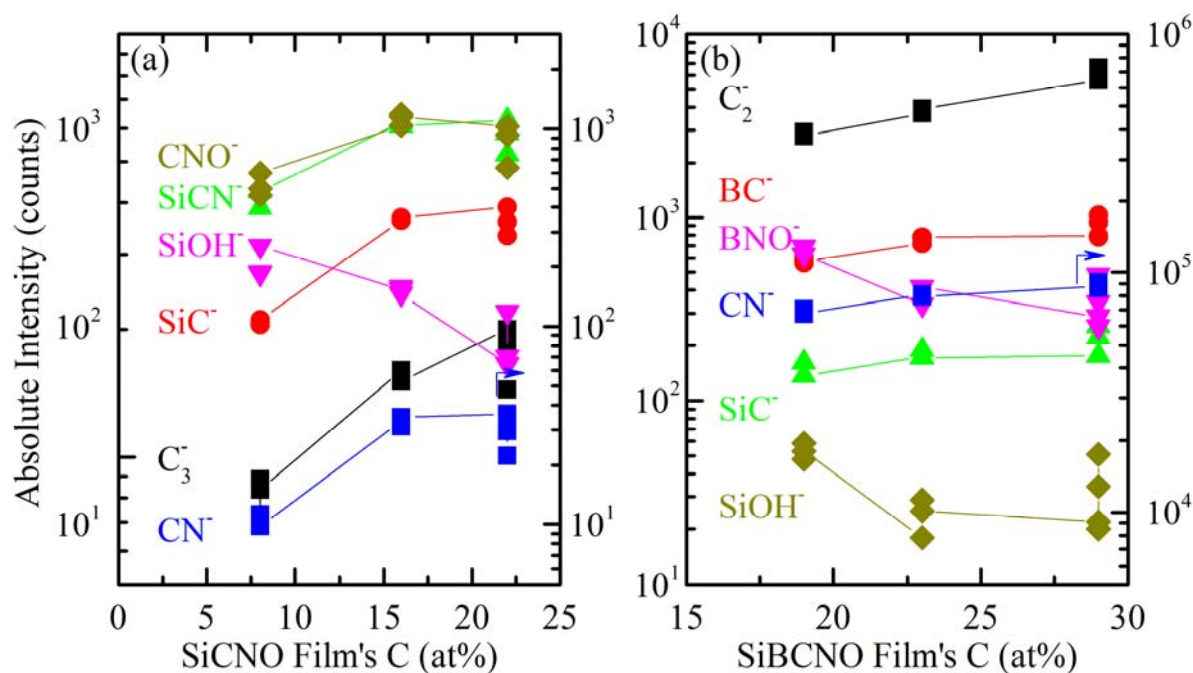

Figure 4.9: Variation of absolute signal intensities of selected secondary anions versus the change in the film's carbon content (a) SiCNO and (b) SiBCNO films.

4.2.4   The Application of Principal Component Analysis

ToF-SIMS data prove invaluable in highlighting the changes to film composition as a result of variations in the flow rates of the reactant gases during deposition. Although small, such chemical composition variations can be discerned from the films' ToF-SIMS data only when the entire spectrum is thoroughly examined. So far in this work, only selected parts of the ToF-SIMS spectra were considered, which provide a limited view of the complex data contained within these spectra. Using direct comparison only to capture the changes, which occurred to the spectral features as a result of variations in film composition, is a lengthy exercise. Therefore, to investigate such differences, two types of MVA will be implemented; HAC and PCA, in order to quantitatively visualise the relationship between film composition and their ToF-SIMS spectra.

Prior to performing MVA, all spectral data are subjected to pre-treatment. This ensures that the ToF-SIMS spectra, which were obtained from each sample, were background corrected to remove unnecessary high background noise so as to extract a pure peak intensity. This was particularly strong at the low amu/z range in the spectra. Fragment peaks which have S/N ratio of more than 3 were then selected and their intensities were normalised. A matrix was then constructed from the experimentally obtained data, which consisted of normalised fragment peaks which were represented by columns whereas film types were represented by rows. No mean-centring was used in this section. Before implementing PCA, HAC was used to group the ToF-SIMS spectra obtained from six different films. In PCA, the resulting clusters were then visualised in new sets of axes (Principal Components) to highlight the similarities and differences between the films. It should be mentioned that despite the fact that PCA could be directly used to analyse the spectra, the usefulness of implementing HAC as a preliminary step lies in the fact that it eliminates any bias by the analyser when grouping the films. The resulting grouping (clustering) is solely based on variations in the ToF-SIMS spectra of the films rather than by the analyser's preconceived notions regarding the films. As a result, after HAC and PCA, the clustered spectra were projected onto a new set of axis that highlighted the highest variations in the data. This was used to correlate the changes in film composition and ToF-SIMS spectral features. The hierarchical clustering of secondary anions is shown in Figure 4.10. The clusters are represented by a structure (commonly referred to as a dendrogram) that resembles the shape of a flowchart. The top of the flowchart represents the cluster grouping of the spectral data and the bottom of the chart represents each collated. The spectra are separated into two main groups; B- and non-B-containing films which are represented by green and red colours, respectively. This distinction is evident at the first branching, indicating that it is the most characteristic feature

among the 19 ToF-SIMS spectra. In order to distinguish between the films, a total of four clusters (sub-classes) were chosen by cutting off the dendogram at the second level as can be seen in Table 4.2 and Figure 4.10.

HAC 1	HAC 2	HAC 3	HAC 4
31.6%	**15.8%**	**15.8%**	**36.8%**
$Si_{36}C_{22}N_{25}O_{16}$	$Si_{39}C_8N_{42}O_{10}$	$Si_{33}B_8C_{19}N_{27}O_{13}$	$Si_{14}B_{24}C_{29}N_{22}O_{11}$
$Si_{40}C_{16}N_{27}O_{15}$			$Si_{19}B_{21}C_{23}N_{25}O_{12}$

Table 4.2: A summary of the hierarchal clustering resulting from cutting off the dendrogram at this second level. The percentages representing the fractions of the total data represented by the each cluster (sub-class) are also included.
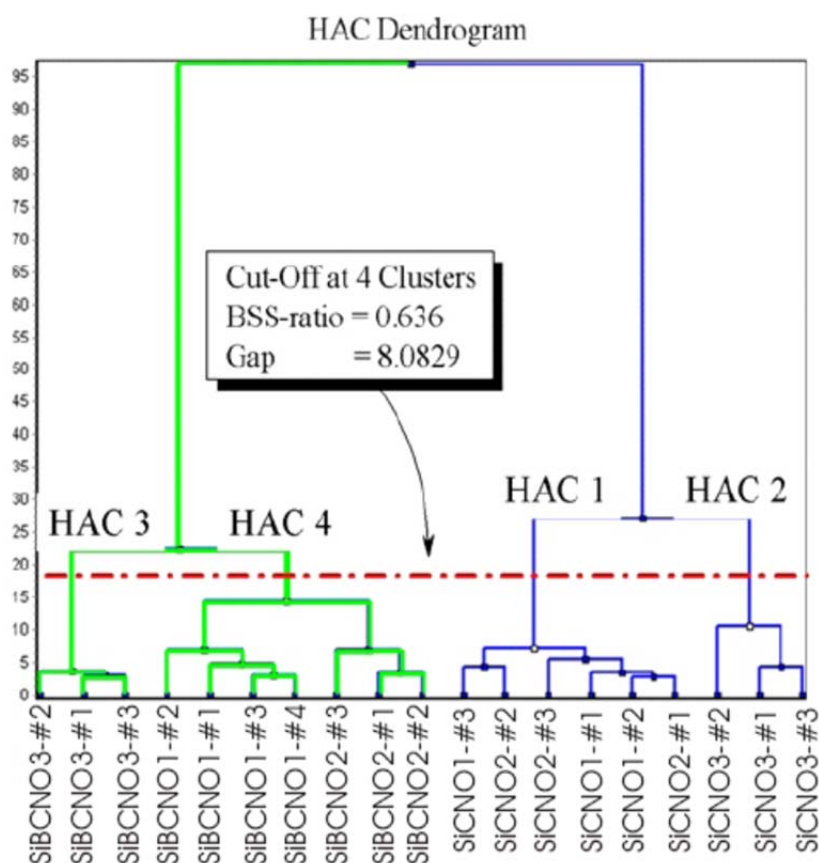
Figure 4.10: The dendrogram showing the separation of SiCNO and SiBCNO films obtained by hierarchical agglomerative clustering (HAC) analysis. The distances between the cluster centres are variance-weighted.

The diagrams which are presented in Figure 4.11(a) and (b) represent the scores and loadings of the three main Principal Components (PC1, PC2 and PC3) which capture 44.2, 19.3 and 10.6% of the variance in the data, respectively and can thereby be used to describe the data adequately. The SiCNO films are located on the right hand side of the diagram while the boron-containing SiBCNO films are located on the left hand side. The loadings diagram indicates the contribution of each variable (amu/z secondary anion peaks) to PC1 and PC2 and its corresponding

distribution in the loadings diagram provides an explanation for the positioning of the films in the scores diagram. In fact, the loadings diagram shows how the variables are divided into two main groups; one with B-containing species and the other without. Secondary anions including 11.009 amu/z (B), 35.007 amu/z (B_2C), 36.024 amu/z (B_2N), and 50.02amu/z (B_2N_2) have negative loadings on PC1 whereas those of 27,977amu/z (Si), 39.976 (SiC), 41.98 (SiN), 53.98 amu/z (SiCN), 54.98amu/z (SiCNH), 67.953amu/z (Si_2C), 69.957amu/z (Si_2N) have positive ones. A similar divide is also evident in the case of high molecular mass species with B-containing secondary anions such as 66.0222 amu/z ($SiCBNH^-$), 68.0131amu/z ($B_4N_2^-$), 75.025 amu/z ($(BN)_3^-$), 77.0298 amu/z (SiC_2BN^-), 103.03amu/z ($(BN)_3N_2^-$), 110.05 amu/z ($(BN)_3BC_2^-$), and 115.03 amu/z ($(BN)_3CN_2^-$), respectively, have negative loadings on PC1. The SIMS spectra of SiCNO appears to be dominated by 79.989amu/z ($Si_2C_2^-$), 81.956 amu/z (Si_2CN^-), 83.96 amu/z ($Si_2N_2^-$), 95.866 amu/z ($Si_2N_2C^-$), 108.9933 amu/z ($Si_2C_2N_2H^-$), and 118.9601 amu/z ($Si_2C_4NH^-$), respectively, which in turn have positive loadings on PC1.

Furthermore, the results of the hierarchal agglomerate clustering, which are superimposed on Figure 4.11(a) show that all six films are remarkably distinguishable based on their ToF-SIMS spectra. While clustering into two sub-classes distinguishes the boron-containing films from those which are B-free, the four-class clustering can further discriminate between the films in a way which reflects their elemental composition. SiBCNO films are divided into two sub-classes; one groups the B-rich films (**SiBCNO1** and **SiBCNO2**) and the other isolates the B-poor ones (**SiBCNO3**) in a similar manner to that the SiCNO films, which are re-grouped into C-rich (**SiCNO1** and **SiCNO2**) and C-poor films (**SiCNO3**) (cf. Table 4.2). This analysis corroborates the results obtained by PCA. In the loadings diagram, the third Principal Component (PC3) which captures 10.61% of the variance in the data provides additional information which corroborates the HAC clustering. The secondary anion peaks which are responsible for re-grouping are shown in different colours in Figure 4.11(b). The B- and C-containing fragments (B_mC_n) populate the lower right-hand side whereas the B-N cones (B_mN_n) and those containing oxygen ($B_mN_nO_l$) are separated and lie in the upper right-hand side with positive loadings on PC3. This explains which kind of fragment are the most prominent in each sub-group. The B-rich films are distinguishable from the rest of the films because they show a greater proportion in (B_mC_n) secondary anions. Similarly, PC3 divides the ToF-SIMS spectra of SiCNO films into two sub-groups such that the anions, namely; those of the types ($Si_mC_nN_l$) and ($Si_mN_nO_l$) have negative and positive loadings on PC3, respectively. The spectra obtained from the C-poor SiCNO films (**SiCNO3**) feature a significantly higher proportion of secondary anions of the types Si_mN_n and $Si_mN_nO_l$ as compared to those which contain carbon such as $Si_mC_nN_l$. A detailed summary of the fragment peaks grouping is listed in Table 4.3.

Cluster	Secondary anion (amu/z values)
HAC 1 (31.6%) $Si_{36}C_{22}N_{25}O_{16}$ and $Si_{40}C_{16}N_{27}O_{15}$ **SiCNO1 and SiCNO2**	CN(26.0060), m(38.00353), Ar(39.9619), SiC(39.9773), C_2O(39.9951) ,CNH_2(41.0135), CNO(42.0023), m(50.00881), SiC_2(51.0179), SiCN(53.98), SiCNH(54.98), Si_2H(56.98528), SiO_2(59.9665), SiC_3(63.97), SiC_2N(65.98684), Si_2C(67.953), Si_2N(69.9587), Si_2NH(70.97929), SiO_3(75.96425), 76.974(76.974), 78.96786(78.96786), Si_2C_2(79.95673), m(79.98983), SiC_2NH(80.99688), Si_2CN(81.9605), SiN_3C(81.9907), SiN_3CH(82.96243), Si_2C_2N(93.96948), m(93.9961), m(162.91119)
HAC 2(15.8%) $Si_{39}C_8N_{42}O_{10}$ **SiCNO3**	NH(15.0110); O(15.995); Si(27.9766); SiH(28.985); NO(29.996); SiN(41.9802); SiNH(42.98); SiO(43.97); SiOH(44.97995); Si_2(55.9552); Si_2H(56.96365); SiNO(57.977); SiNOH(58.9829); $SiNOH_2$(59.99416); m(80.02722); SiN_3B(80.9907); m(82.98637); Si_2N_2(83.93435); Si_2NO(85.95605); 85.9948(85.9948); Si_2NOH(86.95866); m(96.04939); Si_2N_2OH(100.96988); m(103.0006); m(105.00259); m(108.04295); m(109.03944); m(118.90281); m(135.32305)
HAC 3(15.8%) $Si_{33}B_8C_{19}N_{27}O_{13}$ **SiBCNO3**	N(14.02); B_2H_2(24.03115); BO(27.0054); m(31.97149); m(32.97996); 32.99779(32.99779); Cl(34.968); m(36.96612); m(41.00817); m(43.0008); BO_2(42.999); m(44.01217); m(52.01897); 64.02382(64.02382); B_2N_3H(65.02617); B_2N_2O(66.0237); B_2N_2OH(67.021); $B_2N_2OH_2$(68.01495); $B_3N_3H_2$(77.03163); m(78.92011); m(80.91738); 87.98613(87.98613); B_3N_4H(90.03763); m(91.00332); B_3N_3O(91.03521); SiB_2N_3(91.99706); B_3N_3OH(92.03257); $B_3N_3OH_2$(93.02729); B_4N_4(100.03733); B_4N_4O(116.04132)
HAC 4(36.8%) $Si_{14}B_{24}C_{29}N_{22}O_{11}$ and $Si_{19}B_{21}C_{23}N_{25}O_{12}$ **SiBCNO1 and SiBCNO2**	B(10.0000); B(11.0090); C(12.0000); CB(22.0140); CB(23.0090); C_2(24); BN(25.012); B_3(33.022); B_2C(34.007); B_2N(35.025); B2N(36.02187); BNC(37.0223); 38.98591(38.98591); B_2C_2(46.01575); BC_3(47.01093); B_2C_2H(47.02813); 48.01924(48.01924); B_2CNH(49.01483); SiCB(50.98634); B_3C_2(57.02585); B_2C_3(58.02117); 59.01501(59.01501); B_2C_3H(59.02877); B_2C_2N(60.02654); 74.02844(74.02844); $^{10}BB_2N_2C_2$(84.03832); $B_3N_2C_2$(85.03962)

Table 4.3: The peak list which is responsible for grouping the 19 ToF-SIMS spectra into four clusters. The peaks are superimposed on the loading diagram peak list in Figure 4.11(b).
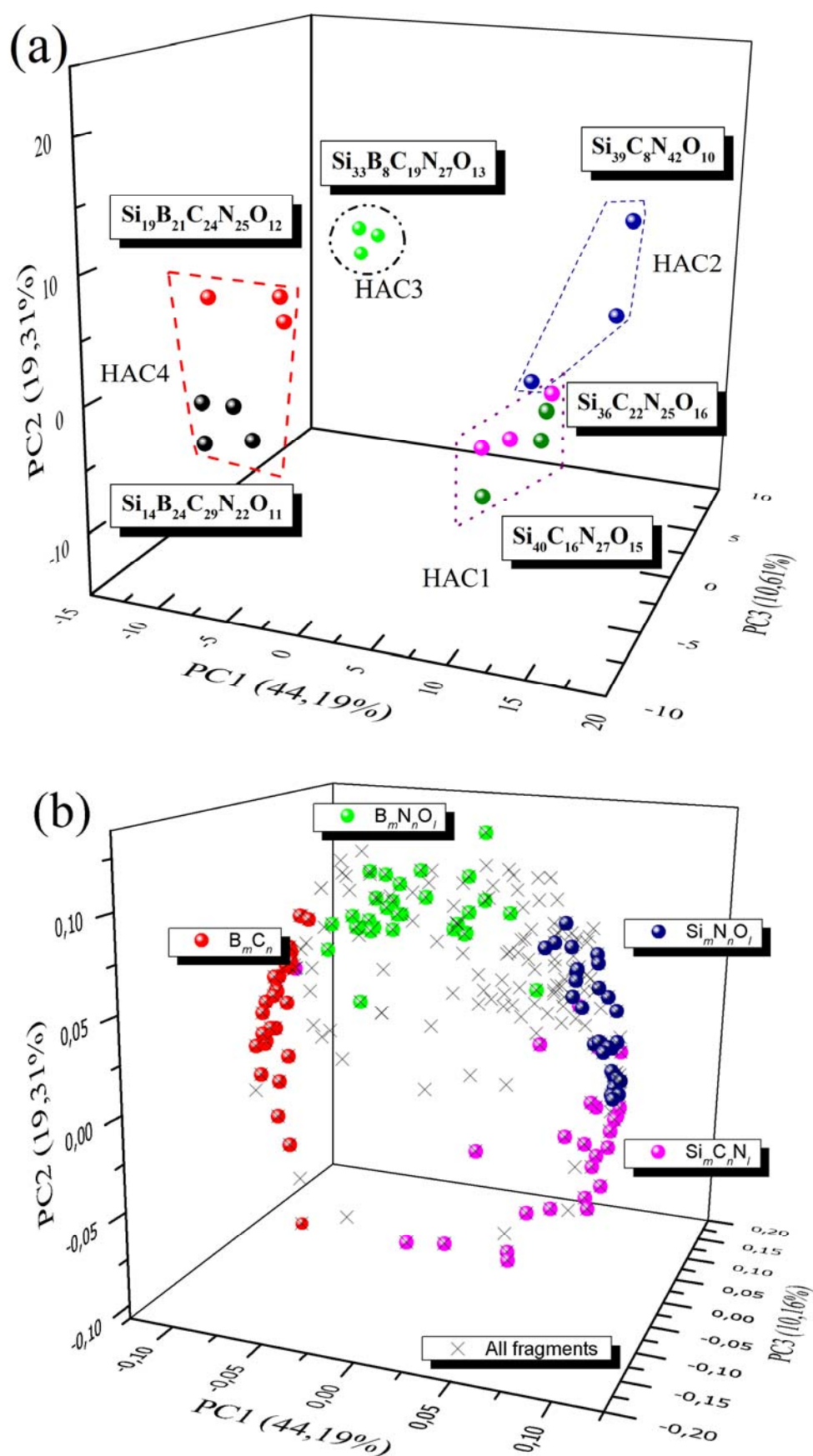
Figure 4.11: The (a) scores and (b) loadings of the first and second Principal Components based on ToF-SIMS surface spectra data extracted from three SiBCNO and three SiCNO films of various compositions.

4.2.5 Comparative Compositional Analysis - Correlations between XPS, FTIR and ToF-SIMS

The section aims to shed more light on the relationship between chemical composition and bonding by examining the various data obtained from a whole host of analytical methods used in this work, namely XPS, FTIR, XRD and ToF-SIMS. The main difficulties, which were encountered when analysing SiBCNO and SiCNO thin films lay in the fact that they consist of light elements and are both totally X-ray amorphous and electrically insulating. Due to these attributes, the analysis of such materials posed several challenges which range from the difficulty of applying straightforward analysis by using Energy-dispersive Spectroscopy due to the fact that these materials were grown in the form of thin films and an interference with the substrate during analysis is inevitable. Despite the fact that applying a multitude of surface sensitive characterisation methods in analysing such materials increases the complexity of the task and is resources-intensive, it is, nevertheless, crucial to obtaining a more comprehensive picture of chemical bonding. Understanding the nature of chemical bonding is central to unveiling the relationships underlying bonding, structure, and synthesis parameters. Such an understanding is curial to designing preparation routes which would yield materials with desirable properties for applications. Also, Using several analytical techniques namely: XPS, FTIR, XRD and ToF-SIMS in the analysis of the films ensures that different volume fractions of these films are probed.

While XPS and ToF-SIMS are highly sensitive to the upper few nanometre of the film surface, both FTIR and XRD probe the whole volume of the grown film. On the other hand, sectioning the film with depth-profiling ToF-SIMS gives information about the homogeneity of the chemical composition and fragmentation pattern of the amorphous materials normal to the film's growth direction. Surface-sensitive FTIR methods such as ATR-FTIR are well-suited to characterising materials with IR-active chemical bonds, this method, however, was not available in the current investigation, which meant that an investigation of the bulk of the films was only possible by FTIR spectroscopy. Nevertheless, when combined with detailed information obtained from XPS and ToF-SIMS, more details about chemical bonding can be revealed.

Treating the negative mode ToF-SIMS spectra using Hieratical Agglomerative Clustering (HAC) resulted in the data, obtained from SiCNO thin films, being divided into sub-groups. The scores of the secondary anions, which contribute to this clustering of the various samples, provide an insight into which bonding species are most prominent in the film.

The ToF-SIMS spectra, which were obtained from the C-poor film with the composition $Si_{38}C_8N_{42}O_{10}$ showed distinctly higher intensities from those of SiN- and SiNO-fragments. This

correlates well with the shift in the binding energy of the Si $2p$ electron to a higher value which indicates that the Si atoms are predominantly bonded to both nitrogen and oxygen. The XPS core level spectrum of the O $1s$ showed similarly dominant Si-O bonds. Also, the blue-shift observed in the FTIR absorption spectra of the band at 886 cm^{-1} is in line with the previous observations reflecting the dominance of the Si-N bonds in the film. Therefore, the core bonding structure in this film can be described as comprising both SiN_x and SiN_xO_y structural units.

On the other hand, both C-rich SiCNO films ($Si_{40}C_{16}N_{27}O_{15}$ and $Si_{36}C_{22}N_{25}O_{16}$) produced ToF-SIMS spectra, which revealed the prevalence of the SiC-, SiCN- and CN-fragments. Similarly, XPS C $1s$ core level spectra were shifted to lower energies indicating an increased proportion of sp^2-bonded C and N in both films. The shift in the binding energies of the Si $2p$ electrons to lower energy signifies the increased contribution of the Si-C bonds. The aforementioned observations correlate well with the red-shift by about 35 cm^{-1} in the main absorption maxima in the FTIR spectra of these two films when compared to that observed in the previous film ($Si_{38}C_8N_{42}O_{10}$). This highlights the diminishing contribution made by the Si-N bonds as well as the increasing contributions from the Si-C bonds. Accordingly, the core bonding structure in these two films can be described as being composed of SiC_x and SiN_x structural units. Additionally there is an increasing contribution from graphitic like C-C and C-N bonds in the films' structure.

With regard to SiBCNO films, a distinguishable pattern was seen when boron was introduced to the bonding network. In the B-poor film with the composition $Si_{33}B_8C_{19}N_{27}O_{13}$, the ToF-SIMS spectra revealed that this film is different from the B-rich films due to the presence of predominantly BN-fragment contributions. This is particularly evident in the high mass secondary molecular anions, in which several fragments with the general formula $(BN)_x$, where x = 1- 4 were detected. Clearly, these are in accordance with the results obtained from the XPS B $1s$ core level spectrum, which showed the presence of B-N bonds in the film. Also, the FTIR absorption band located in the B-N bond vibration region is indicative of the formation of B-N bonds. However, the Si-C and Si-N bonding environments do not vary much from those found in the C-rich SiCNO films. In the B-rich films ($Si_{14}B_{24}C_{29}N_{22}O_{11}$ and $Si_{19}B_{21}C_{23}N_{25}O_{12}$), the addition of further carbon in the film increased the proportion of B-C bonds. Although this was not very clear from the XPS B $1s$ core level spectra, the shift to higher binding energies in the C $1s$ spectra may provide an indication of the increase in the proportion of B-C bonds in these films. However, the ToF-SIMS spectra clearly showed the presence of an increasing proportion of BC- and BCN-fragments in the B-rich films. Because of the very broad absorption in the spectral region corresponding to the B-N and B-C bonds vibrations, the FTIR spectra could not

provide definitive conclusions about the proportion of B-C bonds present in these films. Nonetheless, the detailed analysis of the ToF-SIMS spectra proved very useful in providing clues to the presence of the B-C bond in the films' bonding network. As to the Si-O, Si-C and Si-N bonds in these films, no major differences were detected as compared to the B-free films with both bond types exiting in the film. Therefore, the bonding environments in these films can be described as being composed of SiC_x and SiN_x together with $(BN)_x$ and $(BCN)_y$ structural units. The latter two increased with increasing the films B and C content.

4.3   Film Morphology and Structure

Figure 4.12 illustrates FE-SEM cross-sectional micrographs of several SiCNO and SiBCNO films various compositions. All films showed a typical glass-like fracture with a dense and featureless structure which is to be expected from amorphous films. In addition, the films were strongly adhesive and stable in ambient air, and remain so for several months after deposition without any signs of hydrolysis or delamination.

All the films which were investigated were found to be amorphous and smooth. All X-ray diffraction patterns of the films (cf. Figure 4.13) revealed no reflections other than those of the substrate material, which indicates that the films are of an amorphous structure. In addition, Figure 4.14(a) shows the cross-sectional HRTEM image of a $Si_{33}B_8C_{19}N_{27}O_{13}$ film. Figure 4.14(b) and (c) show the fast Fourier transform (FFT) patterns recorded from the corresponding enclosed areas in Figure 4.14(a). The diffused halo in the FFT pattern in (b) corresponds to the film which appears totally amorphous.

Finally, AFM images (cf. Figure 4.15), which were collected from a 5×5 μm^2 scanned area in a non-contact mode reveal that all the films are extremely smooth as would be expected due to their amorphous structure. Such structure and morphology can be explained in the light of the deposition method used. Due to the ECR's high plasma density and high ion bombardment of the growing surface, amorphous films were always obtained despite the fact that moderately high temperatures were implemented. As a result, both film types can be grown with very low RMS surface roughness of lower than 1 nm and have dense structures.
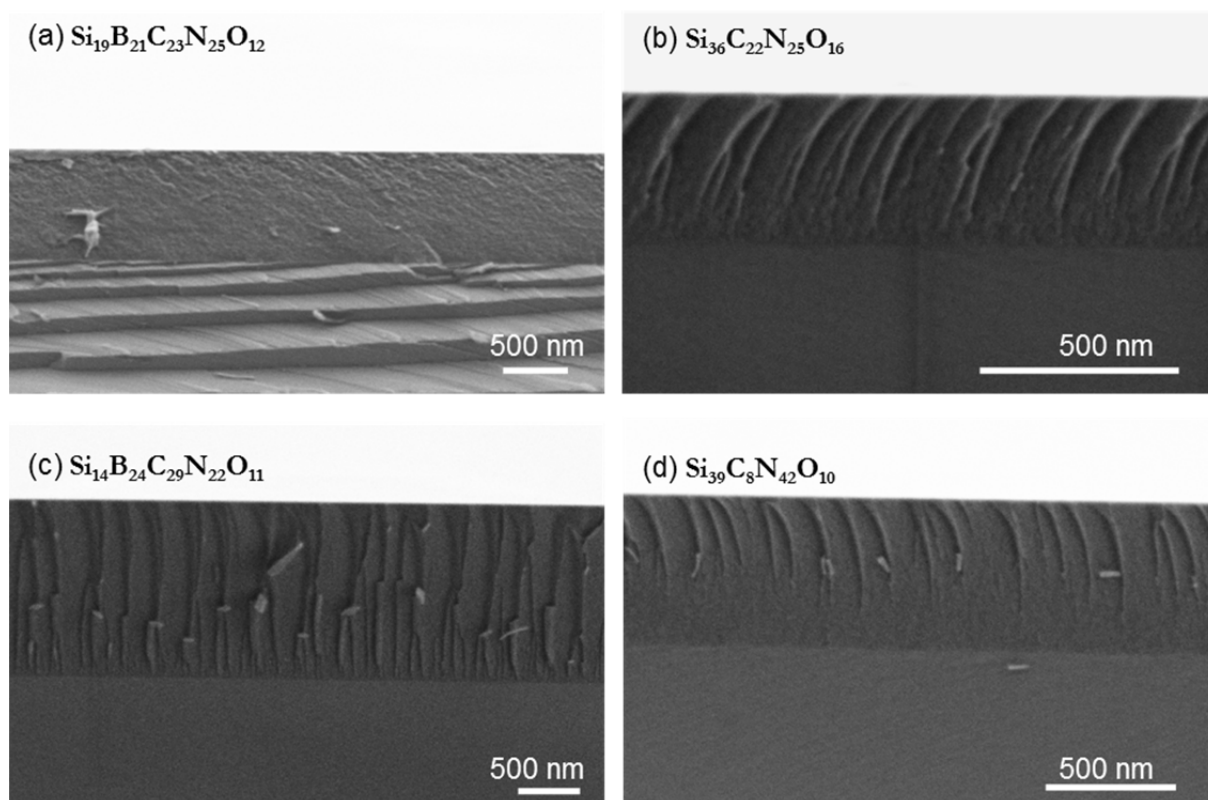
Figure 4.12: FE-SEM fracture cross-section micrographs of (a) Si$_{19}$B$_{21}$C$_{23}$N$_{25}$O$_{12}$, (b) Si$_{36}$C$_{22}$N$_{25}$O$_{16}$, (c) Si$_{14}$B$_{24}$C$_{29}$N$_{22}$O$_{11}$, and (d) Si$_{39}$C$_{8}$N$_{42}$O$_{10}$ films.
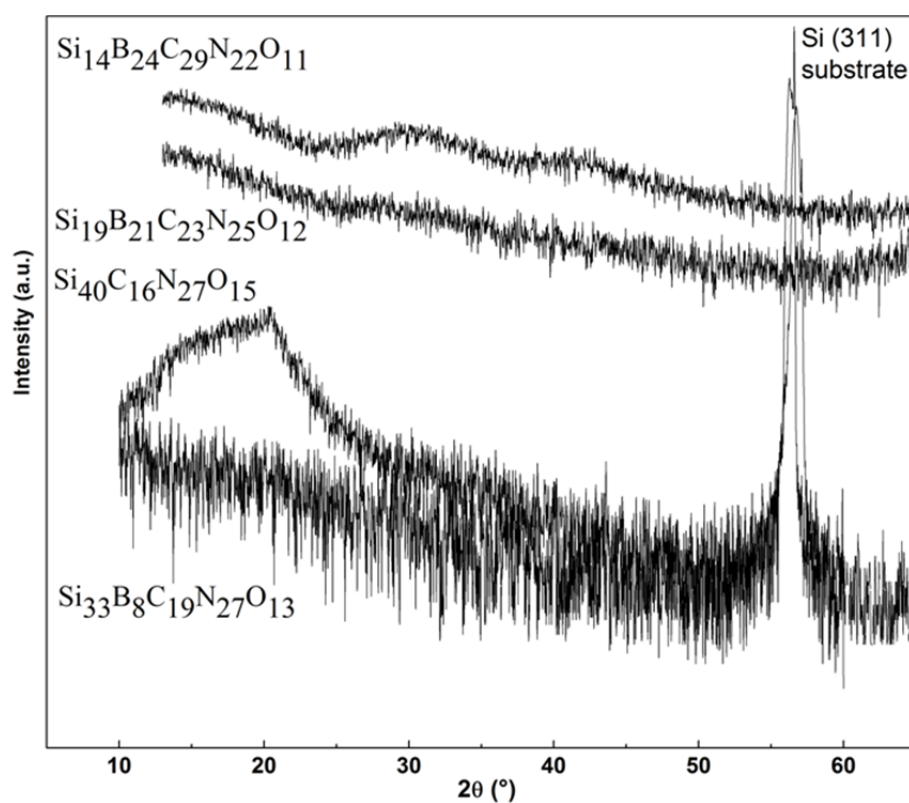

Figure 4.13: X-ray diffraction patterns of some of the as-deposited films grown on single crystal silicon substrates.
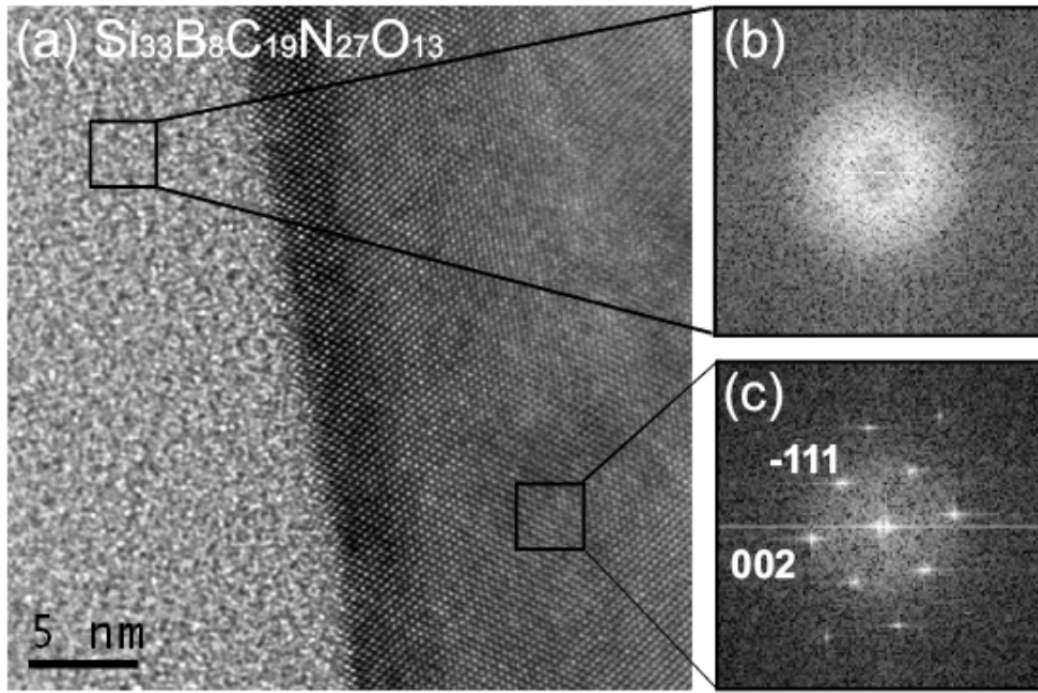
Figure 4.14: (a) A cross-sectional HRTEM image of $Si_{33}B_8C_{19}N_{27}O_{13}$. The squares outline the regions used for FFT where (c) and (d) are the FFT corresponding to a region in the film and a region within the silicon (100) substrate, respectively.
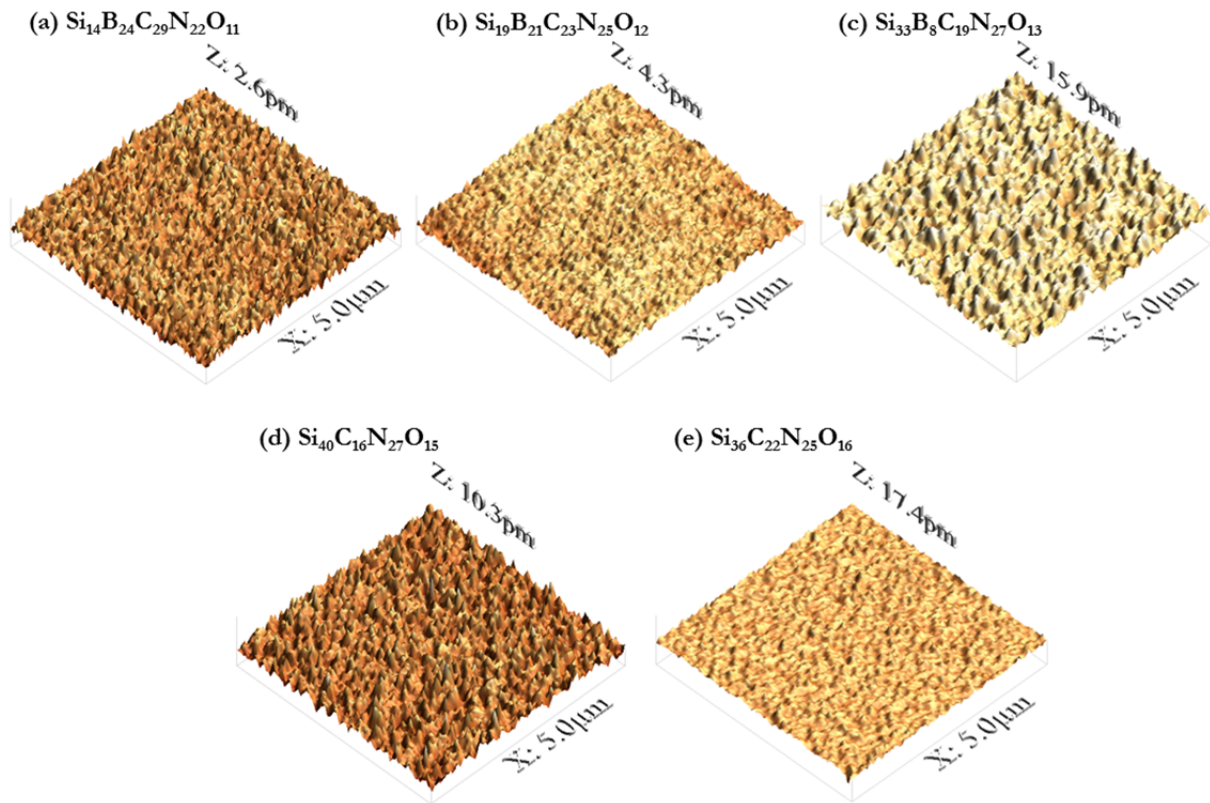
Figure 4.15: 5×5 μm² AFM images showing the surface morphologies of: (a) $Si_{14}B_{24}C_{29}N_{22}O_{11}$, (b) $Si_{19}B_{21}C_{23}N_{25}O_{12}$, (c) $Si_{33}B_8C_{19}N_{27}O_{13}$, (d) $Si_{40}C_{16}N_{27}O_{15}$, and (e) $Si_{36}C_{22}N_{25}O_{16}$. The Z values correspond to the maximum peak-to-trough amplitude difference of each surface. The corresponding calculated R_{rms} values are given in Table 4.4.

4.4   Mechanical Properties Due to Microstructure.

Nanoindentation measurements were performed with a Berkovich diamond indenter with a calibrated area function (as outlined in section 2.2.5.1). The film properties were taken from indents with maximum indentation depths between 43 and 130 nm, which correspond to less than 10% of the total film thickness. These depths were, however, deep enough such that they were not significantly affected by the film's roughness.

Figure 4.16: Typical nanoindentation load-displacement curves of amorphous Si-B-C-N-O films.

Typical loading/unloading-displacement curves of various amorphous SiCNO and SiBCNO films are shown in Figure 4.16. While the area between t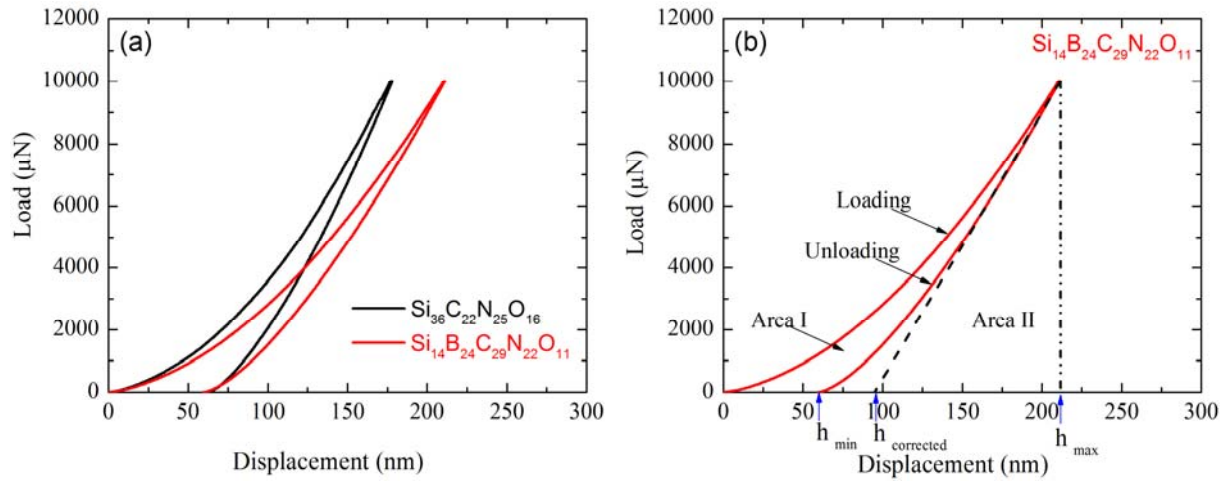he loading and unloading segments of the curve corresponds to the energy dissipated in the film due to plastic deformation, the area under the unloading segment represents the elastic energy for deformation. In addition to the reduced elastic modulus (E_r) and hardness (H) values, values of the film's elastic recovery (W_{el}%) were calculated by integrating both segments of the load-displacement curve. The percentage of the film's elastic recovery can be calculated using the following expression [241]:

$$W_{el} = \frac{W_{el}}{\left[W_{el} + W_{pl}\right]} \times 100\%$$

$$4\text{-}1$$

The values obtained for all films are summarised in Table 4.4. It can be deduced that all the films have a very large elastic recovery as their values lie within the range 90- 97%. This makes them very elastic which have a high resistance to plastic deformation (i.e. high H^3/E_r^2 ratio). Figure 4.17 illustrates how the film mechanical properties change as a function of the B/Si ratio. In general, increasing the B/Si ratio, led to a decrease in both E_r and H values decrease. SiCNO film have reduced modulus (E_r) values in the range 189- 169 GPa while having a hardness of around 24.2($\pm$0.6) GPa, which seems to show no particular trend upon changing the C-content. In

contrast, SiBCNO films exhibit relatively lower reduced elastic moduli and hardness values. Both the hardness and reduced modulus of the B-poor $Si_{33}B_8C_{19}N_{27}O_{13}$ were equal to 23.6($\pm$0.9) and 158($\pm$4) GPa, respectively, which were close to those of SiCNO. However, increasing the film's B-content was linked with a decrease in hardness and reduced moduli reaching a minimum of 18.4($\pm$0.6) and 127($\pm$2) GPa, respectively.

Film	H [GPa]	E_r [GPa]	W_{el}[%]	H/E_r	H^3/E_r^2	R_{rms} [nm]	
$Si_{14}B_{24}C_{29}N_{22}O_{11}$	20.1$\pm$0.4	142$\pm$2	90		0.45	0.22$\pm$0.02	SiBCNO1
$Si_{19}B_{21}C_{23}N_{25}O_{12}$	18.4$\pm$0.6	127$\pm$2	90		0.39	0.23$\pm$0.02	SiBCNO2
$Si_{33}B_8C_{19}N_{27}O_{13}$	23.6$\pm$0.9	158$\pm$4	90		0.53	0.97$\pm$0.11	SiBCNO3
$Si_{36}C_{22}N_{25}O_{16}$	24.2$\pm$0.6	169$\pm$3	93		0.49	0.54$\pm$0.03	SiCNO1
$Si_{40}C_{16}N_{27}O_{15}$	23.2$\pm$0.7	160$\pm$4	97		0.49	0.78$\pm$0.04	SiCNO2
$Si_{39}C_8N_{42}O_{10}$	25.2$\pm$1.4	189$\pm$14	97		0.45		SiCNO3

Table 4.4: A summary of the mechanical properties of SiBCNO films with various compositions.
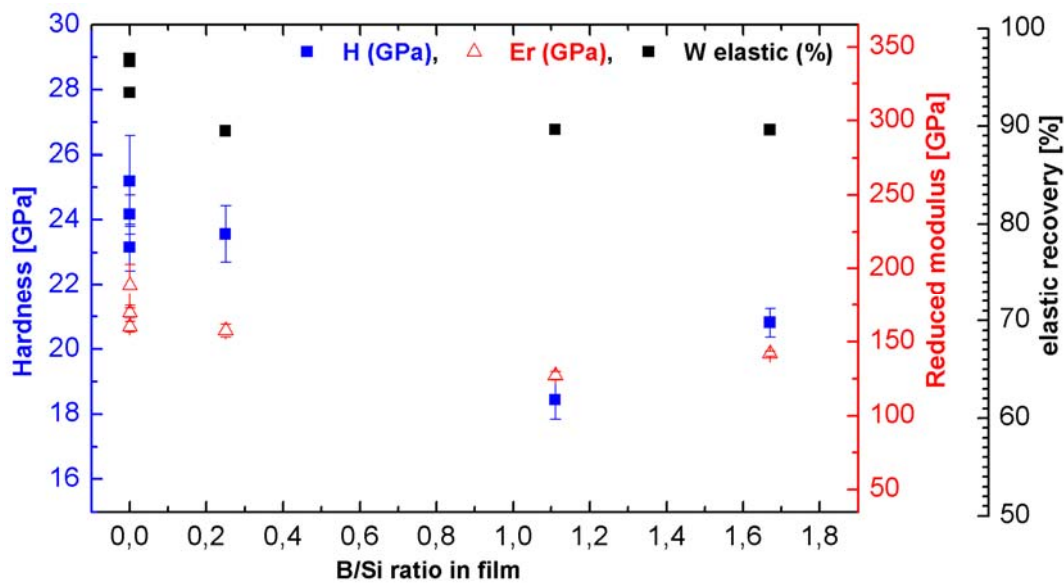
Figure 4.17: The change in the films' mechanical properties as a function of the B/Si ratio.

The drop in H and E_r values in the SiBCNO films is directly proportional to the increase in the amount of their softening B-N bonds. Furthermore, in order to assess the films suitability for tribological applications, the quantities of H^3/E_r^2 and %W_{el}, which correspond to the energy required for plastic deformation and the extent of elastic recovery, respectively, were derived from the nanoindentation results. While both film types exhibited very high elastic recovery, W_{el}% values of SiCNO films were the highest bordering on 97% as compared to those of SiBCNO which were about 10% less elastic. The H^3/E_r^2 values ranged between 0.45 and 0.49

GPa for SiCNO films, whereas SiBCNO containing 8, 21 and 24 at. % B possessed values of 0.53, 0.39 and 0.45 GPa, respectively. The film with the highest elastic strain to failure was SiBCNO prepared with 8 at% B. The result suggests that it may be beneficial to increase the SiCNO film's elasticity slightly by the addition of small concentrations of boron which would not lead to any significant loss in film hardness. As such, this film is more likely to exhibit an improved ability to accommodate applied stresses elastically, and therefore have better resilience. These qualities are highly desirable when applying the film to metallic substrates in practical applications.

4.5   Film Thermal Stability

The high temperature behaviour of the SiCNO and SiBCNO films was examined by means of TGA in an inert Helium atmosphere. As described in section 0, samples of the film-substrate composites were heated up to 1350°C at a heating rate of 5°C/min under a constant flow of Helium. Figure 4.18 shows the mass change of five films with different compositions. In general, no detectable weight loss could be measured in all the samples and the very small mass changes, which were in the range between 1.9% and 3.3%, lay very close to the percentage error of the measurements. The sheer fact that no considerable weight loss is encountered in all the samples indicates that they exhibit significant thermal stability. Furthermore, there seems to be no correlation between the film composition and weight loss. Films which are rich in carbon or in boron show no marked difference in thermal behaviour as a result of the high atomic concentration of either of these two elements.
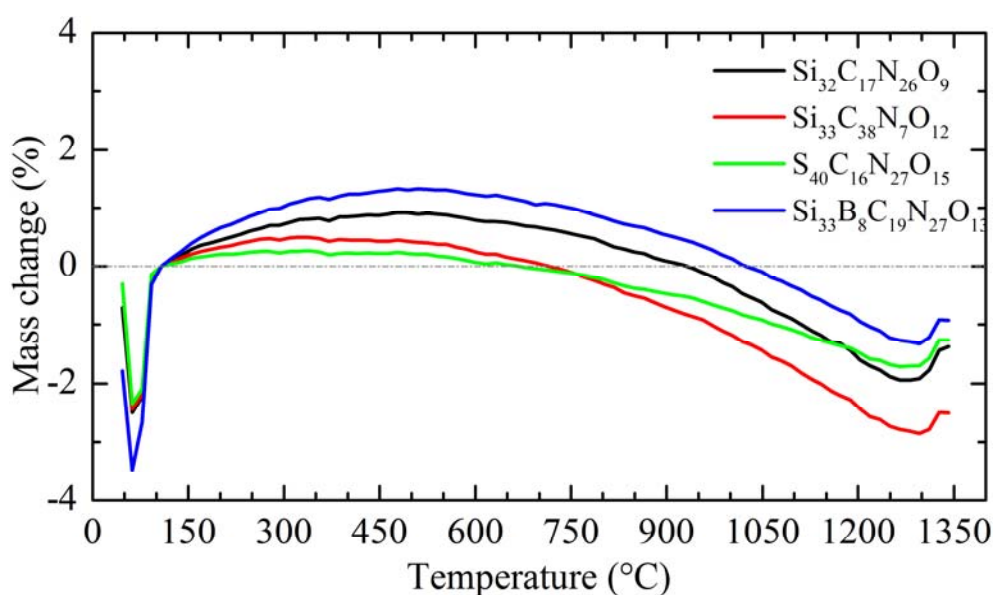

Figure 4.18: TG curves of SiCNO4 ,SiCNO5 ,SiBCNO3, and SiCNO2 measured at a heating rate of 5°C/min in Helium atmosphere.

4.6   Discussion

4.6.1   Influence of Gas Ratio Composition on the Film Composition

4.6.1.1   Addition of Carbon

In these experiments, varying the flow rate of CH_4 and BF_3 have a direct influence on the film carbon and boron contents. Although the silicon-precursor; $Si(CH_3)_4$ contains carbon in the form of a Si-C bond, experiments show that the film retains only a small amount of carbon when only $Si(CH_3)_4$ that is highly diluted in H_2 was used. This indicates that the ionised silane molecules undergo successive gas phase defragmentation in the highly ionising ECR H_2-rich plasma rendering the active $Si(CH_3)_x$ radicals ready to bond with present N_2^+ forming Si-N bonds [242,194]. Without the addition of CH_4 to the gas phase, a carbon-poor film with the composition $Si_{40}C_{16}N_{27}O_{15}$ is deposited. Although all films suffered from significant nitrogen (and oxygen) inclusions due to unavoidable residual and leak gases, increasing the N_2 fraction in the gas phase from 0 to 8 sccm leads to the formation of predominantly Si-N bonds in the film with a the composition $Si_{39}C_8N_{42}O_{10}$, as is evident by both Si $2p$ and N $1s$ core level spectra. Further additions of 1.15 and 5.75 sccm of CH_4 leads to an increase in the carbon content to 16 and 22 at.%, respectively, while the nitrogen content decreases from 42 to 27 and 25 at.%, respectively. Furthermore, the N $1s$ spectra of SiCNO films suggest that the increased carbon content does not significantly form additional bonds with nitrogen. The N $1s$ lineshape shifts to lower energies indicating that nitrogen binds almost exclusively to silicon.

FTIR data did not show an appreciable absorption of C=C bonds due to its well-known reduced efficiency with regards the detection of graphitic carbon bonds [243]. However, it was evident through the systematic red-shift of the main absorption band of SiCNO spectra around 886 cm^{-1}, which was estimated to be about 35 cm^{-1}, that increasing the films' carbon content from 8 to 22 at.% increases the proportion of Si-C bonds. This in turn, means that the addition of carbon to the film is more likely to lead to the formation of Si-C bonds rather than graphitic C=C. Based on both XPS and FTIR data, the main chemical bonding network of SiCNO films is dominated by the tetrahedral SiC_xN_y units with a small amount taking the form of an oxynitride and oxycarbide, which are to some extent connected via sp^2-bonded carbon and nitrogen atoms. A result which is also corroborated by the HAC-PCA analysis of the ToF-SIMS spectra as was seen earlier. In contrast, the carbon network can be viewed as consisting mainly of CSi_x as well as the graphite-like CN and C_2 units.

4.6.1.2 Addition of Boron

SiBCNO films are obtained by the addition of BF_3 during deposition. The H_2 plasma serves to facilitate the reaction between and BF_x and N_2^+ resulting in the formation of B-N bonds. In fact, the experiments which were carried out in this work, as well as those of others have shown that it is only possible to grow a BN phase in the presence of H radicals [100,244]. By increasing the BF_3 flow rate from 0.3 to 1.15 sccm, the film's B-content increases from 8 to 16 at.%, respectively. The B 1s and N 1s core level spectra revealed that the proportion of B-N bonds increased by the addition of BF_3 as marked by the shift in the binding energies of both B 1s and N 1s electrons to higher energies. Boron binds almost exclusively to nitrogen with little to none B-C bonds detected. In addition, the shift in the peak maxima of about 0.8 eV (from 190.5 to 191.3 eV) may be attributed to an increase in the amount of sp^3 B-N as opposed to sp^2 bonds. It would be expected that the proportion of B-C bonds to increase significantly in the absence of nitrogen. However, it is not exactly clear from these experiments how this may take place as it was not possible to exclude it from the plasma during deposition.

The increased proportion of Si-N bonds in all SiBCNO films, particularly in $Si_{14}B_{24}C_{29}N_{22}O_{11}$, which is evident from shift in the binding energy of Si 2p electrons to higher energies, may be attributed to an increase in (BN)-Si bonds via single bonds with nitrogen. The increased intensity of the 970 cm^{-1} peak in the FTIR spectra, which is associated with increasing the B-content supports this argument. This partial occupation of silicon bonding states by nitrogen forces the formation of C-C mutual bonding which is evident in the C 1s spectra by the slight shift in the binding energy to a higher energy. As with boron-free films, the N–Si bonds seem to dominate for nitrogen atoms at lower proportions of N–B and N–C bonds. This feature is a stark contrast to SiBCNO films which were prepared by PVD methods [180]. The films with higher Si-content ($Si_{19}B_{21}C_{23}N_{25}O_{12}$ and $Si_{33}B_8C_{19}N_{27}O_{13}$) contain more SiC_xN_y units similar to those of SiCNO films, whereas the bonding network in the B-rich $Si_{14}B_{24}C_{29}N_{22}O_{11}$ is mainly comprised of B-N units which are interconnected via Si-N and C-C bonds. Furthermore, ToF-SIMS spectra and subsequent HAC and PCA analysis revealed that B-rich films featured higher proportions of BC- and BCN-fragments. This suggests that these films may contain additional $(BCN)_y$ structural units.

Finally, while it is plausible to suggest that residual gases and leaking old and elastomer-sealed deposition reactor would contribute to the incorporation of oxygen and nitrogen in the films given the low growth rate of the films, post-deposition oxidation of the films upper layers may be yet another likely factor. In the past, studies of PVD deposited SiCN(O) [213,245] and similar

CVD [246,247] grown films, both amorphous and crystalline, showed that such films are prone to surface oxidation upon exposure to ambient air. It is then likely for oxygen incorporation into both film types to take place as these films are amorphous and contain an appreciable amount of dangling (lone pairs) and unsatisfied bonds. Upon exposure to air, dangling bonds could very easily terminate with oxygen-containing moieties from water vapour which in turn, undergo surface oxidation, causing an increase in their oxygen content. Film porosity plays a factor but it is quite relevant to these films since a small substrate bias of -30 V was applied during growth and examination of the fracture micrographs showed dense films. Other studies have suggested the use of an increased ion-bombardment in order to densify the structure of such amorphous films in an attempt to lessen their susceptibility to surface oxidation. However, it must be mentioned that such a treatment results in an increase in the film stresses which has an adverse effect on its adhesion and consequently its applicability to technically important substrates.

4.6.2 Effect of Composition on Mechanical Properties

Owing to the high density and high bonding energy of the covalent chemical bonding [248], all SiCNO and SiBCNO films prepared in this work have high hardness, high reduced elastic modulus and very high elastic recovery. The mechanical properties show a specific trend depending on the chemical composition and bonding network. Nanoindentation results show that there is a progressive decrease in hardness, reduced elastic modulus, and elastic recovery of the film as a result of increasing the film B-content (or similarly by increasing its B/Si ratio), which can be explained in the light of the chemical bonding structure. An increase in the ratio of B/Si is a direct result of an increase in the B-content, which tends to form B-N bonds almost exclusively. A great fraction of these bonds exists in the form of sp^2-bonded atoms, which tend to weaken the structure resulting in reduced strength and softened materials. For SiCNO films, the Si-N and Si-C bonds dominate the bonding network with little sp^2-bonded carbon and nitrogen resulting in the highest hardness and reduced modulus values. Furthermore, the calculated H^3/E_r^2 ratio, which represents the degree of resistance to plastic deformation, is considered a useful criterion for assessing the suitability for wear resistance [249,250,251]. It can be inferred from the values obtained that the film with 8 at.% B may be exhibiting an interesting tribological behaviour, since it has a high hardness, which is comparable to that of SiCNO but which is simultaneously more elastic. Further studies need to be carried out in order to verify this assumption. These amorphous and sub-stoichiometric films, which are prepared by the ECR-MWCVD technique, possess interesting and potentially very useful mechanical properties, including high hardness, very large elastic recovery and good adhesion to substrates.

4.7 The Effect of Annealing on Structural and Chemical Properties of Si-B-C-N-O Films.

4.7.1 Introduction

Analysis of the chemical and structural changes associated with annealing experiments help us to understand the various aspects of this particular film system especially in the context of contact tribology at the micro- and nano-levels. Attractive results have been achieved in the case of materials that consist of light elements Si-B-C-N, and which are prepared either in bulk form, or as thin films via either polymer pyrolysis [294] and more recently, via DC magnetron sputtering [60,203]. As far as oxidation resistance and thermal stability are concerned, non-oxide ceramics containing Si-B-C-N have been found to be thermodynamically unstable in the presence of oxygen. Because of their free Gibbs enthalpies (ΔG°_r), their oxidation reaction are exothermic. Having said that, SiBCN can achieve oxidation resistance if the following conditions are met. Firstly, if the oxidation reaction takes place in conditions, where abundant amounts of oxygen are present, then this will result in the formation of a passivating, adhesive and thermally stable oxide. This will then act as a barrier to any further oxidation. Secondly, in instances where silicon is a major constituent as is the case here, oxidation protection is achieved through the formation of a stable amorphous a-SiO_2, wherein oxygen has a fairly low pre-exponential diffusion coefficient in the order of 4.5- 6.7×10^{-5} cm^2/s [252], which prevents further detrimental oxidation of the material. This is central to oxidation protection. It should be mentioned, however, that this behaviour depends entirely on the partial pressure of oxygen in such a way that at a low O_2 partial pressures, the formation of volatile polyatomic oxide species would leads to active oxidation and a consequent material loss. Under such conditions, Si forms volatile SiO(g) species leading to active oxidation and the formation of porous structures. For practical applications, it is vital to avoid such active oxidation conditions. However, under ambient conditions, where the oxygen partial pressure is approximately 2.08×10^4 Pa, silicon-containing ceramics undergo passive oxidation forming a protective oxide barrier. Another factor which contributes to SiBCN oxidation resistance is its microstructure. The amorphous nature of both film bulk and its oxide scale impacts the material's oxidation process. Not only is the diffusion of oxygen in SiO_2 low, the fact that it forms a dense amorphous film makes it effective in passivating the bulk of the film due to its ability to completely and effectively seal the film. Unlike polycrystalline or even nanocrystalline layers which provide adequate low energy diffusion paths via grain boundaries, dense and pore-free amorphous materials form a continuous dense layer which acts as an effective protective diffusion barrier. All this make amorphous Si-B-C-N films attractive candidates for oxidation and corrosion protection.
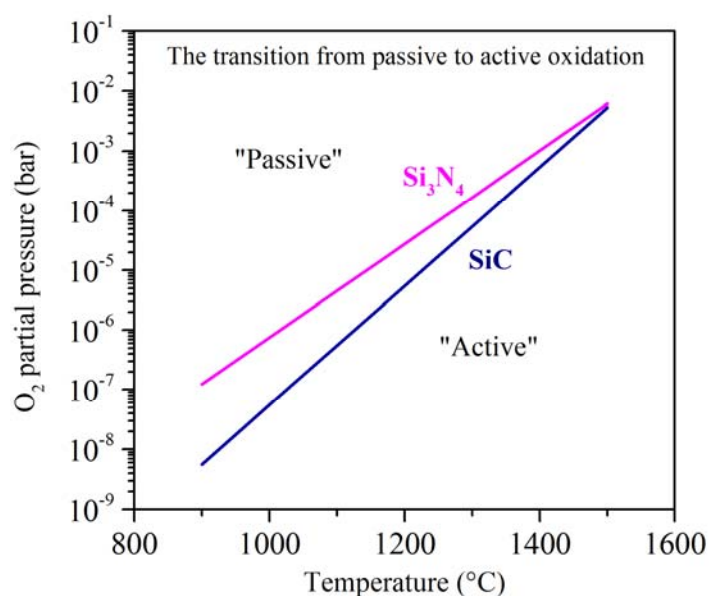
Figure 4.19: A diagram showing the transition between active and passive oxidation of SiC and Si₃N₄ as a function of oxygen partial pressure. Reproduced from reference [253].
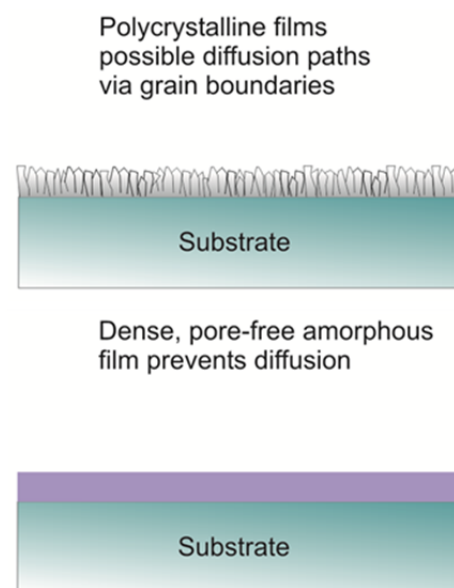
Figure 4.20: Schematic diagram showing the difference in diffusion paths within amorphous and polycrystalline thin films.

In view of the above, this section aims to elucidate the behaviour of Si-B-C-N-O films at high temperatures by: (1) Seeking empirical evidence which demonstrates the extent to which SiCNO and SiBCNO films exhibit oxidation resistance and to highlight some aspects of their oxidation prevention mechanisms with particular emphasis on the effect of boron addition to the films. (2) Understanding at the nano-level the fundamental changes pertaining to the chemical composition of the top surface layers in these films by employing the surface sensitive ToF-SIMS technique. (3) Correlating these changes with those arising from *in-situ* tribological contact at elevated temperatures as well as with those of films that were subjected to heat treatment. This is done in order to understand the roles these changes would most likely play in determining the surface's tribological properties.

The investigation focused on Si-B-C-N-O films owing to their strong adhesion to the substrate. In order to chart and analyse the changes in surface chemical character associated with the oxidative annealing in two temperature ranges: RT- 500°C and 600- 1200°C, combinatorial ToF-SIMS and FTIR analysis was used. ToF-SIMS analysis investigated B-free and B-containing films which were prepared at similar conditions with the exception of using a BF_3/Ar mixture in depositing the B-containing films as listed below:

Film	Gas flow rates (sccm)						MW power (watts)
	$Si(CH_3)_4$	H_2	BF_3	Ar	CH_4	N_2	
SiBCNO6	1.15	98.85	0.58	5.22	5.75	5.8	200
SiCNO6	1.15	98.85	0	0	5.75	5.8	200

4.7.2   Annealing in Ambient Air up to 1200°C.

Thermal annealing was conducted in temperature controlled oven in ambient air. In the case of annealing in the temperature range 100°C to 1000°C, an oven with the model N7/H (From Naber) whereas for annealing in the temperature range 1100- 1350°C, an oven with the model N7 (From Naber). Due to the fact that oven with the N7 model could not start the heating process at temperatures lower than 700°C, heating the samples in the higher temperature range involved a pre-heating step to a temperature of 700°C before introducing them to the high temperature oven. All films were heated with a heating rate of 10°C/min. until the maximum desired temperature is reached. The films were then held at this temperature for 60min. before they were allowed to cool down very slowly to room temperature. Since the oven with the N7/H model did not permit any control over the cooling rate, the cooling rate could not be accurately measured but was significantly lower than 1°C/min. Figure 4.21 shows a schematic diagram of the implemented heat treatment.
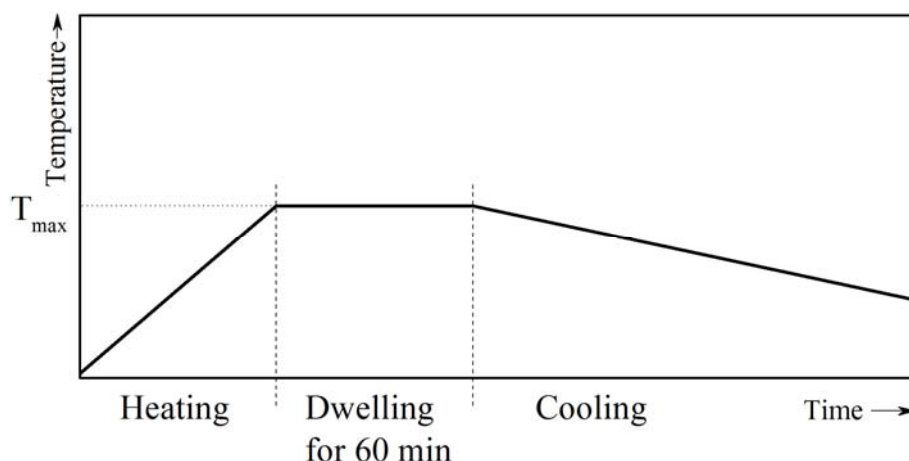
Figure 4.21: A schematic diagram of the implemented annealing treatment.

4.7.2.1   ToF-SIMS Analysis before Annealing

The ToF-SIMS spectra obtained from the surface of two types of films: SiCNO and SiBCNO which were collected after a brief pre-sputtering step with Bi^+-ion is shown in Figure 4.22. While both surfaces share the same kind of species, which appear as secondary ions in the spectra, the fundamental difference lies in the B-containing species. To investigate the differences between both film types, PCA was used to quantitatively visualise the relationship between these two surfaces in a manner similar to that carried out in section (4.2.4). The only exception however, was that HAC was not applied to the films under investigation here. This was deemed acceptable as these films had been chosen specifically because they were categorically different.

Figure 4.23(a) represents the scores on PC1 and PC2 which capture 64.7% and 6.7% of the variance in the data, respectively. Both film types are clearly differentiated in a way which is consistent with the FTIR spectra. The SiCNO sample is located on the right hand side of the diagram while the boron-containing SiBCNO is located on the left hand side of the diagram. The loadings on PC1 and PC2, which were responsible for positioning each set of spectra in the scores diagram are shown in Figure 4.23(b). The diagram clearly demonstrates that the secondary ions can be divided into two main groups: one with B-containing species and one without. In the loadings diagram, one can see that the first PC is dominated by the species SiC, Si, SiN, CN and SiO_2 in the positive direction and by BN, CN_2H, BN_2 and BO_2 in the negative direction. Accordingly, the scores diagram SiCNO shows positive values on the first PC while SiBCNO shows negative values. A detailed peak assignment of the main ToF-SIMS fragment peaks observed in the PC1 loadings is listed in Table A.**1** in the Appendix.
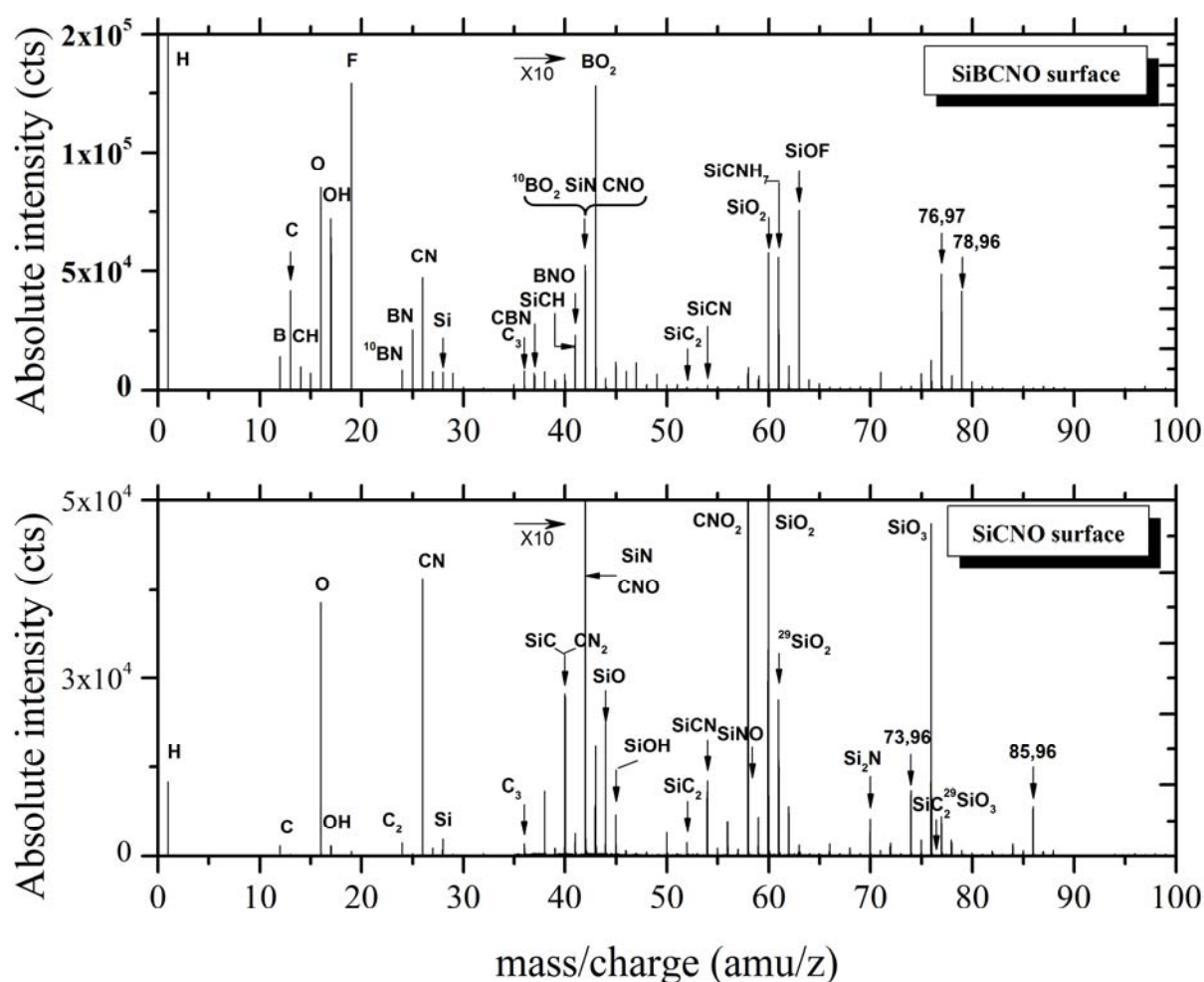

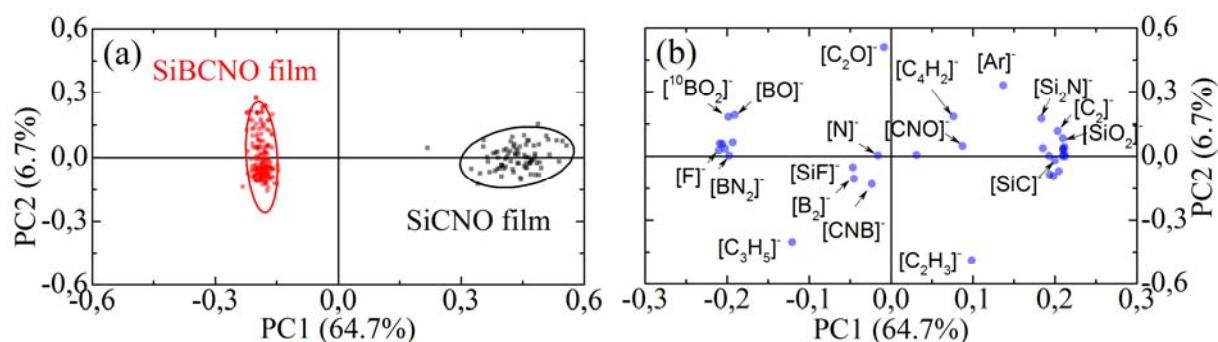**Figure 4.22: ToF-SIMS spectra from amorphous SiCNO and SiBCNO films.**

Figure 4.23: (a) Scores and (b) loadings diagrams of the first and second Principal Components. The scores are confined within 95% probability ellipses.
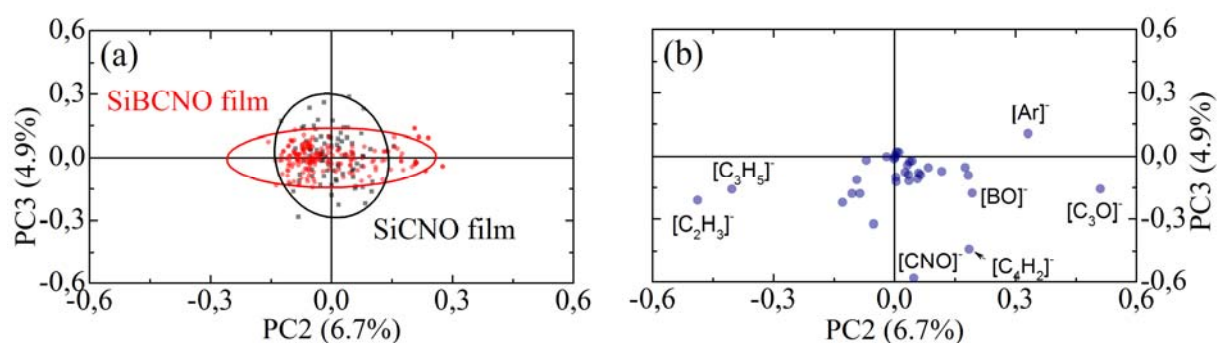
Figure 4.24: (a) Scores and (b) loadings diagrams of the second and third Principal Components. The scores are confined within 95% probability ellipses.

With the exception of PC1, both films were indistinguishable as can be seen from the score and the corresponding loadings diagrams of the second and third Principal Components. Combined, both PC2 and PC3 account for about 12% of the variance in the data (cf. Figure 4.24). In SiBCNO films, B-bonds primarily with N and O and to a much lesser extent to C with no direct bonding to Si. This indicates that apart from the changes in bonding that the additional of boron introduced, both amorphous ceramic films were alike from with regards to the rest of the bonding and have the same fundamental chemical bonding structure. These results are in agreement with the chemical bonding data, which were obtained from FTIR and XPS analysis.

It can be reasonably assumed here that surface bombardment with the O_2^+-primary ion-beam does not result in accumulation of damages in the upper layer of the film, which could give rise to structural changes to the amorphous network, and consequently to the conversion of the films does indeed hold true. This is verified by that fact that the scores of the first Principal Components in either film remained unchanged throughout the entire investigated sputtering depth. This effect can be clearly seen in Figure 4.25, which depicts the progression of the PC1 score as a function of sputtering time. The constant plateau which is observed throughout the

sputtering time of the as-deposited films means that there are no additional secondary anions generated as a result of the re-structuring of the amorphous network. Similar results were also previously seen with amorphous polymer layers deposited on silicon wafers [254].
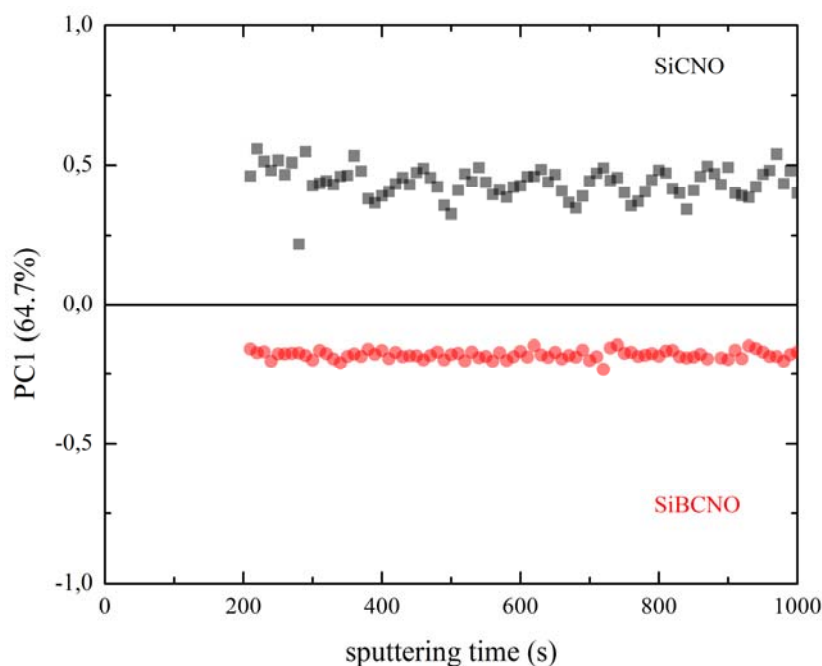
Figure 4.25: The calculated scores of the first Principal Components obtained from the PCA of the normalised data from as-deposited films.

4.7.2.2   ToF-SIMS Analysis of Annealed Films

Surface scans and depth profiles spectra obtained for each annealed film in the temperature range 100- 1200°C were used as input for the multivariate analysis. The data obtained from the as-deposited films were also used as a reference to aid comparison. In the surface scans, a total of 130- 203 fragment peaks from the ToF-SIMS spectra were also used as input. These spectra were obtained from several locations on the film surface. In depth profiling, the signals from a total of 100 secondary anions in the mass spectra were collected from each film at any given temperature. These depth profiles were obtained at time intervals ranging from 0.5 to 10 s. After each sputtering step using O_2^+-primary ion beam took place, a ToF-SIMS spectrum was acquired from the bottom of the ensued crater by using a Bi^+-ion beam. In this manner, a systematic series of ToF-SIMS spectra as a function of sputtering time normal to the film growth direction were obtained. PCA was then used to qualitatively investigate the differences between the chemical compositions of the oxide scales which developed on both film types as a result of the annealing process. In this way, the scores and loadings diagrams of the main Principal Components, which identify the highest variances in the data, are used to visualise the differences between the various annealed surfaces.

I   SiCNO films-annealed in the temperature range 100-500°C

Figure 4.26 shows the PCA results obtained from the annealed SiCNO surfaces in the temperature range 100- 500°C. PC1 and PC2 (describing 55.0% and 22.8% of the total variance, respectively) successfully distinguished between the annealed surfaces. The loadings diagram shows positive peaks (i.e. positive loadings on PC1) for fragments that are more abundant in hydrogen-containing anions as well as non-oxygen containing ones. Whereas the negative peaks (i.e. negative loadings on PC1) are for those, which are more abundant in oxygen and those of high molecular masses. Correspondingly, the scores diagram shows negative scores for the as-deposited SiCNO surface and for the one annealed at 500°C as well as positive scores for those SiCNO films annealed at other temperatures. Detailed assignment of the fragment peaks are listed in Table A.**3** in the appendix.

The loadings on PC1 also show that the O- and H-containing anions have opposite signs indicating that they have opposing effects on the data. The change in the scores on the main Principal Component (PC1) as a function of annealing temperature demonstrated a particular trend with an initial increase in scores at 100°C and 200°C followed by a drop. This trend corresponds well with changes in the normalised relative intensities, which were recorded for the most strongly influencing secondary anions such as SiC, SiCN and their H-containing counterparts as illustrated in Figure 4.28. Also, the normalised intensities of a number of non-O-containing secondary anions vary in accordance with the variation in the main Principal Component (PC1), whereas those O-containing ones follow an opposite trend. On the other hand, the signal intensities from the hydroxyl-containing fragments such as: OH, SiOH, SiO_2H and SiO_3H , increases initially after annealing at 100°C before continuing to drop steadily at higher annealing temperatures as illustrated in Figure 4.28(c). This trend confirms that both the as-deposited SiCNO and the film annealed at 500°C contain an abundance of O-containing species.
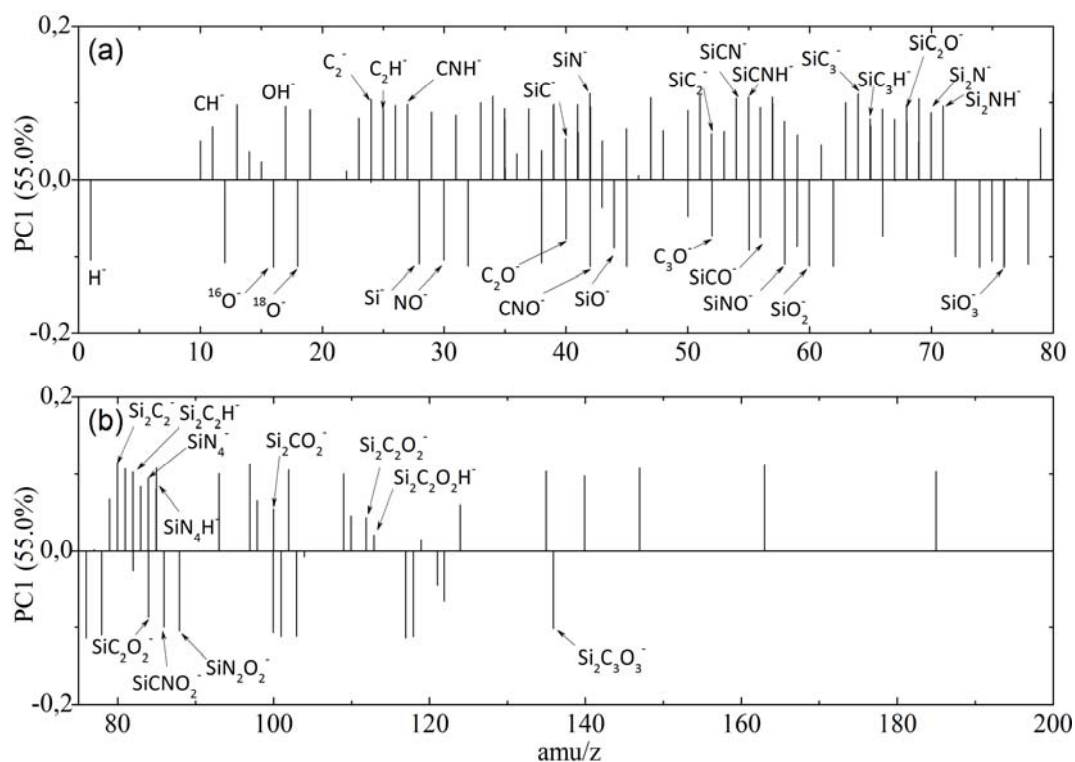
Figure 4.26 The loadings on PC1 (55.04% of variance) of the 130 variables in the mass range (a) 1- 80 amu/z and (b) 75-200 amu/z. The data are obtained from the ToF-SIMS spectra of annealed SiCNO films in the temperature range 100- 500°C.
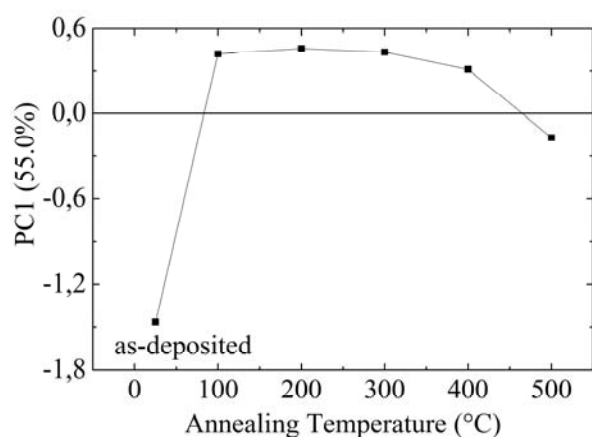
Figure 4.27: The scores on PC1 of the 130 variables (m/z peaks) from each SIMS spectrum obtained from annealed SiCNO films in the temperature range 100- 500°C.
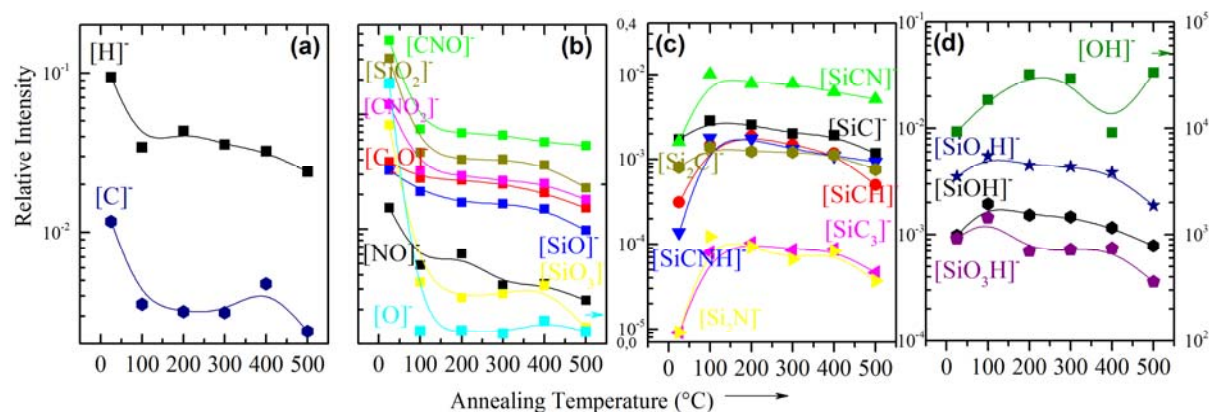
Figure 4.28: Normalised relative intensities of (a) H, C, (b) O, CNO, CNO₂, C₂O, SiO, SiO₂, (c) SiC, SiCH, SiCN, SiCNH, Si₂N, Si₂C, SiC₃, and (d) OH, SiOH, SiO₂H and SiO₃H secondary anions as a function of annealing temperature.

II   SiBCNO films annealed in the temperature range 100- 500°C

In the spectral data dataset obtained from SiBCNO films, the normalised peak intensities of a total of 203 fragments were used as input. The resulting first and second Principal Components captured 64.3% and 16.8% of the total variance in the data, respectively. As with the data generated from the SiCNO film, both PC1 and PC2 successfully distinguished between the as-deposited SiBCNO film and those annealed between 100- 500°C. The scores on PC1 (c.f. Figure 4.30) shows the as-deposited SiBCNO film has a negative score whereas the rest of annealed surfaces had positive ones. The loadings diagram (c.f. Figure 4.29) shows that the peaks with negative loadings are the ones that correspond to the O-containing as well as many H-containing secondary anions, which in turn are responsible for the negative score of the as-deposited sample. This is in stark contrast to a host of fragments with positive loadings on PC1 which could be ascribed to non-O-containing secondary anions. The most prominent peaks with negative loadings include: COB, BNO, CNO, BO_2, CNO_2, SiO_2, SiO_3, C, and C_3 while those with positive loadings correspond to secondary anions such as CB, CN, B_2N_2, BNC_2 and SiCN, to name a few. A complete list of the loadings of all selected the fragments on PC1 and PC2 is shown in Table A.4. The trend which these data showed replicated that which was observed in the variation in the signal intensities of these fragments.

Figure 4.31 shows how the peak intensities of the O-containing secondary anions follow an opposite trend to that observed with the scores on PC1 such that they decrease significantly after as a result of surface annealing. Clearly, the as-deposited SiBCNO surface is the one which contains a considerable amount of O-containing species, thereby, generating a large amount of oxygen-related secondary anions. The heat treatment between 100°C and 300°C has the effect of reducing the proportion of these species. The same can be observed with the H-containing secondary anions where the as-deposited film exhibited the greatest signal dropping to much lower levels after annealing. However, at the annealing temperatures of 400°C and 500°C, there appeared to be a slight but steady increase in the amounts of O-containing species, which is apparent in both their relative signal intensities as well as on the scores on PC1. The non-O-containing secondary anions follow a completely opposite trend as the variation in their signal intensities being mirror-inverted to those of oxygen-related species. The highest signals were recorded for SiBCNO films which were annealed at 100°C and 200°C. The signal intensities then decreased steadily beyond this temperature. With regards to the hydroxyl-containing secondary, the annealed surfaces show the highest intensities of: BOH, B_2OH, SiC_2O_2H, and $B_3N_3OH_2$ at 100°C.
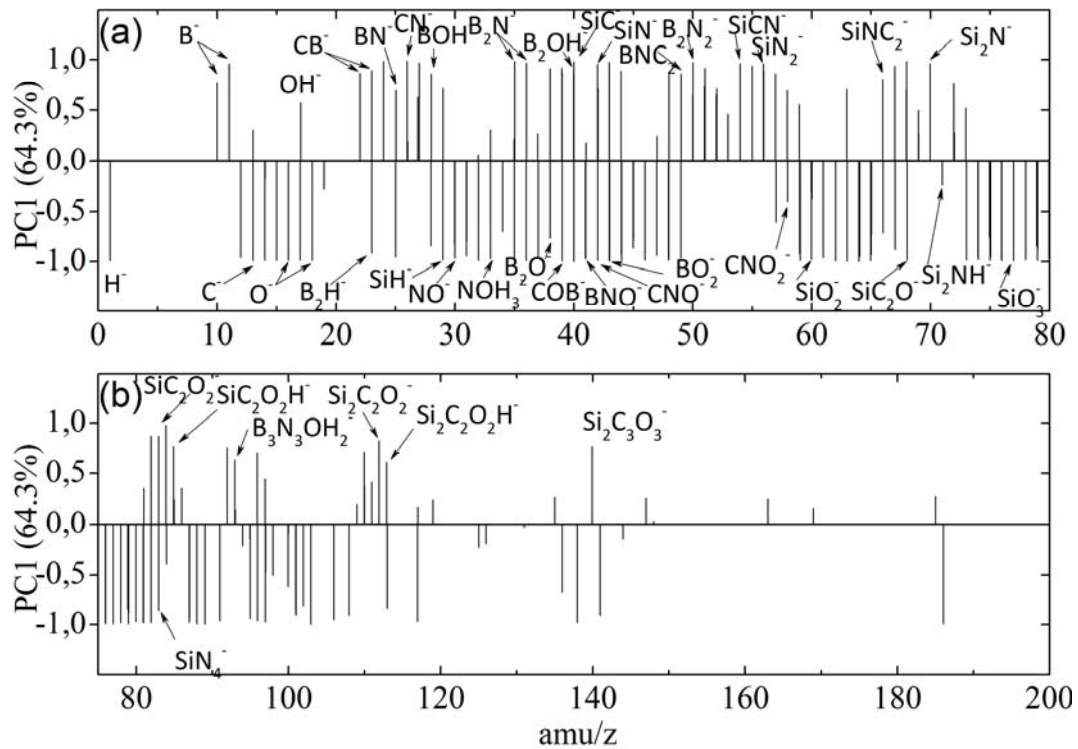
Figure 4.29: The loadings diagrams of PC1 (64.3% of variance) of the 203-variables (m/z peaks) constituting each SIMS spectrum obtained from annealed SiBCNO films in the temperature range RT-500°C.

Figure 4.30: The scores on PC1 of the 203 variables (amu/z peaks) constituting each SIMS spectrum obtained from annealed SiBCNO films in the temperature range 100- 500°C. The spectrum of the as-deposited SiBCNO is added to aid comparison.
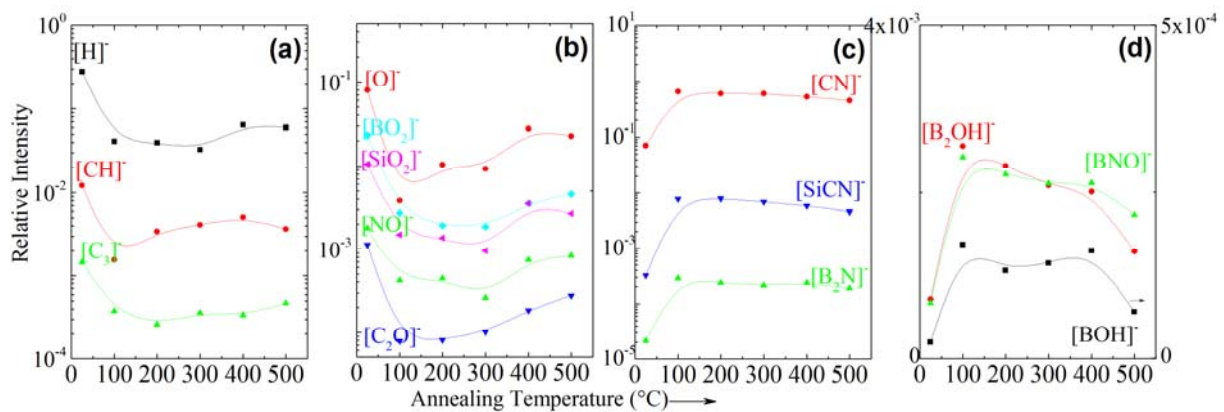
Figure 4.31: Normalised relative intensities of (a) H, C, C_3, (b), O, BO_2, SiO_2, NO, C_2O,(c) B_2N, CN, SiCN, and (c) BOH, BNO, B_2OH anions as a function of annealing temperatures.

III   SiCNO films annealed in the Temperature Range 600- 1200°C

Figure 4.32(a) represents the loadings diagram of all the variables constituting each depth profile spectrum obtained from SiCNO films annealed between 600- 1200°C. It clearly shows that the secondary anions can be divided into two main groups: one which corresponds to O-containing species and another to those species which are free of oxygen. Here the highest loadings on PC1 are those with the following masses (amu/z): 12.0019 (C), 24.0014 (C_2), 26.006 (CN), 27.006 (CNH), 39.9773 (SiC), and 41.9806 (SiN) in the positive direction and of 15.995 (O), 17.0026 (OH), 28.9836 (SiH), 59.966 (SiO_2) and 75.964 (SiO_3) in the negative direction. Accordingly, Figure 4.32(b) represents the scores on PC1 and PC2, which captured 37.1% and 16.7% of the variance in the data obtained from SiCNO films, respectively. The bulk of SiCNO films (obtained at high sputtering times) showed positive scores on PC1, whereas the oxide scale developed on the films showed negative values in accordance with the loadings on PC1. The spectra which were obtained from the films' uppermost layers after annealing at 1100°C and 1200°C lay on the far left hand side of the diagram and displayed negative scores on PC1 and positive scores on PC2. These were clearly separated from the rest of the data. These data points correspond to the spectra collated in the initial 90 and 160s from the films annealed at 1100°C and 1200°C, respectively. It is evident that, the variables which were responsible for positioning these points and which had negative loadings on PC1 and positive on PC2, were those which corresponded to the silicon oxide species. These were the O, SiO_2, SiO_3 secondary anions. These same variables are related to the spectra which were the result of the initial 20s and 30s of sputtering of SiCNO films annealed at 900 and 1000°C, respectively. The sputtering times which corresponded to the transition layer or interface between the oxide scale and the rest of the film had scores which were less negative. A detailed peak assignment of the main ToF-SIMS fragment peaks observed in the PC1 and PC2 loadings is listed in Table A.**2**.
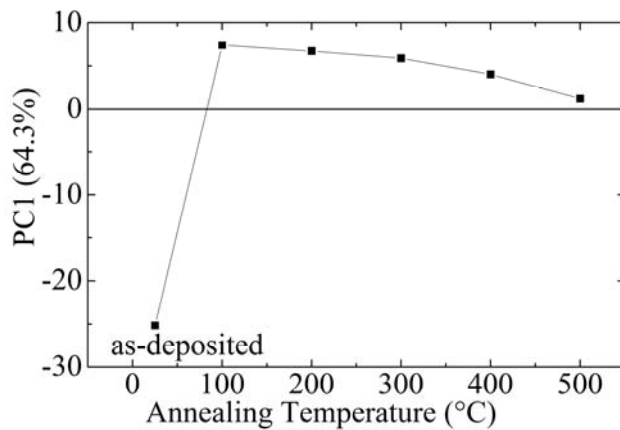
Figure 4.32: (a) The loadings and (b) scores diagrams of PC1 and PC2 of all the variables (amu/z peaks) constituting each spectrum obtained from annealed SiCNO films.

IV   SiBCNO films annealed in the Temperature Range 600- 1200°C

The characteristic scores and loadings diagrams of the two main Principal Components; which captured most of the variance in the ToF-SIMS spectral data of SiBCNO films (56.4% and 12.2%, respectively) are shown in Figure 4.33. As with the diagrams constructed for SiCNO films, the annealed SiBCNO films can be separated based on the presence (or absence) of oxide related species. In the scores diagram, three main regions can be clearly distinguished.

The first region is located on the lower left hand side of the diagram with negative scores on both PC1 and PC2. The scores in this region are a result of collating the spectra from the upper layer of each film, which includes the oxidised region of the film. Positioning the data points in this region is a direct result of variables which have negative loadings on PC1 and PC2. Upon examining the loadings diagram, it appears that the spectra are dominated by O-containing species; namely O, BO_2 and SiO_2 in the negative direction and are therefore responsible for positioning the scores. No C- or N-containing secondary ions appear in this part of the diagram, which indicates that the signal intensities emanating from these species are scarce indicating that the composition of the oxide scale is almost free of any C and N related species. These findings are in agreement with the depth profiles shown in Figure 4.35(a) and (b).

The second region is located on the lower right hand side of the diagram. These data points have positive scores on PC1 but negative scores on PC2. This region corresponds to spectra obtained after sputtering the oxide scale away and therefore corresponds to the bulk of the films. Here PC1 is dominated by the species: C, NH, OH, C_2, BN, CN, CNB, BN_2, SiC, SiN, and B_4C in the

positive direction. These secondary anions therefore emanate from the bulk of the films and correspond to the unoxidised films.

A third region is represented by the scattered scores that span the space between the first and second regions and is dominated by data collected from the films annealed in the upper temperature range (900- 1200°C). The corresponding sputtering times refer to the interfacial regions between the developed oxide scales and the unoxidised bulk of the film. The data are scattered due to the large gradation in the signal intensities recorded for a large number of secondary anions. This in turn marked the interfacial region between the oxide scale and the bulk of the film. Ion-beam induced structural damages to the ceramic film did not occur as is evident by the relatively constant scores of the Principal Components across the sputtering depths. Therefore, the presence of any gradation in PC1 scores in the initial sputtering times in the case of SiBCNO annealed at high temperatures, supports the conclusions that a gradient oxide layer has formed. This can be clearly seen in Figure 4.34, which depicts the change in the scores on PC1 of films annealed in the temperature range 600- 1200°C. A detailed peak assignment of the main fragment peaks observed in the PC1 and PC2 loadings is listed in Table A.**2**. The position of the interfacial region between the oxide scale and the bulk of the film was different in both SiCNO and SiBCNO. The oxide scale which developed on the B-containing films was thicker at higher temperatures as opposed to that grown on the B-free film, which tended to be thinner.
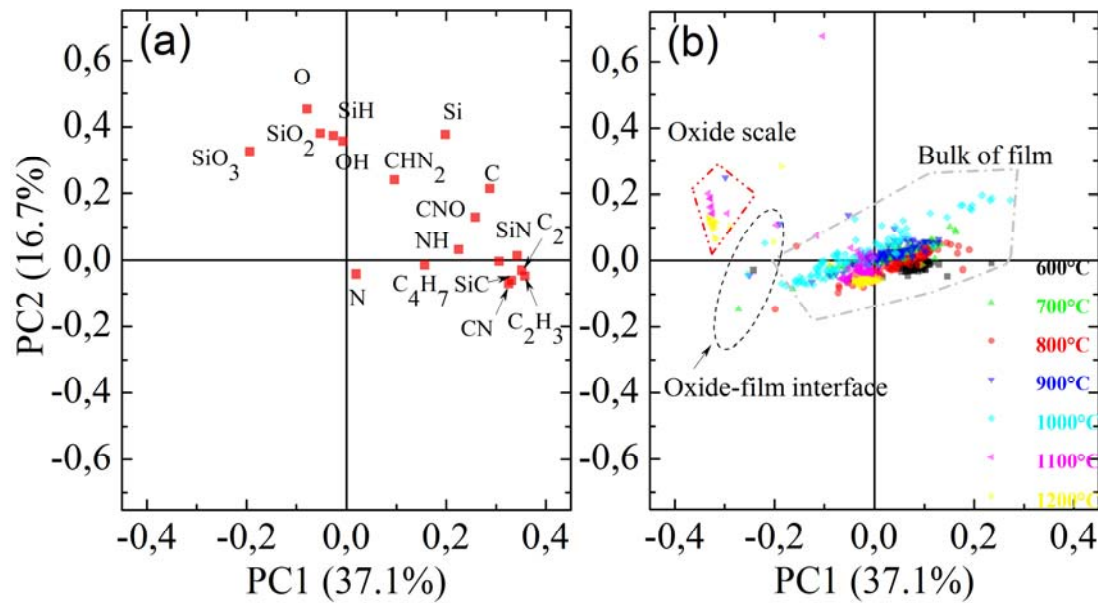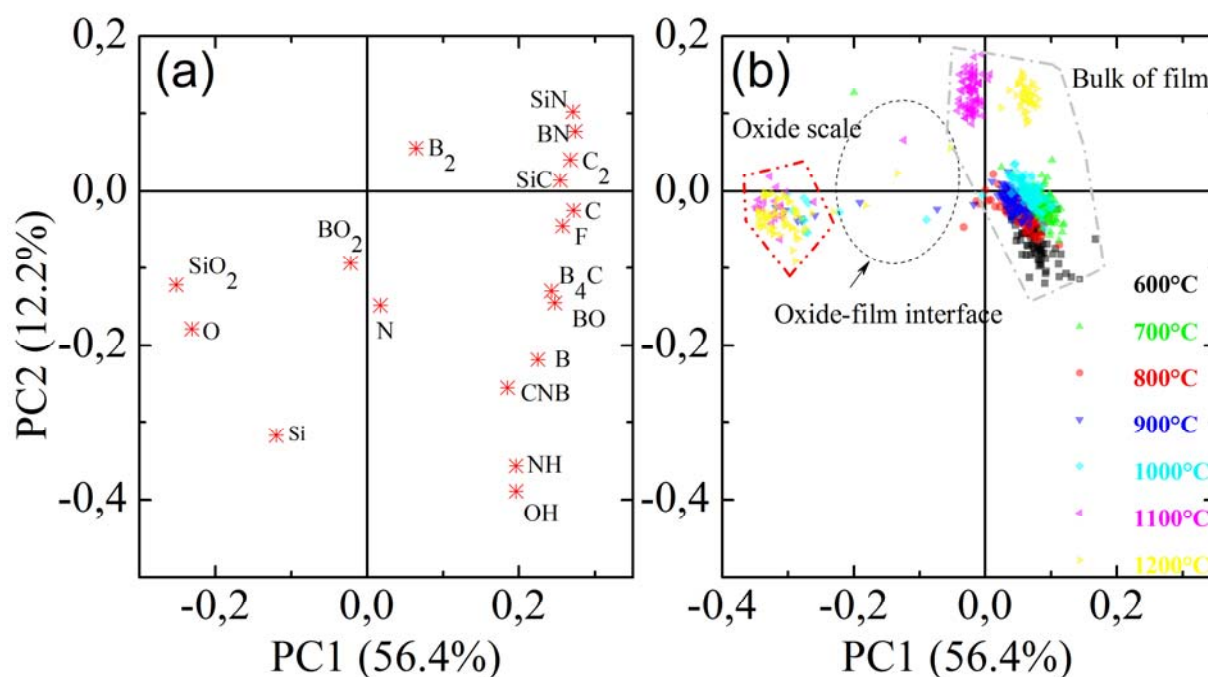

Figure 4.33: (a) the loadings and (b) scores diagrams of PC1 and PC2 of all the variables (amu/z peaks) constituting each spectrum obtained from annealed SiBCNO film.
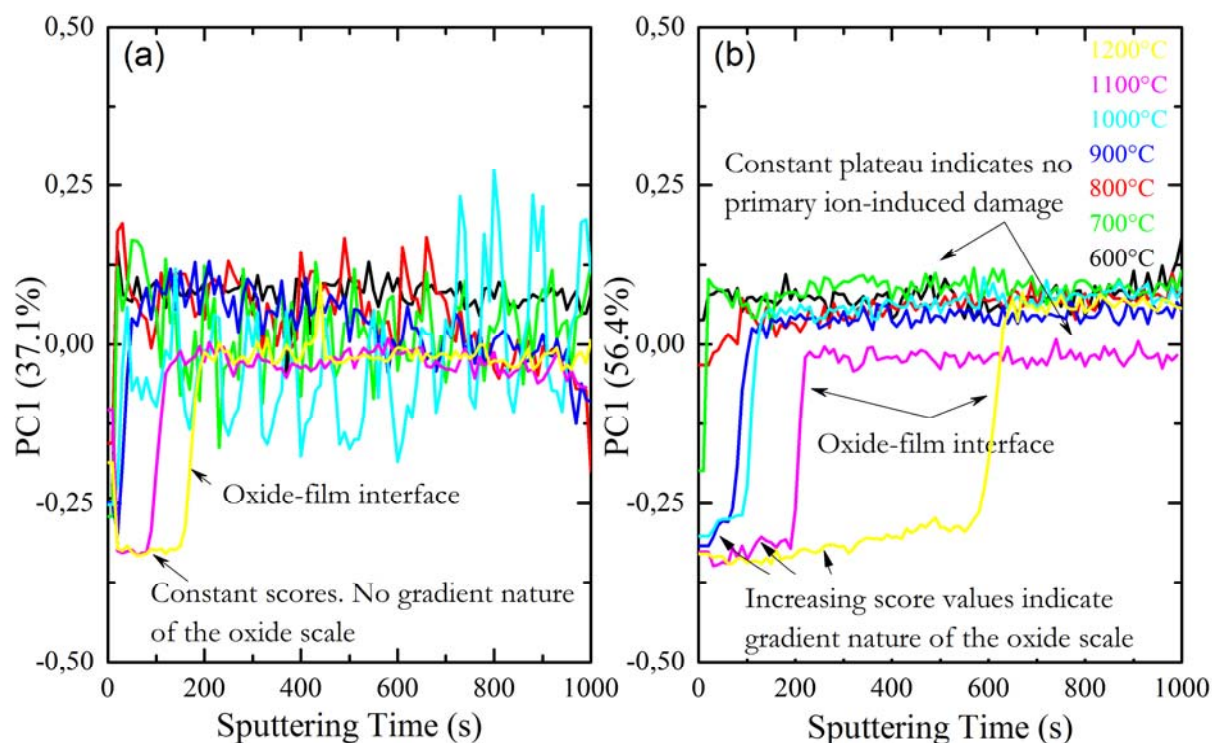
Figure 4.34: The calculated scores on PC1 as a function of sputtering time for (a) SiCNO and (b) SiBCNO films annealed in the temperature range 600- 1200°C.

In view of the aforementioned analysis, it is now possible to follow the changes to the ToF-SIMS spectra as a result of annealing. Selected depth profiles obtained from both film types, which were annealed in ambient air in the temperature range 800- 1200°C, are shown in Figure 4.35 (a) and (b), respectively. In order to monitor the changes associated with higher temperature annealing, the change in the relative intensity of several secondary anions which were among the ones with the highest loadings on the main Principal Component were monitored as a function of sputtering time. No changes in the intensity of any secondary anion were recorded for either film up to 800°C indicating that oxidation treatment up to this temperature has effected no chemical changes in film composition. Any oxide scale which must have formed would have been sputtered away in the initial 10s.

At 900°C, a marked change in the intensities of several markers can be seen. In the case of annealed SiBCNO films annealed at 900°C, an increased signal of O and SiO_2 secondary anions was recorded in the initial 90 s whereas that of B, C, BN and SiN dropped to the level of noise in the same period. After sputtering the annealed film for more than 90 s, the signal intensities of all the secondary anions went back to levels similar to those that were recorded in both the as-deposited films and those annealed at lower temperatures. In the case of annealed SiCNO films, an annealing temperature of 900°C also marked the first onset of a detectable oxide scale formation as can be seen by similar changes in O, SiO_2 signals. These signals dropped sharply

after 40s of sputtering time to reach levels almost equal to those of SiCNO films, which are annealed at lower temperatures. In contrast, both C and SiN signals showed a gradual increase from totally diminished values to higher values after 40s.

In addition, in the profiles obtained from SiBCNO films annealed at the higher temperature range, the signal intensities of the O and CN secondary anions were mirror-inverted throughout the oxide layer. The same pattern was observed with BN and SiN. This suggests the presence of a replacement mechanism in which both nitrogen and carbon are replaced by oxygen. Furthermore, as a result of the oxidation of Si-C, Si-N and B-N bonds, both C and N evolve as gaseous oxides. Similarly, SiCNO films which were annealed at the same temperature range showed a similar depletion of SiC, SiN and CN secondary anions in the initial scans of the oxide layer, which were attributed to the oxidation of Si–C, Si–N and C–N bond.

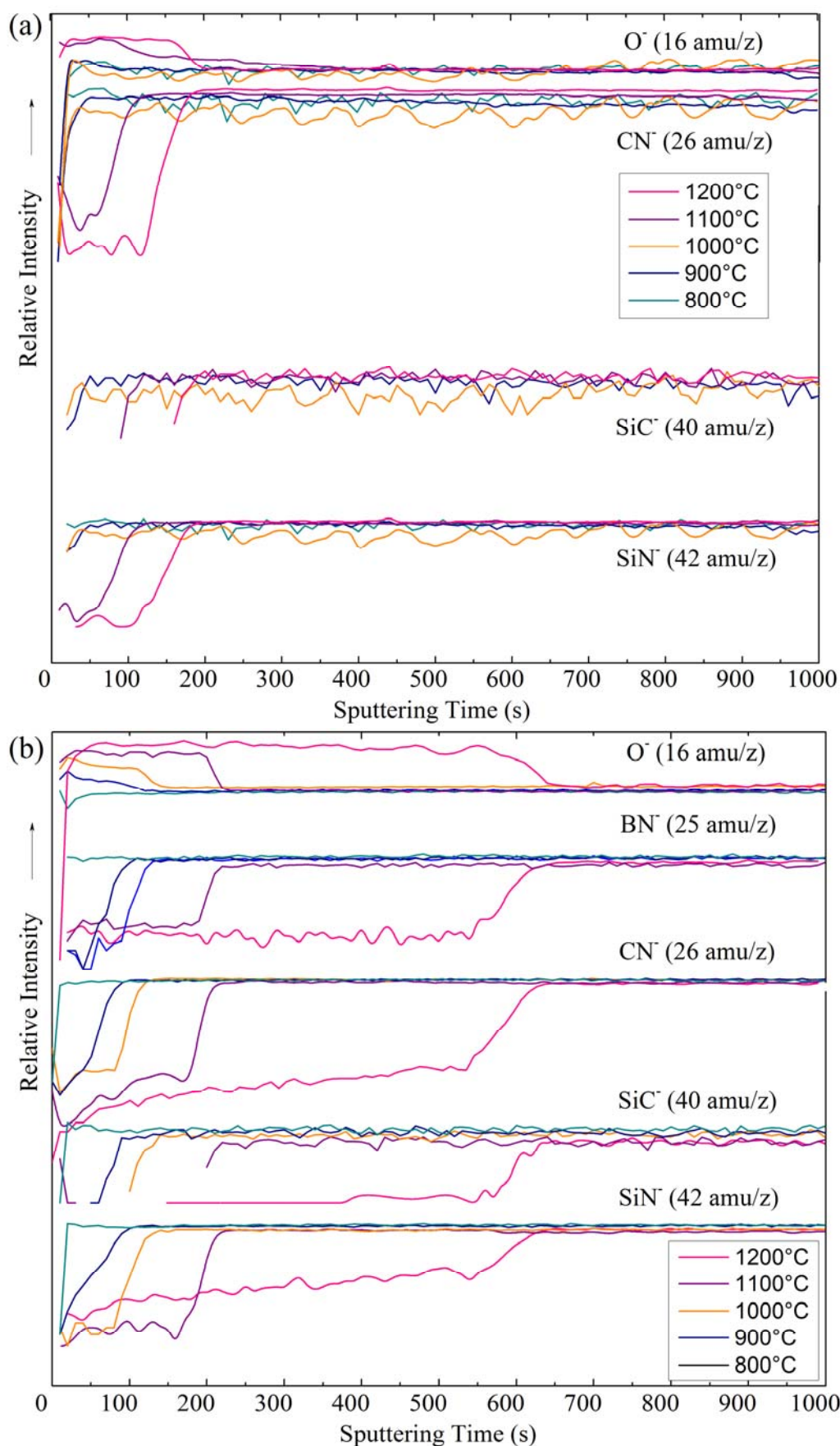**Figure 4.35: (a) The profiles obtained from (a) SiCNO and (b) SiBCNO films annealed in the temperature range 800- 1200°C showing the signal intensities of O (15.995 amu/z) versus (a) BN (25.011 amu/z), (b) CN (26.004 amu/z,) and (d) SiN (41.981 amu/z).**

Up to the temperature of 900°C, both annealed films behaved similarly. Thereafter, the onset of detectable change in surface layer composition was observed. The data revealed that more time is required to sputter the oxide scale which formed on SiBCNO films than was needed for the SiCNO films. Since the thickness of the oxide scale is directly proportional to the time required to sputter it away, it is clear that this oxide scale at this stage tends to grow thicker on SiBCNO as opposed to SiCNO. This is based on the reasonable assumption that the sputtering rate of either oxide layer does not vary greatly despite minute changes in their composition. Figure 4.36(a) and (b) group the signal intensities recorded for the SiO_2 secondary anions, which were collated from both films annealed in the temperature range 600- 1200°C. It is evident that the sputtering time required to remove the oxide scale increased parabolically with increasing the annealing temperature, and that this increase is larger in the case of SiBCNO films. This indicates that a thicker oxide scale developed on annealed SiBCNO films. For example, whereas the time required to remove the oxide scale on a SiBCNO film grown at 1200°C is 600 s, only a fourth of the time was needed to sputter away an oxide scale on a SiCNO film at the same temperature (i.e. 150 s). A summary of the times required to sputter the oxide scales on both films in the temperature range 900- 1200°C is shown in Table 4.5.

Furthermore, the gradation in the scores on PC1 from the SiBCNO data in the interface region which is observed earlier is caused by compositional changes in this region. In fact the profile collected through both BO and BO_2 secondary anions appeared to differ from the other species in that there was an increase in their signal intensities up to 90 s before a plateau was reached. After that, no change in the intensities of all the secondary anions was observed. This suggests that the constituent elements behave differently with regards film oxidation. This hints at the formation of two main regions within the oxide layer. The first is the uppermost region, which was deprived of boron whereas the second appeared to be enriched with boron. This gradual increase in signal intensities became more prominent in films which were annealed at temperatures higher than 900°C as can be seen in Figure 4.37. This suggests boron behaves rather differently. The increased intensities of BO_2 secondary anions near the interface between the oxide scale and the rest of the film may be attributed to the outward diffusion of boron from the inner parts of the film, which then bonds with the inward diffusing oxygen forming B–O bonds in the network. The outer region of the oxide scale appeared to be depleted from boron as a result of the volatilisation of BO_x species which affected the relative proportion of B–O bonds in that part of the film. This effect is also clearly observed in Figure 4.38 which displays the profiles obtained from B secondary anions. Neither this gradual profile nor the increased intensity near the oxide scale-film interface was observed with other B-containing secondary anions such as BN, BN_2, $CNBH_3$ and B_4C, which indicates that any boron left in the oxide scale

exclusively bonds to oxygen and that there were no B-N, B-C bonds retained in the amorphous bonding network.
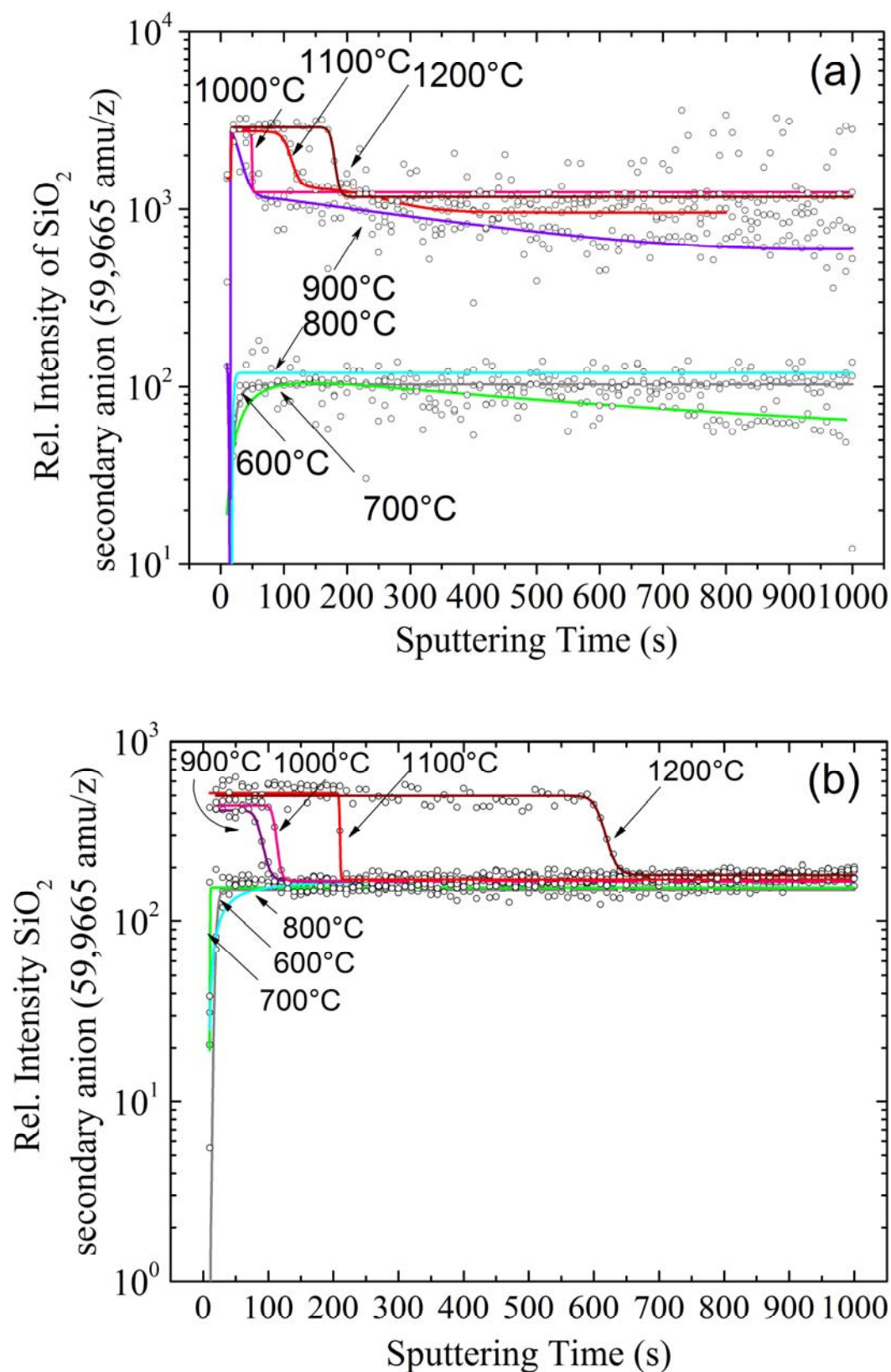
Figure 4.36: Signal evolution of the secondary anion SiO$_2^-$ obtained from (a) SiCNO and (b) SiBCNO films annealed in the temperature range 600°C- 1200°C.
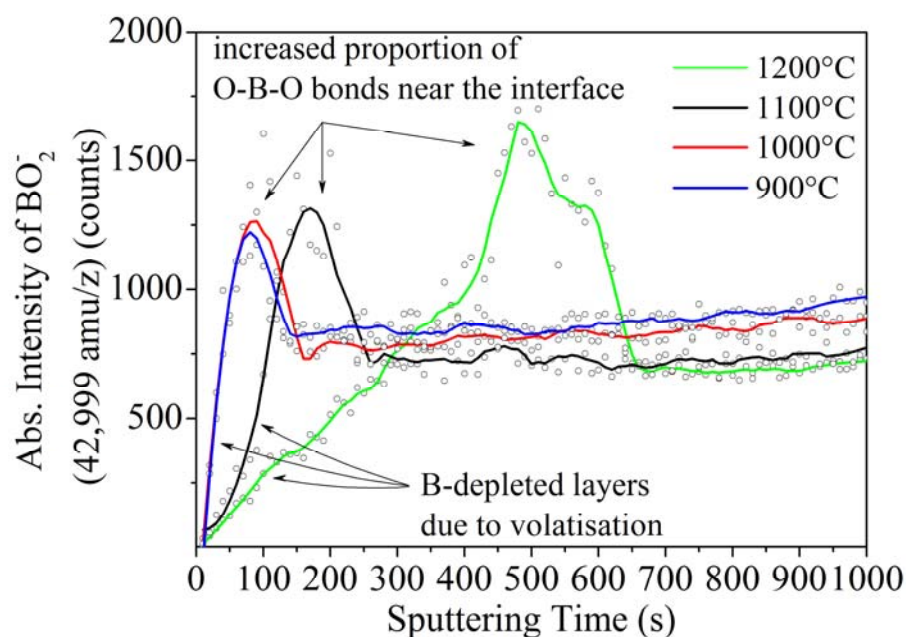
Figure 4.37: Evolution of BO_2 (42:9994 amu/z) secondary anions signals in SiBCNO films annealed in the temperature range 900- 1200°C.

Annealing Temperature (°C)	Sputtering time (s) SiCNO	Sputtering time (s) SiBCNO
900	25	70
1000	40	110
1100	90	200
1200	150	590

Table 4.5: The sputtering times required to remove the developed oxide scale formed by annealing at various temperatures.
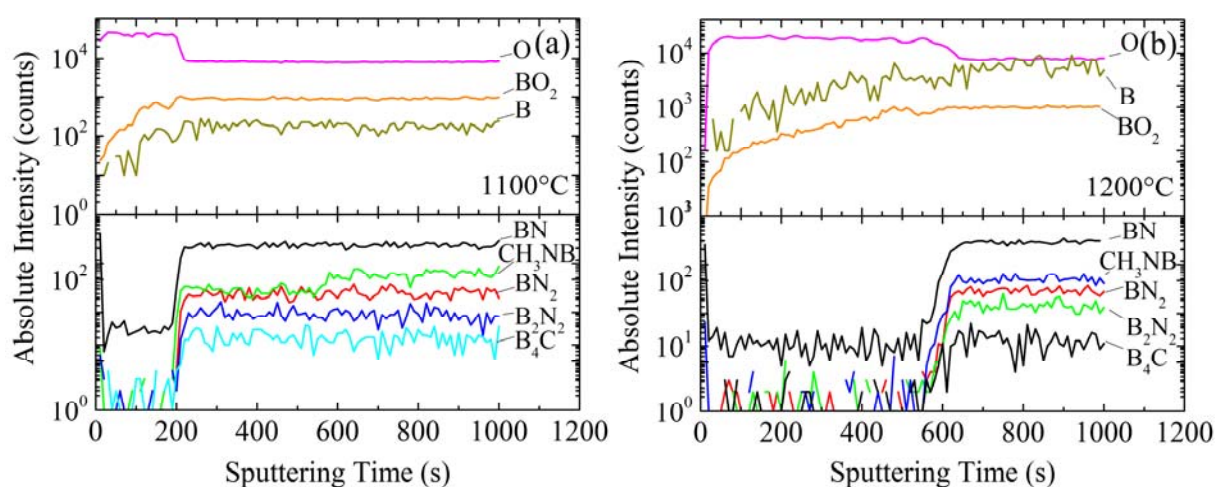
Figure 4.38: Evolution of various B-containing secondary anion signals from SiBCNO films annealed at (a) 1100°C and (b) 1200°C. The intensity profile of O (15.995 amu/z) is added to aid comparison.

4.7.3   Phase Analysis of the Films

4.7.3.1   X-ray Diffraction Analysis

Analysis of both as-deposited films by X-ray diffraction was detailed in section 4.3 and revealed that both films were totally X-ray amorphous. Figure 4.39 shows the diffraction patterns that were obtained from both film types after heat treatment in the temperature range 600- 1350°C and which were then compared with the diffraction pattern of the as-deposited films. It can be seen that both film types retain their amorphous character throughout the oxidation process up to 1350°C. The fairly broad feature in the 2θ range 10°- 25° indicates a completely X-ray amorphous film without any signs of crystallisation of the amorphous network, or the formation of any crystalline phases as a result of oxidation or decomposition. The diffractograms which were collected at grazing incidence and are more sensitive to the film also indicate that any oxide scale which must have been formed remained totally X-ray amorphous.
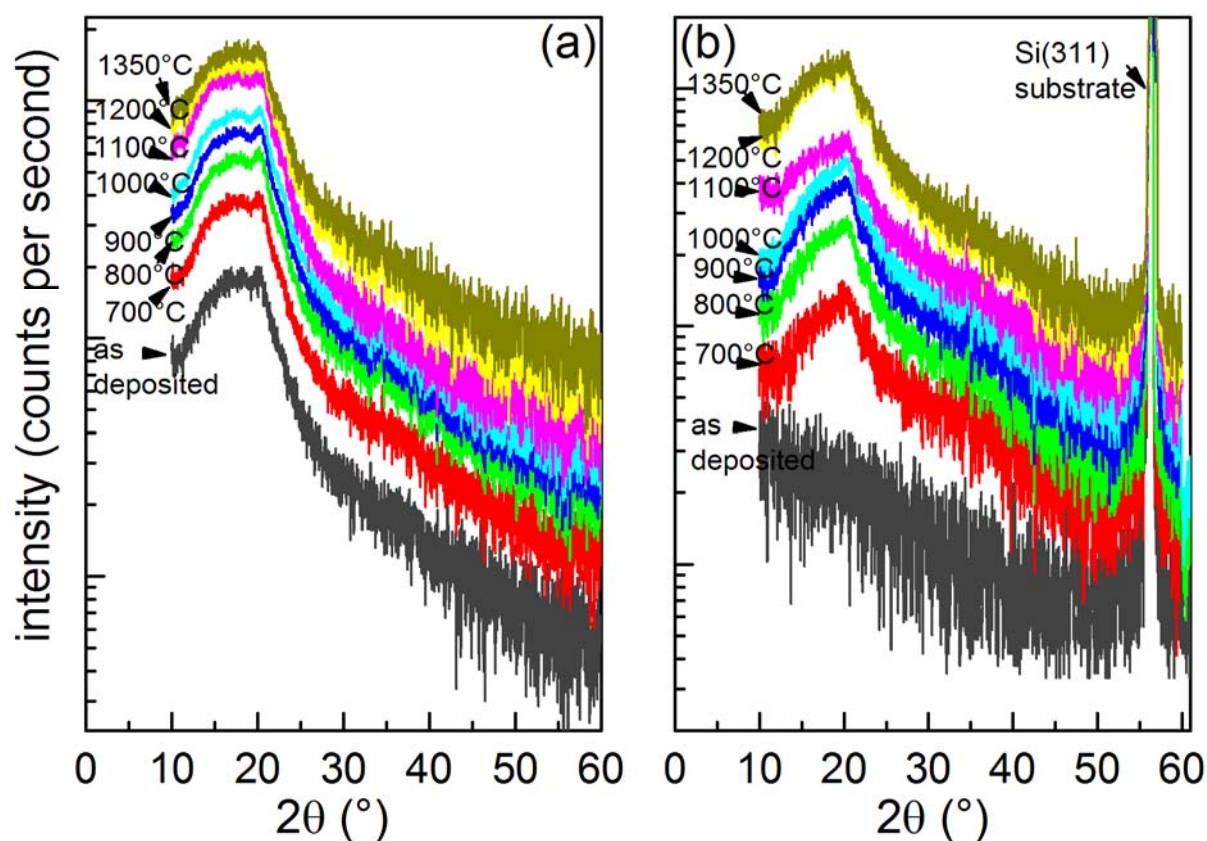
Figure 4.39: XRD patterns of (a) Si$_{40}$C$_{16}$N$_{27}$O$_{15}$ and (b) Si$_{33}$B$_8$C$_{19}$N$_{27}$O$_{13}$ films at various oxidation temperatures.

4.7.3.2 FTIR spectroscopy

FTIR Analysis proved especially useful when investigating oxidation behaviour, as it is a method which is particularly sensitive to changes to chemical bonding, which are not necessarily accompanied by changes in crystallinity. As both coatings and their oxidation by-products were found to be amorphous, FTIR became one of the methods of choice. In this analysis measurements were carried out in transmission mode which was made possible due to the films' thinness. However, due to the ultrathin oxide layer which developed on the film, the signal which emerges from it became heavily masked by the signals emanating from the rest of film. One way to overcome this problem was collect the spectra over a prolonged acquisition time, which would allow an adequate intensity to be collected. The spectra were then arithmetically subtracted from the non-oxidised film/substrate to highlight any changes which may have occurred. This has proved successful in extracting adequate information from the FTIR spectral data.

An examination of the FTIR absorption spectra of the annealed films revealed increasing intensities of the Si-O and B-O bond vibrations as a function of increasing the annealing temperature. Figure 4.40 shows the absorption spectra of films annealed between 600°C and 1200°C that were a result from subtracting the spectral information from the non-oxidised film/substrate system. The intensity of the absorption at around 1100 cm^{-1}, which represents the high frequency mode of the antisymmetric Si-O-Si stretching vibration, was evidently higher at the highest annealing temperatures. It was also clear that the stretching band was asymmetric and had an increasing broadening in the lower wavenumber (lower frequency) side at low temperatures and another broadening at high wavenumbers (high frequency) as the temperature increased. A common feature in the spectra obtained from SiCNO and SiBCNO was the large absorption band width, which signified both the amorphous and sub-stoichiometric character of the oxide scale. The FWHM of the antisymmetric Si-O-Si stretching vibration in stoichiometric thermal SiO$_2$ is similar to crystalline quartz in the order of 75- 85 cm^{-1} [255,256], which is smaller than those obtained from the oxide scale developed on these films. In contrast the FWHM of SiO$_x$ where x values range between 1.6 and 1.9 was found to be 350- 120 cm^{-1}, respectively, for PECVD grown film [256].

In order to extract more information about the nature of the oxide scale, the spectral data were fitted to a model based on the least-squares fitting to a Gaussian function in order to obtain the band characteristics and resolve overlapping bands. This treatment focused on Si-O and B-O bonds which arose as a result of film oxidation.
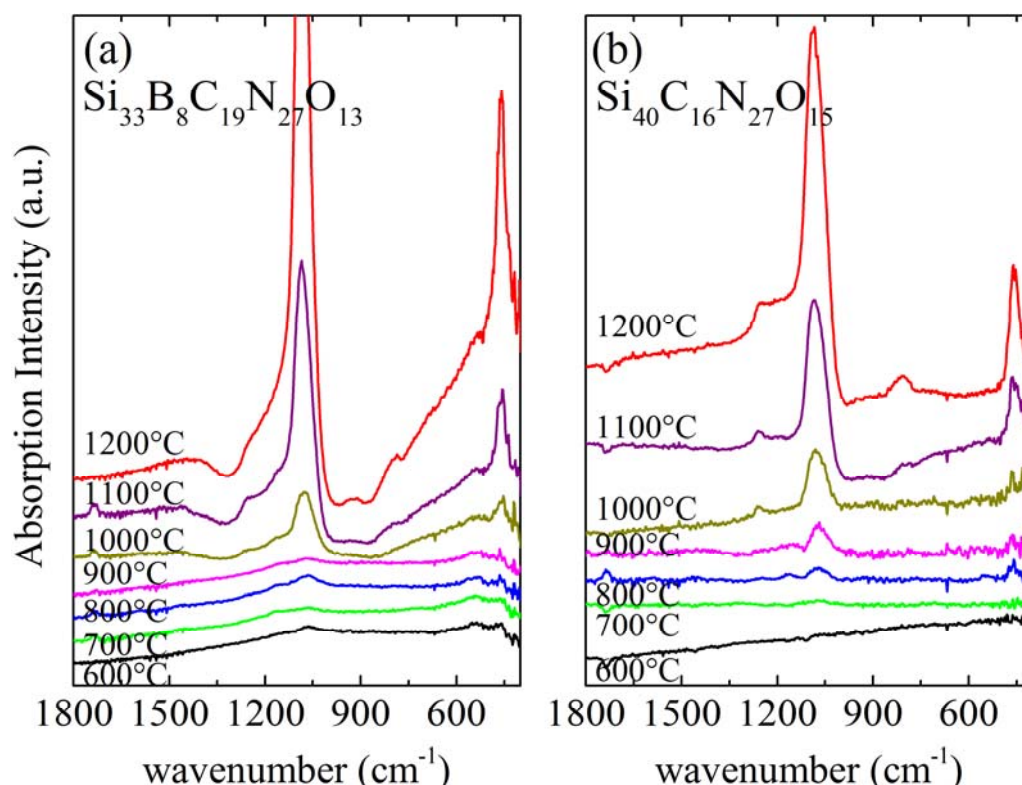
Figure 4.40: FTIR spectra of (a) Si$_{33}$B$_8$C$_{19}$N$_{27}$O$_{13}$ (SiBCNO3) and (b) Si$_{40}$C$_{16}$N$_{27}$O$_{15}$ (SiCNO2) films which were annealed at various oxidation temperatures. These spectra are obtained by subtracting the spectrum of non-oxidised film/substrate systems and all were obtained at normal incidence.

A   The Si-O Absorption Band

The resonance frequency (band position) of the antisymmetric stretching vibration depends on the type and number of bonded atoms as well as on their chemical bonding surrounding (dielectric surrounding). This energy is therefore directly related to the number of bonded atoms and can be used, in this case, to reflect on the stoichiometry of the oxide layers which developed as a result of the oxidative annealing treatment.

The absorption spectra of oxide layers which formed on Si$_{40}$C$_{16}$N$_{27}$O$_{15}$ (**SiCNO2**) and Si$_{33}$B$_8$C$_{19}$N$_{27}$O$_{13}$ (**SiBCNO3**) films as a result of the oxidative annealing are shown in Figure 4.40. In the case of Si$_{40}$C$_{16}$N$_{27}$O$_{15}$ (**SiCNO2**), all absorption bands related to Si-O vibrations were seen in the layers grown at high temperatures of 1100 and 1200°C, while only the strongest stretching asymmetric and rocking bands appeared at lower temperatures. At 700°C, only the strongest stretching asymmetric vibration can be detected, whereas at lower temperatures, the signal falls to noise levels indicating no detectable oxide formation. In the case of the boron-containing Si$_{33}$B$_8$C$_{19}$N$_{27}$O$_{13}$ (**SiBCNO3**), both the dominant Si-O bands as well as two more bands, which were related to the asymmetric stretching and bending of Si-O-B bonds at about 920 cm^{-1} and

675 cm^{-1}, respectively, were observed. These bands were commonly observed in borosilicate glasses [257,258].

All TO bands of the Si-O bond appeared to be asymmetric with large band widths. By increasing the annealing temperature, this band became more intense and was blue-shifted to higher frequencies. This is similar to the ones obtained from thermally grown SiO$_2$ formed on Silicon and unlike those bands pertaining to crystalline quartz. This indicates that the bonding structure affecting the IR absorption is similar to the one found in amorphous SiO$_2$. Furthermore, due to the asymmetric peak profile of the stretching absorption band, which was centred approximately in the region 1020- 1084 cm^{-1}, the peak can be best deconvoluted into two Gaussian profiles [259]. One peak appears at a lower frequency at 1059 cm^{-1} while another is located at a high frequency of 1092 cm^{-1}. These peaks are commonly designated to antisymmetric components AS1-TO and AS2-TO, respectively. At wavenumbers higher than 1100 cm^{-1}, two more additional Gaussian profiles were required to fully fit the band. The positions of each Gaussian sub-peak are listed in Table 4.6 and the result of peak deconvolution is shown in Figure 4.41(a-b). The position of each Gaussian sub-band is plotted against the annealing temperature for both films in Figure 4.41(c). It can be seen that the band position shifts to higher frequencies with increasing the annealing temperature. The existence of two bands indicates that the oxide layer contains two types of Si-O bonding structures. The structures that are associated with these two bands may also be non-homogenously distributed across the oxide layer thickness. The blue-shift in both peaks (AS1-TO and AS2-TO) can be associated with increasing the oxide layer thickness as would be expected to occur as the annealing temperature increases. Previous observation made on thermal SiO$_2$ oxides grown on silicon also confirmed this complex band structure [260].It has already been established that in the case of SiO$_x$ layers, the frequency of the asymmetric stretching vibration scales linearly with respect to the oxide's stoichiometry (i.e. x in the formula SiO$_x$) [261,262,263,264] as follows: x $\approx$ A (ν(Si-O) cm $-$ B. With A and B = 0.011 and 0.02, respectively, or being 0.02 and 19.3, respectively according to other observations [265,266,267]. Regardless of the exact values of these coefficients, it was clear that the band position changed as a function of stoichiometry and that for stoichiometric SiO$_2$ a band position of about 1065 cm^{-1} was observed as opposed to the situation in the oxide thermally grown on silicon showing values in the range 1075- 1080 cm^{-1}.
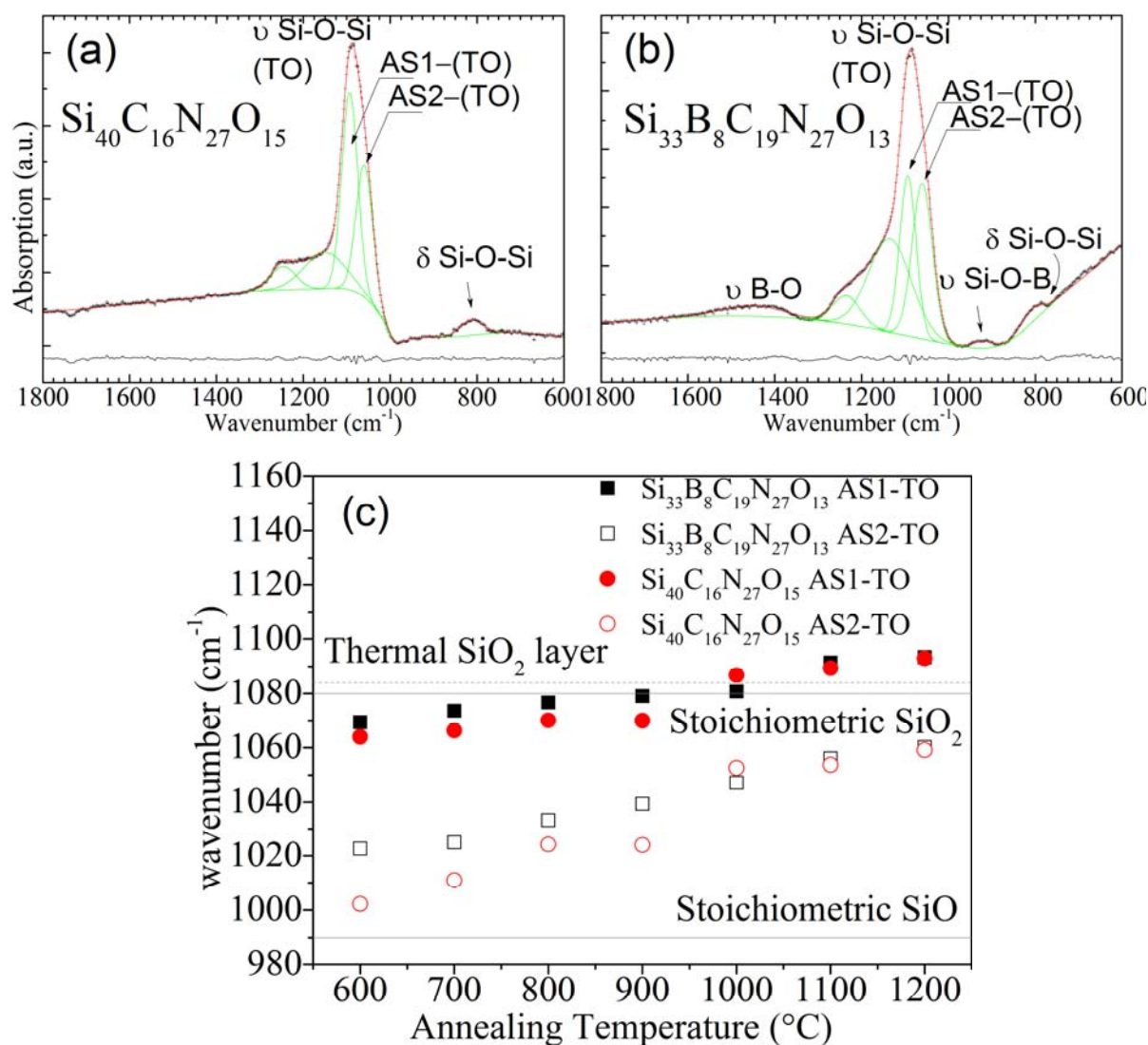
Figure 4.41: Gaussian peak deconvolution of the asymmetric stretching and bending absorption bands of the Si-O-Si group in the oxide scale, which developed on (a) SiCNO2 and (b) SiBCNO3 films at 1200°C. With regards to the oxide scale on the SiBCNO film, additional contributions related to the asymmetric stretching of Si-O-B bonds appear at about 920 cm^{-1} as well as the very broad contribution of the B-O bonds around 1452 cm^{-1}. (c) The band position of AS1 and AS2 TO of the Si-O-Si group in the oxide scale which developed on both SiCNO and SiBCNO films as a function of annealing temperature.

B   The B-O absorption band

The B-O bonds in the oxide network have their characteristic absorption bands in three regions: (i) the first group, which arises from the asymmetric stretching vibrations of the bonds in trigonal BO_3 units, lies in the region 1200- 1600 cm^{-1}, (ii) the second group appears in the region 800-1200 cm^{-1} and originates from the B–O bond stretching in tetrahedral BO_4 units. (iii) the third group, which appears in the region between 550- 710 cm^{-1}, is due to B–O–B bending in the borate network. Variations in the exact band position depend on changes in the local structure surrounding the B-O-B group. These bands have often been observed in borate-based glasses

[268], and in vitreous B_2O_3 [269] at about 720 cm^{-1}, 1260 cm^{-1} and 1420 cm^{-1}, and were attributed to the B-O bonds vibrations in the BO_3 structural units.

Upon examining the oxide scale which developed on the SiBCNO films, it was particularly difficult to spot the symmetric stretching of the B-O bonds clearly. This was due to their strong overlap with the Si-O-Si stretching vibrations whose intensity dominated the FTIR absorption spectra. Both asymmetric and bending vibrations of the B-O-B bonds, on the other hand, lay distinctly away from the regions of Si-O and Si-O-B bonds in the wavenumber range 520-800cm^{-1}. This allows for an unambiguous determination of their positions and line shapes. A comparison between the SiCNO and SiBCNO films revealed that the B-O related vibrations are only evident in the boron-containing film. Figure 4.42 shows part of the subtracted spectra of the oxide scale developed on both films at 600 and 1200°C. The B-O bands are evident in the SiBCNO film and not in the SiCNO one. Accordingly, the B-O-B bending vibrations were detected in the oxide scale of the annealed SiBCNO films at temperatures as low as 600°C. Figure 4.42 also shows the development of these bonds on the oxide scale of the annealed **SiBCNO3** films as the temperature increased up to 1200°C. The spectral profiles collated from the oxide scales on the SiCNO films at the same temperatures were clearly different and did not contain the same contributions from the B-O bonds. The exact band position and full width at half maximum, which were obtained from the least squares parameter fitting of the peaks to a Gaussian function are also shown in Table 4.6. The diagram shows how the intensity of the vibration increases with increasing the annealing temperature.

It is clear from the FTIR results that the oxide scale in case of the SiBCNO films contains two network formers: Si-O and B-O bonds, and evidence of the presence of Si-O-B bonds indicate how these networks may be linked. Clearly the lower intensity of the B-O bonds is a result of the **SiBCNO3**'s lower boron content as opposed to silicon ($Si_{33}B_8C_{19}N_{27}O_{13}$). However, a different scenario arises when considering their evolution relative to the Si-O bond formation. The change in the ratio of the peak area, which corresponds to the B-O-B bending and the adjacent Si-O-Si rocking vibrations as the annealing temperature increases, is depicted in Figure 4.43. The behaviour is parabolic showing a maximum between 800° and 900°C, which corresponds to the highest intensity emerging from the B-O bonds. The increase in the ratio indicates a greater proportion in the fraction of B-O bonds in the oxide at temperatures below 900°C. As the annealing temperature increases further, the Si-O bonds become the more dominant bonds in the oxide, which in turn, decreases the peak area ratio. This observation can be attributed to two factors: the first is that in the SiBCNO film the boron atoms are more prone to bonding with oxygen at lower temperatures. This shows an increase in the intensity of their respective bands

which corresponds to the bending vibration of the group B-O-B. This is reversed at higher temperatures, as Si-O bonds dominate the oxide structure. The second is that the decrease in the proportion of the B-O bonds in the oxide at higher temperatures may be attributed to the volatilisation of the BO_x species. This effect was previously discussed in the context of ToF-SIMS depth profiling, which revealed that the oxide layer exhibited a gradient in the concentration of the BO species across its thickness. This shows that the results from both FTIR and ToF-SIMS are in agreement with regards the distribution of the boron oxide species in the oxide layer which developed on SiBCNO films at high temperatures.
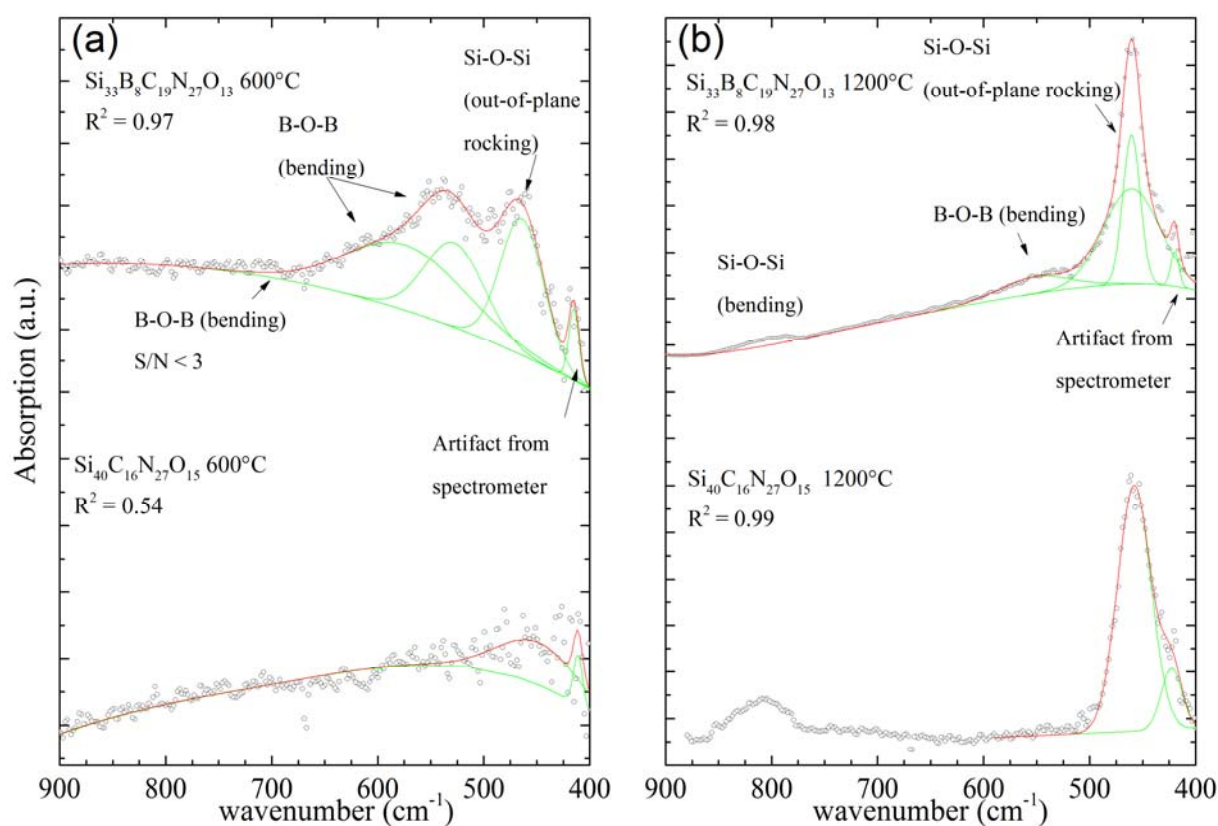
Figure 4.42: The evolution of the bending B-O-B vibrations in the oxide scale which developed on SiBCNO3 films as a function of temperature. The spectra corresponding to oxides on SiCNO are added for comparison. Fitting quality is given as R^2 values.

SiCNO2	600°C	700°C	800°C	900°C	1000°C	1100°C	1200°C
	υ/cm^{-1} (Γ/cm^{-1})	υ/cm^{-1} (Γ/cm^{-1})	υ/cm^{-1} (Γ/cm^{-1})	υ/cm^{-1} (Γ/cm^{-1})	υ/cm^{-1} (Γ/cm^{-1})	υ/cm^{-1} (Γ/cm^{-1})	υ/cm^{-1} (Γ/cm^{-1})
υ(Si-O-Si)1	1064(69)	1066(65)	1070(66)	1070(59)	1087(45)	1089(46)	1093(43)
υ(Si-O-Si)2	1002(34)	1011(70)	1024(44)	1024(147)	1053(41)	1054(46)	1059(45)
δ(Si-O-Si)		711(193)	75297 ()	788(113)	798(37)	812(45)	813(61)
r(Si-O-Si)			461(34)	465(24)	463(21)	458(35)	458(37)

SiBCNO3	600°C	700°C	800°C	900°C	1000°C	1100°C	1200°C
υ(Si-O-Si)1	1069(66)	1074(78)	1077(66)	1079(65)	1081(62)	1091(50)	1093(44)
υ(Si-O-Si)2	1023(139)	1025(119)	1033(103)	1039(106)	1047(86)	1056(51)	1060(55)
δ(Si-O-Si)						809(50)	809(56)
r(Si-O-Si)	464(48)	461(41)	468(21)	460(21)	458 (39)	460(28)	460(19)
υ(Si-O-B)	957(111)	937(127)	930()127	931(103)	934(75)	930(54)	922(48)
δ(Si-O-B)							698(79)
δ(B-O-B)1	464(48)	461(41)	462(21)	460(21)	458(39)	460(28)	460(19)
δ(B-O-B)2	528(66)	537(120)	525(139)	528(151)	533(103)	543(100)	552(78)
δ(B-O-B)3	574(132)	629(60)	657(168)		617(51)		

Table 4.6: The exact band positions and full width at half maxima, which were obtained from the least squares parameter fittings of the peaks to a Gaussian function of the Si-O and B-O related bond vibrations. The first value corresponds to the band frequency in cm^{-1}, whereas the value in brackets corresponds to the full width at half maximum in cm^{-1}.
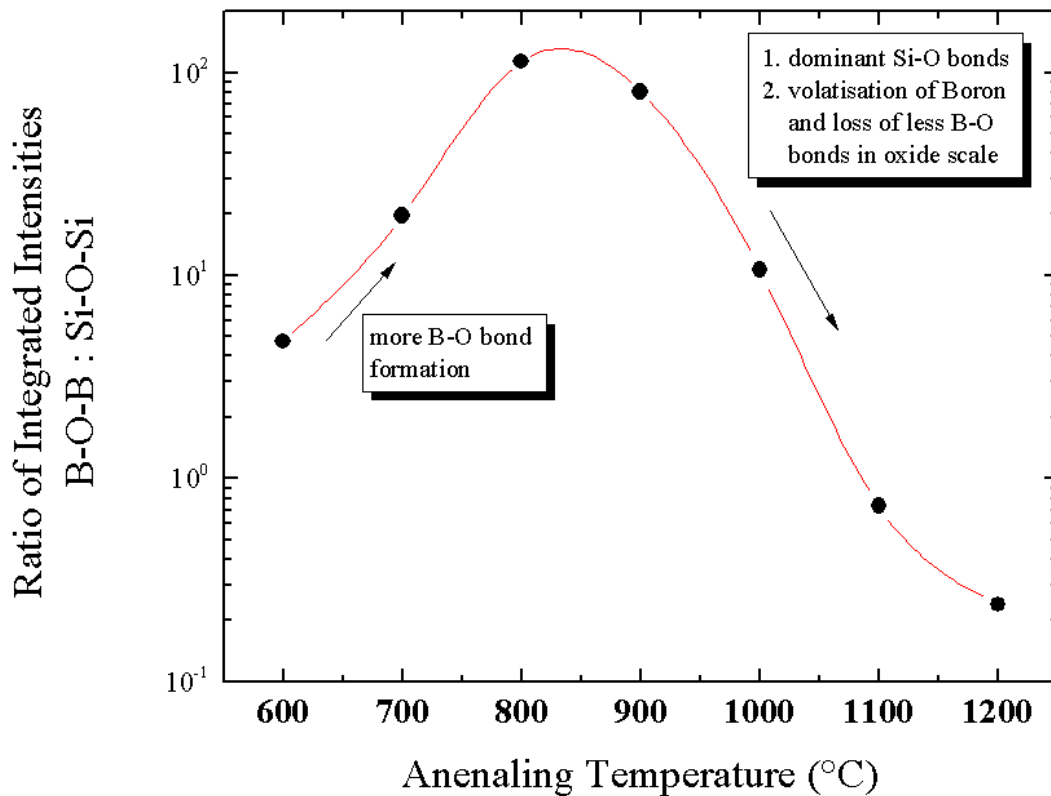
Figure 4.43: The peak area ratio which corresponds to the bending B-O-B and rocking Si-O-Si in oxides developed on the SiBCNO3.

4.7.4   Summary of surface chemical bonding changes as a result of annealing

4.7.4.1   Up to 500°C

The PCA treatment of the ToF-SIMS data proved to be a very useful tool in investigating the changes to chemical composition in the films' surface in an efficient and speedy fashion. The usefulness of PCA lies in its ability to reduce the dimensionality of a complex system, such as the datasets obtained from TOF-SIMS spectra, by installing a new set of coordinates which could then be used to explore and monitor the variations in the data. In addition, correlating the trends of the measured signal intensities and scores on PC1 is based on the valid assumption that the signal intensity is directly proportional to the concentration of those particular secondary ions in the film, provided that the ionisation probability of the species is unchanged in different samples. This is a valid assumption, in this case since the chemical bonding network and the matrix effects remain the same for the various films [270].

Figure 4.26 and Figure 4.30 show the PCA-generated new coordinates, which reveals that the main Principal component (PC1) captured the highest variance in spectra of 55.0% and 64.3% for the SiCNO and SiBCNO films, respectively. Accordingly, these axes can be used reliably to interpret most of the ToF-SIMS data. The scores on PC1 which were obtained from both film types increased as a result of the heat treatment. In the case of SiCNO, the spectra from the as-deposited films have the highest proportions of H- and O-containing molecular anions as opposed to the annealed surfaces. Once the film is heated to 100°C, a noticeable drop in the signal intensity from these species is evident indicating a change in the compositional state of the surface. Figure 4.28 illustrate how the signal intensities of the species: H(1.008 amu/z), C(12.000 amu/z), together with that of O(15.995 amu/z), SiO_2(59.969 amu/z) and SiO_3(75.969 amu/z) are highest for the as-deposited films. A similar trend is observed in the signal intensities from C_2O, CNO and CNO_2. On the other hand, while the signal intensities from the O-containing species drop, that from the hydroxyl-containing ones such as: OH(17.003amu/z), SiOH(44.98amu/z), SiO_2H(60.977 amu/z) and SiO_3H(76.97 amu/z), increases initially after annealing at 100°C before continuing to drop steadily at higher annealing temperatures. These spectral features point to a major difference in the chemical species that are detected by ToF-SIMS and therefore indicate that the composition of the films' uppermost layers changes as a result of annealing.

The high proportion of O-containing species is in fact not unusual for vacuum-deposited amorphous films due to the presence of significant amounts of dangling bonds. These tendencies are practically reversed when it comes to OH-containing species such as OH, SiOH, SiO_2H and SiO_3H. Post-deposition annealing between 100°C- 200°C could have two effects on the film's

surface: the first is that any loosely bonded and physisorbed contaminants with low vapour pressure will be cleared away by volatilisation. The second is that any chemically bonded (chemisorbed) moieties arising from deposition precursors will have hydrolysed at these temperatures. It should be recalled here that tetramethyl silane $(Si(CH_3)_4)$, which is used as the silicon precursor during film growth, hydrolyses partially in humid air at room temperature and elevated temperatures since they act as Lewis acids. Consequently, an increase in the signal intensity from OH-containing species could be observed when annealing takes place in ambient air with RH of ca. 55%. These species, however, will tend to de-populate the surface as a result of decomposition when the temperature rises beyond 200°C, causing their signal intensities to decrease further.

A similar scenario is observed in the case of the B-containing films. The ToF-SIMS spectra taken from the upper layers of the as-deposited SiBCNO show the highest signals from two types of secondary anions: the first is related to H- and O-containing species, whereas the second belongs to the signal from the free carbon species such as C (12.000amu/z) and C_3 (35.999amu/z) secondary anions. The signal intensities of those secondary anions drop sharply in the spectra which are obtained from the annealed films. With regard to the O-containing secondary anions such as: O (16.003 amu/z), NO (29.99 amu/z), C_2O (39.9951 amu/z), BO_2 (43.008 amu/z), and SiO_2 (59.97 amu/z), as the annealing temperature increases there is an initial sharp drop in the signal obtained from those secondary anions. This is followed by a slight increase which could be marking the oxidative change to the films surface. This can be clearly seen in Figure 4.31.

In addition, the spectra of the annealed surfaces show a specific trend with respect to the secondary anions: BOH (28.003 amu/z), B_2OH (39.024 amu/z), BNO (40.011 amu/z), B_2NO (52.02 amu/z), and SiCO (55.97 amu/z). The trend shows how the spectra from as-deposited samples have the lowest signal intensities of these anions whereas that obtained from the film after annealing at 100°C have the highest.

4.7.4.2   Between 600°C and 1200°C

As the temperature increases to 500°C, a continual increase in the amount of O-containing species from the surface spectra is observed, which signifies the onset of changes to the chemical bonding in the surface. The detection of SiO-containing species from the SiCNO films, as well as SiO- and BO-containing ones from the SiBCNO films, coupled with the increase in the thickness of the O-rich layer to about 5 nm, which is roughly double that formed at 100°C, all help to reflect this change. This trend continues and even increases gradually until the temperature

approaches 900°C. Apart from these changes, the chemical bonding and structure of the bulk of the film remain virtually unchanged.

As 900°C the oxide scale formed on SiBCNO is about three times as thick as that of the SiCNO films. This is also confirmed by HRTEM imagery performed on SiBCNO films which showed an oxide scale in the order of 85 nm at 1000°C. Furthermore, both oxide layers remain amorphous in nature and have a composition which is predominantly SiO_x as is the case in the SiCNO and $SiO_x \cdot BO_y$ in SiBCNO films. In the case of SiBCNO, a gradient in the film composition is detected, which reveals a silicon oxide-rich uppermost layer and a boron oxide-rich region near the interface with the bulk of the film. This was corroborated by both ToF-SIMS depth profiles as well as the change in the relative intensities of the Si-O and B-O bond vibrations seen in the FTIR spectra. Additionally, the oxidation process of SiBCNO films involves the formation of B_xO_y species which are partly volatile at temperatures higher than 500°C. Several oxide species leave the SiBCNO films during oxidation, which cause the resultant oxide layer that has formed on the film to be divided into the two aforementioned distinct regions.

In addition, the IR band deconvolution of the Si-O bonds indicates relatively broad band widths in the oxide scale on both film types. This is similar to the wide bands from the amorphous silicon oxide, which is thermally grown on silicon substrates. The stoichiometry of the oxide layer on developed SiCNO and SiBCNO films tends to change as a function of the annealing temperature. At temperatures lower than 900°C, the silicon oxide in both films appears to be sub-stoichiometric, whereas at higher temperatures, the oxide shows a stoichiometry very similar to that of the stoichiometric SiO_2. Apart from the development of an oxide scale, there are no changes to the chemical bonding in the bulk of both films, and structurally, the bulk of all the films remain unchanged up to a temperature of 1200°C.

4.7.5   Film Morphology and Microstructure

Cross-section SEM micrographs of SiCNO and SiBCNO films on a silicon substrate, both before and after the annealing treatment at 1000°C, are shown in Figure 4.44. The fracture micrographs demonstrate no distinct differences between both states of the film, with both fractures appearing featureless, which is indicative of the amorphous character of both film types before and after annealing. The micrographs showed no evidence of material loss, as measurements of film thickness reveal that both films are essentially the same. The slight variation in the thickness measurement from that of the original film thickness, which is no more than 3- 5%, falls perfectly within the percentage margin of error deemed acceptable when determining thickness using SEM. It is noticeable, however, that there is no apparent materials

loss as a result of oxidative annealing treatment at 1000°C for 90 min. In fact, the implemented annealing programme, which included a heating rate of 10°C/min., a dwell time of 90 min. at the maximum temperature, as well as a much slower cooling rate, ensured that the films were exposed to the high temperature oxidative conditions (T >650°C in ambient air) for more than 120 min.. This demonstrates an outstanding resistance to oxidation and degradation.
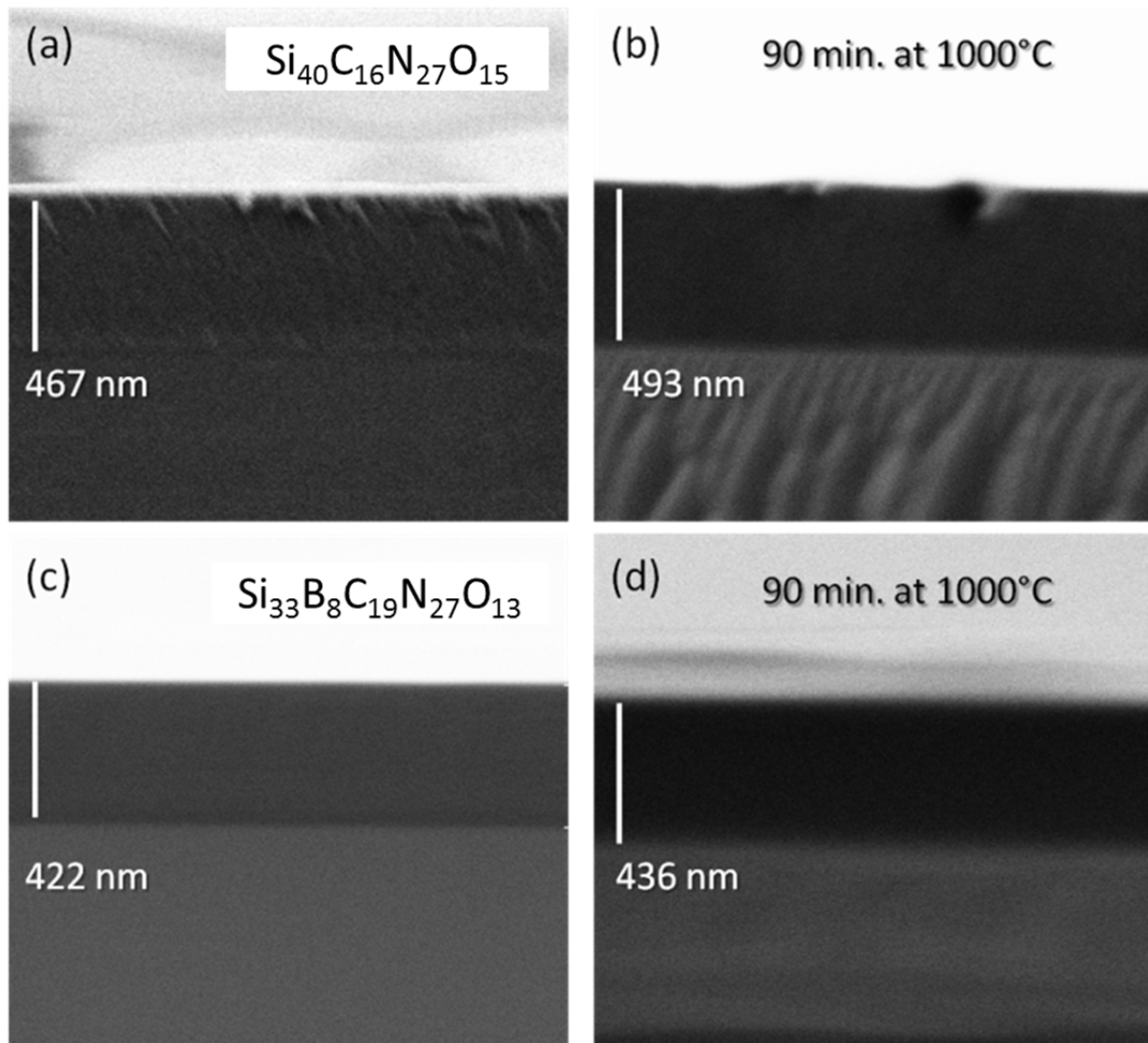
Figure 4.44: FE-SEM fracture micrographs of SiCNO and SiBCNO films on Si substrates before and after annealing at 1000°C.

Further examination of the oxidised films by cross sectional HRTEM investigations indicated that these films form an oxidation scale and that both the bulk of the film and the oxide scale are totally amorphous. Figure 4.45(a) shows a cross-sectional TEM micrograph of an SiBCNO of the composition ($Si_{33}B_8C_{19}N_{27}O_{13}$) after oxidation at 1000°C. The colour contrast between the bulk of the film and the oxide scale is apparent and is indicative of the formation of a thin layer, which has a different electron density than the bulk of the film and whose thickness is in the order of 85

nm. The total film thickness of about 538 nm is close to the values obtained from fracture SEM micrographs. Figure 4.45(b) and (c) represent the high resolution micrograph and the fast Fourier transform (FFT) patterns recorded from the corresponding enclosed area, both of which were taken from the upper 85 nm section corresponding to the oxide layer. The diffused halo in the FFT pattern, which corresponds to the oxide layer, indicates a totally amorphous region. These observations are in agreement with the X-ray diffraction patterns collected from the annealed films at the same temperature (cf. Figure 4.39(b)).

While the details of the chemical composition were presented in detail in section 0, it would be worth reiterating that the elemental composition of the oxide scale, which corresponds to the TEM micrograph shown in Figure 4.45 is composed chiefly of the elements Si, B and O. The ToF-SIMS depth profile obtained from the annealed film is shown in Figure 4.44(d). The signal intensities of Si^- (28 amu/z), B^- (11 amu/z), C^- (12 amu/z) and SiN^- (42 amu/z) and SiO_2^- (60 amu/z) secondary anions, which are representative of the elements Si, B, C, N and O, respectively, were recorded as a function of sputtering time. The intensities of Si^-, B^- and SiO_2^- secondary anions were particularly higher in the first 160 s in comparison with those of C^- and SiN^-. The latter were considerably higher after 170 s. The increased signal intensities of Si^-, B^- and SiO_2^- indicate a higher content of the elements Si, B and O in the upper part of the film after oxidation at 1000°C. This corresponds to an oxide scale which is mainly composed of Si-O-B bonds and is much poorer in C and N. After about 170 s of sputtering the oxide scale, the intensities of Si^- and B^- decreased slightly whereas that of SiO_2^- decreased sharply, which signifies the diffusion limit of oxygen in the film. The signal intensities of C^- and SiN^- increased considerably to levels similar to those of the un-oxidised film. These observations corroborate the results of the HRTEM imagery.
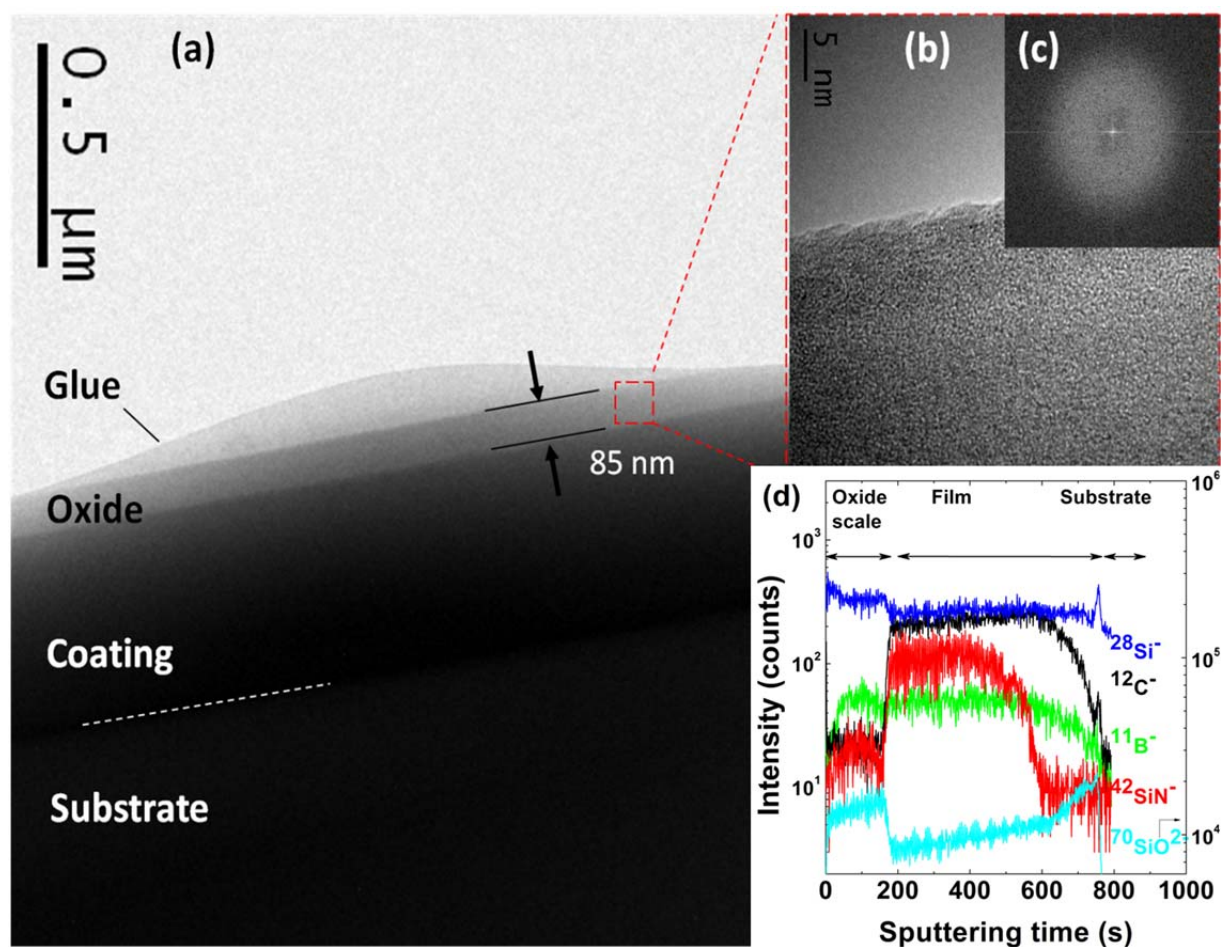
Figure 4.45: (a) A cross-sectional HRTEM micrograph of $Si_{33}B_8C_{19}N_{27}O_{13}$ after oxidation at 1000°C. (b) A high resolution image of the oxide scale. The enclosed area in the upper region of the oxide scale is used for FFT image calculation in (c). (d) The ToF-SIMS depth profile obtained from the same film and which corresponds to the images in (a).

4.7.6 DSC-TGA-MS Analysis

The oxidation behaviour of the films was investigated in ambient air up to a temperature of 1350°C by DSC and TGA. The behaviour was assessed by measuring two quantities: the first was the heat flux generated throughout the oxidation process, and the second was the weight change as a function of exposure time. The heat flow signal (DSC) is based on the determination of the temperature change during the process between the specimen and a reference material and corresponds to the heat flow from or into the specimen. In this investigation, three films with various B-content ranging from 0- 25at.%B (cf. Table 4.7) were studied in order to assess their oxidation resistance and to monitor any changes to the oxidation behaviour as a result of changing the film composition.

The DSC curves in Figure 4.46 belong to several films with various boron contents and feature no sharp signals, with quite broad maxima corresponding to exothermic reactions which are

taking place. For the B-containing films, **SiBCNO4** and **SiBCNO5**, there was a steeper increase in the DSC signal between 720°C and 840°C unlike that of the **SiCNO2**. All curves showed exothermic oxidation processes whose onset temperature could not be marked at a specific point. Similar observations were reported for polymer-pyrolysis boron-containing nitride ceramics [271]. At temperatures approaching 1200°C, the slope of DSC signals decreased and flattened before it dropped slightly at about 1340°C for all films, which could indicate the end of film oxidation. Figure 4.47 illustrates the percentage change in mass of both SiCNO and SiBCNO films versus the annealing temperature. It can be clearly seen that all films exhibit a very small mass change that does not exceed 3% for **SiCNO2** and 2% and 1% for the B-containing **SiBCNO4** and **SiBCNO5**, respectively, which was measured over the entire temperature range. The tendency shown by the weight change followed a very similar pattern to that of the DSC signals. There was a slight mass increase in **SiBCNO4** and **SiBCNO5** up to the temperature of 400°C, which was interrupted by a region of mass loss between 410°C and 700°C before it increased further at higher temperatures and maintained a relatively constant value. For the **SiCNO2** film, the mass increased monotonously up to 1200°C before it levelled off without any intermediate periods of mass loss.

Film	Elemental composition (at.%)[*]	BF_3 flow rate (sccm)	B/Si ratio	B/C ratio
SiCNO2	$Si_{40}C_{16}N_{27}O_{15}$	0	0	0
SiBCNO4	$Si_{15}B_{25}C_{15}N_{33}O_{10}$	1.15	1.7	1.7
SiBCNO5	$Si_6B_{22}C_{39}N_{20}O_8$	0.29	3.7	0.6

Table 4.7: The elemental composition of the films which are subjected to oxidative annealing treatment in ambient air up to 1350°C. (*) The elemental composition of the SiBCNO4 and SiCNO5 films is determined from EDX data, whereas that of the SiCNO2 film is determined by XPS measurements.

In order to explain the change in mass which accompanied the annealing treatment, the resultant effluent gas stream was analysed *in-situ* by a quadrapole mass spectrometer which was implemented in conjunction with DSC-TG analysis. The simultaneously collated mass spectra were used to mark any changes in composition as a result of oxidation in the entire temperature range. The displayed spectra were smoothened using the adjacent averaging method in order to exclude outliers and noise-related roughness. Figure 4.48 shows the evolution of CO_2, NO, as well as some B-containing species which emerged as gaseous products as a result of the oxidation process. In the case of **SiCNO2**, the signal intensity from CO_2 (44 amu/z) decreased initially, as a result of degassing the system (heating chamber and cannula) and maintained a constant value until a temperature of 1100°C was reached. Thereafter, the signal intensity rose sharply as in the

case of NO (30 amu/z) which was associated with the oxidation of the SiCNO film. In contrast, the mass spectra from the B-containing films showed additional signals that corresponded to the species H_2BO_2 (45 amu/z), B_2O_2 (54 amu/z), $H_2B_2O_3$ (70 amu/z) and $H_2B_2O_3$ (72 amu/z), which were observed to have developed as a result of oxidation.

Figure 4.49 shows that the increase in the B_2O_2 signal was first discernible at about 420°C and reached its maximum twice at temperatures of 600°C and 1150°C. The signal which corresponded to $H_2B_2O_3$ followed a similar pattern. The increase in those signals is parallel to the small dip observed in the mass change of **SiBCNO4** at 492°C with a later broader signal starting at about 950°C. The increase in the signals from these boron oxide species is even more pronounced in the case of **SiBCNO5** film as can be seen from Figure 4.50, wherein the three observed maxima between 625°C- 825°C, at 890° and after 1230°C are well correlated with the mass loss periods in the TG curve at nearly the same temperatures. In contrast, the signals obtained from the mass spectra of **SiCNO2** at the mass number 54 amu/z and 70 amu/z remained flat throughout the entire annealing range without any detectable intensity change as would be anticipated from the B-free film. The signals from NO (30 amu/z), which was released from **SiBCNO4** and **SiBCNO5**, followed a similar pattern to that of **SiCNO2** with a sharp increase in its signal at the temperature of 1100°C. On the other hand, the CO_2 (44 amu/z) released from **SiBCNO4** followed a pattern similar to that of **SiCNO2**. The trend observed in **SiBCNO5** showed that CO_2 increased its intensity much earlier at around 400°C and maintained a constant level throughout the rest of the temperature range.

In view of the above, the mass spectra which are collated simultaneously as the films are annealed provide useful data that can explain the difference in the oxidation behaviour of the amorphous ceramic films. The clear correlation between the mass change and the mass spectra of the affluent gases provides a more detailed understanding of the TG curves. Although in general, all films had increased their mass as a result of oxidation, the intermediate periods of mass loss from the B-containing films differentiate them distinctly from the SiCNO film. Overall, the mass increase is due to the fact that in the oxidation of a carbide or nitride, heavier oxygen atoms (16 g/mol) substitute the lighter C (12 g/mol) and N (14 g/mol) atoms in the ceramic, which corresponds to a mass increase of 33% and 22%, respectively. It is therefore expected that Si-based ceramic films would increase their mass as a result of oxidation. However, the mass loss periods in the B-containing films are due to the fact the several boron oxide species are in fact volatile at temperatures exceeding 400°C. This explains the onset of mass loss between 450°C and 490°C as the resultant H_2BO_2 (45 amu/z) and B_2O_2 (54 amu/z) evaporate from the surface causing the overall mass to drop slightly. Additionally, at higher temperatures, B_2O_3 (70 amu/z) and $H_2B_2O_3$

(72 amu/z) are also detected at temperatures exceeding 900°C, which correlates with another period of mass loss in the SiBCNO films.
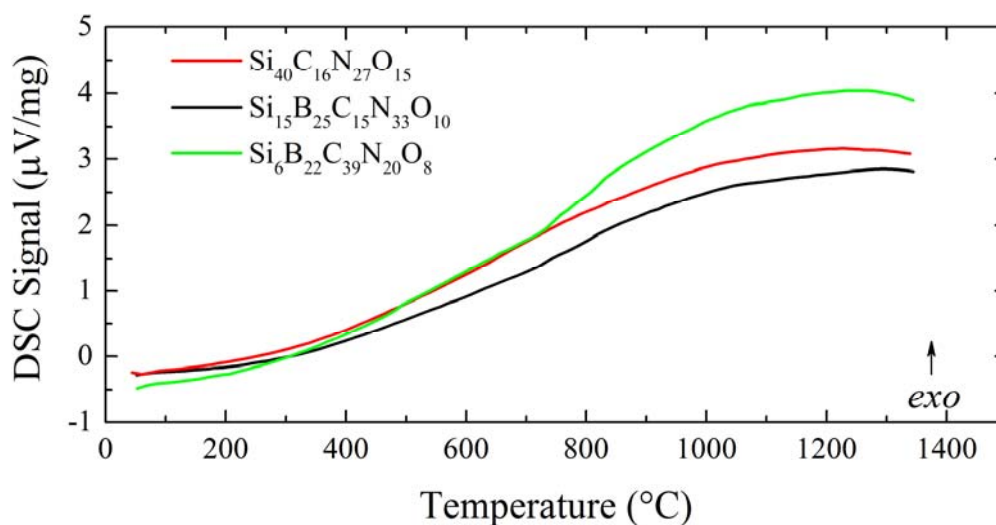
Figure 4.46: DSC curves of SiCNO2, SiBCNO4 and SiBCNO5 measured at a heating rate of 5°C/min in ambient air.
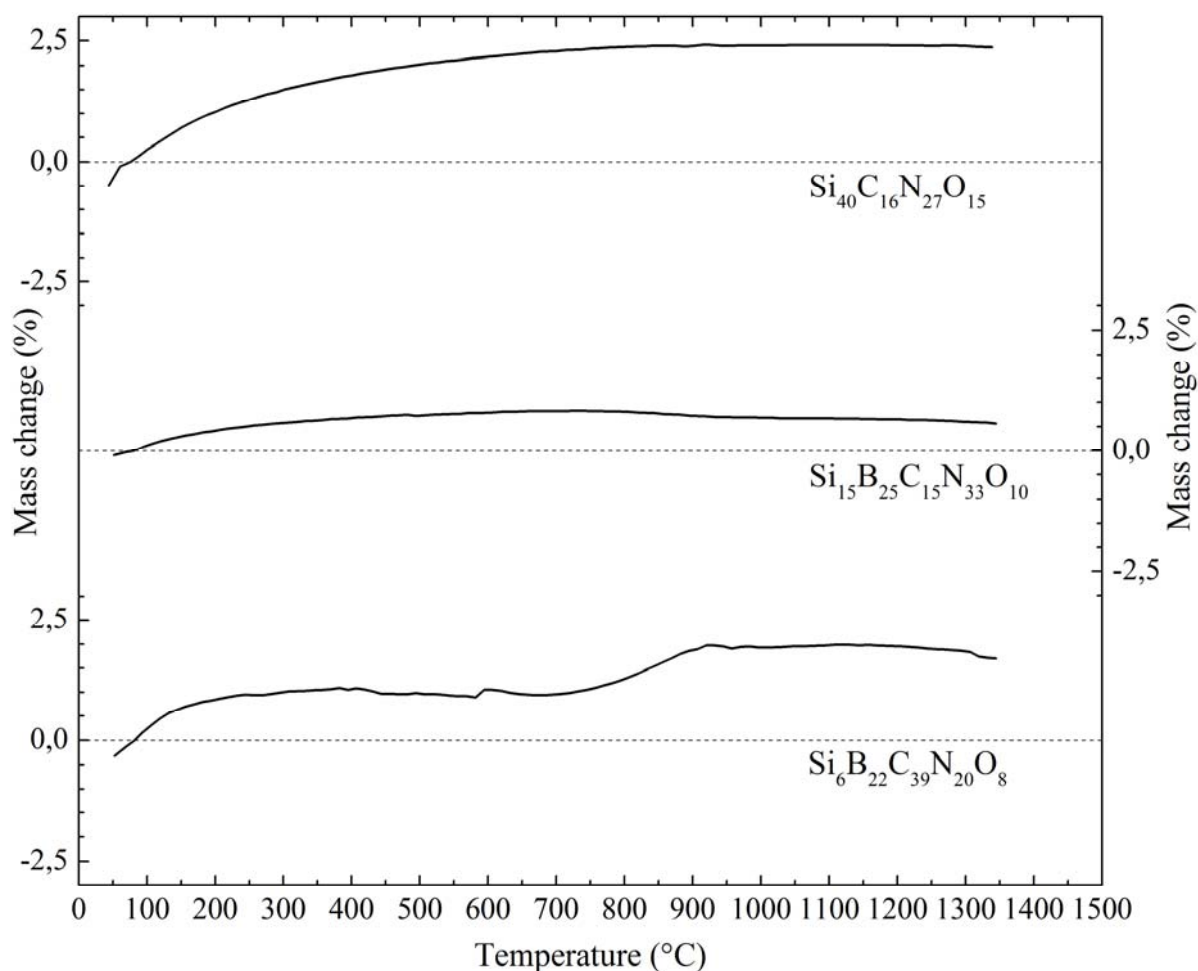
Figure 4.47: TG curves of SiCNO2, SiBCNO4 and SiBCNO5 measured at a heating rate of 5°C/min in ambient air.
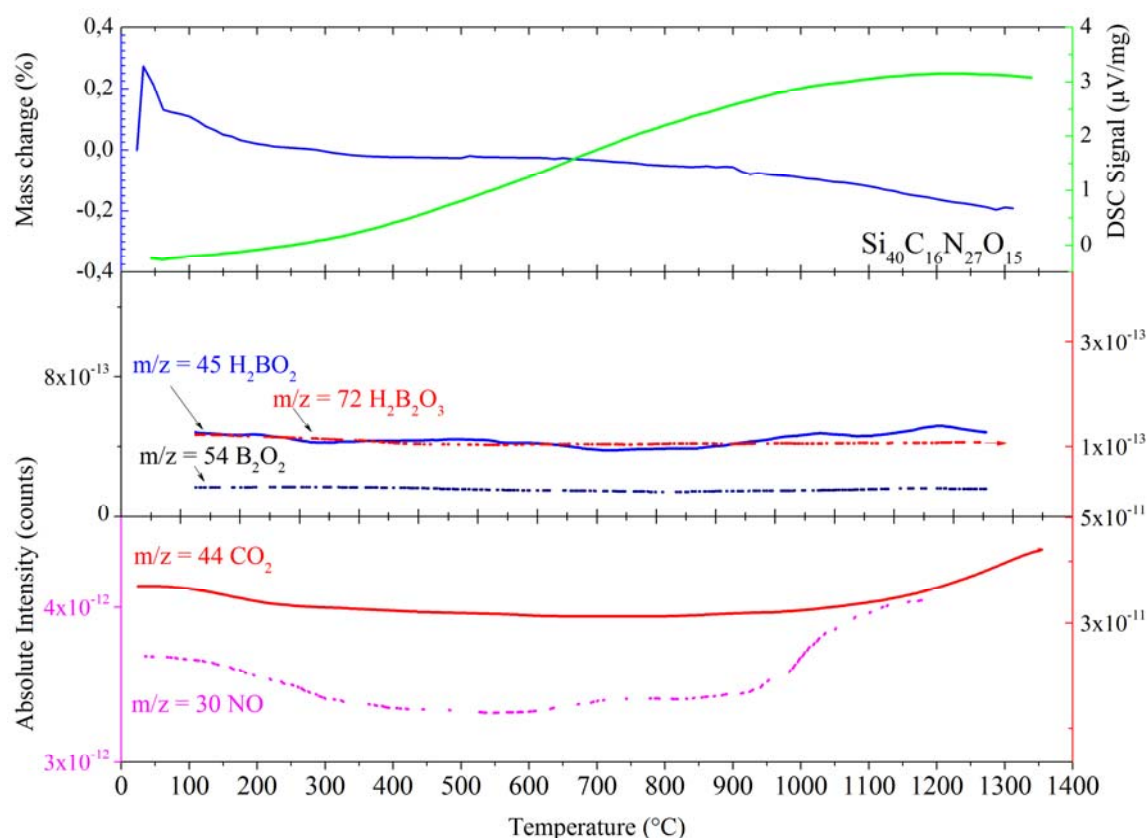
Figure 4.48: The evolution of various gas species that are detected throughout the annealing of film SiCNO2 in the temperature range RT- 1340°C.
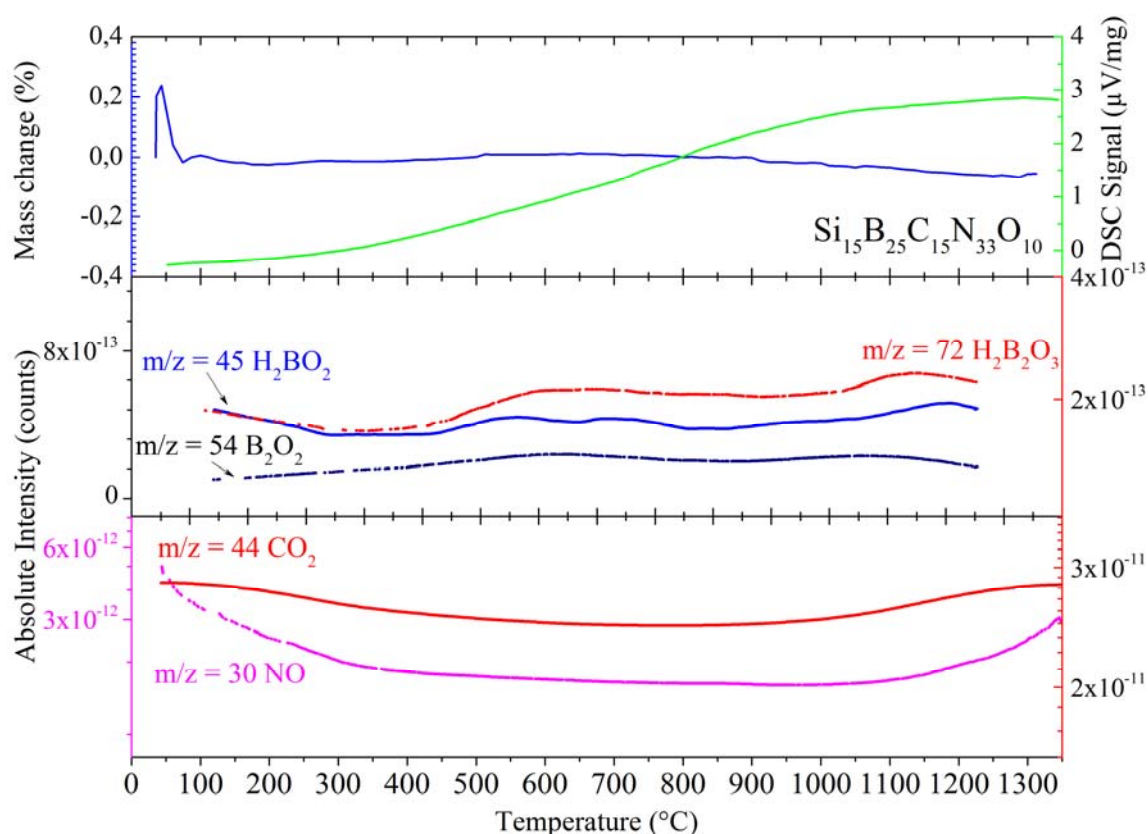
Figure 4.49: The evolution of various gas species throughout the annealing of the SiBCNO4 film which are detected in the temperature range RT- 1340°C.
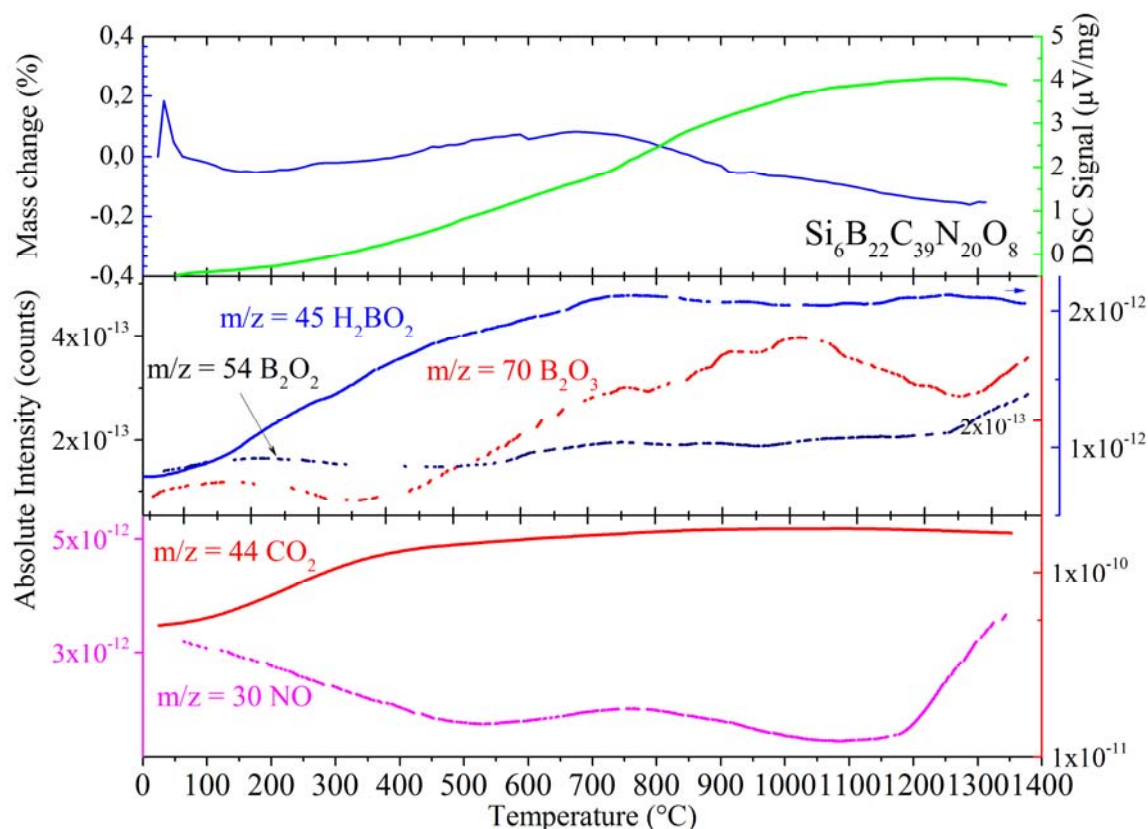
Figure 4.50: The evolution of various gas species as throughout the annealing of the SiBCNO5 film which are detected in the temperature range RT- 1340°C.

These results corroborate those which were obtained from both the FTIR absorption spectra and the surface-sensitive ToF-SIMS depth profiling. These revealed that the protective oxide layer which formed on the SiBCNO films is in fact composed of two regions: an uppermost region which is deprived of boron and another inner part which is boron-rich. These observations are not unique to the films which were prepared in this work as these same observations have been previously made regarding a number of other SiBCNO ceramics [272, 273]. Despite the similarities between these two SiBCNO films, the larger mass loss encountered with the **SiBCNO5** film in the lower temperature range, and the increase in the signals released from CO_2 at about 400°C, indicate that the loss of carbon at this lower temperature could be related to the oxidation of some graphitic carbon nitride or carbon. This would be anticipated from a film with high carbon content such as **SiBCNO5**. Finally, despite the overall mass change in the films investigated in this work, it should be noted that during the heating and cooling cycles, these films were exposed to high temperature oxidative conditions for more than 7.6 hours at temperatures above 650°C. This demonstrates an outstanding resistance to oxidation and degradation.

4.8   Conclusions

Results demonstrated how it is possible to obtain totally amorphous, hard, adhesive and thermally stable SiCNO and SiBCNO films, which could be synthesised by means of ECR-MWCVD using a gas mixture of $Si(CH_3)_4$, CH_4, BF_3 and N_2 in a H_2-He rich plasma. The film boron and carbon content can be varied by adjusting the flow rate of both CH_4 and BF_3 during growth. A wide range of adhesive and X-ray amorphous SiCNO and SiBCNO can also be synthesised at low substrate bias and moderate substrate temperatures. Due to the ECR's high plasma density and high ion bombardment of the growing surface, amorphous films were always obtained despite the fact that moderately high temperatures were implemented. As a result, dense films can be grown with a very low surface roughness with both demonstrating high durability.

Because of the fact that the investigated films were totally amorphous and consisted of light elements, it was necessary to adopt a combinatorial analytical approach to elucidate the complex bonding nature of such materials. XPS, FTIR and ToF-SIMS analyses revealed that both film types exhibited a complex chemical bonding structure. The implementation of HAC and PCA analysis in conjunction with ToF-SIMS spectrometry proved very useful in maximising the amount of information which could be extracted from the spectra. This allowed successful correlations between these analytical methods to be made and helped in shedding more light on the complex bonding situation in these materials. In the case of SiCNO films, oxygen was bonded to silicon and the structure was dominated by SiC_xN_y units with relative proportions of both C and N depending on the flow rate of CH_4. These units appeared to be interconnected by graphite-like C and N multiple bonds. In contrast, SiBCNO was formed upon the addition of BF_3 to the reaction mixture during growth. It emerged that boron bonded to nitrogen almost exclusively and that $(BN)_x$ domains dominated the complex bonding network with a smaller proportion of B-O bonds formed. Furthermore, there was evidence of the formation of $(BCN)_x$ domains in films deposited at high BF_3 flow rates. The similarities between SiBCNO and SiCNO films lay in the fact that both contain structural domains consisting of SiO bonds and $(SiCN)_x$. Despite the fact that these films were deposited at moderately high temperatures, hydrogen inclusions could still be seen.

The films' mechanical properties could also be adjusted by making changes to their chemical composition while keeping their nanostructure unchanged. A film's chemical bonding structure has a direct influence on its hardness and elasticity. All deposited films were hard and exhibited very high elastic recovery which was not less than 90%. It was revealed that SiBCNO tended to be softer than SiCNO due to a higher proportion of the sp^2 B-N bonds. However, by examining

the changes to both hardness and reduced elastic modulus, it emerged that SiCNO films had H^3/E_r^2 ratios ranging between 0.45 and 0.49 GPa, whereas their SiBCNO counterparts possessed values of between 0.39 and 0.53 GPa. It was particularly interesting to observe that the film with the highest elastic strain to failure was SiBCNO which was prepared with 8 at.% B. This highlights the beneficial effect which the addition of B to the film may have in terms of the film's heightened ability to accommodate applied stresses elastically.

The detailed surface-sensitive spectroscopic and spectrometric investigations into the changes, which the films' surfaces underwent as a result of thermal annealing in ambient air can be summarised as follows. Both types of amorphous films show considerable resistance to degradation as a result of the oxidation process. Furthermore, at low temperatures below 400°C, no structural changes occur in both films. The only observation to be made is the fact that a significant desorption of H-terminated species form the surface takes place, which may be attributed to the loss of loosely bonded H-containing moieties in the upper layer of the films. These are likely to have been formed as a result of the amorphous nature of the films, as well as to the existence of unsatisfied dangling bonds. In addition, thermal annealing in ambient air at low temperatures is deemed to have the effect of cleaning the surface from such species. As a result, the surface contains less hydrogen which gives rise to an increased signal intensity from Si-C and Si-N from the SiCNO films as well as from B-N in the case of SiBCNO films.

Annealing favoured also the formation of hydroxyl-containing or terminated species on the surfaces of both SiCNO and SiBCNO films. This was particularly notable in the temperature range 100- 200°C. The content of such species then decreased as the surfaces were annealed at higher temperatures. This may be attributed to a surface hydrolysis of Si- and B- containing moieties followed by possible decomposition as the temperature increased. At temperatures higher than 500°C, the presence of SiO_x and BO_x in the ToF-SIMS spectra of both films indicated the formation of an O-rich layers whose thickness increases with temperature. However, the bulk composition of both films remained unchanged.

While both films formed an amorphous oxide scale, the oxide layer was about three times thicker on SiBCNO than on SiCNO film. Its composition is predominantly SiO_x as is the case in the SiCNO and $SiO_x \cdot BO_y$ in SiBCNO films. The major difference in the case of SiBCNO was attributed to the formation of a gradient oxide layer which reveals a SiO_x-rich uppermost layer and a B_xO_y-rich region near the bulk of the film. This gradation can be attributed to the volatilisation of low molecular weight BO_x species as the temperatures increases beyond 500°C.

DSC-TG-MS analyses show that both films oxidise exothermically, and that they both have, in total, a mass increase of less than 3%. Mass spectrometry shows that in the case of the SiCNO film, only CO_2 and NO are detected at temperatures as high as 1100°C, which is indicative of the film oxidation. While the same is observed with the SiBCNO film that has a lower carbon content, a film with a higher carbon shows an earlier increase in the CO_2 signal, which is indicative of an earlier oxidation. This may be attributed to possible oxidation from graphitic carbon or carbon-nitrogen inclusions in the film. Furthermore, the difference between SiCNO and SiBCNO films lies in the fact that in the case of the latter, intermediate periods of mass loss were encountered at temperatures in the range of 450- 490°C and later on at temperatures exceeding 900°C. During these periods, increasing amounts of various volatile gaseous species including H_2BO_2, B_2O_2 and B_2O_3 are detected by mass spectrometry. The loss of such boron oxide species explains the formation of the two distinct regions in the oxide layer on SiBCNO films as observed by ToF-SIMS.

While both films types exhibit a certain degree of resistance to oxidation, their behaviour is dependent on film composition. As far as improvements to oxidation resistance are concerned, no evidence was found to suggest that including boron in the film would result in improved oxidation resistance. However, having too high an amount of either boron or carbon content leads to weight loss during oxidation, and may not be beneficial in oxidation protection and in fact may adversely affect the films performance.

5   Tribological Investigations of Si-B-C-N-O Films at Room and Elevated Temperatures

5.1   Introduction

Research in the area of thin tribological films aims to design coating materials with the following characteristics in mind. Firstly, that these coatings are thermally stable in application environments, that is, resistant to structural changes or degradation. Secondly, that the coatings are able to provide high temperature durability and lubricity. Not only does research strive to incorporate the aforementioned research when developing novel materials, but it also aims to explore new ways of making classically developed materials smarter and more adaptive.

Carbon films whether crystalline (diamond) or amorphous (certain modifications of diamond-like carbon) are intrinsically hard and have low friction coefficients. They also exhibit superior tribological properties in vacuum or inert atmospheres and at low temperatures. However, these coatings demonstrate serious challenges in applications once the contact temperature increases beyond 300°C. There are ample examples from early work on these films that demonstrate that in vacuum, polished diamond surfaces can provide very low friction and wear against less hard ceramics including SiC and Si_3N_4, but lose their superlubricity at and beyond a temperature of 500°C [320]. This has been attributed to the desorption of adsorbates terminating the dangling bonds which were claimed to have mediated the low tribological contact [274, 275, 276]. Amorphous carbon, on the other hand, fails to continue to provide its superlubricity at temperatures exceeding 300°C, as a result of its rapid graphitisation under contact stresses and oxidative losses in ambient atmospheres [277].

Other low shear strength materials include the lamellar MoS_2 and MoO_3 which have been classically investigated and successfully implemented as effective tribological surfaces [278]. However, these solids also demonstrate certain restrictions with regards to their behaviour at high temperatures. For example, the friction on MoS_2 in air increases rapidly between 300- 400°C before it slowly drops to levels which are still at least three times higher than those at room temperature [278,279,280]. This behaviour is attributed to the loss of sulphur in the oxidative process as sulphur dioxide SO_2.

All these findings have spurred research into other types of environmental tribological coatings including [281] and more recently vanadium micro-alloyed (Ti,Al)N- and (Cr,Al)N-based coating [282,283,284]. Equally interesting are the efforts focusing on Si- and B-containing coatings, which upon exposure to elevated temperatures and oxidative atmospheres, form oxidation products

that have low shear strength and facilitate tribological contact with reduced friction and possibly also reduced wear.

Early examples include the use of SiO_2 and B_2O_3 particles for lubrication as well as early work on boron carbide (generically with the stoichiometry B_4C)[285]. There is some debate regarding the exact mechanism through which boron carbide possesses low friction and low wear. It is known that the formation of hydroxyl terminated superficial boron oxide moieties on the surface of boron carbide facilitate their friction [286,287,288,289]. However, it only does this as long as the contact temperature remains lower than 185°C [288,290,291]. Once these terminations are lost due to the energetically favourable decomposition of boric acid (H_3BO_3), surface friction begins to increase continuously. Here, the tribochemistry regime becomes governed by water-free boron oxide (B_2O_3). The latter, arguably, contributes to low friction only if the contact temperature increases beyond 500°C and is, in fact detrimental, to the contact tribology in the temperature range 200- 500°C [292].

In the case of SiO_2, early experiments have shown that it provides generally low friction up to 800°C [293]. However, little work has focused on the tribological behaviour of SiBCNO coatings at elevated temperatures, which is surprising, since these coatings have a range of mechanically advantageous properties. These range from high hardness, to very high elastic recovery, to high elastic strain to failure, and H^3/E_r^2 ratios up to 0.53. In addition, their remarkable thermal stability up to 1350°C [199] in the thin film form as well as in a substrate/film system, and [60,294] as powders and bulk ceramics up to 1700°C, clearly demonstrates that this material system possesses potentially attractive tribological traits which can be useful in extreme conditions.

The motivation behind investigating the tribological behaviour of hard amorphous SiCNO and SiBCNO is manifold. As discussed in section 4.1, the fact that such films consist of hard ceramics has led to extensive efforts that were aimed at finding synthesis routes, which would enable the fabrication of hard, thermally stable, oxidation resistant and tribologically functional films. There has always been mounting interest in hard amorphous materials which are made of light elements as they offer a variety of potential applications. In the context of their tribological behaviour at elevated temperatures, these ceramics are considered advantageous for several reasons:

(i) Firstly, such materials are remarkably oxidation resistant as they form a protective oxide scale which is both amorphous and dense and works as a diffusion barrier.

(ii) Due to the film's high silicon content, the assumption based on earlier examples is that: tribological contact at high temperatures in the presence of water vapour and oxygen is enhanced by the formation of silica [295].

(iii) In the case of SiCN, due to the presence of silicon in the amorphous films, the high energy surface terminates the dangling bonds with OH hydroxyl moieties upon exposure to ambient air. The formation of Si-O-H and Si-O-O-H bonds provides a self-lubricating layer in the presence of ambient water and oxygen causing the friction coefficient to drop. In fact, this effect of tribo-chemical behaviour has been observed with other types of Si-containing films [296] and is one of the reasons silicon is added to a range of amorphous carbon films to improve their tribological behaviour at elevated temperatures [297,298]. Further examples of silicon-containing compounds [299], which are found to form a self-lubricating layer include: Si_3N_4 [300], Ti_3SiC_2 [301], $TiSi_2$ [302], or SiC [303]. More recently, a range of Ti-based silicon-containing nanocomposites such as TiSiN [304], TiSiBCN [305] and TiAlSiN [306] have demonstrated low friction coefficients in ambient air against steel counterparts. In addition, oxygen has been found to lubricate SiC by the formation of silica and the release of graphite-like material [295].

(iv) With regards to SiBCNO, there is no evidence that the oxidation behaviour worsens significantly due to the inclusion of boron. However, at low temperatures in the range 100-400°C, BO species play a significant role in reducing friction. This may be attributed to the *in-situ* formation of a very lubricious surface layer of boric acid (H_3BO_3) or other metaboric acid species ($HBO_{x=1,2}$), which acts as a self-lubricant. In fact, these observations are not unique to this system with as a number of previous studies have demonstrated that such lubricious layers form on surfaces composed of boron carbides [307], boron carbonitrides [308], as well as other boron-containing compounds such as borided steel [309], and amorphous $AlMgB_{14}$ [310]. In the case of $AlMgB_{14}$ films, relatively low friction coefficients of 0.04, 0.05 at room temperature and 300°C have been reported, while, both friction and wear of BCN films increase at 400°C.

In view of the above, this chapter presents a range of investigations which attempt to examine the suitability of hard and oxidation resistant Si-B-C-N-O films that were synthesised in this work, for tribological contact at high temperatures. It also seeks to use complimentary surface analysis to examine the effectiveness of the top oxidation layer in providing low shear strength surfaces which would function as a lubricator at high temperatures. The tribological behaviour of these films was investigated in two load regimes: the first implements ultra-low loads in the range 10 μN- 500 μN, whereas the second implements higher loads that reach up to 1 N, both at room temperature and elevated temperatures. In addition, the effect of a post-deposition annealing

treatment on these films' tribological behaviour was examined by means of Nanoscratching. Finally, the chapter attempts to explain these findings in the light of the results which were obtained from employing surface sensitive diagnostics using ToF-SIMS.

5.2 Tribological Investigation of Si-B-C-N-O Films.

5.2.1 Nanoscratching at Ultralow Loads (10μN – 500μN)

5.2.1.1 Nanoscratching of As-Deposited Films

The procedure which was used to probe the films is detailed in section 2.2.5.1. In order to gauge the tribological behaviour of the amorphous films against diamond, two types of scratches were implemented: the first involved ramping the scratching load in the range 10 μN to 100 μN, whereas the second was carried out at a constant load of 500 μN. Friction data were extracted from both scratch types by examining the change to the lateral forces as a function of both normal loads and scratch time. A summary of the films' mechanical properties as determined by Nanoindentation is given in Table 5.1.

Film	H [GPa]	E_r [GPa]	W_{el} [%]	H^3/E_r^2	R_{rms} [nm]	Friction Coefficient at $F_N=$	
						10- 100 μN	500 μN
$Si_{14}B_{24}C_{29}N_{22}O_{11}$	20.1±0.4	142±2	90	0.45	0.22±0.02	0.0260±0.003	0.122±0.002
$Si_{19}B_{21}C_{23}N_{25}O_{12}$	18.4±0.6	127±2	90	0.39	0.23±0.02	0.0179±0.003	0.116±0.001
$Si_{33}B_8C_{19}N_{27}O_{13}$	23.6±0.9	158±4	90	0.53	0.97±0.11	0.0281±0.002	0.125±0.001
$Si_{36}C_{22}N_{25}O_{16}$	24.2±0.6	169±3	93	0.49	0.54±0.03	0.0924±0.004	0.126±0.005
$Si_{40}C_{16}N_{27}O_{15}$	23.2±0.7	160±4	97	0.49	0.78±0.04	0.0431±0.002	0.120±0.001

Table 5.1: A summary of the mechanical and tribological properties of SiCNO and SiBCNO films with various compositions.

On analysing the mechanical and tribological data, some distinct differences were revealed. SiCNO films were found to have reduced modulus values in the range 160- 169 GPa, while possessing a hardness of around 24 GPa, which seemed to show no particular trend with regard to changing the films' carbon-content. In contrast, SiBCNO exhibited lower reduced moduli and hardness values. Both the hardness and reduced modulus of the B-poor $Si_{33}B_8C_{19}N_{27}O_{13}$ were 23.6(±0.9) and 158(±4) GPa, respectively, which were close to those of SiCNO. However, increasing the film's B-content reduces its both hardness and reduced modulus significantly reaching a minimum of 18.4(±0.6) and 127(±2) GPa, respectively, for the films with 21 at.% of

boron. This can be explained by a marked increase in the B-N bonds that tend to weaken the film bonding, which results in reduced hardness and elastic moduli.

Figure 5.1(a) and (b) show typical lateral force curves of nanoscratches on SiCNO and SiBCNO films at incremental (10 μN to 100 μN) and constant normal loading (500 μN), respectively. In the measured friction coefficients versus time, an initial increase in the friction coefficient, which corresponded to the loading portion of the scratching curve, a constant value was maintained throughout the entire scratch which lasted 10s. This constant friction corresponds to a steady state friction. Upon completion of the scratching process, an abrupt increase in the friction coefficient could be seen which was caused by retracting the indenter in the unloading stage. It was evident that during the course of scratching, both nano-scratches were smooth showing no signs of any abrupt changes which indicates that both materials are structurally homogenous at the scratch length and that neither slip-stick effects nor pop-ins were encountered. This also indicated the absence of any delamination or cracking events, which may have taken place during scratching, as would be expected at such low loads. In the incremental loading scratches, apart from the initial increase in the lateral force at the onset of the scratch, which corresponds to the loading stage as indicated earlier, the force increased linearly as a function of the normal force.
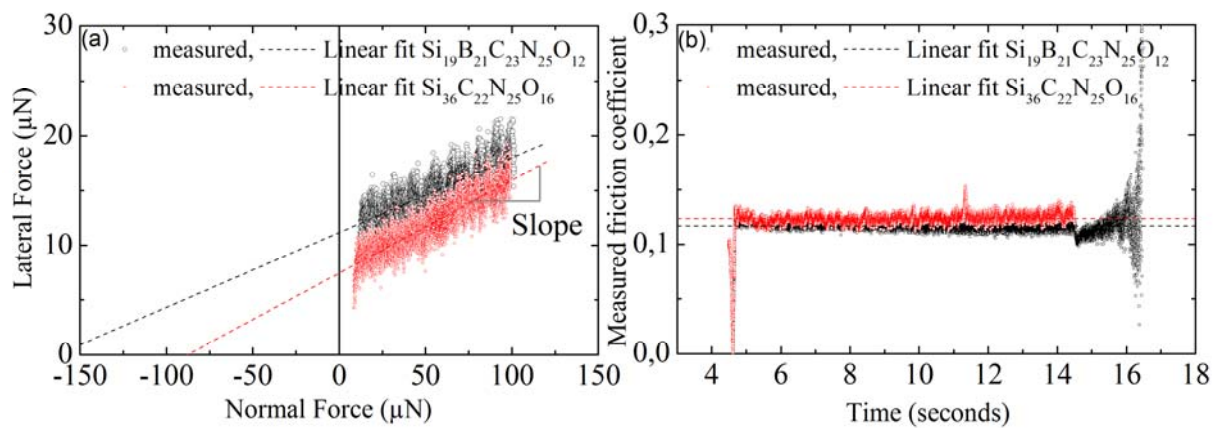
Figure 5.1: (a) A plot of the lateral vs. normal forces for $Si_{36}C_{22}N_{25}O_{16}$ and $Si_{19}B_{21}C_{23}N_{25}O_{12}$ films in contact with the 20 μm conical diamond indenter. The friction coefficient was calculated from the slope of a linear fit. (b) Variation of the measured friction coefficient during the scratch process of the same films under constant normal loading of 500 μN.

The calculated friction coefficients of all films in the load range 10 μN to 100 μN are shown in Figure 5.2(a). Generally, noticeably low friction coefficients of well below 0.1 low friction coefficients were observed in all films. The friction data which were obtained from amorphous-carbon (DLC), nanocrystalline (nc) SiC, and amorphous-BN were included to aid comparison. It is clear to see that amorphous SiCNO and SiBCNO films had much lower friction coefficients than that of DLC or nanocrystalline SiC. Both $Si_{36}C_{22}N_{25}O_{16}$ and $Si_{40}C_{16}N_{27}O_{15}$ had friction

coefficients of 0.092 and 0.043, respectively, whereas the B-containing films showed much lower friction coefficients with values approaching 0.028 and 0.018 for films with the composition $Si_{33}B_8C_{19}N_{27}O_{13}$ and $Si_{19}B_{21}C_{23}N_{27}O_{12}$, respectively. With SiCNO films, decreasing the C-content was associated with a large drop in the friction coefficients. However, the addition of boron to these films resulted in a further decrease in friction coefficients.

A similar trend was also observed with scratches that were performed at the constant load of 500 μN. Figure 5.2(b) shows that while the measured friction coefficients are higher than those calculated from the liner fitting of ramped scratches, the trend remains the same with the B-containing films featuring the lowest friction coefficients. It was also observed that other tribological films such amorphous-BN, amorphous-carbon and nc-SiC films still have the highest values.
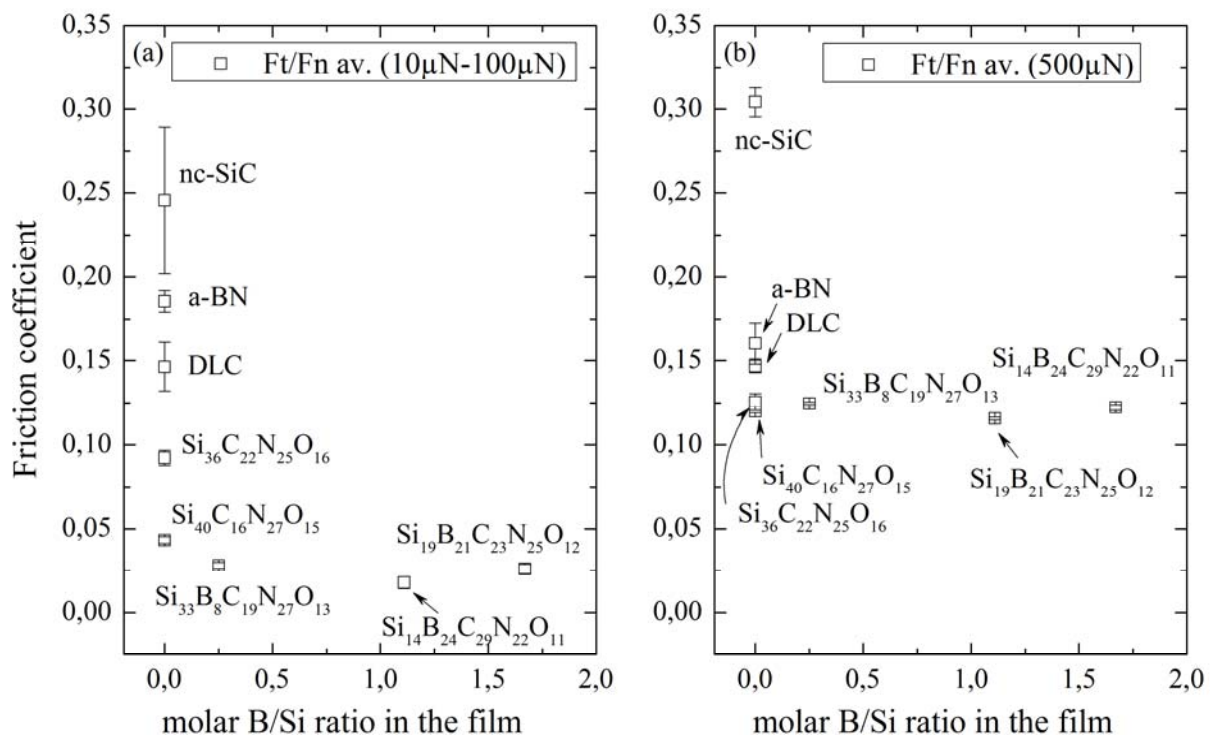
Figure 5.2: The friction coefficient of all the tested films as obtained from nanoscratch testing against a 20 μm conical diamond indenter in the load range (a) 10- 100 μN and (b) 500 μN vs. film composition.

Figure 5.3 (a) and (b) illustrate the variation in friction coefficients obtained from the ramped loading in the load range 10 μN to 100 μN, and under a constant loading of 500 μN, respectively, as a function of the films' reduced elastic modulus (E_r), whereas Figure 5.4 demonstrates how the films friction coefficient changes with their ratio of hardness to reduced modulus (H/E_r). The trend shows how the calculated friction coefficient increases with increasing the reduced elastic modulus, while it decreases with the ratio H/E_r. In fact, this trend appears to be contradictory to a previously proposed model [164], which suggests that based on AFM friction studies that the

nanoscale friction coefficient in sliding under elastic contact regimes, scales linearly with the inverse of the effective elastic modulus ($1/E_{eff}$). The data which are presented in Figure 5.3 follow an entirely opposite trend. This indicates that the ratio of H/E_r plays an important role in determining the sliding friction. In fact, similar observations were made in section 3.8, when scratching Mo-B-N nanocomposites in the same manner to the scratches conducted here. Another model [64], which was constructed based on sliding tribological testing of Cr-N films on multilayered in the systems, has demonstrated that in fact, the ratio of hardness to reduced elastic modulus of a surface is of more relevance to the friction behaviour than merely its elastic modulus (as previously mentioned in section 3.8.1). In the scratch tests presented here, the data appeared to follow this trend under low loadings in the range 10 μN to 100 μN.
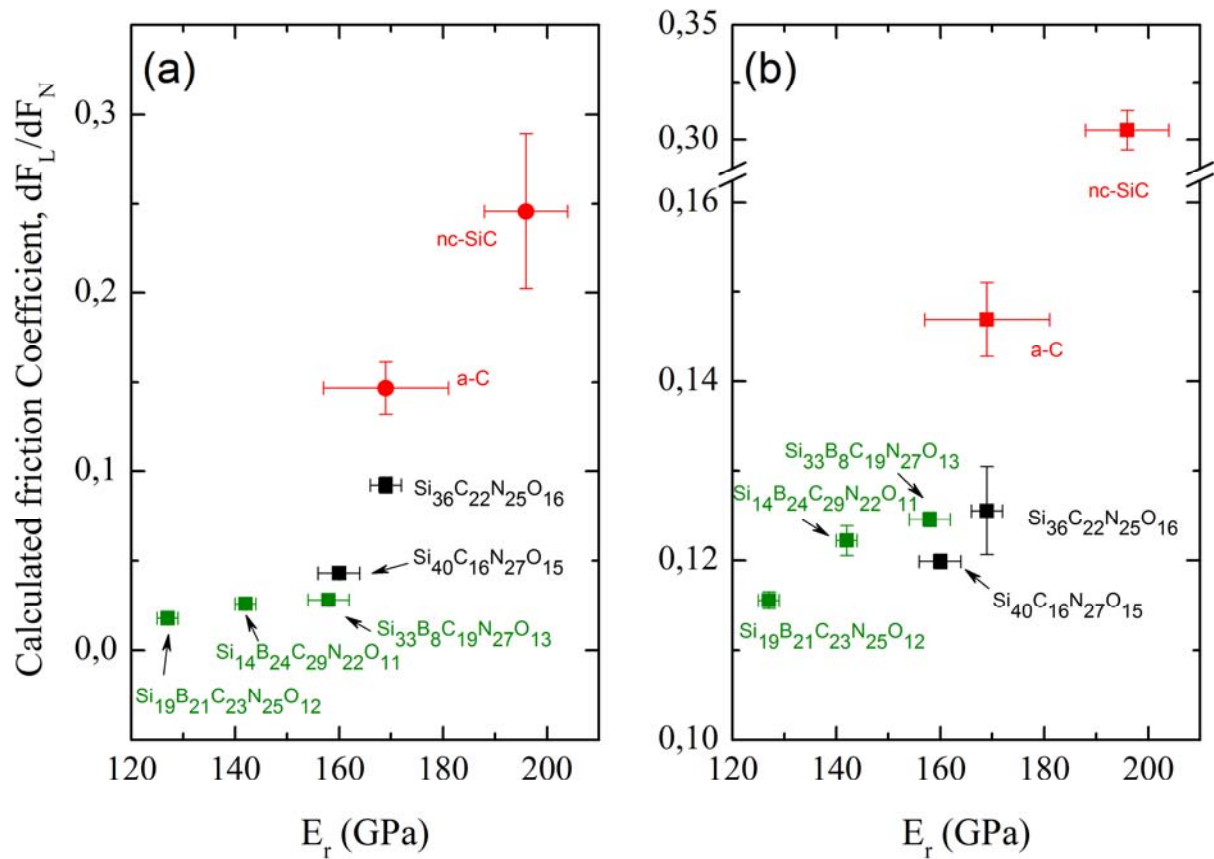
Figure 5.3: The change in the calculated friction coefficients for scratches at (a) ramped 10 μN - 100 μN, and (b) constant 500 μN normal loading as a function of the films' reduced elastic constant. The data which are obtained from amorphous carbon and nanocrystalline SiC are included to aid comparison. The data which corresponds to SiBCNO films are marked in green, SiCNO in black, and a-C and nc-SiC in red.
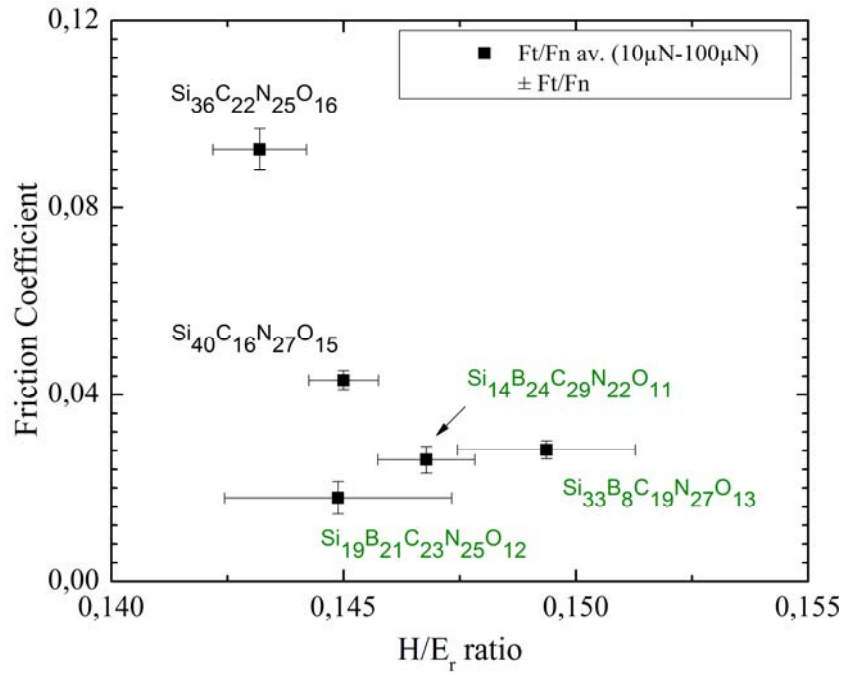
Figure 5.4: The change in the friction coefficients of amorphous SiCNO and SiBCNO films as a function of the films' H/E$_r$ ratio.

Both types of amorphous SiBCNO films had H/E$_r$ ratios in the range 0.133 to 0.149, and these values were dependent on the film composition. As the film's B/Si ratio increased, the film tended to have a higher H/E$_r$ ratio. Similar to the discussion in section 3.8.1, the sinking-in behaviour experienced by SiBCNO films under both elastic and plastic contacts as would be anticipated from the films' E$_r$ and H values, reduces the contact area which in turn reduces the friction coefficient. The ratio H/E$_r$, which describes the extent to which a surface can be stretched before it yields irreversibly, is an indication of the resilience of a surface which describes the surface's ability to absorb energy elastically [40]. In the scratch tests presented here, films with higher H/E$_r$ ratios have lowest friction coefficients under both low loading conditions. This is most prominent in the range 10μN to 100μN. Stiffer films with lower H/E$_r$ ratios have the highest friction coefficients. It appears, therefore, more advantageous to have multi-component amorphous films with slightly higher boron content such that film stiffness decreases without great loss in hardness. These results demonstrate the possibility to control the film's mechanical properties and tribological behaviour by varying film composition and structure. Films with improved elasticity and reduced friction can be obtained in compositions with less carbon and some boron.

5.2.1.2 Nanoscratching of Films Annealed in the Temperature Range 100- 400°C

In this section, the investigated tribological behaviour of SiCNO and SiBCNO films, which were subjected to post-deposition annealing, is presented. The nanoscratch tests were performed in a

similar manner to those carried out on the as-deposited films as detailed in the previous section. The post-deposition annealing process involved heating the film/substrate systems in ambient air in the temperature range 100- 400°C. A detailed description of the annealing process is given in 4.7.2. The study of the effect of post-deposition annealing on friction was carried out on two exemplary films with the compositions $Si_{40}C_{16}N_{27}O_{15}$ and $Si_{19}B_{21}C_{23}N_{25}O_{12}$.

Figure 5.5 and Figure 5.6 illustrate the variations in the friction coefficients of SiCNO and SiBCNO as a function of the post-deposition annealing temperature at both incremental loading in the range 10 μN to 100 μN and at a constant load of 500 μN, respectively. These scratches were performed using a 20 μm diamond indenter at room temperature where the humidity was not controlled during the tests, but remained the same as that of normal ambient air at RH ~55%.

At a constant normal loading of 500 μN, the evolution of friction with scratching time before and after annealing looked essentially the same. The initial increase in the friction coefficient at the start of the scratch corresponded to the running-in phase which did not vary significantly when scratching the same film types even after the annealing treatment. This was followed by a period of constant and lower friction. Although the traces of friction in the SiCNO film appeared slightly less smooth, indicating a slightly higher roughness, no events which could be associated with pop-ins or delaminations could be seen throughout the scratch length. This is true for both as-deposited and annealed SiCNO films.

The ramped scratches in the load range 10- 100μN revealed that both as-deposited films had extremely low friction coefficients against the diamond indenter at room temperature with values of 0.033±0.006 and 0.009±0.002 for SiCNO and SiBCNO films, respectively. Such extremely low friction coefficients could not be achieved after the annealing treatment. In the case of SiCNO, annealing the film at 100°C increases the friction coefficient to about 0.213±0.038. The friction coefficient maintained an equally high value for the film annealed at 200°C of about 0.238±0.074 before it dropped to lower values ranging from 0.121±0.027 to 0.147±0.032 for those films annealed at higher temperatures.

Similar observations were encountered with the B-containing films in which the friction coefficient increased in a similar manner by a factor of thirty to 0.271±0.021 at 100°C before it dropped to lower values in the range 0.107±0.024 to 0.138±0.018 for those films annealed between 200°C and 400°C.

The general trend in the previous data indicates an initial increase in friction after annealing at 100°C by about one order of magnitude. A very similar tendency was observed in the case of

friction coefficients obtained at a constant normal loading of 500 μN, wherein the lowest friction coefficients which were recorded for the as-deposited films were similar for both SiCNO and SiBCNO films and measured 0.116±0.001 and 0.119±0.001, respectively. Friction coefficients then fluctuated marginally around this value but remained higher than those of the as-deposited films with values ranging from 0.136±0.003 to 0.176±0.042. It may also be noticed that the friction is highest when the both film types were annealed at 100°C. A summary of the friction coefficient values at various loads and annealing temperatures is listed in Table 5.2.

Film	Annealing Temperature [°C]	COF slope for F_N = 10-50μN	COF measured at F_N = 500μN
$Si_{19}B_{21}C_{23}N_{25}O_{12}$	As-deposited	0.009±0.002	0.116±0.001
	100	0.271±0.021	0.171±0.002
	200	0.133±0.027	0.139±0.002
	300	0.107±0.024	0.136±0.003
	400	0.138±0.018	0.176±0.042
$Si_{40}C_{16}N_{27}O_{15}$	As-deposited	0.033±0.006	0.119±0.001
	100	0.213±0.038	0.155±0.002
	200	0.238±0.074	0.163±0.003
	300	0.147±0.032	0.146±0.001
	400	0.121±0.027	0.157±0.003

Table 5.2: A summary of the measured and effective friction coefficient values obtained from scratching the films with a 20μm conical diamond indenter at various loads and post-deposition annealing temperatures. The error represents the standard deviation of five scratches.

This may suggest that while the surface roughness of all films did not change as marked by the similarly smooth traces of friction of both the as-deposited and annealed films, these surfaces must have undergone a change that caused the increase in friction after annealing the surfaces at 100°C and beyond. Since the test conditions including: the indenter type and geometry, the relative humidity, as well as surface roughness remained the same throughout the scratch experiments, the observed variations in friction coefficient are likely to be related to chemical changes to the surfaces which were associated with annealing. Therefore, a close examination of these chemical changes that must have taken place may very well provide an explanation for the aforementioned variations in the friction data.
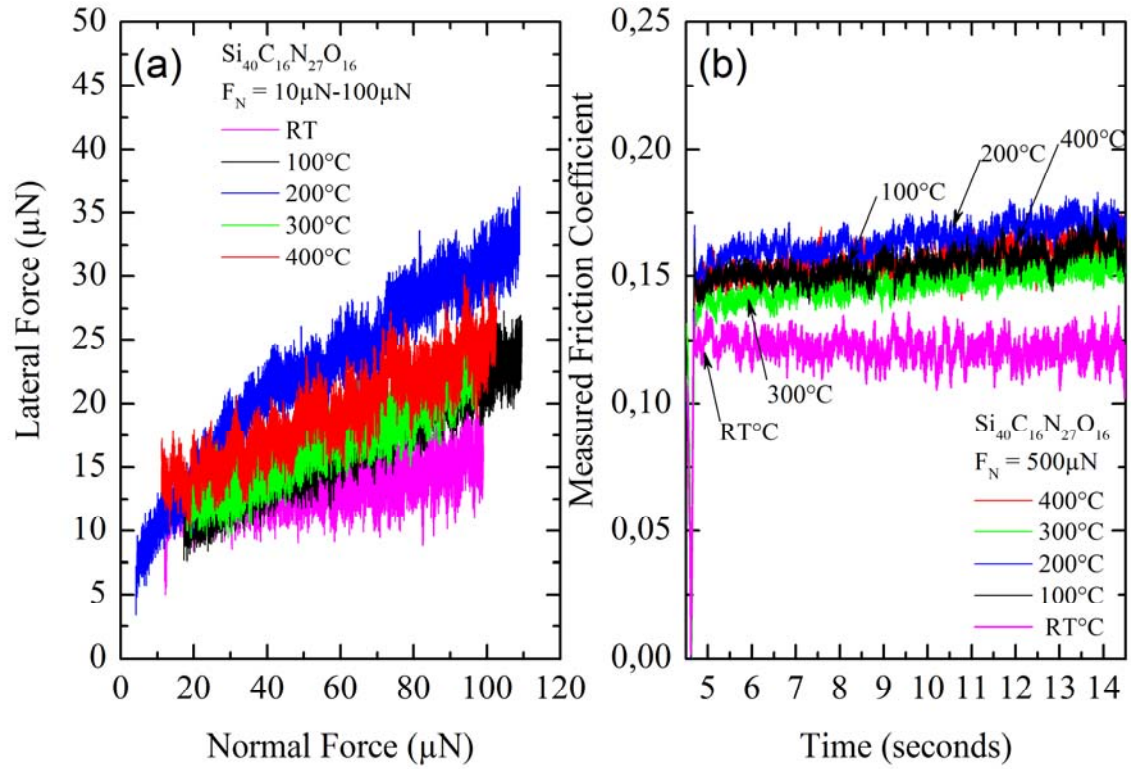
Figure 5.5: (a) The change in lateral versus normal forces for ramped scratches of Si$_{40}$C$_{16}$N$_{27}$O$_{15}$ and (b) the temporal development of the measured friction coefficient of the same films at a constant normal load of 500 μN after post-deposition annealing at various temperatures.
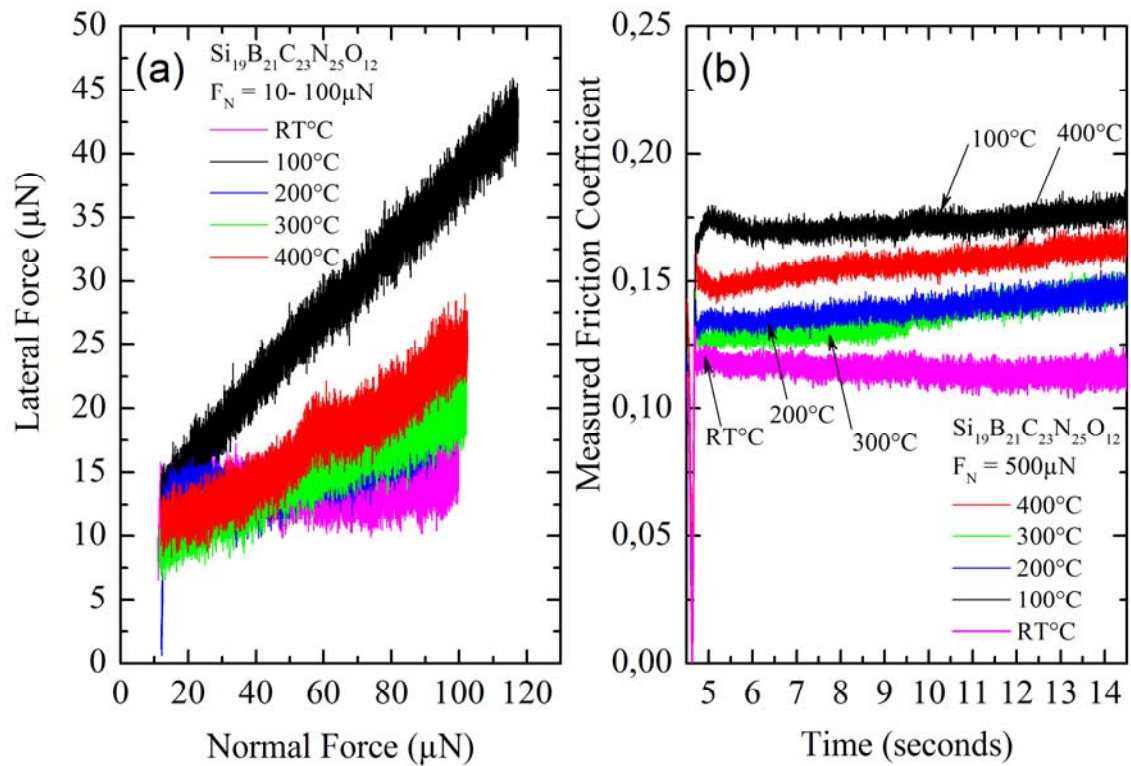
Figure 5.6: (a) The change in lateral versus normal forces for ramped scratches of Si$_{19}$B$_{21}$C$_{23}$N$_{25}$O$_{12}$ and (b) the temporal development of the measured friction coefficient of the same films at a constant normal load of 500 μN after post-deposition annealing at various temperatures.
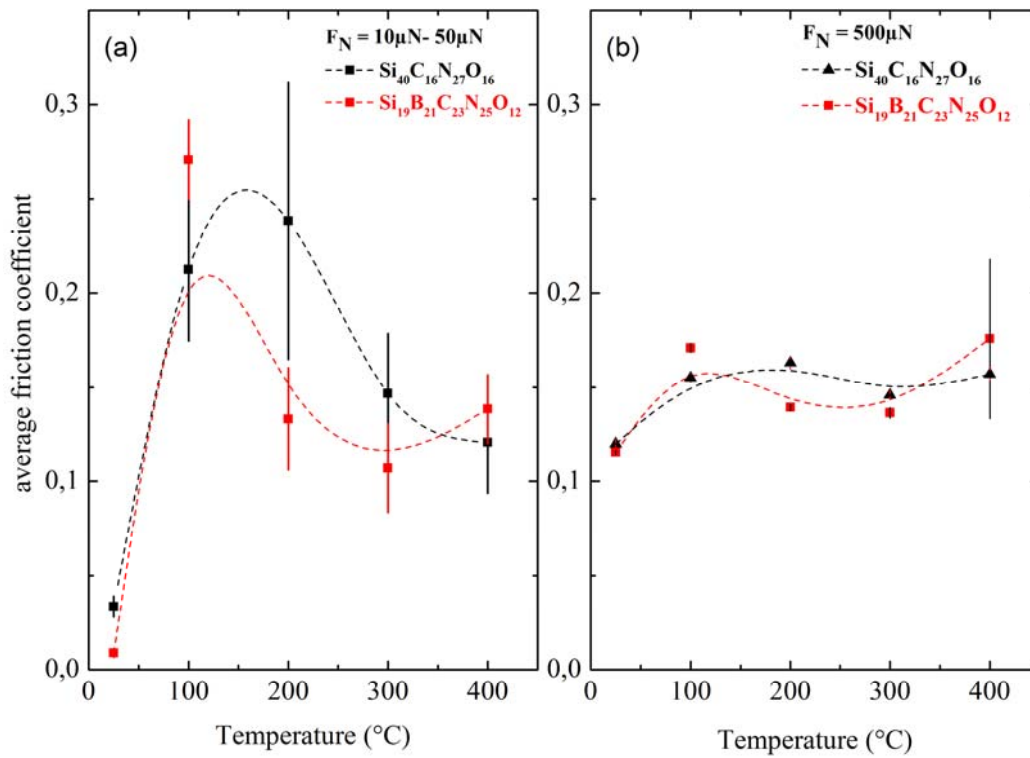
Figure 5.7: The variation in the friction coefficients of Si$_{40}$C$_{16}$N$_{27}$O$_{15}$ and Si$_{19}$B$_{21}$C$_{23}$N$_{25}$O$_{12}$ taken at various annealing temperatures from scratches at the loads of (a) 10- 50 μN and (b) 500 μN.

5.2.2   Reciprocating Sliding at High Loads under Dry Conditions.

The sliding friction and wear resistance of SiCNO and SiBCNO films were investigated using a home-made tribometer testing apparatus, which implemented a ball-on-disk configuration as described in detail in section 2.2.5.2. The tribometer was modified in order to enable the testing of both friction and wear not only at room temperature, but also at elevated temperatures of up to 400°C. In these tests, a total wear track length of at least 2250 mm was used to investigate the tribological behaviour of films of selected compositions. A summary of the films' elemental composition and mechanical properties as determined by Nanoindentation is given in Table 5.3.

The choice fell on these films as their compositions are representative of those films that are the hardest and which have the highest elastic recovery. They were, therefore, considered to be good candidates for use in abrasive wear environments. A spherical commercial grade alumina indenter loaded with 1 N (F = 1.0707N after careful calibration) generated a Hertzian mean contact stress pressure of about 2.5- 2.7 GPa depending on the films' reduced elastic modulus. The contact stress pressure is a function of the load, indenter type and radius as well as the elastic moduli of both the indenter and film. The developed mean contact stress can be expressed as:

$$\sigma_p = \frac{F^{1/3}}{\pi \left[\frac{3}{4} \cdot r_i \cdot \frac{1-v_i^2}{E_i} + \frac{1-v_s^2}{E_s} \right]^{2/3}}$$ **5-1**

Where F is the load applied to the spherical indenter; r its radius; E the elastic modulus and v the Poisson's ratio of the spherical indenter (i) and the substrate (s), respectively. In this calculation, the effective elastic modulus (E^*_{eff}) of all films is obtained from Nanoindentation according to the expression:

$$E^*_{eff} = \frac{E}{1-v^2}$$ **5-2**

All tribological tests were conducted in a reciprocating fashion with the spherical indenter reciprocating at a speed of 2 mm/s with the film underneath the loaded indenter remaining stationary. In order to avoid a remarkable plastic deformation of the substrate, a low load of 1 N was chosen in the tribological tests, which helps to highlight the films' lubricious behaviour.

Film	H [GPa]	E_r [GPa]	H^3/E_r^2	R_{rms} [nm]
$Si_6B_{22}C_{39}N_{20}O_8$	26.7±0.6	181±2	0.58	0.22±0.02
$Si_{38}C_{24}N_{27}O_{11}$	28.6±0.4	193±3	0.63	0.23±0.02

Table 5.3: Elemental composition and mechanical properties of the films tested with reciprocal sliding tests.

Figure 5.8 illustrates the evolution of the friction coefficient (COF) as a function of the distance travelled for SiCNO, SiBCNO and DLC films against the alumina indenter at temperatures in the range 50°C to 400°C. Tests results of the DLC film were included to highlight the main differences in behaviour in comparison to the other amorphous films. It may be noted that it was not possible to test the DLC film at temperatures higher than 300°C, as beyond this temperature, DLC completely burned away and disintegrated. This is to be expected from this type of film although other types of DLC films have sustained temperatures up to 500°C [311]. Such variations in thermal stability of amorphous carbon are to be expected as a result of variations in composition (i.e. sp^3:sp^2 ratio and hydrogen content) and film residual stresses, which are a direct consequence of the deposition method and parameters.

Unlike DLC, all SiCNO and SiBCNO were durable and sustained the wear tests up to 400°C without significant damage despite the formation of cracks on the SiCNO surface, which will be

discussed later. During the relatively short wear tack length, no major signs of delamination were visible in the films and the test did not proceed until the film was completely worn through.

The stationary COF of DLC remained somehow unchanged in the temperature range 50- 200 °C with values remaining between 0.1 and 0.2. No reduction in COF was observed at elevated temperatures, contrary to some previously reported values for hydrogen-containing amorphous carbon (a-C:H), which were tested in humid air in the same temperature range against alumina [312]. The abrupt increase of the COF at 300°C was evident as the values approached 0.6 and simultaneously displayed an increased scattering range. This change is associated with major film failure which is expected from amorphous carbon films as a result from synergetic effects of hydrogen loss and graphitisation induced by the high temperatures [313]. As opposed to DLC, the SiCNO film exhibited a higher COF at all temperatures, with the only difference being that the film sustained the highest test temperature. Although the COF remained relatively constant during reciprocating sliding at 50°C and 100°C, at higher temperatures, the COF dropped after an initial sliding distance was attained. At 200°C, the COF of SiCNO against alumina decreased slightly from 0.6 to values similar to those at lower temperatures of around 0.4. Similar observations were made at 300°C and 400°C as can be seem from Figure 5.8.

In comparison, SiBCNO films started with a relatively high COF of about 0.6 and 0.5 at 50°C and 100°C, respectively, before it dropped to lower values as the temperature increased. Furthermore, these latter COF values remained centred around the values recorded for the stationary COF throughout the 2250 mm sliding distance. As the test temperature increased further to 200°C and 300°C, COF decreased steadily to about 0.2- 0.4, and the data collated with respect to the increased sliding distance showed a larger scatter. At 400 °C, both SiCNO and SiBCNO have a higher COF which tended to decrease as the wear track length increased, and more significantly so, for SiCNO than SiBCNO.

These observations suggest that different tribo-chemical conditions occur at the film-alumina interface arising from the annealing treatment. The stationary COF values obtained as a function of the test temperature for all films against alumina are summarised in Figure 5.12(b). At room temperature, the film with the highest COF is SiBCNO with a value nearing 0.96 while that of SiCNO is only half that value (ca. 0.5). Both values are significantly higher than that of DLC which has a COF as low as 0.23. All three films showed a trend of decreasing COF values between 50°C and 200°C. However, SiBCNO showed the lowest COF of 0.1 and 0.09 at 200°C and 300°C, respectively, before it started to increase beyond this temperature as is the case with the other two films. The lowest COF for SiCNO (ca. 0.2) was recorded at 50- 100°C, whereas that of SiBCNO at 200- 300°C was lower than that of all the other films at all test temperatures.
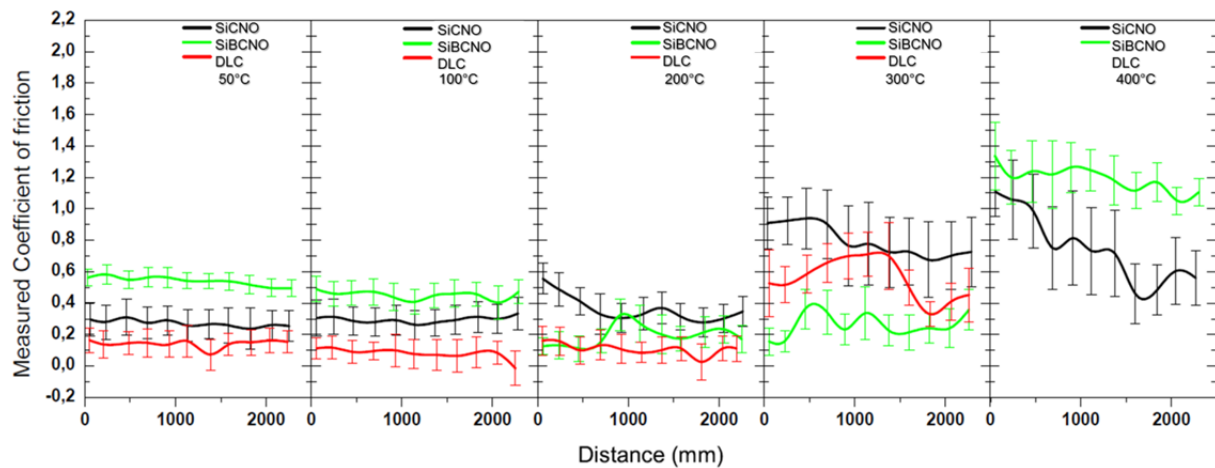
Figure 5.8: The evolution of the friction coefficient with the distance travelled for SiCNO, SiBCNO and DLC films running against an alumina indenter in the temperature range 50- 400°C.

An examination of the wear scars on both SiCNO and SiBCNO surfaces indicated that both are more wear-resistant than alumina and in fact, major wear took place at the alumina indenter; whereas the film suffered only minor wear. This was particularly evident for temperatures between 100 to 300°C on both film types. However, the wear scar profiles indicated that while film wear decreased as the temperature increased from RT to 300°C, it increased suddenly at 400°C. This profile is well correlated with the changes in the COF values mentioned earlier. The COF of SiBCNO decreased steadily between RT and 300°C to values which were lower than those of DLC, indicating special tribo-chemical conditions occurring at the film-alumina interface that are triggered by the elevated temperature.

Detailed analysis of the wear scars on both SiCNO and SiBCNO films using SEM in conjunction with EDS was necessary to reveal the type of wear behaviour. Figure 5.9 and Figure 5.10 show SEM micrographs of the wear tracks on SiCNO and SiBCNO surfaces, respectively, at the end of the test after 400 slides at all test temperatures. The corresponding Energy dispersive X-ray (EDS) scans which were collated from various locations on the surface are also indicated. At RT, the micrographs obtained from SiCNO and SiBCNO showed a large amount of small particle-like debris which was mainly scattered on the outer sides of the wear track. When analysed by EDS, the debris showed major contributions from the elements: Al, Si and O. This indicates that this debris originated from both the alumina counter body and the film, which points to significant wear from both films.

As the test temperature increased, bulky fragments which showed a high signal of Al and Zr in the corresponding EDS spectra, became more frequently observed in the wear track on SiCNO films. These fragments originate from the alumina indenter. This is marked by the intensities of

the X-ray Kα-lines from Al and Zr. Similar observations were obtained from the wear tracks of SiBCNO films. The Si-containing debris were least observed on the wear tracks of SiCNO at 100°C and 200°C as well as those of SiBCNO at 100°C, 200°C and 300°C. The amount of debris, which continued to form a transfer layer along the wear track increased more significantly in SiCNO films with increasing the test temperature to 300°C and 400°C. At 300°C, an increasing amount of Si- and O-containing particles with sizes in the order of 100 nm were mainly observed on the outer sides of the wear track of the SiCNO film. This continued to increase at 400°C. Similar findings were observed with SiBCNO at 400°C. It is interesting to note that the intensity of the O K_α line is higher in the EDS spectrum obtained from the Si-containing wear debris than that of the remaining film, which may suggest that the wear debris underwent extensive oxidation once detached from the film. It was not clear; however, from this test whether or not this oxidation was higher after the particles delaminated from the surface.

Furthermore, signs of micro-cracks and minor delamination events started to form on the surface of SiCNO at 300°C. These delamination events became more frequent on both SiCNO and SiBCNO surfaces at 400°C with Si-containing debris being more frequently detected on the outer sides of the wear track. This debris acted a third body abrasive and led to significant wear. As can be seen from the corresponding EDS scan, Al, Zr and O-containing smeared particles were always to be found in the centre of the wear track, which was a result of indenter wear. Although all the aforementioned observation were made with both film types at all testing temperatures, distinct differences could be seen in the wear tracks of SiCNO films at 100°C and of SiBCNO at 200°C and 300°C (cf. Figure 5.9(c) and Figure 5.10(h)-(i), respectively). The micrographs revealed a smoother wear track with less debris both inside and outside the tracks, which in turn are indicative of reduced wear. In fact, these observations are well correlated with the wear coefficient calculations shown in Figure 5.12, which show that SiCNO undergoes the least wear at 100°C while SiBCNO has least wear at 200°C and 300°C.

Figure 5.9: Wear scars on SiCNO films for tests run at (a) RT°C, (b) 50°C, (c) 100°C, (g) 200°C, (h) 300°C and (i) 400°C against the alumina indenter. The corresponding Energy dispersive X-ray (EDS) spectra are obtained from various locations on the wear tracks for tests run at (e)-(g) and (k)-(m).
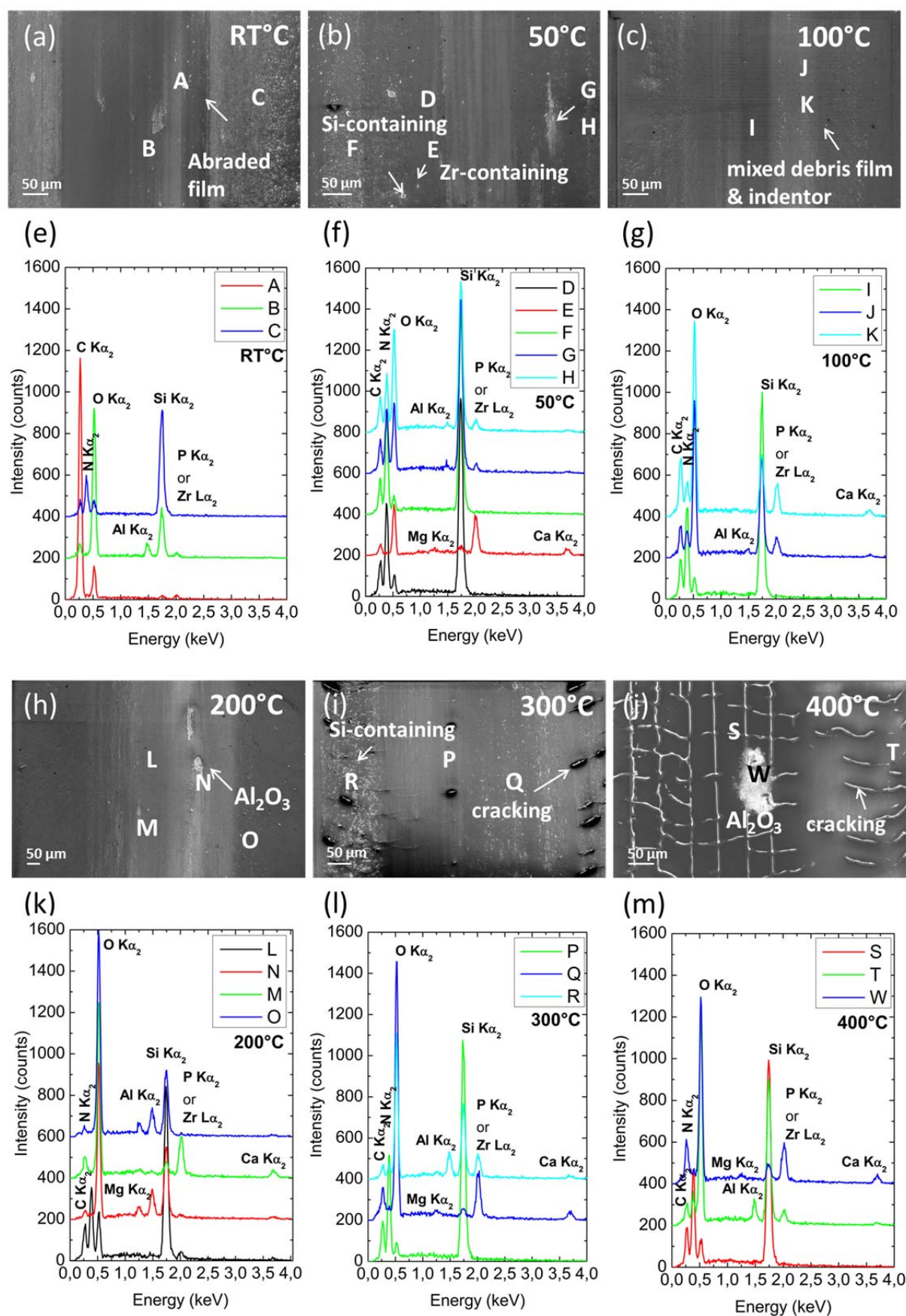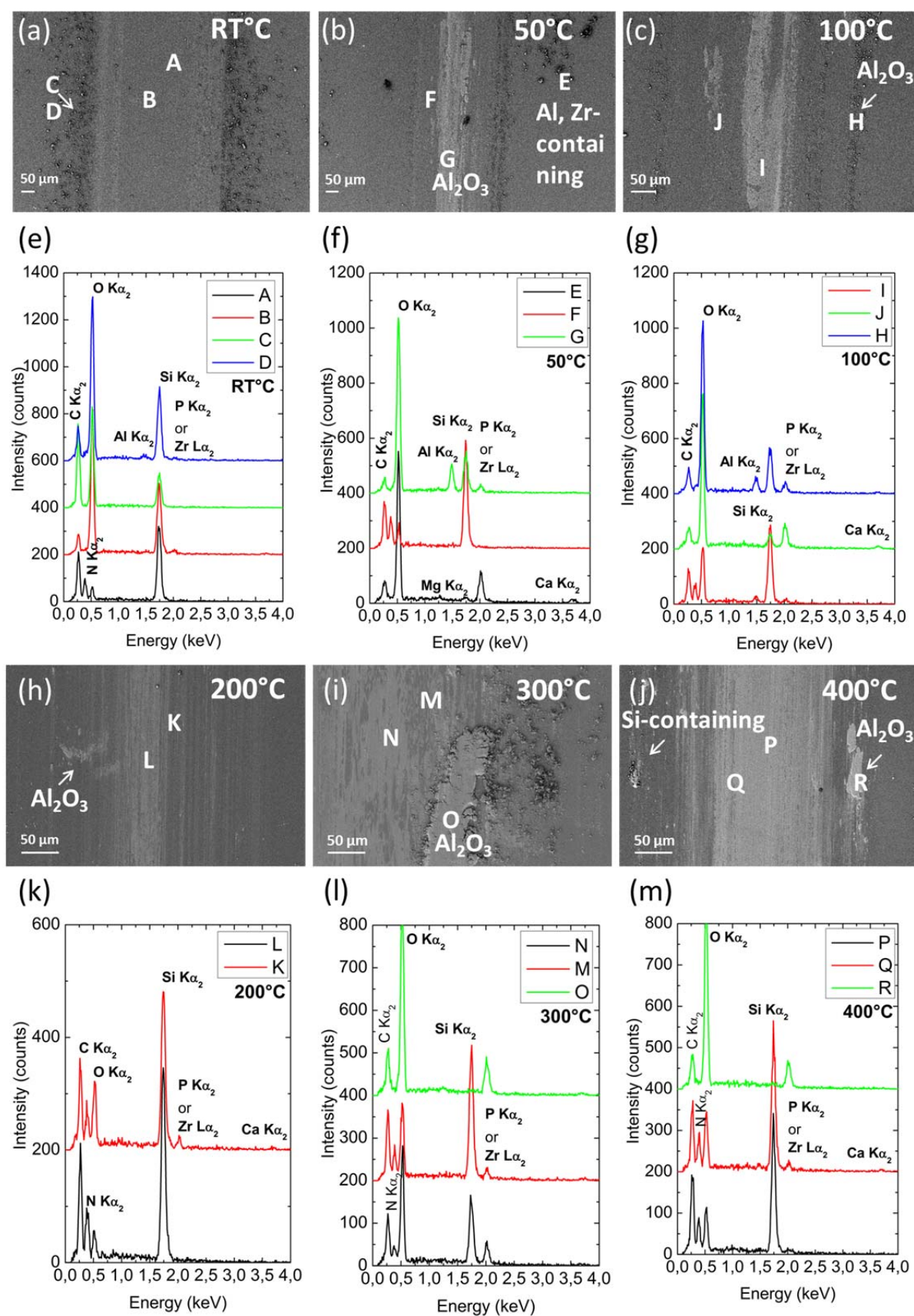
Figure 5.10: Wear scars on the SiBCNO film for tests run at (a) RT°C, (b) 50°C, (c) 100°C, (g) 200°C, (h) 300°C and (i) 400°C against the alumina indenter. The corresponding Energy dispersive X-ray (EDS) spectra obtained from various locations on the wear tracks for tests run at (e)-(g) and (k)-(m).

Wear coefficients (k) were calculated from the volume loss obtained directly from the wear scars. The wear scars were scanned with a laser profilometer in order to calculate the volume loss. The volume loss due to wear was obtained from the cross-sectional area of the displaced material multiplied by the wear track length. Figure 5.11: A two dimensional surface scan showing the cross-sectional areas perpendicular to a wear scar on an initially flat surface (A1 and A2 represent cross-sectional areas of formed ridges and A3 is the cross-sectional area of the displaced material). In this calculation, the choice of the displaced material area was supported by the assumption that: at a large number of reciprocating scratches, the ridges which form in the initial scratch passes cannot withstand further deformation from the subsequent passes and are therefore randomly scattered and removed.

Wear coefficients of the tested films, calculated from the volume of the scratch and divided by the length of the scratch and the normal force, as functions of testing temperatures are shown in Figure 5.12(a). The tendency for both SiCNO and SiBCNO films was that wear was higher at room temperature and was around 2.15×10^{-4} mm^3/Nm, which decreased monotonously to reach values of 3.8×10^{-5} and 1.8×10^{-5} mm^3/Nm for SiCNO and SiBCNO films, respectively, at 100°C. At 200°C, the wear coefficient of SiCNO was a factor 5 higher that of SiBCNO. By increasing the test temperature to 300°C, the boron-containing film appeared to experience the lowest wear with the wear coefficient of about one order of magnitude lower than either that of the same film at room temperature or the SiCNO film at 300°C. In fact, the wear coefficient of SiBCNO between 100°C and 300°C remained somewhat constant and stayed around 2.0×10^{-5} mm^3/Nm. At 400°C, both films demonstrated an increased wear with wear coefficients increasing to 1.4×10^{-4} and 0.95×10^{-4} mm^3/Nm for SiCNO and SiBCNO, respectively.
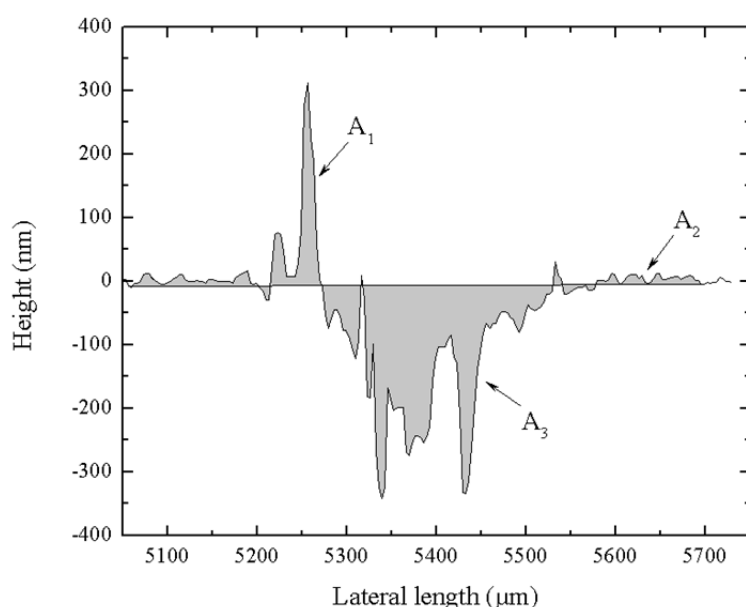
Figure 5.11: A two dimensional surface scan showing the cross-sectional areas perpendicular to a wear scar on an initially flat surface (A$_1$ and A$_2$ represent cross-sectional areas of formed ridges and A$_3$ is the cross-sectional area of the displaced material).

A comparison of both film types reveals that although the difference in wear coefficients remains small, SiCNO appears to have performed better at 100°C, but generally worse than the boron-containing film. This is particularly evident at 200°C and 300°C. Upon a detailed examination of the wear tracks at these temperatures, it is revealed that while both films deteriorated fairly quickly at 200°C- 400°C, they could not resist more than 400 reciprocating sliding runs under an initial average Hertzian contact pressure that does not exceed 2.7 GPa. Although the loads implemented in these tests were chosen to avoid a remarkable plastic deformation of the silicon substrate, the fact that silicon has a relatively low fracture toughness of the order of 0.74 MPa·m$^{1/2}$ [314] contributes to film failure when the cracks which are initiated in the substrate propagate to the films. The formation of conical cracks is revealed in the SEM micrographs obtained at high magnification for both SiCNO and SiBCNO films. Clearly, because of its low fracture toughness, silicon is not a very suitable substrate for these amorphous coatings. Instead of providing adequate support to the film owing to its higher elastic modulus, the silicon substrate initiates the film failure due to the formation of cracks inside the substrate.

These scratch tests indicate that there is a correlation between the films' wear and friction coefficients. For both films, the values of the friction coefficient are lower at temperatures between 50- 300°C than they are at room temperature. The lower friction coefficients which are observed with SiCNO films as the temperature increases from RT to 100°C correlate are very well with the reduction in wear coefficients which implies lower wear rates. As the friction coefficient decreases monotonously from 0.50 at RT to 0.32 at 100°C, the wear coefficient decreases by almost one order of magnitude from 2.19×10^{-4} to its lowest value of 3.8×10^{-5}, respectively. Similarly for SiBCNO, the monotonous decrease in the friction coefficient from 0.95 at RT to 0.09 at 300°C is correlated with the reduction in the wear coefficient by one order of magnitude from 2.13×10^{-4} to reach its lowest value at 1.75×10^{-5}, respectively. These observations indicate the synergetic effect of friction and wear in both film systems.

Nonetheless, both wear coefficients and COF seem to demonstrate a distinct behaviour both at 300°C and 400°C as the sliding distance increases. While the stationary COF in SiCNO at 300°C and 400°C starts off at a high value of around 0.9 and 1.1, respectively, it drops steadily with increasing the sliding distance. This appears to be in contrast to SiCNO wear which increases rapidly at these temperatures. A different observation is made with regards the SiBCNO surface at 400°C. Despite the fact that the film has a wear coefficient of around 9.5×10^{-5} mm^3/Nm which is lower than the values for the same film at RT°C and that of SiCNO at 400°C, the COF of SiBCNO is the highest of all the other films at this temperature.

A plausible explanation for the variation in friction and wear of both film types at elevated temperatures may be provided by considering the lubricious role of the top surface layers which form *in-situ* at the test temperature. Section 5.2.3 aims to explain this difference in behaviour at elevated temperatures by examining the surface layer composition by means of surface-sensitive ToF-SIMS.

Generally, tribological films may wear in two possible scenarios: the first involves the wear of materials as a result of the gradual removal of film materials which is caused by adhesion and abrasion. The second involves wear and film failure by spalling and delamination which is mediated by the formation of cracks. Such cracks may form on either the counter body-film interface or the film-substrate interface [315]. Thus, the reasons for the wear behaviour in both SiCNO and SiBCNO films may be related to the former scenario. The wear type is abrasive wear which takes place in the presence of a third body, that is, originating from both the indenter (at lower temperatures) and the delaminated particles from the films. Despite the rather simplistic and idealised nature of the aforementioned scratch tests, which may not replicate wear under complicated real service conditions, they are still valuable as they provide a somewhat straight forward and relatively quick comparison of the different materials which are subjected to abrasive wear. They also provide some fundamental observations pertaining to the films' behaviour under abrasive wear. Furthermore, under the reciprocating sliding tests, there appears to be no distinct advantage for SiCNO films arising from their exceptionally high elasticity as calculated from nanoindentation (section 4.4). This is due to the fact that the film thickness under abrasive wear plays an important role such that large thicknesses are required to improve abrasion resistance.
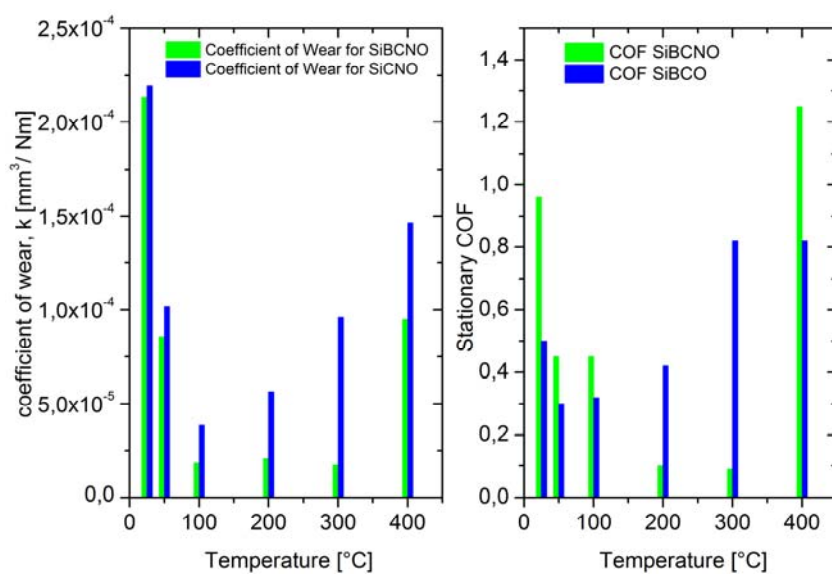
Figure 5.12: A comparison of both wear and static friction coefficients of SiBCNO and SiCNO films in the temperature range RT- 400°C.

5.2.2.1 Effect of films mechanical properties on the reciprocating sliding tests

As determined by the nanomechanical characterisation of the films in section 4.4, SiCNO films are slightly harder than SiBCNO as the latter contain a larger fraction of the sp^2 B=N bonds which tend to weaken and lead to lower hardness. It is known that the frictional force [316,317] is governed by 5-3, which demonstrates that in order for the films to have a smaller frictional force, either a lubricious layer of some sort needs to be present (for example; amorphous carbon, boric acid, silica, etc...) or a film with the right combination of hardness and stiffness that allows it to resist plastic deformation and have therefore lower contact area.

$$F = \tau \cdot A \qquad\qquad\qquad\qquad\qquad \textbf{5-3}$$

Where F is the product of the shear strength (τ) of the lubricant layer (or tribo-transfer layer) and the real contact area (A), which results from both elastic and plastic deformations.

Owing to their high hardness and their significantly higher reduced elastic modulus, amorphous SiCNO films are expected to have a smaller contact area than SiBCNO films under the same normal load and consequently lower friction. This is demonstrated by their somewhat lower friction coefficients when measured at RT, 100°C and 400°C. The friction coefficient of SiCNO is about half that of SiBCNO at RT and about a quarter less at 50°C and 100°C. However, the sliding friction tests reveal that SiBCNO films are the ones with lower friction at 200°C and 300°C. This means that although SiCNO films form a smaller contact area with the counter body, they do not exhibit a lower frictional force. At these temperatures, the shear strength of the surface layers and/or the tribo-transfer layer appears to be the dominant factor, and as it is significantly lower in SiBCNO films, it gives rise to a reduced friction coefficient. In fact, the friction coefficient of SiBCNO films against the alumina counterpart under dry sliding conditions is considerably lower than that of SiCNO films reaching values as low as 0.1. This results show that the inclusion of about 22 at.% B has the beneficial effect of reducing friction and wear at the elevated temperatures of 200°C to 300°C without causing a great loss in film hardness.

Accordingly, the tribological behaviour of both SiCNO and SiBCNO films against alumina at various temperatures is mainly governed by the tribo-chemical processes acting in the contact zone. The relatively high friction and wear coefficients are linked to the formation of transfer layers from the indenter to the film. In each instance, more wear was found on the counter body (the alumina indenter) than on these films. A transfer of Al_2O_3 debris from the indenter acts as a third body abrasive and leads to high fiction values.

At room temperature, despite the fact that the COF of SiCNO (both stationary and dynamic as a function of sliding distance) is about half that of SiBCNO, both films have similar wear in the order of 2×10^{-4} mm^3/Nm. Given that the R_{rms} surface roughness of both films are very low in the order of 0.2 nm, the lower wear which the films experienced is a result of high hardness values which are 28.6±0.4 and 26.7±0.6 GPa for SiCNO and SiBCNO, respectively. The measured wear is a result of abrasive Al_2O_3 particles generated from the indenter as well as minor particles generated from the film. The latter originate because of minor cracking that propagate further with increasing the sliding reciprocations.

Both SiCNO and SiBCNO films tend to have lower friction and wear coefficients as the ambient temperature increases during sliding to 50°C and 100°C. This is also accompanied by smoother wear scars and the formation of a transfer layer consisting of Al_2O_3. EDS spectroscopy cannot clearly distinguish between the increase in the oxygen signal which emanates from the indenter debris and the changes in the oxidation state of the films' surface as a result of the temperature rise.

Quite different friction and wear behaviours are observed in tests conducted at 100°C to 300°C on both films. SiCNO demonstrates the most reduced wear at 100°C whereas the least wear was seen on SiBCNO films in the temperature range 100- 300°C, which is accompanied by a continuously decreasing friction coefficient.

The tests have shown that while both SiCNO and SiBCNO films did not perform superiorly better than DLC at room temperature, they show a distinctly better performance at 200°C and 300°C.

Clearly the results suggest that the reduction in friction leads to a commensurate reduction in wear (cause and effect). The reduced friction coefficient is a result of the formation of a lubricating layer on top of the SiBCNO film. Although it appears that both types of films exhibit a self-lubricating effect at elevated temperatures, it is more likely that the boron addition improves the film's ability during the tribological contact. As EDS scans could not clearly show the presence of the low mass number boron, it was not, therefore, possible to determine the changes to the films that must have taken place as a result of the annealing treatment. It is therefore necessary to investigate the surface composition and chemical structure of the film prior to scratching. Detailed analysis of the changes in the chemical bonding states in the upper surface layers of both films is given in section 5.2.3.

Finally, the failure of SiCNO films is evident from the formation of micro-cracks on the periphery of the wear track. Wear scars examination by SEM micrographs and corresponding

EDS scans under the implemented test conditions; reveal minor spallings or delaminations, which indicate that these are also part of the wear process. These delaminated fragments act as an additional third body abrasive leading to increased film wear. It is not clear why these delaminations occur given that the contact stresses were presumably below that of the von Mises stresses of both films and were therefore considered to be lower than the critical stresses of the films. Two sources for the formation of these micro-cracks are possible. The first is related to the low fracture toughness of the silicon substrate, in which the cracks are possibly initiated and then propagated to the rest of the film. The second source may be related to film fatigue which may be provoked by high friction. This may lead to the formation of micro-cracking and delaminations. However, when the contact becomes lubricated at elevated temperatures by the formation of low shear strength layers, the formation of such fatigue-induced cracks is lessened. This leads to a better tribological film performance as marked by reduced wear and friction.

5.2.3 Correlation between the Surface Chemical Bonding and Composition and Tribological Tests

This section aims to discuss the ways in which the surface analysis of annealed surfaces by ToF-SIMS in conjunction with PCA can be used to interpret the observation obtained in the context of room temperatures tribological tests carried out on annealed films as well as the elevated temperatures tests.

In this investigation, two different types of tribological tests were carried out. The first implemented nanoscratching at ultra-low loads and room temperature. These tests were only carried out on as-deposited films but were also used to gauge the tribological response of the same surfaces after having been subjected to annealing at elevated temperatures. The second was carried out at a higher load and at elevated temperatures. During nanoscratch testing, a diamond indenter was made to scratch the surface at low loads which range from 10- 500µN. The indenter scratches the surface only once and did not revisit the scratched area. Therefore, there was no replenishment of contact layers. On the other hand, because the reciprocating tribological contact tests were carried out at elevated temperature, there was a continuous replenishment of the top layers which are in contact with the counter body.

The PCA generated new sets of coordinates, which captured most of the variance in ToF-SIMS spectra of films annealed at various temperatures can be used as a useful guide to extract surface-sensitive chemical information, which is most relevant to the films' tribological behaviour. In this case variances in the data that are associated with changes in the chemical composition of the surface layers as a result of annealing would be compared and correlated with the changes in the

friction coefficient. The comparison would be used to provide an insight into the effect which surface annealing and the consequent chemical changes have on the tribological behaviour of the materials.

PC1 captured the highest variance in spectra of 55.0% and 64.3% for the SiCNO and SiBCNO films, respectively. Accordingly, these axes can be used reliably to interpret most of the ToF-SIMS data. The scores on the main Principal component PC1 which were obtained from both film types showed an almost parabolic trend in a manner that is very similar to that of the variations in the friction coefficients of both films against diamond (cf. Figure 4.26 and Figure 4.33). This suggests a strong correlation between the findings of the ToF-SIMS spectra and the change in the friction coefficient. This is not surprising as it is widely known for a tribological contact to be determined not only by the mechanical properties of the contact bodies but also by the chemical nature of the surfaces.

The surface of the as-deposited films contained the highest signals from H- and O-containing species. They also showed highest signals from free carbon species such as C and C_3 secondary anions. The major changes to the surface chemical composition in both film types involved the depopulation of its surfaces from hydrogen once the films were annealed. The surfaces of the annealed films have in general a higher proportion of hydroxyl-containing or terminated species such as SiO_xH and B_xO_yH with the highest amounts are found in films annealed between 100°C and 200°C. Furthermore, a closer examination of the ToF-SIMS spectra from all as-deposited and annealed films reveals some common features with regard to a few high molecular mass fragments. Figure 5.13 shows how the signal intensities obtained from the species with the masses, 83.934, 84.938, 93.027, 111.9084, 112.9126, and 139.8887 amu/z vary for both SiCNO and SiBCNO films as function of annealing temperature. Predicting the formula of these high molecular mass secondary anions has proven to be especially difficult due to the large number of possible matching combinations of the lighter elements. This is particularly true for SiBCNO containing materials owing to the lack of published data about such systems. However, when considering the fragmentation pattern, it is possible to construct these large molecules from the smaller fragments. In this case, it can be seen from the spectra that the secondary anion with the mass 139.8887 amu/z can be thought of as the combination of two smaller anions weighing 83.934 amu/z and 55.97 amu/z, which correspond to SiC_2O_2 and $SiCO$ secondary anions, respectively. This gives rise to a molecular anion of the formula $Si_2C_3O_3$. In addition, since all these fragments appear in both films, they are not likely to be B-related since one of the films is B-free.

The ToF-SIMS spectra obtained from the SiCNO films annealed between 100°C and 300°C show the highest signal intensities of SiC_2O_2(83.934 amu/z), SiC_2O_2H(84.938 amu/z), $Si_2C_2O_2$(111.9084 amu/z), $Si_2C_2O_2H$(112.9126 amu/z), and $Si_2C_3O_3$(139.8887 amu/z) (cf. Figure 5.13(a-b)). This indicates that the surface composition of those films include a higher proportion of oxycarbide and hydroxycarbide moieties. The intensities of those secondary anions fall to lower levels as the annealing temperature increases. Similar variations were observed in the case of SiBCNO films with high molecular weight anions such as SiC_2O_2 (83.934 amu/z), SiC_2O_2H (84.938 amu/z), $B_3N_3OH_2$ (93.027 amu/z) as shown in Figure 5.13(c) and (d). In fact the former two secondary anions were found to be common in the spectra obtained from both SiCNO and SiBCNO films with the highest friction coefficients.
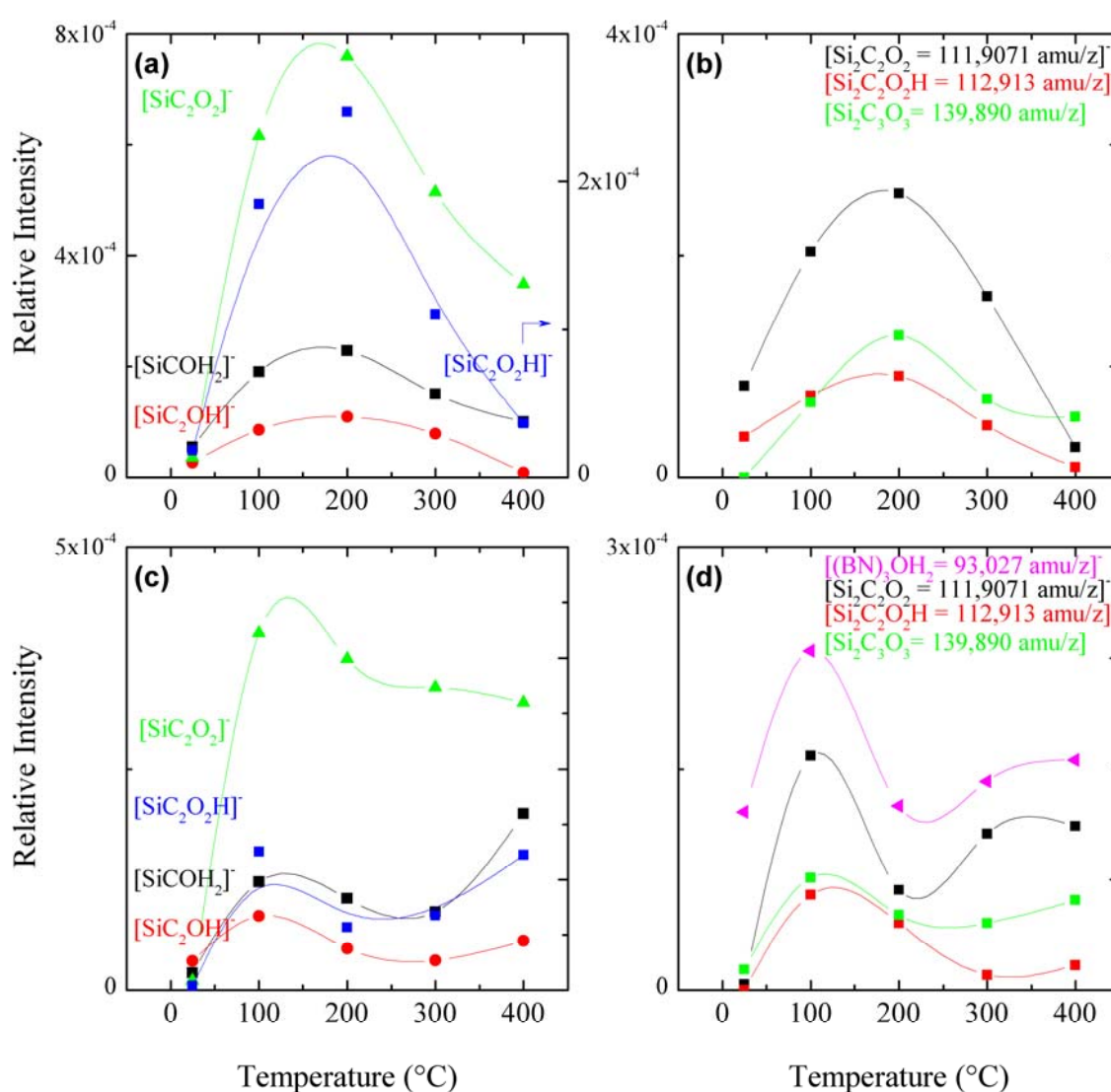

Figure 5.13: The change in the relative signal intensities from selected high mass molecular secondary anions in the spectra obtained SiCNO films in (a) and (b) as well as SiBCNO films in (c) and (d).

5.2.3.1 *Nanoscratching of Films at ultra-low loads:*

In summary the detailed spectral analysis reveals that there are no structural changes to the both film types as a result of thermal annealing in air. Depth profiling reveals that the thickness of the oxide containing layer does not exceed 5 and 10 nm for SiCNO and SiBCNO films, respectively. The contribution of the changes to surface composition and bonding to the friction coefficients obtained from the higher load scratches is less pronounced. No major changes in the friction coefficient values at 500 μN appeared as a result of post-deposition annealing. Since no changes to the film's mechanical properties (i.e. H/E_r and H^3/E_r^2 ratios) took place as a result of annealing, the values of friction coefficient remain somewhat constant. In fact, nano-scratching at a constant load of 500 μN reveals that the friction coefficient remains in the range 0.116 to 0.176 for SiBCNO films and 0.119 to 0.163 for SiCNO films with a maximum friction registered for coatings which are pre-annealed at 100°C.

The effect which post-deposition annealing has on friction coefficient at the lowest loads applied (i.e. 10- 50 μN) is most pronounced and these scratches were more sensitive to the changes in the composition and bonding of the upper most layers. The registered friction coefficients fluctuate in a manner which is similar to the changes in chemical composition and bonding as a result of annealing.

The dominant change in chemical bonding associated with increasing the temperature was the desorption of H-containing species from the surface. Such desorption has the effect of increasing the friction coefficient by a factor of 3.7 and 15 in SiCNO and SiBCNO films, respectively. The phenomenon of annealing-induced hydrogen loss from amorphous films such as has been the subject of discussion in numerous studies, which have investigated hydrogen-containing amorphous carbon films [318,319]. Such desorption of hydrogen from amorphous carbon and diamond films leads to an increase in friction against diamond and various other counter bodies. This is true for tests conducted in low-to-medium humidity environments as well as in inert atmospheres or vacuum. For example, it has been shown [320] that the frictional properties of diamond films against alumina worsen as the test temperature increases to 500°C in ambient air. The study showed that the COF of polished diamond films increases by a factor of 2; from 0.11 to 0.28, as the test temperature increases from room temperature to 500 °C, highlighting the effect that the desorption of hydrogen from the diamond surface has on the increase in friction. Other effects pertaining to the nature of the counter body, which relates to the formation tribological transfer layers and the increased fracture of the alumina surface, should not be ignored.

It is also known from nanoscratch experiments on H-containing amorphous carbon that the H-terminated surfaces experience the weak attractive van der Waals forces. This causes their friction coefficients to be extremely low [321,322]. This is also seen in as-deposited SiCNO and SiBCNO films which show highest H-content. In addition, numerous studies on amorphous carbon film [277,323,324] have demonstrated increased friction coefficient of H-containing films which are subjected to annealing treatment which leads to the loss of the superficial hydrogen. Unlike in vacuum, the loss of surface hydrogen ambient atmosphere is linked with replacing the bonds with OH groups. This investigation revealed similar results, whereby the annealed films showed increased friction coefficients against diamond in such a way that this behaviour may also be attributed to the loss of hydrogen from the films.

Both film types, annealing the surface at 100°C lead to rearranging these surface species by the increasing the functionalisation with OH groups possibly by hydrolysis. It is known that the surface of the diamond indenter is passivated with H-bonds. Despite their low polarity, the C-H bonds will form stronger attractive bonds with the SiCO and SiCOH terminated surface which in turn leads to an increase in the friction coefficient. Therefore, the films' OH groups will form stronger attractive forces with the diamond indenter causing the friction coefficient to increase.

Furthermore, the previous analysis reveals that there are high molecular mass fragments that appeared in all ToF-SIMS spectra, whose intensities vary in a manner that is similar to the change in friction coefficient. Despite the fact that the signal intensities obtained from the high molecular mass fragments are naturally much smaller than those of small molecular masses, the strong correlation with the variations in the friction coefficients suggest that they have a major role in determining the friction coefficients. The variation in their signal intensities with annealing temperature suggest that they are a product of hydrolysis of Si-containing moieties at temperatures lower than 200°C, and that they are also oxidation products of the upper layers.

In the case of SiCNO films, at temperatures higher than 300°C, less of the hydroxyl groups populate the surface as a result of possible decomposition causing the friction coefficient to drop. For SiBCNO films annealing beyond 300°C increases in the signal from O-containing species further. At this stage, the increase may be related to the onset of an oxidative change of the surfaces.

5.2.3.2 *Reciprocating sliding against alumina at high loads:*

It is interesting to observe that the aforementioned species appear to affect the frictional behaviour of the films differently according to changes in the indenter type and test environments. The very same surface chemical changes, which are described in the previous section, will have a different effect when the alumina indenter is used in the micro-scratch tests. In reciprocal sliding at high loads against alumina, the presence of OH-termination appears to be linked to a reduction in the friction coefficient friction when tests are carried out at elevated temperatures.

An increase in the OH-terminated (or containing) groups reduces the friction by proving low shear layers. Therefore, surface annealing reduces the H-termination and produces low shear layers. These layers are continuously replenished during the sliding provided continuous exposure to ambient water vapour in the air and elevated temperatures, and therefore, these bonds and layers dominate the surface resulting in improved tribological behaviour. It should be notes here that the effect of frictional heating, though not quantified, is negligibly small since a slow sliding speed of 37.7 mm/s was used throughout the test. As the test temperature increases beyond 300°C, the effect of these low shear moieties vanishes caused by their possible decomposition. It can therefore be inferred that the presence of OH moieties in the surface rather than merely the oxide is responsible for the lubricious action at elevated temperatures in both SiCNO and SiBCNO films.

5.3 Conclusions

In this chapter, the tribological behaviour of various films in the SiBCNO system is investigated in two load regimes and at various surface conditions and test temperatures. The first load regime examined the frictional properties of both film types against an inert H-terminated diamond indenter in the load range 10- 500 μN. Despite the use of ultralow loads, the type of which is only encountered in specific applications (MEMS), the very small sub-micron contact areas generates considerable Hertzian contact pressures at maximum contact depths, which do not exceed several tens of nanometre makes these nano-scratch tests particularity well suited to probe the "real" mechanical properties and tribological response of thin films.

In this second load regime, the sliding friction and wear resistance of the films were investigated in a ball-on-disk configuration. These tests were carried out at both room and elevated temperatures. In these tests, because of the reciprocating nature of the test at the elevated

temperature against alumina, there will be a continuous replenishment of these species provided that the contact temperature remains at a specific elevated temperature. Therefore, the tribological behaviour of both films is mainly governed by the tribo-chemical processes acting in the contact zone.

With respect to the nano-scratches, the extremely low friction coefficient of the as-deposited SiCNO and SiBCNO films may be attributed to two facts: The first is related to the films mechanical properties, whereas the second is related to the chemical composition of their surfaces.

The mechanical properties of the SiCNO and SiBCNO are dependent on their composition. All tested films have H/E_r ratios in the range 0.133 to 0.149. Higher ratios are found for films with higher boron content (i.e. B/Si ratio). The friction coefficient of the films changed in a manner that depicted the changes in their H/E_r ratios.

In addition, due to the fact that the surface contains significant amount of hydrogen and carbon presumably from ubiquitous contaminants arising from the deposition process. The higher surface hydrogen content causes the low friction coefficients with the H-terminated diamond indenter due to the weak van der Waals interactions ensued. When testing post-deposition annealed films, there is a clear distinction between the surfaces of the as-deposited films and the ones annealed up to 400°C in air. Both as-deposited films have considerably large amounts of H-terminated species whose proportion decreases by desorption at higher temperature. The effect which post-deposition annealing has on friction coefficient is most pronounced at the lowest loads applied (i.e. 10- 50 μN), having said that the data from the higher loads (500 μN) are not dissimilar. This variation is correlated with the increase in the friction coefficient against diamond loaded in the range 10- 50 μN as the annealing temperature increases from 25°C to 100°C by a factor of 6 and 30 for SiCNO and SiBCNO films, respectively.

According to ToF-SIMS depth profiling, an oxygen-rich layer with a thickness of up to 5- 10 nm forms on the surfaces of both films as a result of the annealing process. This oxygen-rich layer is twice as thick on the B-containing film as it is on the SiCNO films. Beneath this layer the chemical composition of either film does not vary significantly despite the small but consistent variation trends which are observed in both films at temperatures beyond 400°C. This indicates the onset of an increase in the proportion of O-containing species in the film's upper layers.

For SiCNO and SiBCNO films annealed in the range 100°C- 400°C, the signal intensities of a number of secondary anions fluctuate in a manner that depicts the change in the COF. The initial increase in signals from these anions could be related to the decrease in the surface H-content

and an initial hydrolysis as the annealing temperature increases to 100°C. As the temperature increases beyond 200°C these hydrolysed moieties possibly decompose liberating the OH containing species from the surface which leads to a drop in the signals from the corresponding secondary anions. In the second stage as the temperature increases beyond 300°C, there is further increase in the signal from O and OH-containing species. At this stage, the increase may be related to the onset of an oxidative change of the surfaces.

In addition, the change in the high molecular mass fragments that appeared in the ToF-SIMS spectra obtained from both films whose intensities vary in a manner that is similar to the change in friction coefficient suggest that similarly an increase in the OH-terminated (or containing) moieties lead to stronger attractive forces with the H-terminated diamond indenter. This causes in the friction coefficient to increase.

Apart from the increase in friction after post-deposition annealing at 100°C, there are no significant changes to the friction coefficients which remain unaffected as there are no significant changes to the film's structure and bonding up to 400°C. Since there are no structural changes taking place in the films as a result of annealing, there was no worsening of the films' tribological performances as a result of annealing. Any worsening of the films' tribological performances is however to be expected at temperature higher than 500°C.

The surface chemical changes, as detected by ToF-SIMS, also affect the sliding tests against alumina at elevated temperatures. The presence of OH-containing on both films in the temperature range 100- 300°C indicate the formation of lubricious layers of the type: Si-C-O-H and B-N-O-H, which are continually replenished throughout the test. These cause the reduction in the measured static and dynamic friction coefficients. The reduction in friction is also accompanied by reduction in wear. The wear behaviour can be described as abrasive involving mainly the debris from the alumina indenter. Minor spallings or delaminations were detected on the sides of the wear tracks indicate that these are also part of the wear process. The self-lubricating nature of the SiCNO films can be improved by the addition of boron.

Finally, the results obtained in this investigation indicate that the use of amorphous films in the Si-B-C-N-O system is invaluable when it comes to low friction surfaces and wear reduction, especially when applied to technical tools which are subjected to elevated temperatures. As a result of changes to composition, films with improved elasticity and reduced friction can be obtained in compositions with less carbon and some boron. This will undoubtedly have the desired effect of increasing the life time of these tools. This may pave the way to design a whole array of new generation of components that can operate in particularly severe conditions.

6   Summary and Outlook

6.1   Summary

This thesis has presented the research work that was carried out in order to deposit a number of thin films systems. The synthesised materials were characterised with regard to their composition, chemical bonding and structure as well as to their mechanical and tribological properties. Microwave plasma enhanced CVD as well as magneto-active ECR-MWCVD methods were used to deposit several film systems including: (a) Nanocrystalline composites based on the nitrides of Molybdenum and Boron. (b) Multi-component films based on the light elements Si-B-C-N-O system. The following summarises the main research findings for each film system:

6.1.1   Nanocomposite Thin Films in the Mo-B-N System.

The attractiveness of a plasma-based vapour deposition technique lies in its ability to enable distinct chemical and structural designs of surfaces in an atom-by-atom fashion. With such methods, it is possible to establish specific surface reaction conditions upon which phases of various chemical activities form simultaneously. The formation of Mo_2N/BN nanocrystalline composites was made possible using a hybrid technique which included electron cyclotron resonance (ECR)- plasma-assisted CVD and ion- beam assisted deposition. The use of the ECR ion beam to induce *in-situ* sputtering of Mo offered the advantage of introducing the highly ionised metal ions into the gas phase. The highly ionised ECR ion beam sputtered and deposited *in-situ* MoN and Mo_2N phases. Simultaneous surface reactions leading to the formation of a nanocomposite structure with two different nitride phases of the elements Mo and B was only possible by the addition of H_2 and BF_3. Ionised BF_x and H species reacted in excess N_2^+ ions to from the BN phase alongside fcc-Mo_2N. The overall reactions can be summarised as follows:

$$2\ Mo + N_2 \rightarrow Mo_2N \tag{1}$$

$$BF_3 + \tfrac{1}{2}\ N_2 + 1\tfrac{1}{2}\ H_2 \rightarrow BN + 3\ HF \tag{2}$$

It is important to note that in the aforementioned implemented conditions, reaction (2) could only take place in the presence of H_2. Deposition experiments carried out in the absence of H_2 flow did not produce a BN phase; instead, only molybdenum nitride films were deposited. High BF_3/H_2 ratio led to the formation of nanocomposites with increasing amounts of BN. In the case of Mo-B-N nanocomposites, although the formula of the cubic molybdenum nitride phase is simplified as Mo_2N, experimental evidence indicated that this phase exists as a non-stoichiometric one. A complex chemical bonding situation was revealed by XPS. The multi-valent Mo in the nitride suggested the formation of non-stoichiometric compounds. However,

the oxidation state of Mo remained lower than VI. Despite the absence of any detectable molybdenum boride phase, evidence provided by XPS of the formation of Mo-B bonds suggested that such bonds are formed only across the grain boundaries. This is in agreement with the fact that B has a very low solubility in both Mo and MoN, and that there are no known thermodynamically stable or metastable ternary Mo-B-N compounds.

Both detailed HRTEM and XRD investigations confirmed that under such reaction conditions, the sizes of the γ-Mo_2N crystallites can vary from 2 nm to 170 nm. This leads to the assumption that both nitrides grew in a competitive manner which led to the formation of a composite; thereby rendering BN as an X-ray amorphous phase, while markedly reducing the crystallite size of γ-Mo_2N. Depending on the deposition conditions, the mass fraction of each constituent phase as well as their growth strains could be changed. The γ-Mo_2N phase was under compressive macro- and micro-stresses whose extent increased as the film's BN fraction increased.

Based on the mass fraction of both nitrides, the nanocomposites could have hardness values in the range 12- 18.5 GPa while at the same time having H^3/E_r^2 values ranging from 0.12 to 0.26 GPa. While the addition of 17.6at% of boron does not change film hardness significantly, it had a marked effect on film elasticity. More elastic and therefore more compliant films resulted from the addition of controllable amounts of boron nitride which led to an increase in the films' ability to accommodate stresses elastically before yielding. This criterion (hardness together with elastic strain to failure) could then be used to assess the films suitability for tribological applications.

The tribological properties of nanocomposites were evaluated by carrying out nanoscratches in the ultralow load range of 10 μN to 500 μN using a chemically inert diamond indenter. Generally, low friction coefficients were observed in the case of B-containing nanocomposites with values lower than 0.21. The results elucidated the relationship between the film composition and microstructure on the one hand and its mechanical and tribological behaviour on the other. There were specific film compositions which corresponded to the highest elastic deformability as quantified by the H^3/E_r^2 ratio. Increasing the film's B-content did not always increase this ratio; indeed, the relationship can be described as somewhat parabolic. In addition, nanocomposite films with high H^3/E_r^2 ratios tended to have low friction coefficients against the diamond indenter.

6.1.2   Multi-component Hard Thin Films in the Si-B-C-N-O System.

Multi-component SiCNO and SiBCNO films were synthesised by means of ECR-MWCVD using a gas mixture of $Si(CH_3)_4$, CH_4, BF_3 and N_2 in a H_2-He- rich plasma. By employing a

substrate bias of -30 V and a temperature up to 900°C, films with the following characteristics were obtained. These were found to be totally amorphous, hard with very high elastic recovery, adhesive as well as thermally stable, and had a wide range of compositions. Film composition in terms of carbon and boron could be varied by adjusting the flow rate of both CH_4 and BF_3 during growth. The films' dense and amorphous character together with their very low surface roughness were all a direct result of high ion bombardment invoked by the ECR's high plasma density.

The implementation of a combinatorial approach to thin film characterisation proved to be very useful in elucidating the relationship between deposition parameters and film composition and chemical bonding. Detailed XPS, FTIR, XRD and ToF-SIMS analyses revealed a very complex picture pertaining to the chemical bonding in the SiCNO and SiBCNO films. The C-poor SiCNO films consisted mainly of SiN_x structural units whereas the C-rich films were composed of both SiC_x and SiN_x structural units. All SiCNO films contained SiO_x bonds in their network. Additionally, there was an increasing contribution from graphitic like C-C and C-N bonds in the films' structure. With regard to SiBCNO films, a distinguishable pattern was seen when boron was introduced to the bonding network. In the B-poor films, all the boron bonded exclusively to nitrogen while the Si-C and Si-N bonding environments did not vary significantly from those found in the C-rich SiCNO films. There were indications of increasing proportions of B-C bonds in the B-rich films. Therefore, the bonding environments in these films can be described as being composed of SiC_x and SiN_x together with $(BN)_x$ and $(BCN)_y$ structural units. The latter two increased with increasing the films' B and C content. Similarly the B-containing films contained mainly SiO_s and to a lesser extent BO_x bonds.

The films' mechanical properties could be tailored by adjusting their chemical composition while keeping their nanostructure unchanged. While all deposited films were hard and exhibited very high elastic recovery of more than 90%, SiBCNO films tended to be softer than SiCNO. This was due to their higher proportion of sp^2 B-N bonds. The films' resilience as expressed by the H^3/E_r^2 ratio was high ranging between 0.45 and 0.49 GPa for SiCNO and 0.39 and 0.53 GPa for the SiBCNO films. There were also particular compositions that corresponded to the highest elastic strain to failure as in the case of the SiBCNO films which were prepared with 8 at.% B (H/E_r ratio of 0.167). The addition of small amounts of B was beneficial as it increased the film's resilience.

As far as oxidation resistance and thermal stability are concerned, SiCNO and SiBCNO demonstrated attractive relevant properties. DSC-TGA-MS as well as ToF-SIMS analyses revealed that both material systems demonstrated high thermal stability and oxidation resistance.

When tested in ambient air at temperatures up to 1350°C, both SiCNO and SiBCNO film form a passivating oxide scale which is predominantly composed of amorphous silicon oxide. At temperatures lower than 500°C, the thickness of the oxide scale ranged between 5 and 10 nm for SiCNO and SiBCNO films, respectively. ToF-SIMS analysis revealed that the most prominent changes in the signal intensities occurred with H-, and O- as well as OH-containing secondary anions. Both as-deposited surfaces showed the highest signal intensities of H- and O-containing secondary anions, whereas those annealed between 100- 300°C showed particularly higher intensities from non-oxygen containing anions, as well as from those of OH-containing species. These findings suggest that the surfaces of both film types underwent changes which involved the simultaneous loss of hydrogen and the addition of hydroxyl termination as the films are annealed in the temperature range 100- 300°C. In the case of the B- containing film, a mixture of silicon and boron oxides formed an oxidation barrier. The upper layers of the passivating oxide scale appeared to be B-poor as a result of the volatilisation of the molecular boron oxide species at temperatures higher than 500°C. The thickness of the oxide scale that developed on the SiBCNO films was more than that formed on SiCNO at all temperatures. The results showed no distinct advantages to oxidation resistance by incorporating boron in the films. Apart from the development of an oxide scale, there were no changes to chemical bonding in the bulk of both films, and structurally, the bulk of all the films remained unchanged up to a temperature of 1200°C. The only detectable change which took place at 1100°C and 1200°C was the loss of hydrogen from the bulk of the film.

The tribological behaviour of the films is directly related to film composition and the chemical bonding state of the films' upper surface layers. When scratched by a diamond indenter at loads ranging from 10μN to 100μN, both films had noticeably low friction coefficients of well below 0.1. The films superseded both amorphous carbon and nanocrystalline silicon carbide films which were tested under the same conditions. In the case of SiCNO films, decreasing the C-content by about 8 at.% was accompanied by a large drop in the friction coefficients. However, the addition of boron to these films resulted in a further decrease in friction coefficients. All the films that were tested had a RMS surface roughness in the range of 0.22 – 0.97 nm. The results also revealed that the friction coefficients increased with increasing the films' reduced elastic moduli and decreased with increasing the H/E_r ratio. These results demonstrate how to control the film's mechanical properties and tribological behaviour by adjusting film composition and structure. Films with improved elasticity and reduced friction could also be obtained in compositions with less carbon and some boron.

When the films, which were annealed in ambient air in the temperature range 100- 400°C, were scratched at the same loads, the friction coefficients were highest for surfaces annealed between 100°C and 300°C. When similar test conditions were maintained, the observed variations in the friction coefficients were found to be closely related to the chemical changes which occurred to the surfaces that were associated with annealing. As-deposited SiCNO and SiBCNO had the highest amount of residual hydrogen as a result of the ubiquitous remains from the deposition process. These contributed to lowering the friction coefficient. Upon annealing in air, surface termination with hydroxyl moieties replaced the surface hydrogen, which in turn increased the friction coefficient.

When SiCNO and SiBCNO films were scratched with alumina in the temperature range RT- 400°C, reduced friction and wear were observed at temperatures in the range of 50- 100°C for SiCNO films and in the range of 100- 300°C for SiBCNO films. The very same changes to surface composition, which contributed to a rise in the friction coefficient against diamond, contributed to a decrease in friction when scratched by alumina. The OH-terminated surface layers provided a low shear layer which acted as a self-lubricator and contributed to a decrease in friction; and consequently wear up to a temperature of 300°C. As the test temperature increased beyond 300°C, the loss of the hydroxyl groups by the possible decomposition and subsequent oxidation of the surface led to a greater increase in both friction and wear. The difference in the performance of SiCNO and SiBCNO films arose from the variations in the tribo-chemical conditions which occurred at the film-alumina interface as a result of the annealing treatment.

6.2   Outlook and recommendation for future work

The realisation of such material will open the door for further investigations both at fundamental and application-specific levels aiming at optimising the film properties to aid the industrial large scale implementation of these systems. Aspects pertaining to the further development of the multi-component thin films which were discussed in this work include:

I   With reference to Mo-B-N nanocomposite thin films:

1. In the context of Mo-B-N system, the fact that such a unique film microstructure can be brought about by employing a hybrid method will be the basis of further investigations aiming at exploring the usefulness of hybrid CVD/PVD methods to nanocomposites. The controllable deposition of nanocomposite films in the Mo-B-N system could pave the way for the preparation a new class of hard and tribological coatings which should gain great interest in wear resistance applications. Of particular interest here is the possibility of optimising the

film resilience and toughness without significant compromise to hardness via microstructural control. As such the films may be useful in application where the surface coating is subjected to intermittent or alternating impact loading forces.

2. The versatility of using *in-situ* ion beam sputtering in conjunction with ECR-MWCVD open new possibilities for the synthesis of a range of transition-metal based nanocomposites. Further improvements to the design of the electrodes can be pursued to improve film homogeneity over a large substrate area is another aspects to be considered. Use can be made of some of the design work which was carried out parallel to the work presented in this dissertation to explore several design concepts which can be implemented.

3. With regard to the deposition parameters there are a number of factors which can be further investigated. This includes studying the influence of substrate bias: increasing the bombarding ion energy by introducing a negative substrate bias which may influence the formation of BN phase in the nanocomposite. Both DC- and RF-biases can be of interest.

4. In order to give a more accurate quantification of the films stresses, it is necessary to obtain accurate values of the composites elastic moduli and Poisson's ratio by using an independent method. In addition, for better quantification of the films' thermal stresses the thermal properties of molybdenum nitrides, both stoichiometric and sub-stoichiometric should be measured. It was surprising to find out in during conducting this research that these values are as of yet not available in published databases.

II   With reference to thin films belonging to the Si-B-C-N-O:

1. Up-grading the old CVD deposition equipment is necessary in order to improve the reactor's vacuum quality by replacing the old elastomer sealing and installing a new pumping unit.

2. The shielding effects which dielectric SiCNO and SiBCNO films demonstrated during the substrate bias assisted deposition can be circumvented by employing RF-substrate biasing as a means of increasing the ion energy can open further possibilities for the preparation of hard films.

3. From a practical point of view, both SiCNO and SiBCNO films exhibit attractive oxidation resistance characteristics with minimum degradation. These results could have far reaching implications especially in the context of applying this material system as protective coatings for extreme conditions. Ones in which the surface is subjected to harsh thermal loading conditions which could be arising from high temperature applications as well as from friction.

4. Films that have attractive properties such as those obtained in this work may be considered very useful for a number of applications such as those in the automotive, aerospace and

tooling applications, where surfaces are subjected to high mechanical and thermal loading conditions. The development of such multi-component hard films may very well play a crucial part in the production of a new-generation of technically important and versatile hard films. Based on the finding obtained in the context of developing hard amorphous ceramic coatings containing Si-C-N, a project with a world leading industrial manufacturer of automobile supplies was formulated and work commenced under non-disclosure agreement.

Appendix

The complete peak list assignment and their scores on the main Principal Components.

Table A.1: A detailed peak assignment of the main ToF-SIMS fragments with significant loadings from PCA of the negative ion ToF-SIMS spectra of the as-deposited SiCNO and SiBCNO films. The number following the species represents the amu/z ratio.

PC1 (64.7%)	
Negatively loaded anions	$C_2O(39.9951)$; $N(14.0016)$; $CNB(37.0162)$; $NH_2(22.9903)$; $SiF(46.9757)$; $C_3H_5(41.0415)$; $BO(27.0054)$; $B(11.0095)$; $BN_2(39.0165)$; $BO_2(43.0008)$; $CHN_2(41.0135)$; $BN(25.0129)$; $^{10}BN(24.0165)$; $F(19.0006)$
Positively loaded anions	$O(15.9953)$; $Si(27.9766)$; $SiN(41.9806)$; $CN(26.006)$; $OH(17.0026)$; $SiO_2(59.9665)$; $C(12.0019)$; $N_2H(29.0085)$; $C_2(24.0014)$; $SiC(39.9773)$; $B_3N_2(61.0187)$; $CH_3NB(40.0379)$; $Si_2(55.9567)$; $NH(15.0108)$; $Si_2N(69.9587)$; $Ar(39.9619)$; $BNH_2(27.0279)$; $CNO(42.0064)$; $B_2N_2(50.0263)$; $C_4H_7(55.058)$
PC2 (6.7%)	
Negatively loaded anions	$O(15.9953)$; $SiC(39.9773)$; $SiF(46.9757)$; $N_2H(29.0085)$; $CH_3NB(40.0379)$; $B_3N_2(61.0187)$; $NH_2(22.9903)$; $CNB(37.0162)$; $C_3H_5(41.0415)$; $BNH_2(27.0279)$
Positively loaded anions	$C_2O(39.9951)$; $Ar(39.9619)$; $BO(27.0054)$; $B_2N_2(50.0263)$; $BO_2(43.0008)$; $S_{i2}N(69.9587)$; $C_2(24.0014)$; $SiO_2(59.9665)$; $B(11.0095)$; $^{10}BN(24.0165)$; $BN(25.0129)$; $CNO(42.0064)$; $SiN(41.9806)$; $NH(15.0108)$; $CHN_2(41.0135)$; $CN(26.006)$; $OH(17.0026)$; $F(19.0006)$; $Si(27.9766)$; $C_4H_7(55.058)$; $BN_2(39.0165)$; $N(14.0016)$; $C(12.0019)$; $Si_2(55.9567)$

Table A.2: Peak assignment of the main ToF-SIMS fragment with significant loadings from PCA of the negative ion ToF-SIMS spectra of the as-deposited and annealed SiCNO surfaces (600-1200°C). The number following the species represents the amu/z ratio. All fragments are arranged with decreasing loadings on the PC.

PC1 (37.1%)	
Positively loaded anions	C_2H_3(27.0054); C_2(24.0014); SiN(41.9802); SiC(39.9773); CN(26.006); Si_2(55.9552); C(12.0019); CNO(42.0064); NH(15.0108); Si(27.9766); C4H7(55.058); CHN_2(41.0135); N(14.0016)
Negatively loaded anions	OH(17.0026); SiH(28.9836); SiO_2(59.9665); O(15.9953); SiO_3(75.964)
PC2 (16.7%)	
Positively loaded anions	O(15.9953); SiO_2(59.9665); Si(27.9766); SiH(28.9836); OH(17.0026); SiO_3(75.964); CHN_2(41.0135); C(12.0019); CNO(42.0064); NH(15.0108); SiN(41.9802)
Negatively loaded anions	Si_2(55.9552); C_4H_7(55.058); C_2(24.0014); N(14.0016); C_2H_3(27.0054); SiC(39.9773); CN(26.006)

Table A.3: Detailed peak assignment of the main ToF-SIMS fragment with significant loadings on the main Principal Component from PCA of the negative ion ToF-SIMS spectra of the as-deposited and annealed SiCNO surfaces. The number following the species represents the amu/z ratio.

PC1 (55.0%)	
Negatively loaded anions	m(67.0184), C_2(24.0023), m(103.9533), SiN_3C(81.9918), m(42.9903), m(121.0343), CH_3OF(50.0198), B_2O(38.0082), m(121.9260), CH_2F_2(52.0194), m(66.0161), SiN_2(55.9795), CN_2(40.0111), m(58.9791), SiN_4(83.9762), SiO(43.9755), C_4H_7(55.0500), m(71.9758), m(85.9644), m(135.9303), H(1.0078), NO(29.9978), m(87.9547), m(74.9795), m(99.9749), C(12.0016), CHNB(38.0237), Si(27.9784), m(77.9622), CNO_2(57.9763), m(75.9878), m(102.9608), m(100.9685), SiO_2(59.9702), m(117.9455), m(31.9714), m(61.9705), O(18.0039), CO_2H(44.9992), CNO(41.9988), SiO_3(75.9631), m(116.9595), m(73.9777), O(15.9971).
Positively loaded anions	SiC_2N_2(79.9858), m(96.9920), SiN(41.9721), SiC_3(63.9749),

$C_4H_3O7(162.9934)$, m(51.0156), $B_2C(34.0071)$, m(84.9928), m(146.9927),

m(56.9627), SiOB(54.9876), $SiC_2N_2H(80.9730)$, m(46.9752),

SiCN(53.9817), m(101.9550), $C_3HO_2(68.9891)$, $^{10}BN(24.0186)$,

$C_3H_3O_6(134.9948)$, $C_3OF_7(184.9954)$, m(81.9589), m(46.9965),

SiOF(62.9730), m(92.9971), $NOH_3(32.9999)$, m(108.9906), m(56.9907),

$BN_2(39.0162)$, CNH(27.0059), $Si_2C(67.9741)$, m(139.8895),

SiCH(40.9753), CH(13.0083), CN(26.0067), m(70.9788), COB(39.0013),

OH(17.0032), BNOH(42.0070), m(83.9320), SiCOH(55.9554),

Cl(34.9682), CNB(36.9655), m(65.9851), F(19.0005), BN(25.0138),

NOHF(50.0055), SiH(28.9790), Si2N(69.9767), CF(30.9970),

m(82.9637), m(84.9378), CB(23.0098), m(64.9790), m(34.9941),

m(66.9842), m(57.9526), m(67.9840), m(65.0185), $^{11}B(11.0105)$,

m(78.9694), SiHO(44.9815), m(97.9360), m(48.0018), $SiC_2H(52.9895)$,

BNO(41.0113), $SiC_2(51.9772)$, m(123.9542), m(59.0160), m(99.9938),

SiC(39.9747), B(10.0140), $BO_2(43.0013)$, m(68.9638), m(109.9608),

m(60.9751), m(111.9071), $F_2(38.0001)$, N(14.0277), $C_3(35.9996)$,

NH(15.0101), SiF(46.9753), m(112.9133), $C_3H_3O_5(118.9503)$,

$CH_4F(35.0250)$, ^{10}BC (22.0114), $^{30}SiO(45.9722)$, m(76.9720).

Table A.4: A detailed peak assignment of the main ToF-SIMS fragments with significant loadings on the main Principal Component ensued from PCA of the negative ion ToF-SIMS spectra of the as-deposited and annealed SiBCNO surfaces. The number following the species represents amu/z ratio. All fragments are arranged with decreasing loadings on the PC.

PC1 (64.3%)	
Positively loaded anions	CN(26.00353); m(67.979); m(24.01696); $B_2N(35.02604)$; m(40.01131); $SiC_2O_2(83.93238)$; m(42.98099); $B_2N_2(50.02228)$; $B_2N(36.01685)$; BO(27.00438); SiCN(53.98402); $Si_2N(69.97945)$; SiCOH(55.95572); B(11.01088); SiN(41.98083); m(66.98819); m(54.99068); m(38.98536); m(51.02665); m(38.00144); CB(23.01); SiO3.9747); SiCO(55.98073); $B_2OH(39.02414)$; m(48.01952); SiC(39.97657); m(82.96278); m(81.95895); CB(22.0134); m(56.96339); m(28.00326); $BNC_2(49.02995)$; $B_2C(35.00988)$; $Si_2C_2O_2(111.90842)$; m-65.98(65.9833); $SiC_2O2H(84.93833)$; $Si_2C_3O_3(139.88865)$; B(10.01336); $Si_2O(71.95218)$; $m_4(91.95925)$; m(50.98656); m(29.00421); m(42.03656); $B_2NO(52.02357)$;

m(109.93709); Si₂C(67.95699); m(62.94314); m(95.92447);

BN(25.02397); m(57.95187); SiC₂(51.97965); m-50.00881(50.00813);

m(92.97207); m(26.8772); Si₂C₂O₂H(112.91266); m(17.04187);

m(58.96303); m(72.95933); Si2CH-68.965(68.96518); SiC₂H(52.98753);

m(96.93179); m(110.9682); C₂(24.00058); m(109.98413); m(85.97558);

m(80.99442); m(13.04167); m(32.98044); m(71.9776); m(184.99383);

C₃HO₂(68.9999); m(36.96618); C₃H₃O₆(134.99439); m(146.99646);

m(162.99279); m(46.99615); m(84.98191); m(118.99979); Cl(34.96891);

m(108.99199); m(26.04252); CHN₂(41.03198); m(116.99895);

m(168.99919); B₃N₃OH₂(93.03426); m(31.97123); m(147.98701)

Negatively loaded anions	C₂O(39.9962); SiC₃(63.97339); m(62.97346); m(43.00135); SiO₂H₂(61.98893); m(89.02844); m(102.96984); BN₂(39.01072); SiO₃H(76.97304); m(1.00768); m(64.97061); CH(13.00891); m(87.98474); C₃(36.00037); m(186.04947); m(31.98946); m(78.96808); m(75.98925); NH(15.0129); (16.01896); m(74.99318); m(44.01431); m(59.01763); O(18.00206); SiO₃(75.96427); B₄N₂(68.01642); CNO(42.00173); N(14.01666); m(43.01936); m(34.99292); OH(17.00393); m(45.99539); m(73.01156); m(47.98451); SiH(28.98428); m(77.98213); m(73.98519); SiO₂(59.97005); m(80.91773); m(137.9491); O(15.99603); SiN3C(81.97173); m(47.97995); m(86.97614); Si₂C₂H(80.96715); m(96.96663); NOH₃(32.99828); m(48.00188); CNB(37.00831); m(79.9579); m(40.98557); m(116.95816);C3H5(41.00468); B₂CNH(49.0099); NO(29.99395); m(95.9619); SiO₂H(60.97858); C(12.00108); m(91.02375); m(73.97415); m(25.00844); B₃N₃(75.02834); m(105.96997); m(64.02976); CF(30.98101); SiO₄H₃(94.98991); SiF(46.9765); m(43.99371); m(87.0051); m(65.0072); m(58.98828); B₂H(23.02089); m(140.94005); m(107.95718); m(101.00418); m(67.02044); m(78.9968); m(100.96808); SiHO(44.98138); m(82.98142); m(40.01811); m(78.92033); Si(27.9761); BO₃H(59.99453); m(113.00405); m(29.98087); m(101.94962); m(79.96663); m(30.9983); CHO₂(45.0006); B₂O(38.01691); m(74.95492); mm(65.04283); m(66.00368); B₂C(34.00813); m(135.96181); m(99.95977); m(56.98953); m(64.00131); m(29.97172); m(97.96683); m(96.99241); SiN₄(83.98744); SiNO(57.97823); B₂C₂N(60.02495); m(59.93954); F(18.99897); Si₂NH(70.97899); m(124.9926); m(93.99275);

m(125.95871); N(14.05111); m(143.96594); m(94.96285); m(99.99726); m(130.98697)

Table A.5: Peak assignment of the main ToF-SIMS fragment with significant loadings from PCA of the negative ion ToF-SIMS spectra of the as-deposited and annealed SiBCNO surfaces (600-1200°C). The number following the species represents the amu/z ratio.

PC1 (56.4%)	
Positively loaded anions	BN(25.0129); C(12.0019); SiN(41.9806); C_2(24.0014); CN(26.006); F(19.0006); SiC(39.9773); BO(27.0054); B_4C(55.9567); BN_2(39.0165); B(11.0095); OH(17.0026); NH(15.0108); CNB(37.0162); $SiCH$(40.9845); B_2(22.0189); N(14.0016)
Negatively loaded anions	BO_2(43.0008); N_2H(29.0085); Si(27.9766); O(15.9953); SiO_2(59.9665)
PC2 (12.2%)	
Positively loaded anions	$SiCH$(40.9845); N_2H(29.0085); BN_2(39.0165); CN(26.006); SiN(41.9806); BN(25.0129); B_2(22.0189); C_2(24.0014); SiC(39.9773)
Negatively loaded anions	C(12.0019); F(19.0006); BO_2(43.0008); SiO_2(59.9665); Si_2(55.9567); BO(27.0054); N(14.0016); O(15.9953); B(11.0095); CNB(37.0162); Si(27.9766); NH(15.0108); OH(17.0026)

References

[1]   R. Riedel, A. Kienzle, W. Dressler, L. Ruwisch, J. Bill, and F. Aldinger, *Nature*, **382(6594)** (1996) 796.

[2]   W. R. Fahrner (ed.), *Handbook of diamond technology*, Trans Tech Publ. (2000).

[3]   X. Jiang, J. Philip, W. J. Zhang, P. Hess, S. Matsumoto, *J. Appl. Physics* **93(3)** (2003) 1515.

[4]   V.V. Brazhkin et al., *Philos. Mag. A* **82** (2002)231. Y. Zhang et al., *Phys. Rev. Lett.* **94** (2005)145505. Y. Zhang et al., *Phys. Rev. B* **73** (2006)144115.

[5]   K. Kim, Walter R. L. Lambrecht, and B. Segall, *Physical Rev. B*, **53(24)** (1996) 16310.

[6]   Z. Pan, H. Sun, Yi. Zhang, and Ch.Chen, *Physical Review Letters* **102 (5)** (2009) 055503.

[7]   A. Y. Liu, M. L. Cohen, *Science* **245** (1989) 841.

[8]   M. L. Cohen, *Solid State Commun.* **92** (1994) 45.

[9]   M. L. Cohen, *Mater. Sci. Eng. A,* **209** (1996) 1.

[10]   R. Q. Zhang, K. S. Chan, H. F. Cheung, and S.-T. Lee*, Appl. Phys. Lett.* **75** (1999) 2259. H. Sun, S. H. Jhi, Roundy D., M. L. Cohen, and S. G. Louie, *Phys. Rev.B* **64** (2001) 094108. Zhou X-F, Sun J, Fan Y-X, Chen J, Wang H-T, Guo X, He J and Tian Y *Phys. Rev. B* **76** (2007) 100101. Y. Zhang, Sun H, and Chen C *Phys. Rev. Lett.* **93** (2004) 195504. S. Chen, X. G. Gong, and S.-H. Wei*, Phys. Rev. Lett.* **98** (2007) 015502. E. Kim, T. Pang, W Utsumi., V. L. Solozhenko, and Y. Zhao, *Phys. Rev. B* **75** (2007) 184115. C. Q. Zhuang, X. Jiang, J. J. Zhao, and X Jiang. *J. At. Mol. Sci.* **1** 126 (2010) 12. J. Zhao., C. Zhuang, and X. Jiang *Diamond Relat. Mater.* **19** (2010) 1419. C. Zhuang, J. Zhao, X. Jiang, and X. Jiang *J. Phys.: Condens. Matter* **21** (2009) 405401.

[11]   Chunming Niu, Yuan Z. Lu, Charles M. Lieber. *Science*, **261** (1993) 334.

[12]   S. Muhl, J. M. Méndez, *Diamond and Related Materials*, **8** (1999) 1809.

[13]   Knittle E, Kaner R B, Jeanloz R and Cohen M L *Phys. Rev. B* **51** (1995) 12149.

[14]   V. L. Solozhenko, D. Andrault, G. Fiquet, M. Mezouar, and D. C. Rubie, *Appl. Phys. Lett.* **78** (2001) 1385.

[15]   Y. Zhao, D. W. He, L. L. Daemen, T. D. Shen, R. B. Schwarz, Y. Zhua, D. L. Bish, J. Huang, J. Zhang, G.Shen, J. Qian and T. W. Zerda, *J. Mater. Res.* **17** (2002) 3139.

[16]   R. B.Kaner, J. J. Gilman, S. H.Tolbert. Science **308** (2005) 1268.

[17]   A. L. Ivanovskii, *J. Superhard Materials*, **33(2)** (2011) 73.

[18]   J. Haines, J.M. Léger, *Phys. Rev. B* **48** (1993) 13344.

[19]   L. Rao, E. G. Gillan, R. B. Kaner, *J. Mater. Res.* **10** (1995) 353.

[20]   H.-Y. Chung, M.B. Weinberger, J. B. Levine, A. Kavner, J.M.Yang, S. H. Tolbert, R. B. Kaner, *Science* **316**(**5823)** (2007) 436.

[21]   R.W. Cumberland et al., *J. Am. Chem. Soc.* **127** (2005) 7264.

[22]   J. Qin, D.He, J. Wang, L. Fang, L. Lei, Y. Li, J. Hu, Z. Kou, and Y. Bi. *Adv. Mater.* **20** (2008) 4780.

[23]   S. Veprek. *J. Vac. Sci. Technol. A* **17(5)** (1999) 2401.

[24]   S. Veprek and S. Reiprich. *Thin Solid Films* **268** (1995) 64.

[25]   S. Veprek, S. Mukherjee, P. Karvankova, H.-D. Männling, J. L. He, K. Moto, J. Prochazka, and A. S. Argon. *J. Vac. Sci. Technol. A* **21(3)** (2003) 532.

[26]   Y. L. Orlov, *The Mineralogy of the Diamond*, Wiley, New York, (1977).

[27]   V. A. Petrovsky, A. A. Shiryaev, V. P. Lyutoev, A. E. Sukharev, and M. Martinis. *Eur. J. Mineral.* Fast Track DOI: 10.1127/0935-1221/2010/0022-1978.

[28]   Y. Moriyoshi, M. Kamo, N. Setaka, Y. Sato. *J. Mat. Sci.* **18** (1983) 217.

[29]   V. V. Brazhkin and A. G. Lyapin. *Chapter 1 The Bridge Between The Ideal and Real Mechanical Properties for Superhard Materials.In Innovative Superhard Materials and Sustainable Coatings for Advanced Manufacturing.* J. Lee and N. Novikov (eds.) NATO Science Series. Springer-Verlag (2004).

[30]   J. Musil, *Surf. Coat. Technol.* **125**, (2000) 322.

[31]   S. V. Tsybulya, S. V. Cherepanova, G. N. Kryukova. *Chapter 4 Full Profil Analysis of X-ray Diffraction Patterns for Investigation of Nanocrystalline systems.* In *Diffraction Analysis of the Microstructure of Materials.* E. J. Mittemeijer and P. Scardi (Eds). Springer-Verlag. Berlin-Heidelberg (2004).

[32]   R. W. K. Honeycombe, *Plastic Deformation of Metals*, 2nd Edn. Edward Arnold, London (1984).

[33]   J. Schiotz, F. D. Di Tolla, and K. W. Jacobsen, *Nature* **391** (1998) 561.

[34]   J. Schiotz and K. W. Jacobsen, *Science* **301** (2003) 1357.

[35]   E. Ma. *Science* **305** (2004) 623.

[36]   Zhiwei Shan, E. A. Stach, J. M. K. Wiezorek, J. A. Knapp, D. M. Follstaedt, S. X. Mao *Science* **305** (2004) 654.

[37]   J. F. Archard, *J. Appl. Phys.* **24** (1953) 981.

[38]   T. A. Stolarski, *Tribology in Machine Design*, Butterworth-Heinemann, London (2000) p.14.

[39]   T.L. Oberle, *J. Metals* **3** (1951) 438.

[40]   A. Leyland and A. Matthews, *Wear* **246** (2000) 1.

[41]   K.L. Johnson, *Contact Mechanic*s, Cambridge University Press, London, UK (1985).

[42]   D. Tabor, *The Hardness of Metals*, Oxford University Press, London, UK,(1951).

[43]   T.Y. Tsui, G.M. Pharr, W.C. Oliver, C.S. Bhatia, R.L. White, S. Anders, A. Anders, I.G. Brown, *Mater. Res. Soc. Symp. Proc.* **383** (1995) 447.

[44]   N. J. M Carvalho, E. Zoestbergen, B. J. Kooi, J. Th. M. De Hosson. *Thin Solid Films.* **429(1–2)** (2003) 179.

[45]   E. Voglia, W. Tillmannb, U. Selvadurai-Lasslb, G. Fischerb, J. Herperb. *Applied Surface Science.* **257(20)** (2011) 8550.

[46]   J. Musil, F. Kunc, H. Zeman, H. Polakova. *Surface and Coatings Technology* **154** (2002) 304.

[47]   S. Veprek, P. Nesladek, A. Niederhofer, F. Glatz, M. Jilek and M. Sima, *Surf. Coat. Technol.* **(108–109)** (1998) 138.

[48]   S. Veprek, *Surf. Coat. Technol.* **97** (1997) 15.

[49]   J. Musil, P. Karva´nkova´, J. Kasl, *Surf. Coat. Technol.* **139** (2000) 101.

[50]   J. Musil, J. Vlček, *Surf. Coat. Technol.* **(142–144)** (2001) 557.

[51]   F. Regent, J. Musil, *Surf. Coat. Technol.* **(142–144)** (2001) 146.

[52]   S. Zhang and N. Ali. (Eds.), *Nanocomposite Thin Films and Coatings: Processing, Properties and Performance.* Imperial College Press (2007).

[53]   S. Zhang, H. L. Wang, S.-E. Ong, D. Sun, X. L. Bui. *Plasma Process. Polym.* **4** (2007) 219.

[54]   S. Mahieu, P. Ghekiere, D. Depla, R. De Gryse, *Thin Sold Films*, **515** (2006) 1229.

[55]   F. M. d'Heurle, *Metall. Trans.*, **1** (1970) 725.

[56]   P. H. Mayrhofer, C. Mitterer, L. Hultman, H. Clemens, *Progress in Materials Science* **51** (2006) 1032.

[57]   Th. Göbel, S. Menzel, M. Hecker, W. Brückner, K. Wetzig, Ch. Genzel. *Surface and Coatings Technology.* **(142-144)** (2001) 861.

[58]   J. Musil, P. Zeman, *Solid State Phenomena*, **127** (2007) 31.

[59]   J. Musil, V. Šatava, P. Zeman, R. Cerstvý, *Surf. Coat. Technol.*, **203** (2009) 1502.

[60]   J.Vlček, S. Hřeben, J. Kalaš, J. Čapek, P. Zeman, R. Čerstvý, V. Peřina, and Y. Setsuhara, *J. Vac. Sci. Technol. A* **26(5)** (2008) 1101.

[61]   P. Colombo, G. Mera, R. Riedel, and G. D. Soraru, *J. Am. Ceram. Soc.*, **93(7)** (2010)1805.

[62]   A.H. Tavakoli , P. Gerstel, J.A. Golczewski, and J. Bill, *Acta Materialia* **58** (2010) 6002.

[63]   G. Chandra and T. E. Martin, "*Rapid Thermal Process for Obtaining Silica* Coatings", U.S. Patent 5059448 (1991).

[64]   N. Wangyang, Y.-T. Cheng, M. J. Lukitsch, A. M. Weiner, L. C. Lev, and D. S. Grummon. *Appl. Phys. Lett.* **85** (2004) 4028.

[65]   J. Musil, M. Louda, Z. Soukup, and M. Kubasek, *Diamond Relat. Mater.* **17**, (2008) 1905.

[66]   J. Musil, P. Novák, R. Čerstvý, and Z. Soukup. *J. Vac. Sci. Technol. A* **28(2)** (2010) 244.

[67]   Q. Liu, Q.F. Fang, F.J. Liang, J.X. Wang, J.F. Yang, and C. Li, *Surf. Coat. Technol.*, **201** (2006) 1894.

[68]   S. J. Heo, K. H. Kim, M. C. Kang, J. H. Suh, and C.-G. Park, *Surf. Coat. Technol.*, **201** (2006) 4180.

[69]   S. G. Hong, D.-W. Shin, and K. H. Kim, *Sci. Eng. A*, **487(1-2)** (2008) 586.

[70]   T. Suszko, W. Gulbiński, and J. Jagielski, *Surf. Coat. Technol.* **200** (2006) 6288.

[71]   W.Gulbiński and T. Suszko, *Surf. Coat. Technol.*, **201** (2006) 1469.

[72]   S.M. Aouadi, Y. Paudel, W.J. Simonson, Q. Ge, P. Kohli, C. Muratore, and A.A. Voevodin, *Surf. Coat. Technol.*, **203** (2009) 1304.

[73]   J.Han, J. Jia, J. Lu, J. Wang, *Tribology Letters,* **34** (2009) 193.

[74]   ISO Central Secretariat, Metallic Materials-*Instrumented Indentation Test for Hardness and Materials Parameters*, ISO 14577 (ISO Central Secretariat, Geneva, Switzerland, (2002).

[75]   Determination of Hardness and Modulus of Thin Films and Coatings by Nanoindentation (INDICOAT), European project, Contract No. SMT4-CT98-2249, NPL Report MATC(A) (24, May 2001).

[76]   P. E. J. Flewitt and R. K. Wild, *Physical Methods for Materials Characterisation*, Chapter 6, IOP Publishing, Bristol (1994).

[77]   http://srdata.nist.gov/xps/ [last visited 29.04.2012].

[78]   S. G. Lipson, H. Lipson, and D. S. Tannhauser, *Optical Physics*, 3rd Ed., Cambridge University Press. New York, (1995).

[79]   C. Kittel (ed.), *Introduction to Solid State Physics*, 7th ed., Wiley, New York, (1996), p.35.

[80]   ION-TOF Münster technical notes.

[81]   R.G. Wilson, F.A. Stevie, and C. E. Magee. *Secondary Ion Mass Spectrometry*, John Wiley & Sons, Inc. (1989).

[82]   J. C. Vickerman. ToF-SIMS: an overview. *In ToF-SIMS: Surface Analysis by Mass Spectrometry*. J. C. Vickerman, D. Briggs (eds). Surface Spectra and IM Publications, Manchester. (2001) pp.1- 40.

[83]   I. S. Gilmore, M. Seah, *Appl. Surf. Sci.* **187** (2002) 89.

[84]   Richard. G. Brereton. *Chemometrics: Data Analysis for the Laboratory and Chemical Plant.* John Wiley & Sons Ltd, Chichester, (2003).

[85]   M.S. Wagner, D.J. Graham , B. D. Ratner, D. G. Castner, *Surface Science* **570** (2004) 78.

[86]   V. S. Smentkowski1, S. G. Ostrowski1, M. R. Keenan, *Surface and Interface Analysis Special Issue: Special Issue on Multivariate Analysis*, **41(2)** (February 2009) 88. See also references cited therein.

[87]   Ricco Rakotomalala, *TANAGRA: un logiciel gratuit pour l'enseignement et la recherche*, in Actes de EGC'2005, RNTI-E-3, **2** (2005) 697.

[88]   F.W. Young, *ViSta: The Visual Statistics System*. Research Memorandum 94-1b, L.L Thurstone Psychometric Laboratory, University N. Carolina, 2nd Edition, (August 1996).

[89]   J. H. Ward, *J. of Amer. Statist. Assoc.* **58** (1963) 236.

[90]   M. S. Wagner, D. J. Graham , B. D. Ratner, and D. G. Castner. *Surface Science* **570** (2004) 78.

[91]   D. Louer and J.I. Langford, *J. Appl. Cryst.*, **21** (1988) 430.

[92]   I. C. Noyan and J. B. Cohen, *Residual Stress, Measurement by Diffraction and Interpretation*, Springer-Verlag, New York, (1987).

[93]   V. Hauk, *Structural and Residual Stress Analysis by Nondestructive Methods*, Elsevier, Amsterdam, (1997).

[94]   B. J. Briscoey, L. Fiori, and E. Pelillo, *J. of Physics D: Applied Physics*, **31** (1998) 2395.

[95]   W. C. Oliver, and G. M. Pharr, *Journal of Material Res.*, **7** (1992) 1564.

[96]   A. C. Fischer-Cripps, *Nanoindentation*, 2nd edition, Mechanical Engineering Series, Springer-Verlag, New York, LLC, (2004).

[97]   B. Derjaguin, *Research in surface forces*, Consultant Bureau, New York, **2** (1996) 312.

[98]   Jianping Gao, W. D. Luedtke, D. Gourdon, M. Ruths, J. N. Israelachvili, and Uzi Landman, *J. Phys. Chem. B* **108** (2004) 3410.

[99]   Datasheet of a technical grade aluminosilicate ceramic as obtained from the supplier: Kager GmbH.

[100]   H. Abu Samra, T. Staedler, I. Aronov, J. Xia, C. Jia, B. Wenclawiak, and X. Jiang, *Surface and Coatings Tech*nology **204** (2010) 1919.

[101]   D. J. Kim, H. S. Sim, S.-II. Kim, Y.T. Kim, and H. Jeon, *J. Vac. Sci. Technol. A* **20** (2002) 194.

[102]   C. W. Lee and J. G. Kim, *Physica Status Solidi B*, **241(7)** (2004) 1645.

[103]   C. Louro, R. Lamni, and F. Lévy. *Surface and Coatings Technology* **200** (2005) 753.

[104]   B. Rother and H. Kappl, *Surf. Coat. Technol.* **73** (1995) 14.

[105]   M. Zhou, M. Nose, and K. Nogi, *Surf. Coat. Technol.* **183** (2004) 45.

[106]   S.-T. Lin and C. Lee, *Materials Chemistry and Physics*, **82(3)** (2003) 691.

[107]   A. A. Goncharov, A. V. Agulov, and V. V. Petukhov, *Technical Physics Letters*, **35(12)** (2009) 1140.

[108]   A. A. Goncharov, V. V. Petukhov, and V. A. Stupak, *Inorganic Materials*, **44(5)** (2008) 500.

[109]   S.-T. Lin and C. Lee, *Applied Surface Science*, **253(3)** (2006) 1215.

[110]   C. Mitterer, A. Übleis, and R. Ebner, *A* **140** (1991) 670.

[111]   E. Brandstetter, C. Mitterer, and R. Ebner, *Thin Solid Films* 201, 123 (1991).

[112]   P.H. Mayrhofer, C. Mitterer, and H. Clemens, *Z. Metallkd.* **96** (2005) 5.

[113]   S. Jayaraman, J. E. Gerbi, Y. Yang, D. Y. Kim, A. Chatterjee, P. Bellon, G. S. Girolami, J. P. Chevalier and J. R. Abelson, *Surface and Coatings Technology*, **200(22-23)** (2006) 6629.

[114]   T. P. Mollart *et. al. Surf. Coat. Technol.* **(74-75)** (1995) 491.

[115]   P. Rogl and J. C. Schuster, *Phase Diagrams of Ternary Boron Nitride and Silicon Nitride Systems. Monograph Series on Alloy Phase Diagrams* (1992) Ohio, ASM International. pp.64-67.

[116]   S. Watanabe, S. Miyake, and M. Murakawa, *Diamond Films and Technology*, **7** (1997) 139.

[117]   S. Watanabe, S. Miyake, and M. Murakawa, *Surf. Coat. Technol.*, **(76-77)** (1995) 600.

[118]   M. Keunecke, K. Yamamoto, and K. Bewilogua, *Thin Solid Films*, **(398-399)** (2001) 142.

[119]   M. Saito, T. Yasuhara, H. Murakami, and N. Ohtake, *J. Solid Mech. and Mater. Eng.*, **3(2)** (2009) 217.

[120]   R.J. Brotherton and H. Steinberg: *Progress in Boron Chemistry*, Vol. 2, Pergamon Press, New York (1970).

[121]   J. Neidhardt, Z. Czigány, B. Sartory, R. Tessadri, M. O'Sullivan, and C. Mitterer, *Acta Mater.* **54** (2006) 4193.

[122]   J.F. Moulder, W. F. Stckle, P. E. Sobol, K. D. Bomben. in *Handbook of X-Ray Photoelectron Spectroscopy*, Physical Electronics Inc., Minnesota (1995).

[123]   C. D. Wagner, W. M. Riggs, L. E. Davei, J. F. Moulder and G. E. Muilenberg. *Handbook of X-Ray Photoelectron Spectroscopy*. Perkin-Elmer Corporation (1978).

[124]   J.H. Scofield, *J. Electron Spectrosc. Rel. Phen.* **8**, 129 (1976).

[125]   R. R. Pawar, *Current Science*, **36** (1967) 428.

[126]   H. Jehn, P. Ettmayer: *J. Less-Common Met.*, **58** (1978) 85.

[127]   J.-G. Choi, *Korean J. Chem. Eng.*, **28(4)** (2011) 1133.

[128]   G.T. Kim, T.K. Park, H. Chung, Y.T.Kim, M. H. Kown, J. G. Choi, *Appl. Surf. Sci.* **152** (1999) 35.

[129] Y. Wang, R. Y. Lin. *Materials Science and Engineering B* **112** (2004) 42.

[130] Z.B. Zhaobin Wei, P. Grange, B. Delmon. *Applied Surface Science* **135** (1998) 107.

[131] Takano I., Isobe S., Sasaki T.A., Baba Y. *Appl. Surf. Sci.* **37** (1989) 25.

[132] N. Laidani, M. Anderle, R. Canteri, L. Elia, A. Luches, M. Martino, V. Micheli, G. Speranza, *Appl. Suf. Sci.* **157** (2000) 135.

[133] V. Linss, S.E. Rodil, P. Reinke, M.G. Garnier, P. Oelhafen, U. Kreissig, F. Richter, *Thin Solid Films*. **467** (2004) 76.

[134] J. P. Riviere, M. Cahoreau, and Y. Pacaud, *Thin Solid Films* **227** (1993) 44.

[135] X.-A. Zhao, C. W. Ong, K. F. Chan, Y. M. Ng, Y. C. Tsang, C. L. Choy, and P. W. Chan, *J. Vac. Sci. Technol. A* **15** (1997) 2297.

[136] H. P. Baldus, and M. Jansen, *Angewandte Chemie-International Edition in English*, **36(4)** (1997) 329.

[137] C. Guimon, D. Gonbeau, G. P. Guillouzo, O. Dugne, A. Guette, R. Naslain, and M. Lahaye, *Surf. Interface Anal.*, **16** (1990) 440.

[138] C.D. Wagner, J. F. Moulder, L. E. Davis, W. M. Riggs. Perking-Elmer Corporation, Physical Electronics Division (Appendix).

[139] G. Mavel, J. Escard, P. Costa, Castaing, *J. Surf. Sci.* **35** (1973) 109.

[140] I. Konyashin, J. Bill, and F. Aldinger, *Chem. Vapor Deposition*, **3(5)** (1997) 239.

[141] D. Litvinov and S. Khizroev, *Appl. Phys. Lett.*, **74(7)** (1999) 955.

[142] D. Litvinov and R. Clarke, *Appl. Phys. Lett.*, **71** (1997) 1969.

[143] S.-H. Lin, and B. Feldman, *Solid State Commun.*, **96(1)** (1995) 29.

[144] R. J. Nemanich, Annu. *Rev. Mater. Res.*, **21** (1991) 535.

[145] R. G. Wilson, F. A. Stevie, and C. W. Magee. *Secondary ion mass spectrometry*. Wiley, New York, (1989) App E.

[146] A. Ganin, Dissertation: *Plasma-unterstützte Herstellung von Übergangsmetallnitriden*, Universität Stuttgart (2005).

[147] J.E. Lowther, *Journal of Alloys and Compounds* **364** (2004) 13.

[148] R.W.G. Wyckoff, *Crystal Structures*, Interscience Publishers, Easton, PA, USA (1960).

[149] D. Balzar, H. Ledbetter, *J. Appl Cryst.*, **26** (1993), 97.

[150] J. I. Langford, *J. Appl. Cryst.* **11** (1978) 10.

[151] D. Balzar and H. Ledbetter, *Adv. X-ray Anal.* **38** (1995) 397.

[152] D. Balzer, *Voigt-function model in diffraction line-broadening analysis, a chapter to appear in Microstructure Analysis from Diffraction, edited by R. L. Snyder, H. J. Bunge, and J. Fiala, International Union of Crystallography (1999).* The chapter is downloaded from http://www.ccp14.ac.uk/ccp/web-mirrors/balzar/div853/balzar/IUCRbook.pdf [last visited 30.04.2012].

[153] W. A. Rachinger, *J. Sci. Instrum.* **25** (1948) 254.

[154] D. Louer and J. I. Langford, *J. Appl. Cryst.* **21** (1988) 430.

[155] E. J. Sonneveld, R. Delhez, Th. H. de Keijser, and E. J. Mittemeijer *Mat. Sci. Forum* **(79-82)** (1991) 85.

[156] G. Abadias, A. Michel, C. Tromas, C. Jaouen, and S.N. Dub. *Surface and Coatings Technology*. **202** (2007) 844.

[157] G. Abadias, L. E. Koutsokeras, P. A. Patsalas, W. Leroy, D. Depla, S.V. Zlotsi, and V.V. Uglov. *In-Situ Stress Evolution during Growth of Transition Metal Nitride Films and Nanocomposites. Nanomaterials: Applications and Properties (NAP-2011).* Vol. 1-II, pp.355-364.

[158] R H Knibbs. *J. Phys. E: Sci. Instrum.* **2** (1969) 515.

[159] Louis E. Toth, Refractory Metals, Transition Metal Carbides and Nitrides, Academic Press, New York and London (1971) p.4, 5, 31-34.

[160] A.Lahav, K. A. Grim, and I. A. Blech. *J. Appl. Phys.* **67**, (1990) 734.

[161] C. Sarioglu, U. Demirler, M. K. Kazmanli, and M. Urgen, *Surface and Coatings Technology* **190** (2005) 238.

[162]   G. Stoney, *Proc. R. Soc. Lond.* A May 6, **82** (1909) 172.

[163]   W. Ni, Y.-T. Cheng, C.-M. Cheng, and D. S. Grummon, *J. Mater. Res.* **19** (2004) 149.

[164]   E. Riedo and H. Brune, *Appl. Phys. Lett.* **83** (2003)1986.

[165]   W. C. Oliver and G.M. Pharr, *J. Mater. Res.* **19(1)** (2004) 3.

[166]   A. Bolshakov and G.M. Pharr, *J. Mater. Res.* **13(4)** (1998) 1049. s

[167]   Thorsten Staedler. Ph.D. Thesis, Technischen Universität Braunschweig, (2001).

[168]   Y.-T. Cheng and C.-M. Cheng, *Philos. Mag. Lett.* **78** (1998) 115.

[169]   S. Nakayama, *Pure Appl. Chem.*, **62(9)** (1990) 1751.

[170]   M. K. Kazmanli, M. Urgen, A. F. Cakir, *Surf. Coat. Technol.* **167** (2003) 77.

[171]   J. Danroc, A. Aubert and R. Gillet, *Thin Solid Films*, **153** (1987) 281.

[172]   J. Valli, U. Mäkelä and H. T. G. Hentzell, *J. Vac. Sci. Technol. A*, **4** (1986) 2850.

[173]   V.P. Anitha, S. Vitta and S. Major, *Thin Solid Films*, **245(1-2)** (1994) 1.

[174]   P. J. Rudnik, M. E. Graham, and W. D. Sproul, *Surf. Coat. Technol.*, **49(1-3)** (1991) 293.

[175]   T. Suszko, W. Gulbiński, and J. Jagielski, *Surf. Coat. Technol.*, **194(2-3)** (2005) 319.

[176]   E. O. Hall, *Proc. Phys. Soc. B* **64**, (1951) 747.

[177]   N. J. Petch, *J. Iron Steel Inst.* **174**, (1953) 25.

[178]   E. Arzt, *Acta Mater.* **46** (1998) 5611.

[179]   P. H. Mayrhofer, Habilitation thesis, University of Leoben (2004).

[180]   J. Vlček, Š. Potocký, J. Čížek, J. Houška, M. Kormunda, and P. Zeman, *J. Vac. Sci. Technol. A* **23(6)** (2005) 1513.

[181]   J. Houška, J. Vlček, Š. Potocký, V. Peřina, *Diamond and Related Materials* **16** (2007) 29.

[182]   P. T. B. Shaffer, E. D. Whitney, US Patent 35547171971 (1968).

[183]   W. Dressler, R. Riedel, *Int. J. Refract. Met. Hard Mater.* **15** (1997) 13.

[184]   A. Badzian, T. Badzian, W. D. Drawl, R. Roy, *Diamond Relat. Mater.* **7** (1998) 1519.

[185]   A. Jalowiecki, J. Bill, M. Friess, J. Mayer, F. Aldinger, R. Riedel, *Nano-Structured Mater.* **6** (1995) 279.

[186]   M. A. Rooke, P. M.A. Sherwood, *Chem. Mater.* **9** (1997) 285.

[187]   M. Haltrich, G. Wahl, J. Arndt, R. Suchentrunk, *Proc. Electrochem. Soc.* **25** (1997) 1223.

[188]   D. Hegemann, R. Riedel, C. Oehr, *Chem. Vap. Deposition* **5** (1999) 61.

[189]   Y. Manabe, T. Mitsuyu. *J. Appl. Phys.* **66** (1989) 2475.

[190]   M. M. Guraya, H. Ascolani, G. Zampieri, J. H. Dias da Silva, M. P. Cantão, and J. I. Cisneros, *Phys. Rev. B* **49** (1994) 13446.

[191]   D. E. Koteckia, and J. D. Chapple-Sokol, *J. Appl. Phys.* **77(3)** (1995) 1284.

[192]   R. E. Sah, F. Rinner, H. Baumann, R. Kiefer, M. Mikulla, G. Weimann, and M. Dammann, *J. Electrochem. Soc.*, **150(7)** (2003) F129.

[193]   M. J. Hernández and M. Cervera and J. Piqueras and M. A. González and M. Avella and T. del Caño and J. Jiménez, *Journal of The Electrochemical Society*, **154(4)** (2007) H325.

[194]   Ines Dani, PhD thesis, ECR-Plasmadiagnostik im System Ar-H$_2$-N$_2$-TMS und Charakterisierung der entstehenden SiC$_x$N$_y$:H-Schichten, Technischen Universität Chemnitz (2001).

[195]   J. J. Wu, K.H. Chen, C. Y. Wen, L. C. Chen, X.-J. Guo, H. J. Lo, S. T. Lin, Y.-C. Yu, C.-W. Wang, E.-K. Lin, *Diamond and Related Materials,* **9(3–6)** (2000) 556.

[196]   L. Barbadillo and M. Cervera and M. J. Hernández and P. Rodríguez and J. Piqueras and S. I. Molina and A. Ponce and F. M. Morales, *Applied Physics A-materials Science and Processing,* **76(5)** (2003) 791.

[197]   Cervera, M. J. Hernandez, J. Piqueras, C. Morant, P. Prieto, E. Elizalde, snd J. M. Sanz, *J. Vac. Sci. Technol. A*, **22** (2004) 640.

[198]   A. Vijayakumar, R. M. Todi, and K. B. Sundaram. *Journal of the Electrochemical Society*, **154(4)** (2007) H271.

[199]   J. Houska, J. Vlček, S. Hreben, M. M. M. Bilek and D. R. McKenzie. *Europhysics Letters*, **76(3)** (2006) 512.

[200] J. Houška, J. Čapek, J. Vlček, M. M. M. Bilek and D. R. McKenzie. *J. Vac. Sci. Technol. A*, **25(5)** (2007) 1412.

[201] J. Čížek, J. Vlček, Š. Potocký, J. Houška, Z. Soukup, J. Kalaš, P. Jedrzejowski, J.E. Klemberg-Sapieha, L. Martinů, *Thin Solid Films* **516** (2008) 7286.

[202] J. Čapek , S. Hřeben, P. Zeman, J. Vlček, R. Čerstvý, J. Houška. *Surface and Coatings Technology* **203** (2008) 466.

[203] J. Kalaš, R. Vernhes, S. Hřeben, J. Vlček , J.E. Klemberg-Sapieha, L. Martinu. *Thin Solid Films* **518** (2009) 174.

[204] O. Durand-Drouhin, M. Lejeune, M. Clin, M., and J. Henocque, *Mater. Sci. Semicond. Proc.*, **4(1–3)** (2001) 335.

[205] J. Binner and Y. Zhang, Journal of Materials Science Letters 20 (2001) 123.

[206] L. Bergström, R. J. Pugh, *Journal of the American Ceramic Society*, **72(1)** (1989) 103.

[207] M.R. Alexander, R.D. Short, F.R. Jones, M. Stollenwerk, J. Zabold, W. Michaeli, *J. Mater. Sci.* **31** (1996) 1879.

[208] T. Shirasaki, A. Derré, M. Ménétrier, A. Tressaud, and S. Flandrois, *Carbon* **38** (2000) 1461.

[209] F. J. Gómez, P. Prieto, E. Elizalde, and J. Piqueras, *Appl. Phys. Lett.* **69** (1996) 773.

[210] X.-C. Xiao, Y.-W. Li, L.-X. Song, X.-F. Peng, and X.-F. Hu, *Appl. Surf. Sci.* **156** (2000) 155.

[211] T. Berlind, N. Hellgren, M. P. Johansson, and L. Hultman, *Surf. Coat. Technol.* **141** (2001) 145.

[212] J. Zemek, M. Jelínek, V. Vorlíček, M. Trchová, and J. Lančok, *Diamond Relat. Mater.* **9** (2000) 548.

[213] Y. Gao, J. Wei, D. H. Zhang, Z. Q. Mo, P. Hing, and X. Shi, *Thin Solid Films* **377** (2000) 562.

[214] G. Soto, E. C. Samano, R. Machorro, and L. Cota, *J. Vac. Sci. Technol. A* **16** (1998) 1311.

[215] H. Lutz, M. Bruns, F. Link, and H. Baumann, *Thin Solid Films* **332** (1998) 230.

[216] J. Zemek, A. Luches, G. Leggieri, A. Fejfar, and M. Trchova, *J. Electron Spectrosc. Relat. Phenom.* **76**, (1995) 747.

[217] S. M. Castanho, R. Moreno, and J. L. G. Fierro, *J. Mat. Sci.* **32** (1997) 157.

[218] E. Paparazzo, *J. Phys. D.* **20** (1987) 1091.

[219] E. Paparazzo, *Journal of Electron Spectroscopy and Related Phenomena*, 50(1) (1990) 47.

[220] V.I. Nefedov, D. Gati, B.F. Dzhurinskii, N.P. Sergushin, Y.V. Salyn, *Zh. Neorg. Khimii* **20** (1975) 2307.

[221] Strohmeier B.R., *Appl. Surf. Sci.* **40** (1989) 249.

[222] G. Spitzer, D. A. Kleinman, and D. Walsh, *Phys. Rev.* **113,** 127 (1959).

[223] D. R. Lee, G. Lucovsky, M. S.Den, and Ch. Magee, *J. Vac. Sci. Technol.* A, **13** (1995) 1671.

[224] Polycrystalline 3C-SiC which we deposited on Si(100) wafer by means of MWCVD at 700°C (not shown here).

[225] M.J. Hernandez, J. Garrido, J. Piqueras: *J. Electrochem. Soc.* **141(11)** (1994) 3234.

[226] D.K. Basa, F.W. Smith: *Thin Solid Films* **192** (1990) 121.

[227] Y. Catherine, G. Turban, *Thin Solid Films* **60**, (1979) 193. N. Saito, T. Yamada, Y. Yamaguchi, I. Nakaaki, N. Tanaka: *Philos. Mag. B* **52** (1985) 987. S. Day, D. Das, A.K. Barna: *Solar Energy Mater.* **15** (1987) 45. H. Rubel, B. Schroeder, W. Fuhs, J.K. Krauskopf, T. Rupp, K. Bethge: *Phys. Status Solidi.* **139** (1987) 131. S.W. Rynders, A. Sheeline, P.W. Bohm: *J.Appl. Phys.* **69** (1991) 2951.

[228] E. G. Brame, J. L. Margrave, and V. W. Meloche, *J. Inorg. Nucl. Chem.* **5** (1957) 48.

[229] Lehmann, W.J. and Shapiro, I., *Spectrochim. Acta* **17(4)** (1961) 396.

[230] Mutsukura, N. and Akita, K., *Thin Solid Films*, **349** (1999) 115.

[231] Geick, R., Perry, C.H., and Rupprecht, G., *Phys. Rev.* **146(2)** (1966) 543.

[232] S.-H. Lin, B. Feldman, *Solid State Commun.* **96(1)** (1995) 29.

[233]   R.J. Nemanich, *Annu. Rev. Mater. Res.* **21** (1991) 535.

[234]   F.J. Gomez, J. Martinez, J. Garrido, C. Gomez-Aliexandre, J. Piqueras, *J. Non-Cryst. Solids* **191** (1995) 164.

[235]   Z. J. Zhang, S. Fan, C.M. Lieber, *Appl. Phys. Lett.* **66** (1995) 3582.

[236]   V.P. Tolstoy, I. V. Chernyshova, and V. A. Skryshevsky, *Handbook of Infrared Spectroscopy of Ultrathin Films*, John Wiley & Sons, New York (2003) pp. 445- 452.

[237]   Y. Catherine and G.Turban, *Thin Solid Films*, **70** (1980) 101.

[238]   K. B. Clark, J. A. Bardwell, and J.-M. Baribeau, *J. Appl. Phys.* **76** (1994) 3114.

[239]   Z.-H. Zhou, E. S. Aydil, R. A, Gottscho, Y. J. Chabal, and R. Reif, *J. Electrochemical Soc.* **142** (1993) 195.

[240]   K. M. Mar and G. M. Samuelson, *Solid State Technol.*, (1980) 137.

[241]   J. Musil, F. Kunc, P. Zeman, H. Polakova, *Surface and Coatings Technology* **154** (2002) 304.

[242]   S. Nakayama, *Pure Appl. Chem.* **62(9)** (1990) 1751.

[243]   J. H. Kaufman, S. Metin, and D. D. Saperstein, *Phys. Rev. B*, **39** (1989)13053.

[244]   (a) W. J. Zhang and S. Matsumoto, *Chem. Phys. Lett.* 330 (2000) 243. W. J. Zhang and S. Matsumoto, K. Kurashima, and Y. Bando, *Diamond Relat. Mater.* **10** (2001) 1881. W. J. Zhang, C. Y Chan, X. M. Meng, M. K. Fung, I. Bello, Y. Lifshitz, S.-T. Lee, and X. Jiang. *Angew. Chem., Int. Ed.* **44** (2005) 4749.
          (b) W. J. Zhang, Y. M. Chong, I. Bello and S. T. Lee, *J. Phys. D: Appl. Phys.* **40** (2007) 6159 and referenced cited therein.
          (c) K. Larsson, *Thin Solid Films*, **515(2)** (2006) 401. K. Larsson and J.-O. Carlsson, J. *Phys. Chem. B*, **103 (31)** (1999) 6533.

[245]   W. K. Choi, T. Y. Ong, L. S. Tan, F. C. Loh, K.L. Tan, *J. Appl. Phys.* **83** (1998) 4968.

[246]   A.Y. Liu, M.L. Cohen, *Phys. Rev. B* **41** (1990) 10727.

[247]   D.H. Zhang, Y. Gao, J. Wie and Z.Q. Mo. *Thin Solid films* **377-378** (2000) 607.

[248]   R. Riedel, *Adv. Mater.* **4(11)** (1992) 759.

[249]   A. Leyland, A. Matthews, Wear **246** (2000) 1.

[250]   J. Musil, *Surface and Coatings Technology* **125** (2000) 322.

[251]   J. Musil, *Surface and Coatings Technology* **201** (2007) 5148.

[252]   K. Kajihara, H. Kamioka, and M. Hirano, *J. Appl.Physics* **98** (2005) 013529.

[253]   Yu. G. Gogotsi, V. A. Lavrenko, *Corrosion of High-Performance Ceramics*. Springer-Verlag, Berlin-Heidelberg, (1993).

[254]   M.S. Wagner, D.J. Graham, B.D. Ratner, D. G. Castner, *Surface Science* **570** (2004) 78.

[255]   G. Lucovsky, M. J. Manitini, I. K. Srivastava, and E. A. Irene, *J. Vac. Sci. Technol. B* **5** (l987) 530.

[256]   S.S. Chao, Y. Takagi, G. Lucovsky, P. Pai, R.C. Custer, J.E. Tyler, J.E. Keem. *Applied Surface Science* **26** (1986) 575.

[257]   R. L. Siqueira, I. V. P. Yoshida, L. C. Pardini, M. A. Schiavon, *Materials Research* **10(2)** (2007) 147.

[258]   G. D. Soraru, N. Dallabona, C. Gervais, F. Babonneau, *Chem. Mater.* 11 (1999) 910.

[259]   C. T. Kirk. *Phys. Rev. B* **38** (1988) 1255.

[260]   I. P. Lisovskii, V. G. Litovchenko, V. G. Lozinskii, and G. I. Steblovskii, *Thin Solid Films* **213(2)** (1992) 164.

[261]   M. Nakamura, Y. Mochizuki, K. Usami, Y. Itoh, and T. Nozaki, *Solid State Communication*, **50** (1984) 1079.

[262]   H. Ono, T. Ikarashi, K. Ando, and T. Kitano, *J. Applied Physics* **84** (1998) 6064.

[263]   G. Lucovsky, S. Y. Lin, P. D. Richard, S. S. Chao, Y. Takagi, P. Pai, J. E. Keem, and J. E. Taylor, *J. Non-Crystalline Solids* **75** (1985) 429.

[264]   K. A. Buckle, K. Pastor, C. Constantine, and D. Johnson, *J. Vac. Sci. Technology B* **10** (1992) 1133.

[265]   D. Tsu, G. Lucovsky, and B. Davidson. *Phys. Rev. B* **40** (1989) 1795.

[266]   J. Knights, R. Street, and G. Lucovsky. *J. Non-cryst. Solids* (**35- 36)** (1980) 279.

[267]   B. Hinds, F. Wang, D. Wolfe, C. Hinkle, and G. Lucovsky*J. Vac. Sci. Tech. B* **16** (1998) 2171.

[268]   S. G. Motka, S. P. Yawale, S. S. Yawale, *Bull. Mater.Sci.* **25** (2002) 75.

[269]   G. Fuxi, *Optical and Spectroscopic Properties of Glass*, Springer-Verlag, Berlin (1991) p. 32.

[270]   L. van Vaeck, A. Adriaens, and R. Gijbels, *Mass Spectrom. Rev.* **18** (1999) 1.

[271]   T. Jäschke and M. Jansen, *Journal oft he European Ceramic Society*, **25** (2005) 211.

[272]   M. Jansen, *Solid State Ionics* (**101–103)** (1997) 1.

[273]   M. Kroschel, Amorphe B/Si/C/N-Hochleistungskeramiken aus Einkomponenten-vorläufern, dissertation (2001).

[274]   M. Gardos and S. Gabelich, *Tribology Letters* **6** (1999) 79.

[275]   M. Gardos and S. Gabelich, *Tribology Letters* **6** (1999) 87.

[276]   M. Gardos and S. Gabelich, *Tribology Letters* **6** (1999) 103.

[277]   H. Ronkainen, K. Holmberg, *Environmental and Thermal Effects on the Tribological Performance of DLC Coatings*. In *Tribology of diamond-like carbon films*, A. Erdemir, C. Donnet. (eds) Springer (2008).

[278]   M. Gardos, *Tribology Transactions* **31(2)** (1988) 214.

[279]   W. O. Winer, *Wear* **10** (1967) 422.

[280]   D. C. Cranmer, *Tribol. Trans.* **31** (1988) 164.

[281]   A. Voevodin and J. S. Zabinski, *Thin Solid Films* **370** (2000) 223.

[282]   K. Kutschej, et al. *Surf. Coat. Technol.* **(188-189)** (2004) 358.

[283]   P. H. Mayrhofer, *et al. Surf. Coat. Technol.* **(177-178)** (2004) 341.

[284]   R. Franz, J. Neidhardt, B. Sartory, R. Kaindl, R. Tessadri, P. Polcik, V. H. Derflinger, and C. Mitterer, *Tribology Letters* **23(2)** (2006) 101.

[285]   A. Erdemir, C. Bindal, C. Zuiker, and E. Savrun. *Surface and Coatings Technology* **86-87** (1996) 507.

[286]   A. Erdemir, G. R. Fenske, R. A. Erck, F. A. Nicholas, D. E. Bush, *Lubr. Eng,* **47** (1991) 179.

[287]   A. Erdemir, O. L. Eryilmaz, G. R. Fenske, *Surf. Eng,* **15(4)** (1999) 291.

[288]   X. Ma, W. N. Unertl, *J. Mater. Research*, **14(8)** (1999) 3455.

[289]   A. Abou Gharam, M.J. Lukitsch, M.P. Balogh, and A.T. Alpas, *Thin Solid Films* **519(5)** (2010) 1611.

[290]   R. L. Johnson, and H. E. Sliney, *Ceramic Bulletin.* **41** (1962) 504.

[291]   M. B. Peterson, S. F. Murray, and I. J. Florek, *ASLE Trans..* **2** (1960) 225.

[292]   B. Prakash, J. P. Celis, *Tribol Lett.* **27** (2007) 105.

[293]   Y. Pauleau, P. B. Barna. *Chapter entitled: Solid lubricant coatings: Their performance and applicability at temperature extremes.* In *Protective Coatings and Thin Films: Synthesis, Characterization and Applications.* (E. W. Roberts, J. J. Anderson and S. G. Gould) p.148.

[294]   D. Mocaer, R. Pailler, R. C. Naslain, Richard, J. P. Pillot, J. Dunogues, et al. *J. Mater. Sci.* **28** (1993) 2615. J. Bill and F. Aldinger, *Adv. Mater.* **7** (1995) 9. M. Monthioux, O. Delverdier, *J. Eur. Ceram. Soc.* **16** (1996) 721. H. J. Kleebe, D. Suttor, H. Müller, G. Ziegler, *J. Am. Ceram. Soc.* **81** (1998) 2971. R. Riedel, H. J. Kleebe, H. Schönfelder, F. Aldinger. *Nature* **374** (1995) 526. R. Riedel, W. Dressler. *Ceram. Int.* **22** (1996) 233.

[295]   J.M. Martin, T. Le Mogne, and M. Gardos, *Proceedings of the Conference of ITC*, Nagoya, Japan, (1990) 1407.

[296]   C. Muratore, J.J. Moore and J.A. Rees, *Surf. Coat. Technol.* **163–164** (2003) 12.

[297]   K. Oguri and T. Arai, *Surface and Coatings Technology,* **47** (1991) 710.

[298]   F Zhao, H X Li, L Ji, Y F Mo, WL Quan, H D Zhou and J M Chen. *J. Phys. D: Appl. Phys.* **42** (2009) 165407.

[299]   S. Wilson and A.T Alpas, *Wear* **245** (2000) 223.

[300]   J. Xu and K. Kato, *Wear,* **245** (2000) 61.

[301] Y. Zhang, G.P. Ding, Y.C. Zhou, and B.C. Cai, *Materials Letters* **55** (2002) 285.

[302] S. Wilson and A.T. Alpas, *Wear* **245** (2000) 223.

[303] P. Cong, T. Li, Sh. Mori. *Wear* **252** (2002) 662. And reference (3) cited therein.

[304] S. H. Kim, J. W. Jang, S. S. Kang, K. H. Kim, *Journal of Materials Processing Technology* **(130-131)** (2002) 283.

[305] I.-W. Park, B. Mishra, K.H. Kim and J.J. Moore, *Materials Science Forum* **539-543** (2007) 173.

[306] In-Wook Park, Sung Ryong Choi, Ju Hyung Suh, Chan-Gyung Park, Kwang Ho Kim, *Thin Solid Films* **(447-448)** (2004) 443.

[307] A. Erdemir, C. Bindal, and G. R. Fenske, *Appl. Phys. Lett.* **68** (1996) 1637.

[308] D. Kurapov and J. M. Schneider, *Plasma Chemistry and Plasma Processing*, **25(6)** (2005) 613.

[309] C. Bindal and A. Erdemir, *Appl. Phys. Lett.* **68** (1996) 923.

[310] Y. Tian, A. F. Bastawros, C. C. H. Lo, A. P. Constant, A. M. Russell, and B. A. Cook, *Appl. Phys. Lett.* **83** (2003) 2781.

[311] W. -J Wu, M.-H. Hon, *Surf. Coat. Technol.* **111** (1999) 134.

[312] H. Liu, A. Tanaka, K. Umeda, *Thin Solid Films* 346 (1999) 162.

[313] A.Vanhulsel, B. Blanpain, J.-.P. Celis, J. Roos, E. Dekempeneer, and J. Smeets, *Surf.Coat. Technol.* **98** (1998) 1047. A. Erdemir, C. Donnet. *Tribology of diamond and diamond-like carbon films: an overview*. In *Wear – Materials, Mechanisms and Practice*. G.W. Stachowiak (ed.), Wiley, London, (2005). A. Erdemir, G. R. Fenske, *Tribol. Trans.* **39(4)** (1996) 787. H. Liu, A. Tanaka, K. Umeda, *Thin Solid Films* **346** (1999) 162.

[314] Y. Sun, D. Zuo, D. Li, R. Chen and M. Wang. *Key Engineering Materials*, **375-376** (2008) 52.

[315] S. Hogmark, S. Jacobson, and M. Larsson, *Wear* **246** (2000) 20.

[316] F. P. Bowden and D. Tabor, *Friction and Lubrication of Solids: Part I*, Oxford University Press, New York, (1950).

[317] S. Jahanmir, (ed.) *Friction and wear of ceramics*. Marcel Dekker Inc., New York, (1994) p.137.

[318] W. J. Wang, T. M. Wang, B. L. Chen, *Nuclear Instruments and Methods in Physics Research Section B: Beam Interactions with Materials and Atoms*, **117(1-2)** (1996) 140.

[319] K. E. Spear, P. John, and P. Dismukes, *Synthetic diamond: emerging CVD science and technology*, Electrochemical Society, John Wiley & Sons. Inc. NY (1994). p.129.

[320] B.K. Gupta, A. Malshe, B. Bhushan, V. Subramaniam, *J. Tribol.* **116** (1994) 445.

[321] C. Donnet, J. Fontaine, A. Grill and T. Le Mogne, *Tribol. Lett.* **9(3-4)** (2000) 137.

[322] J. Fontaine, C. Donnet, A. Grill and T. Le Mogne, *Surf. Coat. Technol.* **146-147** (2001) 286.

[323] A. Erdemir, C. Donnet. *Tribology of diamond and diamond-like carbon films: an overview*. In G. W. Stachoviak (ed.) *Wear Materials Mechanisms and Practice*, Wiley, London, (2005).

[324] H. Liu, A. Tanaka, K. Umeda, *Thin Solid Films* **346** (1999) 162.

CURRICULUM VITAE

Name: Hisham Abu Samra
Date of Birth: 29th October, 1975
Place of Birth: Algeria
Gender: Male
Marital Status: Married and a Father of one child
Nationality: Jordanian

Education:

1993– 1997   Bachelor of Science in Chemistry, University of Jordan, Jordan
2002– 2004   Master of Science in Chemistry, University of Siegen, Germany
2004– 2010   Research Associate "wissenschaftlicher Mitarbeiter, University of Siegen, Germany

Selected Scientific Contributions:

Peer-reviewed own publications related to this work:

H. Abu Samra, T. Staedler, J. Xia, I. Aronov, C. Jia, B. Wenclawiak and X. Jiang. "Deposition and characterisation of nanocrystalline Mo_2N/BN composite coatings by ECR plasma assisted CVD". *Surface and Coatings Technology*, **204(12-13)** (2010) 1919. (doi:10.1016/j.surfcoat.2009.11.016)

H. Abu Samra, A. Kumar, J. Xia, T. Staedler, X. Jiang. „Development of a new generation of amorphous hard coatings based on the Si–B–C–N–O system for applications in extreme conditions". *Surface and Coatings Technology*, **223** (2013) 52. (http://dx.doi.org/10.1016/j.surfcoat.2013.02.028)

Other peer-reviewed joined publications:

H. Abu Samra, R.J. Hong and X. Jiang. "The preparation of diamond/tungsten carbide composite films by microwave plasma assisted chemical vapor deposition". *Chemical Vapor Deposition* **13(1)** (2007) 17.

V. Srikanth, H. Abu Samra, T. Staedler and X. Jiang. "Nanocrystalline diamond/β-SiC composite interlayers for the deposition of continuous diamond films on W and Mo substrate materials". *Surface & Coatings Technology* **201** (2007) 8981.

M. W. Zhu, J. H. Xia, R. J. Hong, H. Abu Samra, Hui Huang, T. Staedler, J. Gong, C. Sun and X. Jiang. "Heat activated structural evolution of sol-gel derived ZnO thin films." *Journal of Crystal Growth*, **310(4)** (2008) 816.

Zhuang C., Li X., Zhao J., H. Abu Samra and Jiang X. "Fluctuations of tensile strength and hardness of c-BC2N crystals induced by difference in atomic configurations." *J. Phys.: Condens. Matter* **23** (2011) 465401.

B. Gorr, S. Burk S, T. Depka, C. Somsen, H. Abu-Samra, H.-J. Christ, and G. Eggeler. "Effect of Si addition on the oxidation resistance of Co–Re–Cr-alloys: Recent attainments in the development of novel alloys". *International Journal of Materials Research* **1** (2012) 24.

Hisham Abu Samra
October 2013